UNIVERSITÀ
DEGLI STUDI
DI PADOVA

Sede Amministrativa: Università degli Studi di Padova

Dipartimento di Scienze Chimiche

CORSO DI DOTTORATO DI RICERCA IN: Scienze ed Ingegneria dei Materiali
CICLO XXIX

Design and synthesis of metallo-supramolecular architectures towards advanced materials

Tesi svolta con il supporto finanziario della Fondazione Ca.Ri.Pa.Ro.

Coordinatore: Chiar.mo Prof. Gaetano Granozzi

Supervisore: Chiar.ma Prof. Lidia Armelao

Dottorando: Jacopo Tessarolo

ABSTRACT

Self-assembly is a key step to obtain functional supramolecular objects towards complex matter. With self-assembly of metal ions and well-designed polytopic ligands it is possible to access a particular class of supramolecular functional materials: metal-organic polygons and polyhedra endowed with confined space and functional properties deriving from the building blocks. Herein, firstly is presented a system that in solution self-assembles in a collection of Cu(II) based boxes: a rhomboid and a triangle in dynamic equilibrium. This system is a small constitutional dynamic library (CDL). The designed introduction of well-suited guests allows to orchestrate the system response and select the triangular box by host-guest interactions. This system is an excellent bench test to explore the possibility to modulate the reactivity of guest molecules. Two examples of reactivity in the environment of the triangular host are here reported: the oxidation of a guest molecule under soft conditions and an extremely selective C-N bonds cleavage of another guest molecule. The nature of this multifaceted system has been unraveled by a combination of FT-IR spectroscopy, absorption spectroscopy and single crystal structural studies. Afterward, the synthesis of two new ligands libraries, a series of bis-*β*-diketone ligands and a series of tris-*β*-diketone ligands, specifically designed for the self-assembly of metallo-supramolecular cages, has been developed. The two libraries have been combined with both *d*-block metals and lanthanoid ions in order to self-assemble metal-organic polyhedra. By reaction of the tris-*β*-diketone with Fe^{3+} ions, the rational design and the self-assembly of a series of Fe_4L_4 supramolecular tetrahedra with space confined cavities able to host guest molecules has been achieved. The formation of the capsules is confirmed by single crystal X-ray diffraction studies. The bis-*β*-diketone ligands have been reacted with Eu^{3+} ions leading to the self-assembly of a series of charged $[Eu_2L_4]^{2-}$ and neutral $[Eu_2L_3]$ dimeric capsules. In these systems, the structural features of metallo-supramolecular cages are combined with the peculiar optical properties of lanthanoid ions, leading to the self-assembly of luminescent coordination-driven capsules. The capsules have been studied through ESI-MS and ^{1}H-NMR analyses. Luminescence and quantum yields have been characterized.

INDEX

ABBREVIATIONS AND ACRONYMS

DABCO	1,4-diazabicyclo[2.2.2]octane
CCDC	Cambridge crystallographic data centre
CDL	Constitutional dynamic library
cy-C_6	Cyclohexane
DMF	Dimethylformamide
DPA	Diphenylamine
DPB	Diphenylbenzene
DPM	Diphenylmethane
ESI-MS	Electrospray ionization mass spectrometry
EtOH	Ethanol
FT-IR	Fourier transform infrared spectroscpoy
G	Guest
HMT	Hexamethylenetetramine
LOP	Lanthanide-organic polyhedra
Me3-Tr	2,4,6–trimethyl–1,3,5–triazinane
Me-Tr	1-methyl-1,3,5-triazinane
MeCN	Acetonitrile
MOP	Metal-organic polygon or polyhedra
NMR	Nuclear magnetic resonance
n-C_6	*n*-hexane
n-C_7	*n*-heptane
o-LH_2	*o*-bis(3-acetylacetone)benzene
PTA	1,3,5-triaza-7-posphaadamantane
PTAO	1,3,5-triaza-7-posphaadamantane-7-oxide
Pyr	Pyrimidine
PXRD	Powder X-ray diffraction
s-Tr	1,3,5-triazine
TEA	Triethylamine
THF	Tetrahydrofuran
TMG	1,1,3,3,-tetramethylguanidine
TPA	Triphenylamine
TPB	Triphenylbenzene
TPM	Triphenylmethane
TPPO	Triphenylphospine oxide

CHAPTER 1

Introduction

1.1 Self-assembly of coordination driven metal-organic assemblies.

Self-assembly is a crucial concept in modern science and for this reasons it has received great attention over the last decades. The study of how pre-existing components (building blocks) spontaneously organize themselves in ordered structures by means of reversible interactions is fundamental for several fields of science[1]. Self-assembly is a scale-independent phenomenon and finds applications that range from chemistry, biology and material science, to manufacturing, robotics and construction[2]. Different types of self-assembly are possible. Static self-assembly is probably the most common and leads to systems that are at global or local equilibrium while dynamic self-assembly leads to the formation of structures only if the system is dissipating energy[1]. A better knowledge of self-assembly is important in order to understand life; in fact living systems are based on cells, that can be considered as the basic structural and functional units of life. A cell, "the basic building blocks of life", derives from self-assembly of smaller molecules; for instance, lipids molecules self-assemble to form the cell membrane[3]. At the same time, it is possible to exploit self-assembly for the development of complex materials, starting from relatively simple building blocks, properly designed. This is a powerful strategy to make ensembles of nanostructures as well as complex macromolecules or functional materials. When considering self-assembly at the molecular scale, the interactions involved are non-covalent and weak interactions, such as van der Waals, electrostatic and

hydrophobic effect as well as hydrogen and coordination bonds. The presence of relatively weak interactions allows the reversibility of the processes: products can assemble and disassemble into the initial components. With a proper design of the initial building blocks, that can be molecules, metal ions, peptides or nanoparticles, it is possible to achieve a huge numbers of assemblies with a large variety and complexity of functions[4]. Weak interactions such as van der Waals, π−π stacking, dipole−dipole, hydrophobic−hydrophilic, and hydrogen bonding lack in directionality, making it difficult to predict the shape and size of the self-assembled products. At variance, metal-ligands coordination bonds are highly directional, allowing to partially design and hence to control the structure of self-assembled metal-organic assemblies. For this reason, metal-ligand based self-assembled structures have emerged as a paradigm for new materials. In this thesis, the work is focused on the self-assembly of a class of functional materials: coordination driven metal-organic assemblies. Coordination-driven molecular and supramolecular architectures are generated from the self-assembly of metal centres and well-designed polytopic ligands held together *via* coordination bonds. By combination of these building blocks it is possible to achieve a large number of systems that can be divided in three main classes: *i*) molecular assemblies[5] (grids, boxes cages, knots, rotaxanes, helicates and polyhedral capsules), *ii*) metal coordination polymers and frameworks[6], and *iii*) surface confined architectures[7] (Figure 1). The possibility to vary the metal ions and modulate the ligands allows the design of systems with a large variety of properties, which can be related to the metal, to the ligand or to their synergistic interaction. Among others, their applications include molecular storage and separation, [5b,6a] catalysis, [5b, 6a] magnetic storing, logic and electrical switches[5a] and spin valves[5c], just to cite a few.

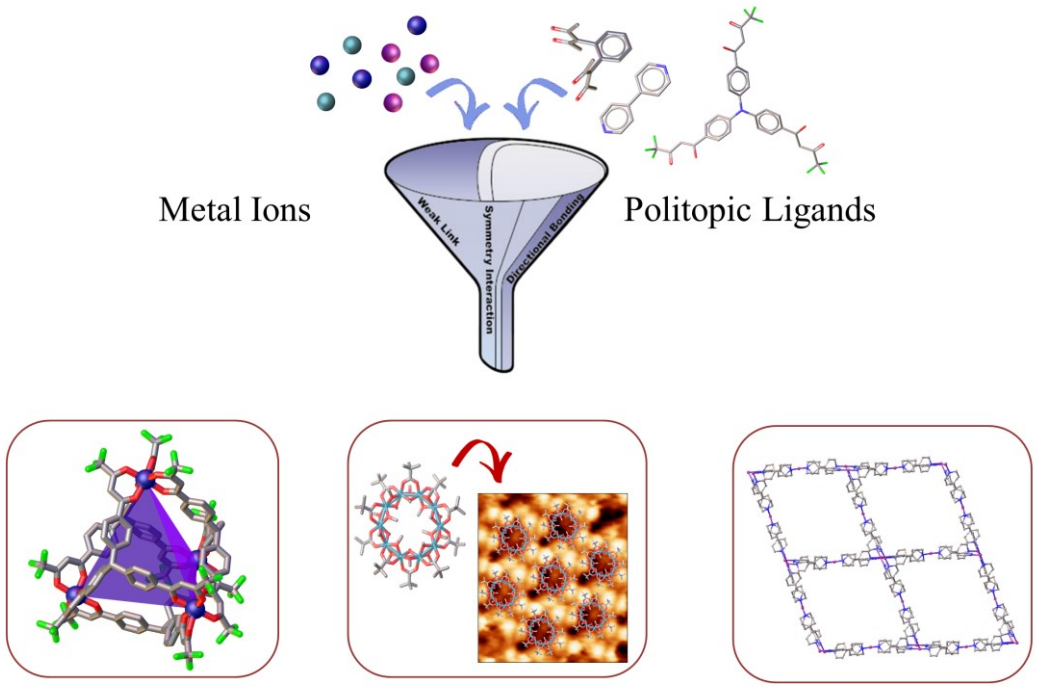

Figure 1. Coordination driven architectures: discrete molecular assemblies, surface confined architectures and extended networks.

The systems presented and studied in this work belong to the first class of these assemblies (class *i*). The study has been focused on the formation of metal-organic polygons or polyhedra (MOPs) characterized by the presence of well-defined confined space inside the metallo-supramolecular structure. This particular type of assemblies presents some common features with the metal-organic polymers and frameworks (MOFs) such as the design strategies, the synthesis and the functional properties. The design of both species relies on a similar combination of metal centres with polytopic ligands: both structures are characterized by the presence of confined space inside the structure and functional properties deriving from the building blocks and their combination. However, MOFs are infinite networks of metal centres or inorganic clusters bridged by organic ligands, while MOPs are discrete architectures obtained by self-assembly of the starting building blocks. Thus, even if the two classes of materials are strongly connected each other's, there are some remarkable differences[8].

Studies on molecular boxes and capsules have received increasing attention since the first examples of molecular squares have been reported by Fujita and co-workers[9]. Discrete 2D assemblies with closed superstructures are known as metallomacrocycles (like the circular helicates[10]) and coordination metal-organic polygons (triangles, squares,

pentagons, hexagons).[9,11] Discrete 3D assemblies are known as molecular capsules or coordination metal-organic polyhedra.[1b,12] Thanks to the power of the self-assembly process, a plethora of self-assembled cages have been obtained[13]. Great attention on these systems derives from the possibility to access coordination architectures with well-defined shapes and geometries at the nanoscale. The enclosed internal void provides an isolated environment (from bulk solution) into which guest molecules may bind. Meanwhile chemists gain experience in designing and synthesizing MOPs, the number of functions and applications exploited by these systems increases. The possibility to construct assemblies with different size and shapes of the internal cavities allows these systems to be extremely selective when interacting with specific guest molecules, becoming an important bench test for the study of self-assembled systems with molecular recognition and selection properties. Moreover, due to their structural features, combined with the possibility to introduce functional properties, these systems can find applications as molecular vessels, for compounds inclusion and molecular protection, as molecular reactors, for confined space catalysis, as drug delivery systems or to develop supramolecular sensors.[12b,13b,14b,15]

Metallo-supramolecular architectures are held together thanks to robust, but reversible, coordination bonds. Differently from other weak interactions, coordinative bonds have a variety of bonds strengths and geometries, which vary depending on the metal ion and the ligand. Furthermore, interactions between metal centres and polytopic ligands take place in specific spatial orientations. The strategies to self-assemble molecular boxes and capsules rely on the use of rigid polytopic ligands, bearing nitrogen-, oxygen-, sulphur- and phosphorous-donor atoms, and metal ions with different coordination geometries. Rigid polytopic ligands allow to define coordination vectors as the direction in which the coordination bonds take place. At the same time, coordination geometry of the metal centres defines a set of symmetric bonding vectors radiating at fixed angles from the centre of the metal ion. When considering metal complexes involving chelating ligands, the coordination vectors are considered as the vectors that bisect the chelate ring. For a proper design of the metallo supramolecular polygons and polyhedra, the building blocks should bond together in a manner that fulfil the symmetric and geometric requirements of the designed product. To do this, the polytopic ligands and the coordination sphere of the metal centres must have a symmetric shape with a C_n rotation axis with respect to the *n* binding sites. The specific spatial orientations of the metal-ligands interactions and the

symmetry of the ligand itself allow a prediction of the shape of the designed MOPs[5b,13a,16]. Figure 2 shows some examples of coordination vectors and angles deriving from the metal coordination (Figure 2 *a*) and from the ligand geometries (Figure 2 *b*), together with the C_n axis of the building blocks.

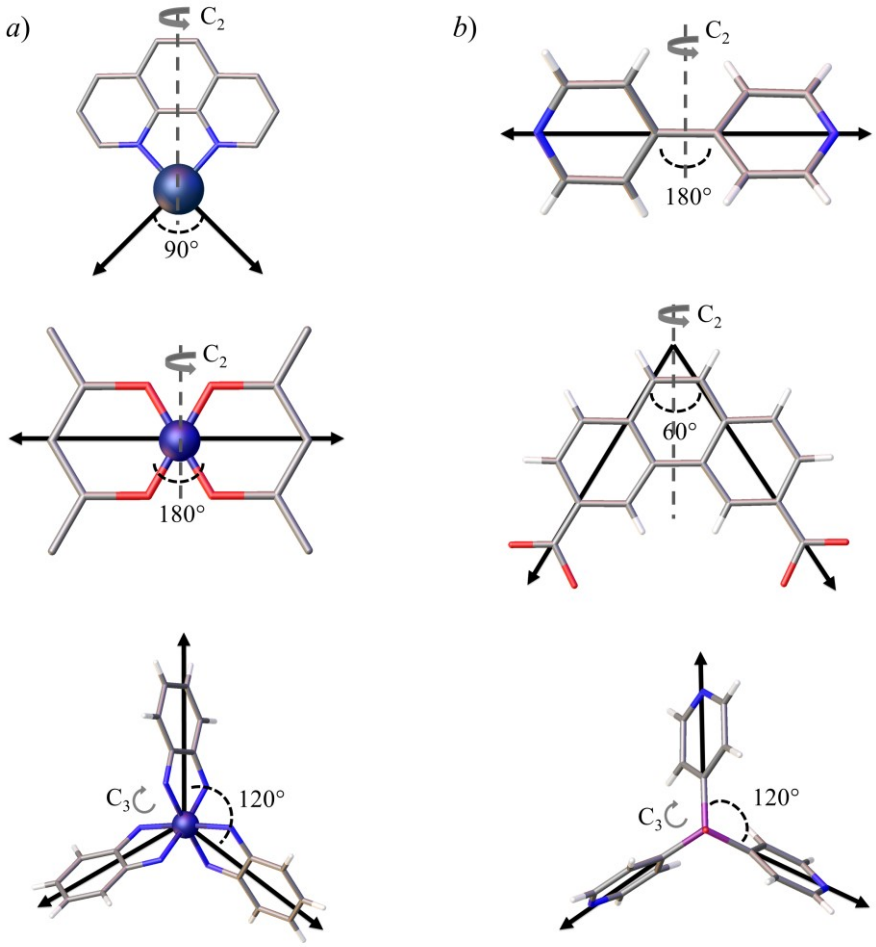

Figure 2. Examples of coordination vectors and angles for *a*) metal centres and *b*) ligand molecules.

The self-assembly process and the final obtained structures are strongly dependent on the nature of the initial building blocks. High conformational flexibility of the ligands can lead to a failure of the rational design process. For example, when comparing similar ligands, even tiny differences may affect the formation of the metallo-supramolecular architecture, making difficult to predict the structure of the final product[16,17]. This effect is amplified as the number of starting building blocks increases and the supramolecular capsule gets bigger, like for instance the self-assembling of supramolecular species with a number of components comparable with that seen in nature (≈ 100).[18] Considering the intrinsic flexibility of many of the ligands, coupled with the reversibility of coordination bonds, the formation of mixtures of oligomers in dynamic equilibrium is not uncommon.

When more assemblies are thermodynamically accessible and reversible interactions are working, a dynamic system is established. Nice examples of equilibrating architectures are the coordination *Constitutional Dynamic Libraries* (CDL), first described by Lehn, and not rare in the synthesis of discrete coordination architectures[19a,20] (Figure 3). A CDL is an ensemble of molecular or supramolecular objects in dynamic equilibrium. Such equilibrium is based on the continuous change of its constituents through dissociation and recombination of the different components.

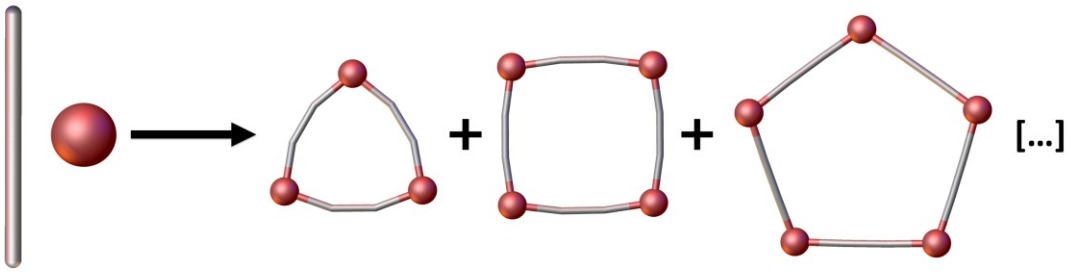

Figure 3. Schematic representations of a CDL of three or more components: a triangular trimer, a square tetramer and a pentagonal pentamer are reported.

The dynamic nature of these assemblies gives chemists the possibility to study the effect of external stimuli, in order to have the capability to control the equilibrating species and to orchestrate the system through the desired functionality. In some cases, this has been achieved by tuning the system parameters (*i.e.* concentration, solvent and temperature)[20] or through external stimuli (as for instance different cations or anions)[15], and also by the use of template molecules.[21] By means of external stimuli, complex responses can be achieved, including multiple structural rearrangements[13b]. An interesting approach to achieve and control structural rearrangements is the introduction of additional components to the system, taking advantage of the dynamic nature of these metallo-supramolecular architectures. Since building blocks of MOPs disassemble and rearrange, the addition of new components, such as different building blocks, or a change in the stoichiometry of the starting reagents, can lead to the formations of new discrete architectures accompanied by supramolecular transformations[17,22]. Moreover, the supramolecular metal-organic polygons or polyhedra are developed in order to have confined cavities able to interact with guest molecules. This allows the guest molecules to act as a stimulus for the selection of the systems. Guest molecules, as well as solvents, anions and cations, can act as a template for the system. Introduction of guest can lead to

a selection of species from CDL, or can lead to structural transformations of the starting discrete assembly[22].

Self-assembly of metallo-supramolecular cages usually leads to the formation of products that are stable at the equilibrium. In contrast, the most sophisticated supramolecular structures, *i.e.* biological systems, require a continuous consumption of energy, with the controlled reactions of reactive species as fuel, to maintain assemblies in the functional state and the system out of equilibrium[23]. The possibility to use a chemical fuel as external stimulus for these assemblies is very attractive, since this would add a temporal dimension for developing supramolecular systems with nature-like properties. Recently, Nitschke and co-workers developed a system in which a metal-organic architecture is maintained for a definite period of time by consuming a chemical reactive as fuel. This method allows a time-dependent control over guest binding, allowing to direct the uptake and release of the guest from the metallo-supramolecular host[24]. This is a very young but promising field for the functional applications of metallo-supramolecular architectures.

1.2 Supramolecular hosts to tune guest reactivity.

Due to their confined spaces MOPs can be considered as molecular flasks with a scale dimension comparable to the reactants. These systems are reminiscent of Nature's enzymes. In fact, control on the size and shape of the confined space allows metal-organic cages to be extremely selective over the substrates (guest molecules). Moreover, the possibility to functionalize the supramolecular capsule allows to obtain water soluble species, stable at physiological pH, or to have a cavity that is chemically distinct from the bulk solvent. Combination of these properties allows the access to unique chemical reactions and pathways, making metallo-supramolecular assemblies good candidates for developing artificial enzymes and to study chemical reactivity in confined space[14,25].

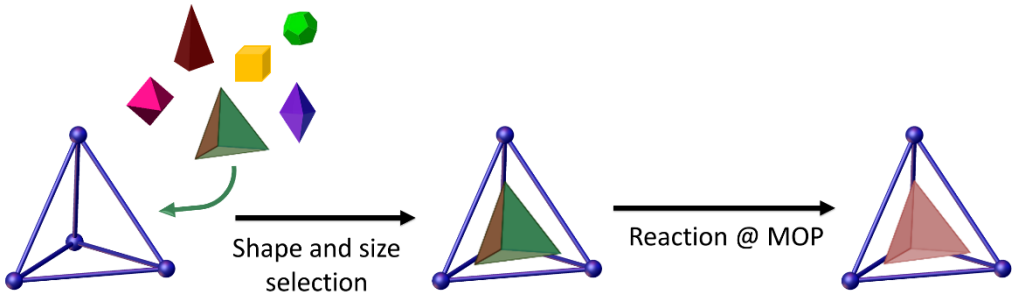

Figure 4. MOPs can select a specific guest on the base of size, shape and chemical affinity. Guests can undergo chemical reactions inside the MOP cavity.

Coordination driven supramolecular species can be used as molecular flasks to tune the reactivity of small molecules. It is possible to use the geometrical constrains of the confined space and the host-selectivity among substrates in order to stabilize specific guest, or specific conformations. MOPs can be used both for storing reactive species, *i.e.* protecting them from degradation, or for selectively induced reactivity with stereochemical control[14,26,27]. For instance, an impressive example of molecular storage has been reported by Nitschke and co-workers. They developed a system in which the highly reactive P_4 molecule is stabilized in water solution when hosted in a Fe_4L_6 metallo supramolecular assembly. The great stabilization relies on the good affinity of the P_4 guest with the host cavity, combined with the fact that the oxidised product would not fit the cavity due to steric hindrance (Figure 5 *a*). Hence, Fe_4L_6 capsule stabilizes P_4 by blocking its reactivity since P_4O_{10} can not form inside the capsule[26b]. Other examples are reported by Fujita and co-workers, in which different supramolecular capsules have been used to achieve the synthesis of unusual regioisomers, or to a high degree of selection on the substrate reactivity. Fujita reports various reactions, such as Diels-Alder cycloaddition, Knoevenagel condensation of photochemical dimerizations that lead to high degree of product selectivity when the reaction takes place in a square-pyramidal or in an octahedral cage. The stereoselectivity of the reactions is possible by taking advantage of the orientation induced by the capsule to the substrate[12b,27]. Examples have been reported on the use of MOPs as molecular containers for transition metal catalysts. In this case, transition metals catalysts are hosted inside the molecular cavity and the pocket acts as the effective reactor for chemical transformations (Figure 5 *b*). In this way, it is possible to perform homogeneous transition metal catalysis, with the advantage of a confined space, such as the selectivity on both substrates and products, and the possibility to tune the reactivity environment, for instance by creating a hydrophobic cavity in a water soluble capsule[14b,25,28]. The possibility to modulate the confined space environment properties, such as the hydrophilicity of the host cavities, has been used by Fujita et. al.[26a] to develop coordination-driven nano-spheres with general formula $Pd_{12}L_{24}$. These capsules have been used to perform the sol-gel synthesis of monodisperse oxide nanoparticles in a hydrophobic media inside their pockets. The supramolecular cage interior has been functionalised with the aim to create a hydrophilic confined space in

order to host hydrophilic species and to promote the sol-gel process inside the sphere. Letting the sol-gel process happen inside the sphere gave access to a precise control on the nanoparticles dimensions according to the volume of the supramolecular cavity (2 or 4 nm) (Figure 5 *c*)[26a]. Another approach to tune guest reactivity is to take advantage of the functional properties of the capsule. A nice example is the use of transition metals with catalytic properties directly as building blocks of the metal-organic supramolecular assembly. If a metal that can expand its coordination is present, the guest molecules can coordinate it and therefore it can be activated and undergoes chemical transformations[14].

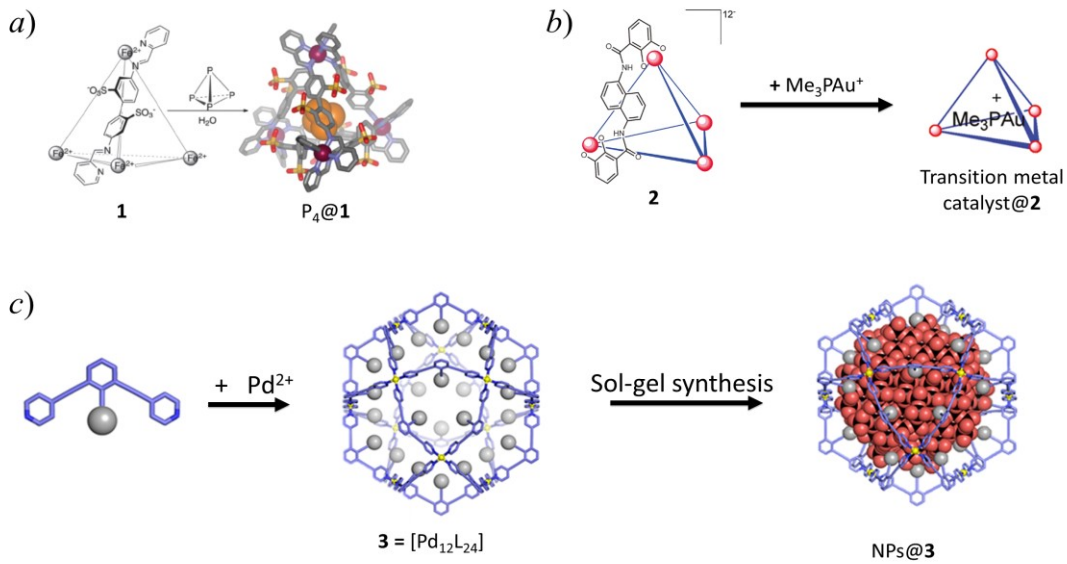

Figure 5. Selected examples of reactivity in metallo-supramolecular architectures. *a*) Highly reactive P_4 molecule is stabilized inside a supramolecular tetrahedron[26b]. *b*) Transition metal catalyst can be hosted inside metal-organic cages[28]. *c*) $Pd_{12}L_{24}$ nano-sphere has been used to synthesize precise size nanoparticles [26a].

1.3 Lanthanide based coordination-driven architectures as functional materials.

The features of the new materials derive from the metal, the ligands or from the synergy of the building blocks taken together. In order to endow the MOPs with emission properties, fluorescent polytopic ligands as components of the supramolecular architecture can be used. This approach has emerged in the last years, resulting in a variety of luminescent metal-organic polygons and polyhedra that find applications in detection of metal ions, anions and small molecules or even for mimic of natural photo-systems[29]. The introduction of functional properties in the supramolecular system through selected

fluorescent building blocks is possible in different ways. Fluorophores groups can be introduced in different positions of the ligands, for instance as *endo*- or *exo*-substituent groups, resulting in the presence of the functional groups inside or outside of the final MOP. This way, combined with the peculiar confined space of the MOPs, allows to design species with a great selectivity towards guest-analyte molecules or ions. The interaction between guest molecules and the host environment can modify the optical properties of the system, for instance by quenching or increasing the luminescence of the host-guest metallo-supramolecular architectures (Figure 6). This generates a supramolecular system that, after selection towards target guest molecules, can modify the emission properties resulting in possible applications for sensing or for optical switches.

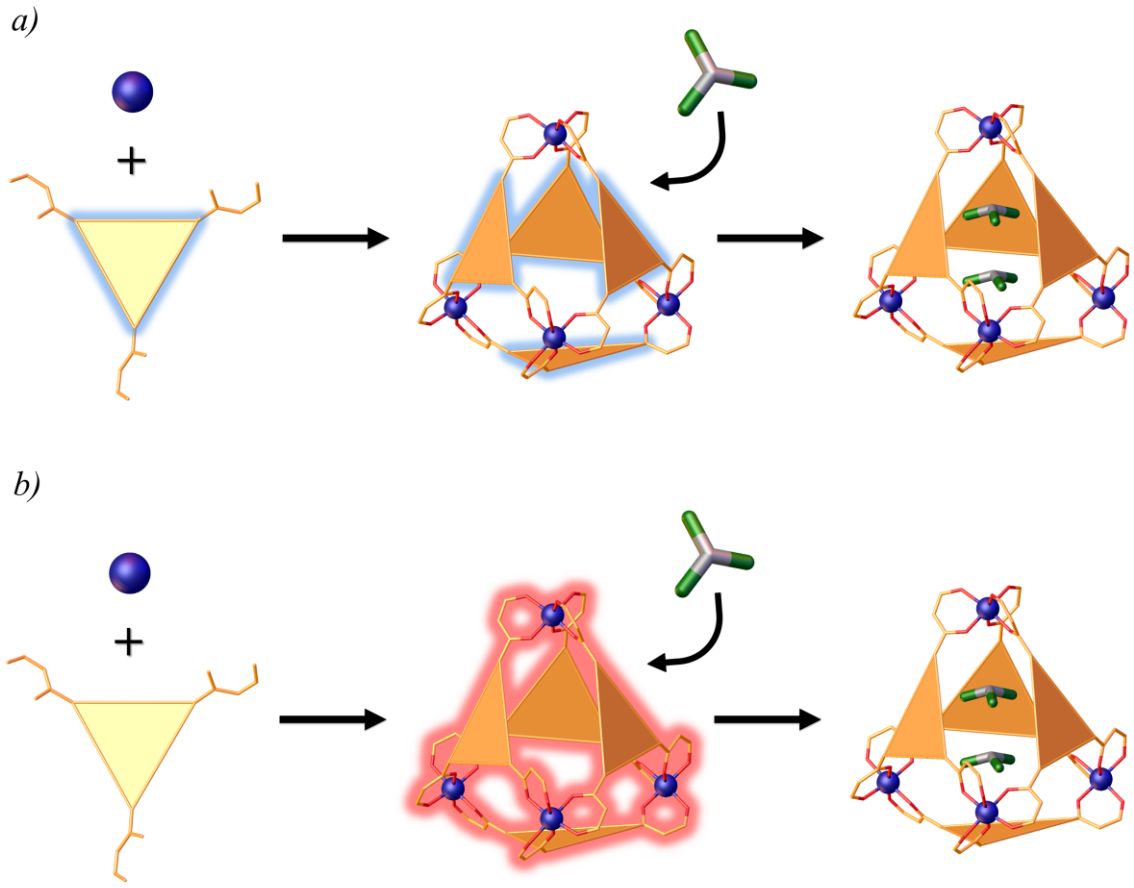

Figure 6. Scheme of the synthesis of luminescent MOPs: after the interaction with specific guest molecules luminescence is quenched. *a*) Luminescence is due to a moiety in the ligand, *b*) luminescence derives from a combination of the ligand and the metal.

Another approach to introduce light-emitting properties takes advantage of the antenna effect in lanthanide complexes (Figure 6 *b*). Up to date, most of MOPs have been

obtained starting from transition metal ions while the use of lanthanide ions as building blocks for supramolecular capsules is still in its infancy. Lanthanide-containing molecules are potential tools as luminescent probes, contrast agents and magnetic materials[30]. These properties can be combined with the peculiar structural properties of coordination-driven architectures, resulting in the self-assembly of lanthanide-organic polygons and polyhedra (LOPs). Synthesis of LOPs is less explored than their transition metals analogues since lanthanide ions can adopt a variety of coordination numbers and geometries and therefore the design and prediction of new lanthanide-based polygons and polyhedra is challenging. However, the self-assembly of LOPs is a very promising field in order to synthesize functional materials with optical and magnetic properties. Lanthanide ions have very narrow emission bands, mostly in the visible and near infrared range, resulting from shielding of the 4f orbitals by the filled 5s and 5p sub-shells. Their electronic transitions are parity forbidden, resulting in long luminescent lifetimes on the scale of the microseconds. Moreover, lanthanide ions often have unpaired f-shell electrons and exhibit strong paramagnetism, finding applications as NMR shift reagents and are promising for the development of single molecular magnets.

Interesting examples of lanthanide-based metal-organic capsules have been reported by Bunzli and Sun[31]. The authors reported a stereocontrolled self-assembly of Eu(III) tetrahedral cages with luminescent properties. Thanks to an appropriate design of the ligands, a R and S bis(tridentate) and a R and S tris(tridentate) ligands, the self-assembly of chiral supramolecular cages was controlled and the study of the self-sorting of the system was reported. When R and S bis(tridentate) ligands are combined with Eu(III), the system forms a dynamic mixture of all the possible tetrahedral capsules. When only R and S tris(tridentate) ligands are used, their chirality is transferred through the self-assembly process and the Δ and Λ chiral tetrahedral capsules are formed. Another interesting example regards an europium-based capsule, recently synthesised by Albrecht, Rissanen and co-workers, in order to develop a luminescence sensor able to interact with biological systems[32]. The authors report the self-assembly of a dimeric helicate structure able to selectively interact with adenosine monophosphate (AMP) over adenosine diphosphate (ADP) and adenosine triphosphate (ATP) molecules. Differently from the previously synthesised probes, this Eu(III)-dimeric helicate is able to interact with both the phosphate and the adenosine moieties and the interaction is clearly detected by variation on the luminescence properties of the complex. These examples show how

the combination of LOPs structural and functional properties allows to develop luminescent materials with high selectivity for molecular recognition, from chiral species to biological systems. Regarding the magnetic properties, nice examples have been reported by Yan and co-workers, in which they developed a series of triple stranded and quadruple stranded helicates, based on bis-*β*-diketonate ligands and Dy(III) lanthanide ions[33]. In one case, they have investigated the structural changes, moving from triple to quadruple stranded helicate, as function of the stoichiometry of the ligand and by blocking two Dy(III) position with a bipyridyl ligand[33a]. In the other example, the authors investigate the change of the crystal structure as function of the crystallization solvent[33b]. All this structural changes can be used to tune the magnetic properties of the systems. Magnetic studies have been performed on all the self-assembled dysprosium-based helicates showing slow magnetic relaxation under zero dc field for some of the obtained LOPs and single molecular magnet behaviour for the others.

1.4 Objective of thesis work.

Design and control over self-assembly and selection processes of MOPs is still a challenging aspect in the development of supramolecular architectures. Moreover, the possibility to endow supramolecular cages with functional properties, coupled with MOPs space confinement properties is an emerging and promising field to develop new functional materials. To this aim, this work reports the design, synthesis and characterization of new metallo-supramolecular architectures. In CHAPTER 2, the application of a previously synthesised metallo-supramolecular box that allows to tune the reactivity of guest molecules is presented. The system is a CDL composed by a dimer and a trimer, generated by Cu^{2+} ion and a bis-*β*-diketone ligand. The trimeric species is selected by the introduction of a guest molecule to the system. It has been found that this system is an excellent bench test to study the effect of metallo-supramolecular boxes on the guest reactivity. In particular, the oxidation of a guest molecule following a post-assembly functionalization approach and a highly selective guest de-methylation, activated by the metallo supramolecular host are presented and discussed. The oxidation is triggered by the addition of a co-solvent to the system that acts as an external stimulus used to drive the system through the final product. Moreover, the possibility to recover the oxidised guest molecule has been successfully explored. In the second case, templated

self-assembly allows the formation of a host-guest triangle in which the starting guest undergoes to a selective C-N bond cleavage.

In CHAPTER 3, the synthesis of two new libraries of *β*-diketone ligands is reported. The first library is composed of a series of bis-*β*-diketone ligands, while the second library by a series of tris-*β*-diketone ligands. The ligands have been specifically designed as suitable building blocks for the synthesis of coordination driven metallo-supramolecular architectures with different size and shapes, using *d*- and *f*- block metals. The chelating group of all ligands is the acetylacetone moiety, while the ligands differ for the scaffolds and the substituent groups. The different scaffolds allow to achieve supramolecular structures with different size and shape, as well as to study the effect of the flexibility of the ligand on the MOPs formation.

CHAPTER 4 reports the synthesis of new metallo-supramolecular capsules. In the first part, the self-assembly of a supramolecular tetrahedra, based on the tris-*β*-diketone ligands and Fe^{3+} ions, has been reported. Self-assembly of these building blocks lead to the formation of supramolecular tetrahedra endowed with space confined cavity, suitable for host-guest interactions. The structure of the new MOPs has been characterized by single crystal X-ray diffraction. Structural studies clearly show that these systems possess accessible cavities for guest molecules to go in or out, thus confirming that self-assembly of Fe^{3+} ions with tris-*β*-diketone ligands generates a promising system for exploring host-guest supramolecular chemistry. In the second part, the self-assembly of a series of Eu-based luminescent supramolecular capsules has been reported. The capsules have been obtained by self-assembly of Eu^{3+} with the ligands of bis-*β*-diketone library. Through a stoichiometric control of the reagents, it is possible to obtain a series of charged $[Eu_2L_4]^{2-}$ and neutral $[Eu_2L_3]$ dimeric cages. The nature of these systems has been unravelled by a combination of UV-Vis and FT-IR absorption spectroscopies, ESI-MS spectrometry, single crystal structural studies and NMR spectroscopy. Moreover, the LOPs functional properties have been investigated. Absorption, excitation and emission behaviour has been studied, and photoluminescent quantum yields have been determined.

CHAPTER 5 reports a summary of the preminent results and future perspectives for the coordination-driven assemblies described in this thesis work. CHAPTER 6 reports all the synthetic procedures and experimental details.

1.5 Bibliography.

1. G. M. Whitesides, B. Grzybowski *Science* **2002,** *295*, 2418.
2. For selected examples see: *a*) A. Falvello, S. Tibbits *Proceedings of the Association for Computer Aided Design in Architecture 2013: Adaptive Architecture*, **2013**; *b*) S.Tibbits *Architectural Design*, **2012**, *82,* 68; *c*) S. Tibbits, Self-Assembly Lab : experiments in programming matter. Abingdon, Oxon New York, NY: Routledge, **2016**; *d*) http://www.selfassemblylab.net/.
3. L. J. Prins *Acc. Chem. Res.*, **2015**, *48*, 1920.
4. For selected examples see: (*a*) J. S. Chen, P. Li, I. Hod, P. Z. Moghadem, Z. Kean, R. Q. Snurr, J. T. Hupp, O. K. Farha, J. F. Stoddart, *J. Am. Chem. Soc.* **2016**, *138*, 14242; (*b*) X. Hou, C. Ke, Y. Zhou, Z. Xie, A. Alngadh, D. T. Keane, M. S. Nassar, Y. Y. Botros, C. A. Mirkin, J. F. Stoddart, *Chem. Eur. J.* **2016**, *22*, 12301; (*c*)B. Lewandowski,G. De Bo1, J. W. Ward, M. Papmeyer, S. Kuschel1, M. J. Aldegunde, P. M. E. Gramlich, D. Heckmann, S. M. Goldup, D. M. D'Souza, A. E. Fernandes,D. A. Leigh, *Science*, **2013**, *339*, 189.
5. For selected examples see: (*a*) M. Ruben, J. Rojo, F. J. Romero-Salguero, L. H. Uppadine, J.-M. Lehn, *Angew. Chem. Int. Ed.* **2004**, *43*, 3644; (*b*) R. Chakrabarty, P. S. Mukherjee, P. J. Stang, *Chem. Rev.* **2011**, *111*, 6810; (*c*) M. Urdampilleta, S. Klyatskaya, M.-P. Cleuziou, M. Ruben, W. Wernsdorfer, *Nature Mater.* **2011**, *10*, 502.
6. For selected examples see: (*a*) G. Férey, *Chem. Soc. Rev.* **2008**, *37*, 191; (*b*) O. M. Yaghi, Q. Li, *MRS Bull.* **2009**, *34*, 682.
7. For selected examples see: (*a*) N. Lin, S. Stepanow, F. Vidal, K. Kern, M. S. Alam, S. Strömsdörfer, V. Dremov, P. Müller, A. Landa, M. Ruben, *Dalton Trans.* **2006**, 2794; (*b*) N. Lin, S. Stepanow, M. Ruben, J. Barth, *Top. Curr. Chem.* **2009**, *287*, 1; (*c*) M. Marschall, J. Reichert, A. Weber-Bargioni, K. Seufert, W. Auwärter, S. Klyatskaya, G. Zappellaro, M. Ruben, J. V. Barth, *Nature Chem.* **2010**, *2*, 131; (*d*) D. Kühne, F. Klappenberger, W. Krenner, S. Klyatskaya, M. Ruben, J. V. Barth, *PNAS* **2010**, *107*, 21332.
8. T. R. Cook, Y.-R. Zheng, P. J. Stang, *Chem. Rev.* **2013**, *113*, 734.
9. M. Fujita, J. Yazaki, K. Ogura, *J. Am. Chem. Soc.* **1990**, *112*, 5645.
10. For selected examples see: (*a*) B. Hasenknopf, J. M. Lehn, B. O. Kneisel, G. Baum, D. Fenske, *Angew. Chem. Int. Ed. Engl.* **1996**, *35*, 1838; (*b*) B. Hasenknopf, J. M. Lehn, N. Boumediene, A. DupontGervais, A. VanDorsselaer, B. Kneisel, D. Fenske, *J. Am. Chem. Soc.* **1997**, *119*, 10956; (*c*) *O.* Mamula, A. von Zelewsky, G. Bernardinelli, *Angew. Chem. Int.Ed.* **1998**, *37*, 290; (*d*) G. Mezei, P. Baran, R. G. Raptis, *Angew. Chem. Int. Ed.* **2004**, *43*, 574; (*e*) S. R. Halper, S. M. Cohen, *Angew. Chem. Int. Ed.* **2004**, *43*, 2385; (*f*) A. A. Mohamed, A. Burini, R. Galassi, D. Paglialunga, J. R. Galan-Mascaros, K. R. Dunbar, J. P. Fackler, *Inorg. Chem.* **2007**, *46*, 2348.
11. For selected examples see: (*a*) M. T. Youinou, N. Rahmouni, J. Fischer, J. A. Osborn, *Angew. Chem. Int. Ed. Engl.* **1992**, *31*, 733; (*b*) P. J. Stang, D. H. Cao, *J. Am. Chem. Soc.* **1994**, *116*, 4981; (*c*) P. J. Stang, B. Olenyuk, *Angew. Chem. Int. Ed. Engl.* **1996**, *35*, 732; (*d*) F. A. Cotton, C. Lin,

C. A. Murillo, *J. Am. Chem. Soc.* **2001**, *123*, 2670; (*e*) C. S. Campos-Fernandez, R. Clerac, J. M. Koomen, D. H. Russell, K. R. Dunbar, *J. Am. Chem. Soc.* **2001**, *123*, 773; (*f*) C. S. Campos-Fernandez, B. L. Schottel, H. T. Chifotides, J. K. Bera, J. Bacsa, J. M. Koomen, D. H. Russell, K. R. Dunbar, *J. Am. Chem. Soc.* **2005**, *127*, 12909; (*g*) S. H. Hwang, P. S. Wang, C. N. Moorefield, L. A. Godinez, J. Manriquez, E. Bustos, G. R. Newkome, *Chem. Commun.* **2005**, 4672; (*h*) G. R. Newkome, T. J. Cho, C. N. Moorefield, G. R. Baker, R. Cush, P. S. Russo, *Angew. Chem. Int. Ed.* **1999**, *38*, 3717; (*i*) J. R. Hall, S. J. Loeb, G. K. H. Shimizu, G. P. A. Yap, *Angew. Chem. Int. Ed.* **1998**, *37*, 121; (*l*) P. J. Stang, N. E. Persky, J. Manna, *J. Am. Chem. Soc.* **1997**, *119*, 4777; (*m*) P. N. W. Baxter, R. G. Khoury, J. M. Lehn, G. Baum, D. Fenske, *Chem.*s*Eur. J.* **2000**, *6*, 4140.

12. (*a*) D. L. Caulder, K. N. Raymond, *Acc. Chem. Res*. **1999**, *32*, 975; (*b*) M. Yoshizawa, J. K. Klosterman,, M. Fujita, *Angew. Chem. Int. Ed*. **2009**, *48*, 3418.
13. *(a*) T. R. Cook and P. J. Stang, *Chem. Rev.***2015**, *115,* 7001; (b) A. J. McConnell, C. S. Wood, P. P. Neelakandan and J. R. Nitschke, *Chem. Rev.***2015**, *115,* 7729.
14. (*a*) S. H. A. M. Leenders, R. Gramage-Doria, B. de Bruin and J. N. H. Reek, *Chem. Soc. Rev.*, **2015**, *44*, 433; (*b*) C. J. Brown, F. D. Toste, R. G. Bergman and K. N. Raymond, *Chem. Rev.* **2015**, *115*, 3012.
15. N. Busschaert, C. Caltagirone, W. Van Rossom and P. A. Gale, *Chem. Rev.* **2015**, *115*, 8038.
16. N. J. Young and B. P. Hay, *Chem. Comm.* **2013**, *49*, 1354.
17. J. Mosquera, T. K. Ronson, and J. R. Nitschke, *J. Am. Chem. Soc.* **2016**, *138*, 1812.
18. D. Fujita, Y. Ueda, S. Sato, H. Yokoyama, N. Mizuno, T. Kumasaka, and M. Fujita, *Chem*, **2016**, *1*, 91.
19. *a*) J.M. Lehn, *Chem. Soc. Rev.* **2007**, *36*, 151; (*b*) B. Hasenknopf, J.-M. Lehn, N. Boumediene, A. Dupont-Gervais, A. Van Dorsselaer, B. Kneisel, D. Fenske, *J. Am. Chem. Soc.***1997**, *119*, 10956.
20. For selected examples see: (*a*) T. Yamamoto, A. M. Arif, P. J. Stang, *J. Am. Chem. Soc.* **2003**, *125*, 12309; (*b*) T. Weilandt, R. W. Troff, H. Saxell, K. Rissanen, C. A. Schalley, *Inorg. Chem.* **2008**, *47*, 4588; (*c*) F. A. Cotton, C. A. Murillo, R. Yu, *Dalton Trans.* **2006**, 3900; (*d*) M. Ferrer, A. Pedrosa, L. Rodrìguez, O. Rossell, M. Vilaseca, *Inorg. Chem.* **2010**, *49*, 9438; (*e*) S. Ghosh, P. S. Mukherjee, *Inorg. Chem.* **2009**, *48*, 2605; (*f*) M. Schweiger, S. R. Seidel, A. M. Arif, P. J. Stang, *Inorg. Chem.* **2002**, *41*, 2556; (*g*) K. Uehara, K. Kasai, N. Mizuno, *Inorg. Chem.* **2010**, *49*, 2008.
21. (*a*) B. Hasenknopf, J.-M. Lehn, N. Boumediene, A. Dupont-Gervais, A. Van Dorsselaer, B. Kneisel, D. Fenske, *J. Am. Chem. Soc.* **1997**, *119*, 10956; (*b*) M. Scherer, D. L. Caulder, D. W. Johnson, K. N. Raymond, *Angew. Chem. Int. Ed.* **1999**, *38*, 1587; (*c*) Y. Kubota, S. Sakamoto, K. Yamaguchi, M. Fujita, *PNAS* **2002**, *99*, 4854; (*d*) M. Albrecht, I. Janser, J. Runsink, G. Raabe, P. Weis, R. Fröhlich, *Angew. Chem. Int. Ed.* **2004**, *43*, 6662; (*e*) C. S. Campos-Fernández, B. L. Schottel, H. T. Chifotides, J. K. Bera, J. Bacsa, J. M. Koomen, D. H. Russell, K. R. Dunbar, *J. Am. Chem. Soc.* **2005**, *127*, 12909; *(f)* M. Pawlicki, L. Latos-Grazynski, *Angew. Chem. Int. Ed*. **2012**, *51*, 11205.
22. W. Wang, Y.-X. Wang and H.-B. Yang, *Chem. Soc. Rev.*, **2016**, *45*, 2656.

23. (*a*) E. Mattia, and S. Otto, *Nature Nanotech.* **2015**, *10*, 111. (*b*) E. Karsenti, *Nature Rev. Mol. Cell Biol.*, **2008**, *9*, 255.
24. C. S. Wood, C. Browne, D. M. Wood, and J. R. Nitschke *ACS Cent. Sci.*, **2015**, *1*, 504.
25. Z. J. Wang, K. N. Clary, R. G. Bergman, K. N. Raymond and F. D. Toste, *Nature Chemistry,* **2013**, *5*, 100.
26. (*a*) Y. Inokuma, M. Kawano, M. Fujita, *Nature Chem.* **2011**, *3*, 349; (*b*) P. Mal, B. Breiner, K. Rissanen, J. R. Nitschke, *Science,* **2009**, *324*, 1697; (*c*) B. Breiner, J. R. Nitschke, J. W. Steed, P. A. Gale, *Supramolecular Chemistry: From Molecules to Nanomaterials*, **2012**, *vol. 4*, Reactivity in Nanoscale Vessels, 1575, John Wiley & Sons.
27. (*a*) T. Murase, Y. Nishijima and M. Fujita, *J. Am. Chem. Soc.* **2012**, *134*, 162. (*b*) M. Yoshizawa, M. Tamura, M. Fujita, *Science*, **2006**, *312*, 251.
28. Z. J. Wang, C. J. Brown, R. G. Bergman, K. N. Raymond, and F. D. Toste, *J. Am. Chem. Soc.* **2012**, *133*, 7358.
29. L. Xu, Y.-X. Wang, H.-B. Yang, *Dalton Trans.,* **2015**,44, 867.
30. J.-C. G. Bünzli, C. Piguet, *chem. Rev.* **2002**, *102*, 1897.
31. L.-L. Yan, C.-H. Tan, G.-L. Zhang, L.-P. Zhou, J.-C. Bünzli, Q.-F. Sun *J.Am.Chem.Soc*, **2015**, *137*, 8550.
32. J. Sahoo, R. Arunachalam, P. S. Subramanian, E. Suresh, A. Valkonen, K. Rissanen, M. Albrecht *Angew. Chem. Int. Ed.*, **2016**, *55*, 9625.
33. a) P. Chen, H. Li, W. Sun, J. Tang, L. Zhang, P. Yan, *CrystEngComm,* **2015**, *17*, 7227, b) H. Li, P. Chen, W. Sun, L. Zhang, P. Yan, *Dalton Trans.,* **2016**, *45*, 3175.

CHAPTER 2

Coordination assemblies as confined host to tune guest reactivity

2.1 Self-assembly and sorting of Cu^{2+} and bis-(3-acetylacetone)benzene molecular architectures.

Discrete boxes and cages deriving from coordination driven metallo-supramolecular assemblies are intriguing host systems to study cage-driven chemical transformations. Recently, we developed a metallo-supramolecular triangle obtained from the self-assembly of Cu^{2+} metal ions and the *ortho* bis-(3-acetylacetone)benzene ligand (*o*-LH_2), suitable for investigating the confinement effect on the guest reactivity. Detailed studies showed that the building blocks self-assemble in a constitutional dynamic library (CDL) of two coordination polygons where a dimeric rhomboid $[Cu(o\text{-}L)]_2$ and a trimeric triangle $[Cu(o\text{-}L)]_3$ are both accessible and in dynamic equilibrium. Such equilibrium is based on the continuous change of its constituents through dissociation and recombination of the different components. The CDL has been fully characterized and the equilibrium constants between the two constituents have been determined[1]. In dynamic systems the capability to control the equilibrating species through selection mechanisms becomes fundamental. The dimeric species is selected quantitatively by crystallization of the system while, as soon as $[Cu(o\text{-}L)]_2$ are re-dissolved, the CDL is promptly restored (Figure 7). The triangular species is more difficult to select, however, the calculated structure shows a pocket big enough to host small molecules. This feature allows to select the triangular species according to a molecular recognition mechanism in

which a well-suited molecule acts as a guest to form a {G@[Cu(*o*-L)]$_3$} host-guest assembly. The selection of the triangle undergoes two possible paths: *i*) after the CDL formation, the guest molecule acts as an external stimulus inducing the selection of the system upon the formation of the {G@[Cu(*o*-L)]$_3$} host-guest triangle; *ii*) the same host-guest species is obtained by a guest templated self-assembly of the starting building blocks (Cu^{2+}, *o*-LH_2, G) (Figure 8).

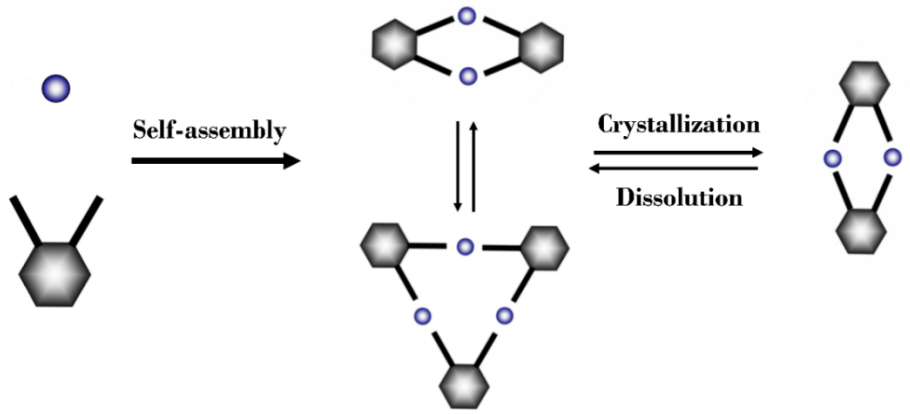

Figure 7. Scheme of the self-assembled CDL.

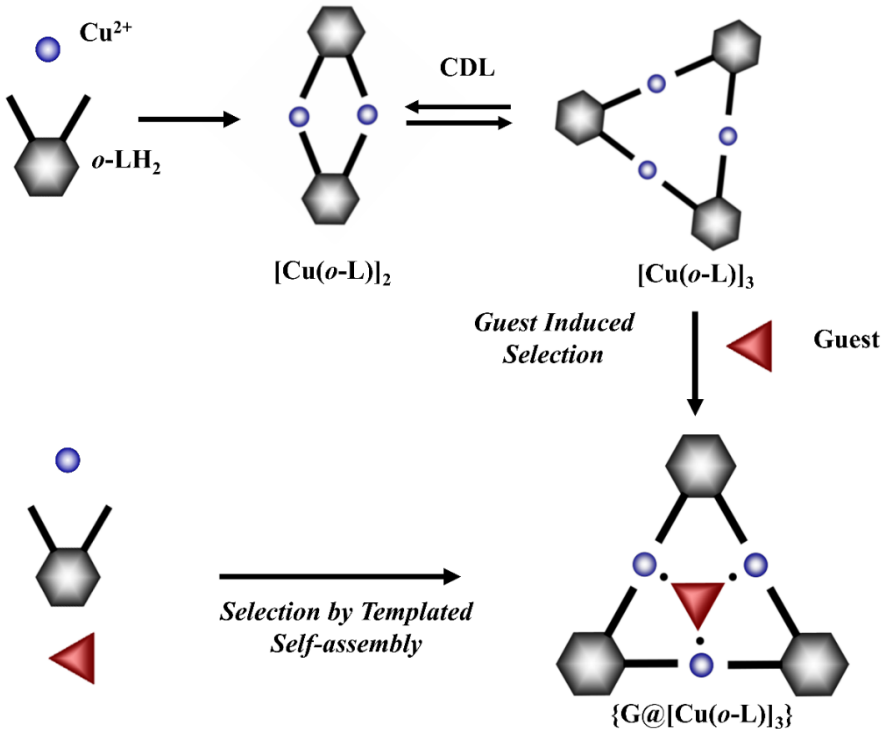

Figure 8. Representation of the two possible *molecular recognition* selection processes.

Different guests, with different shapes and coordination behaviour, can be successfully hosted by the molecular triangle (Figure 9)[2,3]. Guest competition studies, together with guest exchange studies and the determination of the association constants, allow to demonstrate that the selection is thermodynamically driven and to determine a selectivity-affinity correlation among the different guests (Table 1, Table 2).

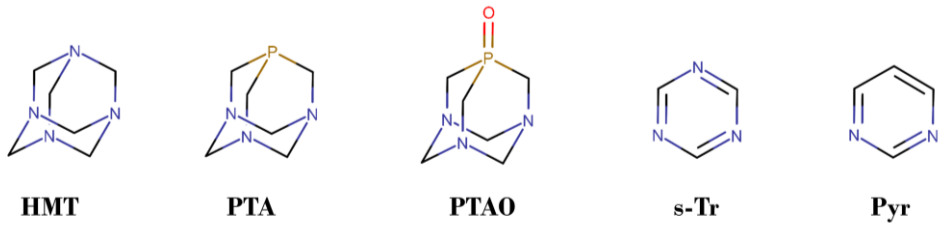

Figure 9. Different guests successfully used in the synthesis of {G@[Cu(*o*-L)]$_3$} triangles.

Table 1. Thermodynamic parameters for the host–guest association at 298.15 K.

	HMT	**s–Tr**	**PTA**	**PTAO**	**Pyr**
ΔH° (kJmol^{-1})	–74.47 (± 6.99)	–62.20 (± 2.41)	–19.82 (± 1.16)	–37.80 (± 3.75)	–47.42 (± 2.32)
ΔS° (Jmol^{-1}K^{-1})	–129 (± 23)	–120 (± 8)	–2 (± 4)	–67 (± 13)	–114 (± 8)
ΔG° (kJmol^{-1})	–35.85 (± 0.14)	–26.48 (± 0.06)	–19.35 (± 0.12)	–17.75 (± 0.06)	–13.53 (± 0.06)
log K_{HG}	6.28 (3)	4.64 (1)	3.39 (2)	3.11 (1)	2.37 (1)

Table 2. Host selectivity (*S*) toward guest pairs at 298.15 K. $S_{HG/HG'} = K_{HG}/K_{HG'}$. Where K_{HG} and K_{HG}' are the association constants for the host H with G and G' guests, respectively.

Guest pair	S
HMT/Pyr	8130
HMT/PTAO	1480
HMT/PTA	776
s–Tr/Pyr	186
HMT/s–Tr	44
s–Tr/PTAO	34
s–Tr/PTA	18
PTA/Pyr	11
PTAO/Pyr	6
PTA/PTAO	2

This system is an excellent bench test to study the effect of metallo-supramolecular boxes on the guest reactivity. In this chapter *i*) the oxidation of a guest molecule and *ii*) a highly selective guest de-methylation are presented and discussed. In the first case, a post-functionalization of the metallo-supramolecular architecture is achieved. This results is a challenging approach that is successfully only in the presence of robust self-assembled architectures. Moreover, the possibility to recover the oxidised guest molecule is successfully explored. In the second case, the templated self-assembly path allows the formation of a host-guest triangle in which the starting guest undergoes a selective C-N bond cleavage.

2.2 Post-assembly guest oxidation.

Metal-coordination assemblies with general formula {G@[Cu(*o*-L)]$_3$} have been obtained using the guests reported in Figure 9; among these, PTA and its oxide PTAO are included. Both {PTA@[Cu(*o*-L)]$_3$} and {PTAO@[Cu(*o*-L)]$_3$} host-guest species have a robust supramolecular motif and quite strong and comparable host-guest association constants (log K_{HG}^{PTA} = 3.39 (± 2) and log K_{HG}^{PTAO} = 3.11 (± 1) at 298 K). Moreover, in the supramolecular assembly the PTA molecule coordinates the host Cu atoms with three N atoms, representing a rare example of a μ_3-PTA molecule with the P atom not coordinated to a metal centre[4]. This coordinating mode for PTA leaves the P atom available to explore a series of well-known PTA derivatizations of practical interest[4] (Figure 10).

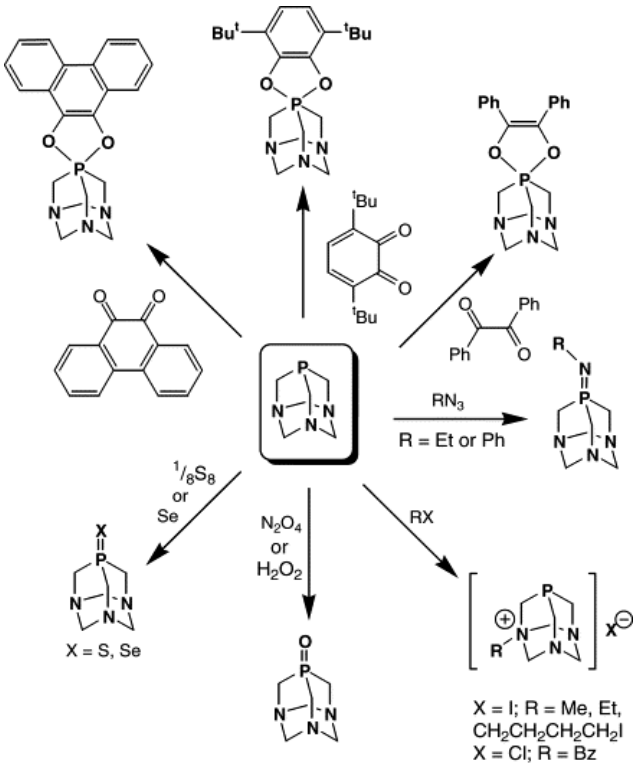

Figure 10. Scheme of PTA possible functionalizations[4a].

The previous synthesis and characterization of these species, combined to the robust self-assembled architectures and to the host-guest association stability, paves the way to study the guest oxidation performed inside the supramolecular environment of the polygon pocket.

PTA molecule is widely used as neutral P-donor ligand to form complexes with transition metal ions[4]. It has received great attention due to its properties to solubilize transition metal complexes in water, allowing applications in homogeneous or biphasic catalysis. Moreover, PTA and derivatives complexes with transition metals find applications in medicinal chemistry, as antitumoral compounds, and for their photoluminescence properties[4a]. This ligand is interesting also due the high hydrophilicity, combined with thermal and chemical stability. To obtain its oxide (PTAO), strong oxidation agents are usually required. It is usually oxidised with 30% H_2O_2,[5a] nitrogen tetroxide[5b] or diluted H_2O_2 solutions in presence of rhenium based catalyst[5c]. Examples are also reported where PTA is partially oxidized in the presence of metal ions that are reduced (Ni(II),[6a] Co(II)[6b, 6c] and Cu(II)[6d]). Slight susceptibility to oxidation occurs in the PTA-BH_3 adduct which is air-stable for weeks at solid state, whereas in solution it shows sign of oxidation over the course of days[7].

When dissolved in chloroform or in dichloromethane, as well as in the solid state, {PTA@[Cu(*o*-L)]$_3$} is very stable in air. The stability has been checked over months and purity of the compound has been confirmed by single crystals X-ray diffraction studies, elemental analysis, UV-Vis and FT-IR spectroscopies. However, when dissolved in a chloroform-acetonitrile solution and left in a closed vial, {PTA@[Cu(*o*-L)]$_3$} spontaneously oxidizes to {PTAO@[Cu(*o*-L)]$_3$}. The oxidation is easily followed *via* FT-IR spectroscopy by monitoring the appearance of the diagnostic P=O stretching band at *ca.* 1160 cm^{-1}. As shown in Figure 11, first evidence of the guest oxidation occurs already after 6 hours, then the band intensity increases over time. After one week, the formation of dark green cube shaped single crystals occur and single crystal X-ray diffraction confirms the formation of the oxidised product {PTAO@[Cu(*o*-L)]$_3$}. After three weeks, a quantitative crops of single crystals was obtained from the chloroform-acetonitrile solutions, leaving the solution from emerald green to almost colourless. Again, single crystals X-ray analysis performed on several crystals, confirmed that the unit cell corresponds to the crystalline structure of {PTAO@[Cu(*o*-L)]$_3$} (CCDC 971598) (Figure 12)[3]. The same experiment has been repeated in a Schlenk tube under an argon atmosphere, but in this case FT-IR analysis did not show any trace of the P=O stretching band, as evidence that no oxidation occurs.

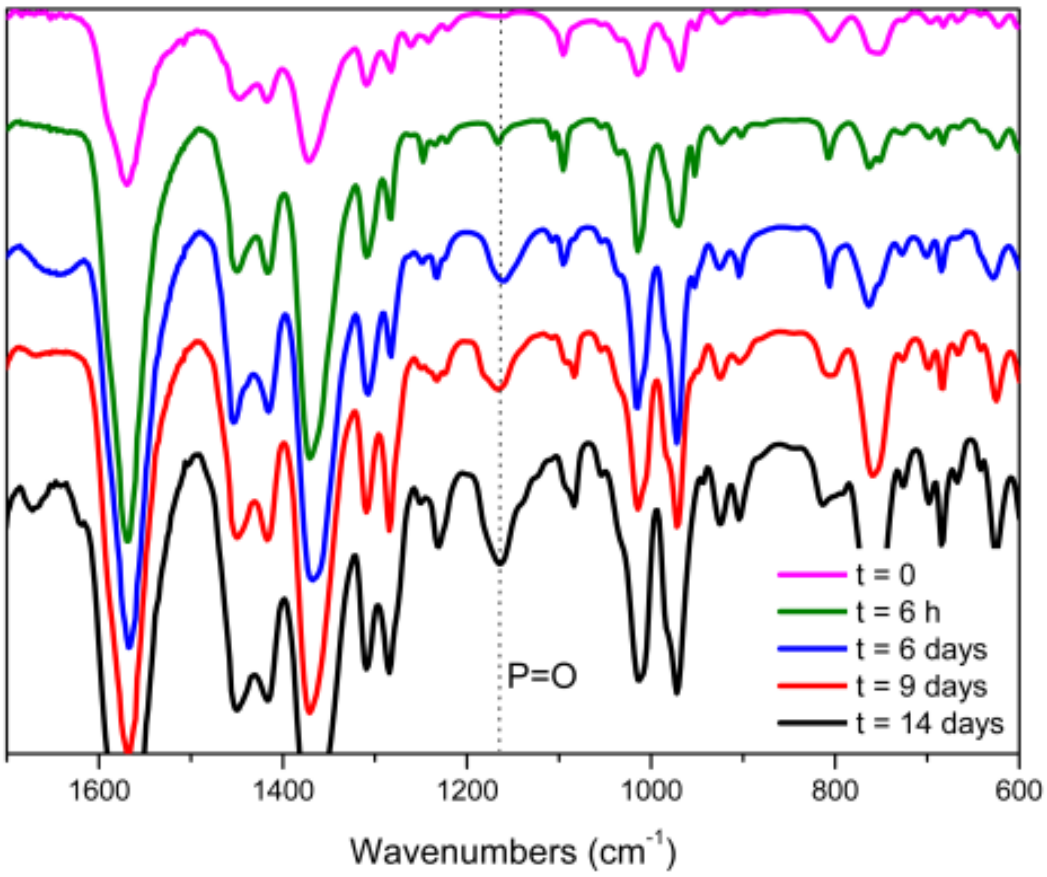

Figure 11. Normalized FT-IR spectra of {PTA@[Cu(o–L)]$_3$} in a $CHCl_3/CH_3CN$ solution. The P=O band intensity increments at increasing time.

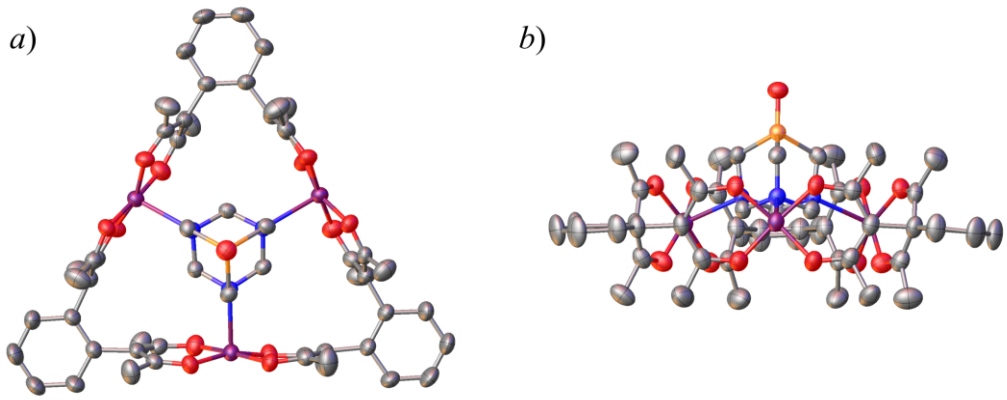

Figure 12. X-ray crystal structure of {PTAO@[Cu(o–L)]$_3$}, *a*) front view, *b*) side view. Thermal ellipsoids drawn at the 50% probability level. Colour code: Cu purple, N blue, O red, C grey, P orange, H atoms are omitted for clarity.

Since the co-solvent role appears to be fundamental in order to oxidise the PTA guest molecule, the same experiment has been performed with other co-solvents. When using ethanol as co-solvent, the FT-IR spectra show similar results to the one previously

obtained using acetonitrile; after few days the P=O stretching band at *ca.* 1160 cm^{-1} appears (Figure 13).

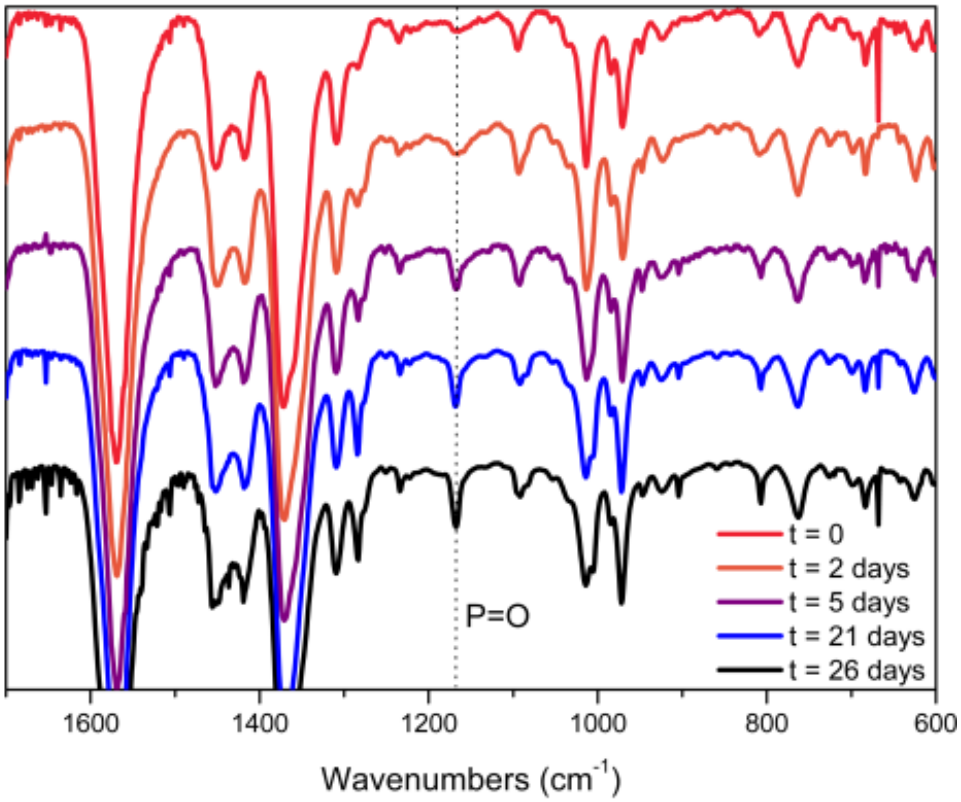

Figure 13. Normalized FT-IR spectra of {PTA@[Cu(*o*–L)]$_3$} in a $CHCl_3$/EtOH solution. The P=O band intensity increments at increasing time.

The reported experiments demonstrate that the oxidation of the PTA guest molecule occurs in mild conditions, when hosted in the [Cu(*o*-L)]$_3$ supramolecular assemblies. However, FT-IR measures show that the oxidation product is formed over several days. The oxidation rate can be significantly incremented by bubbling air in chloroform/co-solvents solutions, reaching a full PTA oxidation within few hours. Different co-solvents have been tested: methanol, ethanol, acetonitrile, ethyl acetate, tetrahydrofuran, 1,4-dioxane, acetone, *n*-hexane, cyclo-hexane and *n*-heptane (Table 3). {PTA@[Cu(*o*-L)]$_3$} has been dissolved in a 1:1 chloroform/co-solvent solution and air has been bubbled under vigorous stirring. FT-IR spectra have been periodically collected to check the presence of the P=O stretching band, all the spectra are reported in CHAPTER 6 (Figure 107-Figure 116). Tetrahydrofuran, methanol and ethyl acetate gave the best oxidation results. On the contrary, using alkanes as co-solvents, the PTA guest molecule did not undergo oxidation even over one day of continuous air bubbling.

Table 3. List of selected co-solvents used for the chloroform/co-solvent oxidation experiments of {PTA@[Cu(*o*-L)]$_3$}.

Co-solvent	Guest oxidation
Methanol	✓
Ethanol	✓
Acetonitrile	✓
Ethyl Acetate	✓
Tetrahydrofuran	✓
1,4-dioxane	✓
n-hexane	✗
Cyclohexane	✗
n-heptane	✗

Figure 14 reports a comparison between the FT-IR spectra of {PTA@[Cu(*o*-L)]$_3$}, dissolved in chloroform/*n*-heptane and chloroform/methanol solutions, collected at the beginning of the reaction, after two hours and after one day. Using methanol as co-solvent, the P=O stretching band is clearly present after two hours, while using *n*-heptane no evidence of the oxidation has been found, even after 24 hours.

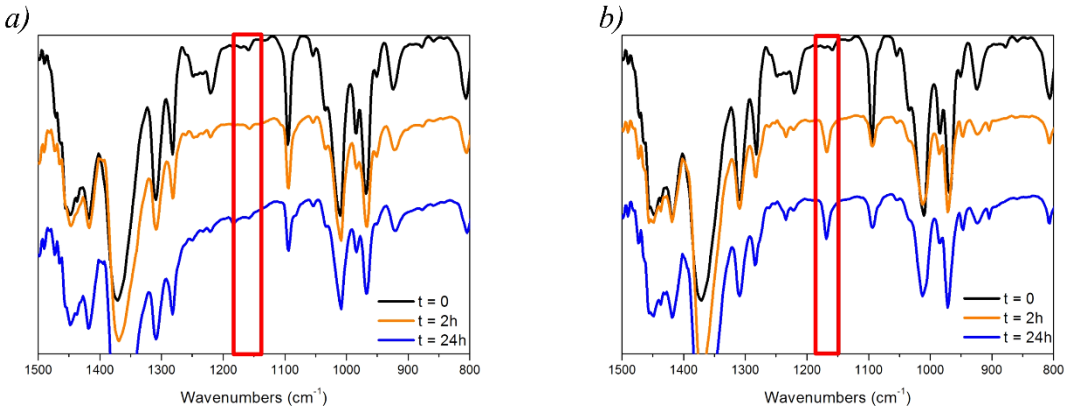

Figure 14. *a*) Normalized FT-IR spectra of {PTA@[Cu(*o*-L)]$_3$} in a $CHCl_3$/*n*-heptane solution. *b*) Normalized FT-IT spectra of {PTA@[Cu(*o*-L)]$_3$} in a $CHCl_3$/methanol solution. Red area highlights the region of the diagnostic P=O stretching band.

Subsequently to the PTA oxidation, the possibility to recover the oxidised guest has been explored. To this aim, the previously studied [Cu(*o*-L)]$_3$ host-guest properties have been exploited (Table 1).

A combination of air-bubbling oxidation and guest-exchange reaction[3] have been used and the reactions have been followed by UV-Vis spectroscopy (Figure 15). Firstly, the absorption spectrum of {PTA@[Cu(*o*-L)]$_3$}, in chloroform solution, has been collected. Then acetonitrile has been added to the system, in order to obtain a 1:1 chloroform/acetonitrile solution, and air has been bubbled overnight, under vigorous stirring. The guest oxidation has been confirmed by a combination of FT-IR and UV-Vis spectroscopy. The absorption spectrum changes to the characteristic {PTAO@[Cu(*o*-L)]$_3$} one (Figure 15). The guest recovery is then possible by using the HMT molecule to perform a guest-exchange. HMT forms the most stable host-guest complex among all the guest used (log K_{HG}^{HMT} = 6.28 (± 3) at 298 K) and it is able to displace the other guests. Addition of HMT to a chloroform solution of the oxidised guest leads to a colour variation, monitored by UV-Vis spectroscopy (Figure 15), due to PTAO guest replacement by HMT. {HMT@[Cu(*o*-L)]$_3$} dissolves in warm toluene (T=50°C), while PTAO is insoluble in these conditions. Hence, the chloroform solution has been evaporated, {HMT@[Cu(*o*-L)]$_3$} dissolved in warm toluene, and PTAO is recovered upon centrifugation. The same experiment has been repeated with a chloroform/tetrahydrofuran solution. In this case, the oxidation of the guest has been achieved in 6 hours of air bubbling. In both experiments PTAO has been recovered almost quantitatively, the yield is 96% for the chloroform/acetonitrile solution and 98% for the chloroform/tetrahydrofuran solution.

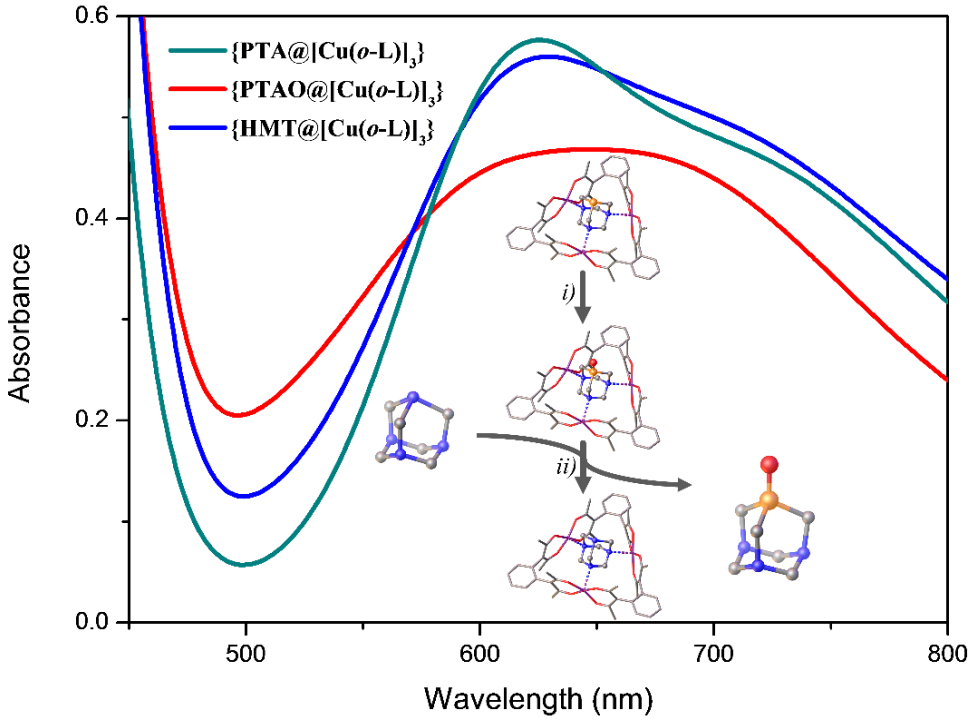

Figure 15. UV-Vis spectroscopy of the oxidation and guest-exchange. *i*) PTA is oxidized by bubbling air in a {PTA@[Cu(*o*–L)]$_3$} $CHCl_3$/acetonitrile overnight or in a $CHCl_3$/THF solution for 6 h. *ii*) PTAO is recovered after guest exchange with HMT.

Previous experiments demonstrate that co-solvents play an important role as a trigger for the guest oxidation. In addition, it has been found that the co-solvent plays an important role also in the crystallization of the complexes, affecting the crystalline structures of the host-guest triangles. From chloroform/*n*-hexane solution no oxidation occurs and single crystals of {PTA@[Cu(*o*-L)]$_3$}[3] have been obtained, while, as shown before, in a chloroform/acetonitrile solution {PTA@[Cu(*o*-L)]$_3$} oxidise to {PTAO@[Cu(*o*-L)]$_3$} and single crystals of this species have been obtained. However, when ethanol is used as co-solvent and the solution is left in a closed vial, after two weeks the solution turns from emerald green to blue and after three weeks a micro-crystalline blue precipitate has been obtained in almost quantitative yield. The new compound has been characterized by single crystal X-ray diffraction together with powder X-ray diffraction studies (sections 6.3.1 and 6.4). The oxidation of {PTA@[Cu(*o*-L)]$_3$} in a chloroform/ethanol solution leads to the formation of a 1D coordination polymer with formula {[(PTAO)$_2$(H_2O)[Cu(*o*–L)]$_8$][Cu(*o*–L)]$_2$}$_\infty$ (hereafter, {[(PTAO)$_2$@[Cu$_8$][Cu$_2$]}$_\infty$). Along with the oxidation in soft conditions, ethanol as co-solvent induces a host structural rearrangement. The coordination polymer structure is composed of two alternating subunits: a {Cu$_2$} dimer and a {Cu$_8$} ring connected each other through a PTAO

molecule. The $\{Cu_2\}$ subunit reminds the structure of the $[Cu(o\text{-}L)]_2$ dimer obtained from the CDL *via* selective crystallization[1] (Figure 16). In this case the apical positions of Cu^{2+} atoms of the $\{Cu_2\}$ subunits are coordinated by a nitrogen atom of the PTAO molecule. The $\{Cu_8\}$ ring is folded in a sort of *double arrow* structure (Figure 17), leading to two triangular cavities. The pockets are reminiscent of the $[Cu(o\text{–}L)]_3$ metallo-supramolecular triangle cavity, in fact the $\{Cu_8\}$ ring hosts two guest molecules. X-ray single crystal diffraction analysis indicates the existence of strong structural correlations between the $\{Cu_8\}$ ring and the CDL constituents. The $\{Cu_8\}$ ring can be described as composed by "open triangles" (Figure 18, blue part) connected by "open dimers" (Figure 18, red part). It can be hypothesized that $\{Cu_8\}$ analogues are involved as transitory intermediates in the CDL self-assembly and in the equilibrium of the two constituents ($3[Cu(o\text{–}L)]_2 \rightleftharpoons 2[Cu(o\text{–}L)]_3$). At variance of the $\{PTAO@[Cu(o\text{–}L)]_3\}$ species, in the coordination polymer PTAO interacts with the $\{Cu_8\}$ ring also through the P=O moiety. A CCDC database research did not reveal any other example of P=O···Cu interaction involving the PTAO ligand (P=O···Cu 2.362(2) Å). In $\{[(PTAO)_2@[Cu_8][Cu_2]\}_\infty$ there are two μ_4-PTAO molecules with two nitrogen atoms coordinated to two Cu atoms of the $\{Cu_8\}$ ring, while the third nitrogen atom connects the alternating $\{Cu_2\}$ and $\{Cu_8\}$ subunits. Interestingly, this 1D coordination polymer is formed only as a consequence of the PTA oxidation from a chloroform/ethanol solution of $\{PTA@[Cu(o\text{-}L)]_3\}$. In fact, crystallization of $\{PTAO@[Cu(o\text{-}L)]_3\}$ using the same solvent/co-solvent combination, leads to single crystals of the host-guest $\{PTAO@[Cu(o\text{-}L)]_3\}$ triangle, previously reported[3], without evidence of structural rearrangement to the coordination polymer. Powder diffraction X-ray studies (PXRD) have been performed in order to assure the quantitative and selective formation of the $\{[(PTAO)_2@[Cu_8][Cu_2]\}_\infty$ species. Experimental data fit very well the calculated diffractogram, obtained from the single crystal structure, confirming the phase purity. The PXRD diffractogram reported in Figure 19 shows the quantitative formation of the polymeric chain, and it confirms the purity of the new compound obtained with yield > 90%. Also in this case the same experiment has been repeated in a Schlenk tube under an argon atmosphere. Again, no oxidation occurs as proved by FT-IR analysis and the solution colour remains emerald green, without turning to blue.

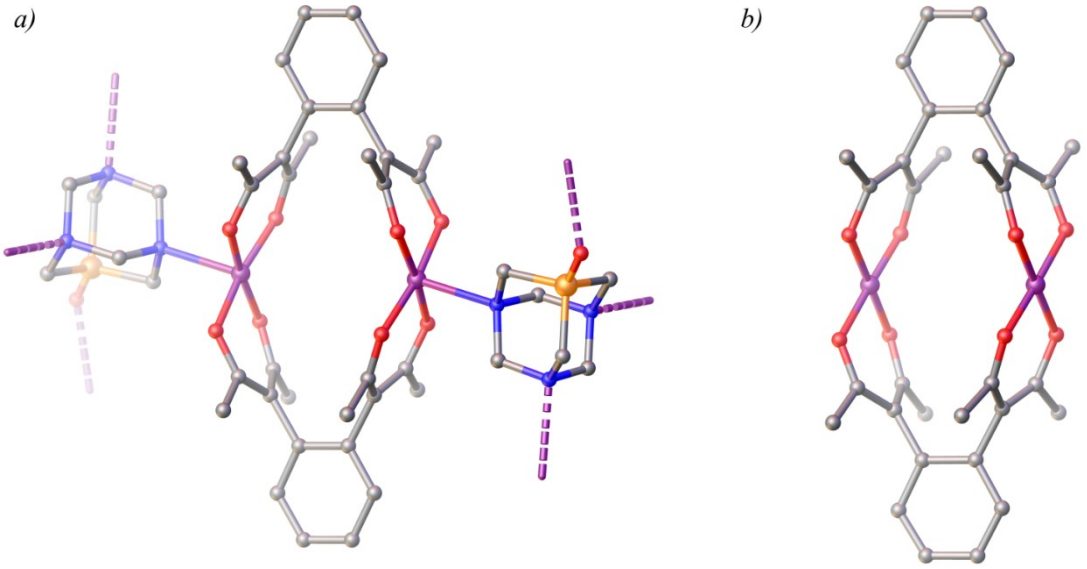

Figure 16. a) $\{Cu_2\}$ subunit in $\{[(PTAO)_2@[Cu_8][Cu_2]\}_\infty$ and b) $[Cu(o–L)]_2$ dimer[1] crystallized from a chloroform/acetone mixture. H atoms are omitted for clarity.

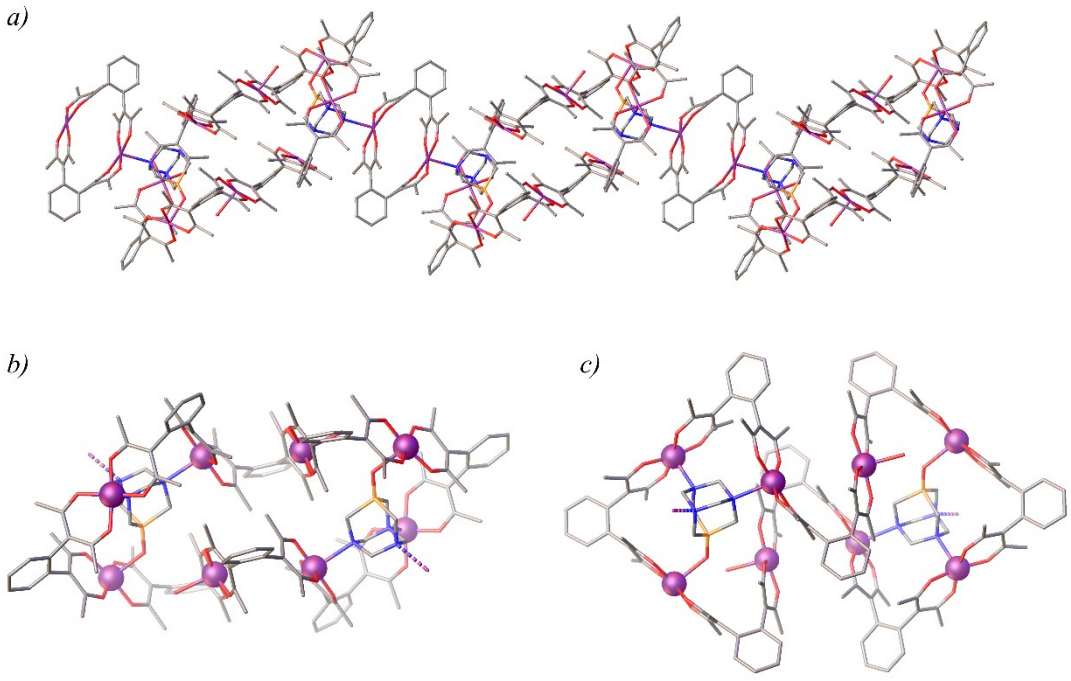

Figure 17. *a)* Capped sticks view for the crystal structure of $\{[(PTAO)_2@[Cu_8][Cu_2]\}_\infty$: polymeric chain of alternating $\{Cu_2\}$ and $\{Cu_8\}$ units; *b*) and *c*) side and top views of the *double arrow* $\{Cu_8\}$ ring. Colour code: Cu purple, P orange, N blue, O red, C grey, H atoms are omitted for clarity.

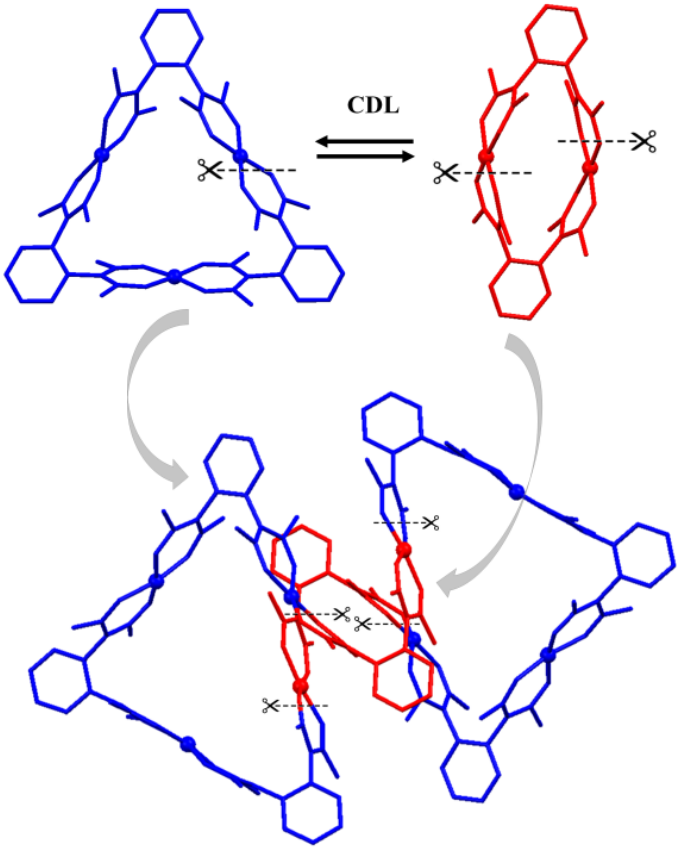

Figure 18. Structural correlation among the two CDL constituents and the $\{Cu_8\}$ ring. PTAO guests in the $\{Cu_8\}$ ring have been omitted for clarity.

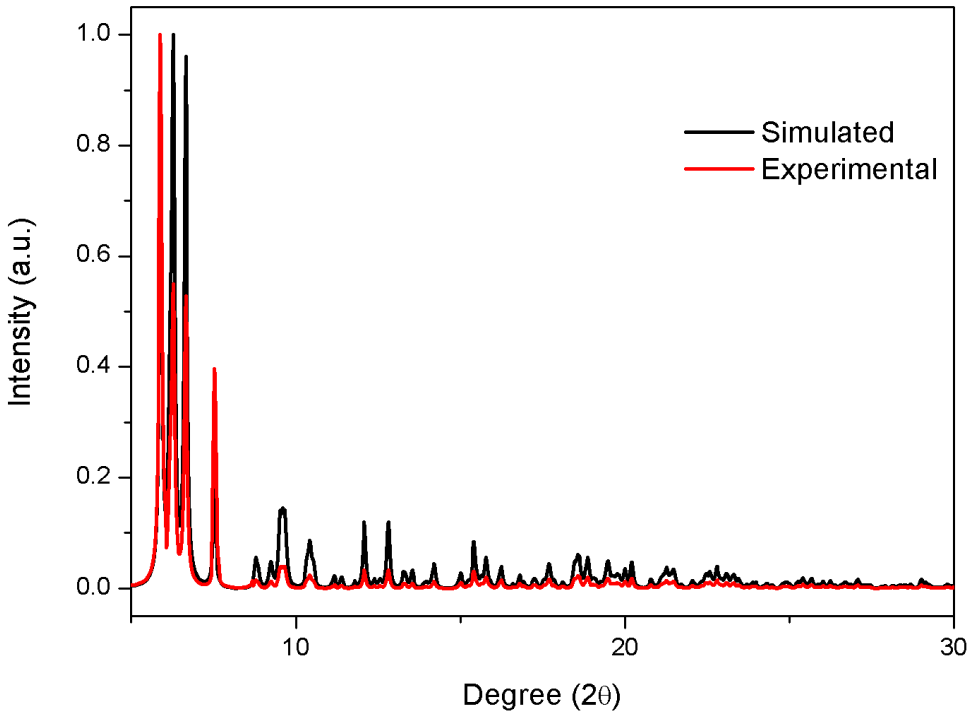

Figure 19. Experimental and simulated $\{[(PTAO)_2@[Cu_8][Cu_2]\}_\infty$ PXRD patterns (normalized intensity).

In summary, the [Cu(*o*-L)]$_3$ metallo-supramolecular cage can be used as a suitable environment for PTA oxidation under mild conditions. The {PTA@[Cu(*o*-L)]$_3$} species is stable in $CHCl_3$ solution, air bubbling or temperature increase do not oxidise the system. However, the [Cu(*o*-L)]$_3$ box activates the reactivity of the guest molecule and the addition of a co-solvent acts as a trigger to promote the oxidation. As reported in Figure 20, polar co-solvent as acetone, methanol, ethanol, acetonitrile, ethyl acetate or tetrahydrofuran allow the air oxidation of {PTA@[Cu(*o*-L)]$_3$} to {PTAO@[Cu(*o*-L)]$_3$}, while using alkane co-solvent as *n*-hexane, *n*-heptane or cyclohexane oxidation does not occur.

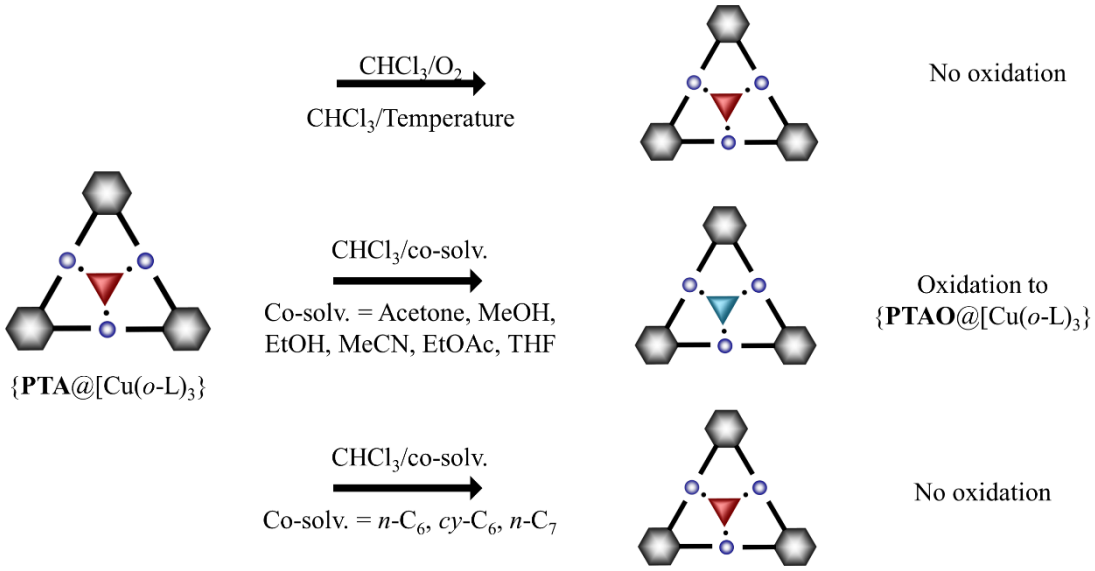

Figure 20. The addition of a co-solvent to the $CHCl_3$ solution acts as trigger to promote the oxidation of {PTA@[Cu(*o*-L)]$_3$} to {PTAO@[Cu(*o*-L)]$_3$}.

Together with the oxidation, the co-solvent plays an important role also in the crystallization of the studied compound. As summarized in Figure 21, single crystals of {PTA@[Cu(*o*-L)]$_3$} have been obtained from $CHCl_3$/*n*-hexane. The alkane co-solvent allows to access the crystal structure of the starting assembly. However, by using acetonitrile as co-solvent the guest is oxidised and single crystal of {PTAO@[Cu(*o*-L)]$_3$} isolated. Finally, by using ethanol as co-solvent the oxidation of the guest is obtained along with a structural rearrangement to {[(PTAO)$_2$@[Cu$_8$][Cu$_2$]}$_\infty$ 1D coordination polymer.

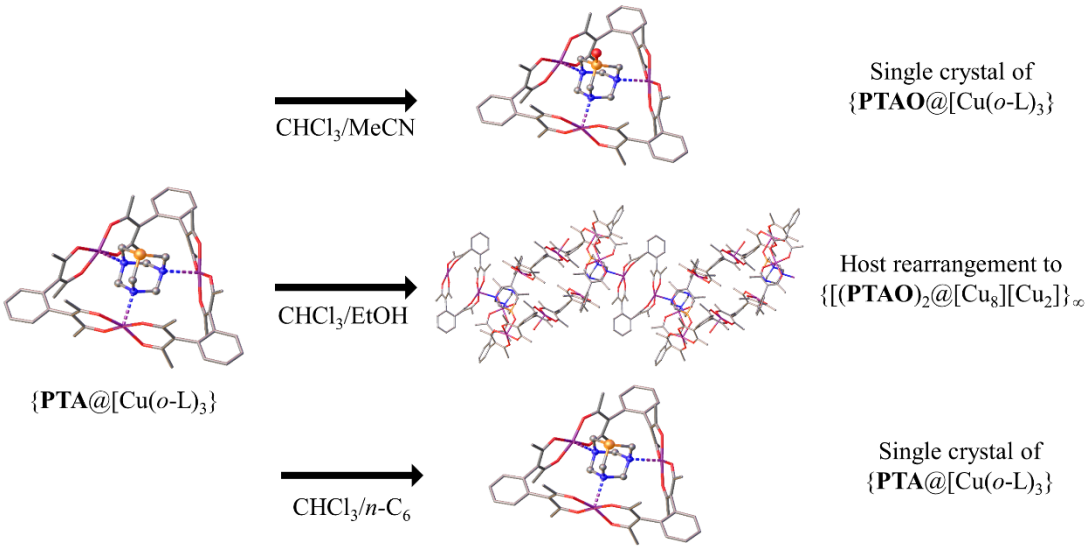

Figure 21. Co-solvents allow to obtain different crystallization products.

2.3 Templated-assembly guest de-methylation.

Beside the guests reported in Figure 9, 1,3,5-trimethil-1,3,5-triazinane (hereafter Me_3-Tr) has been chosen as a good candidate for triangle selection from the dimer-trimer CDL (Figure 22). Me_3-Tr molecule contains three floating methyl groups and has higher flexibility compared to the other guests. In fact, the methyl groups can flip from equatorial to axial position, leading to different conformers. At the same time this guest molecule possesses σ-donor atoms necessary to coordinate the Cu^{2+} ions and a three-fold symmetry; both features are ideal requirements for a possible [Cu(*o*-L)]$_3$ guest.

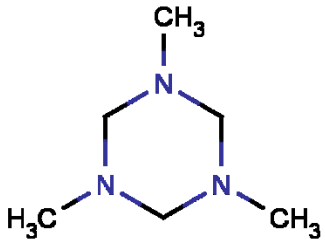

Figure 22. Me_3-Tr molecule as possible guest for [Cu(*o*-L)]$_3$ triangle.

For these reasons, Me_3-Tr has been added to a [Cu(*o*-L)]$_n$ (n = 2, 3) solution, in order to perform the guest induced selection of the triangular polygon. From this experiment no evidence of the host-guest species occurs. The system has been allowed to react for two days with an excess of the guest molecule. No colour change has been observed and the UV-Vis spectrum has the typical shape of the [Cu(*o*-L)]$_n$ (n = 2, 3) CDL[1] (Figure 24).

Moreover, from this solution [Cu(*o*-L)]$_2$ single crystals have been isolated in quantitative yield. In order to explain this reactivity, the Boltzmann distribution of the Me$_3$-Tr conformers has been calculated using the Dreiding force field[8] in the framework of Marvin Sketch software. The plot reports the percentage of the *i-th* conformer as a function of its energy. To be allocated in the triangle pocket, the methyl groups are required to be in axial conformation; however, from the Boltzmann distribution it appears clear that the axial conformer (green triangle) is substantially absent in solution (Figure 23). On the basis of the [Cu(*o*-L)]$_3$ pocket dimensions, obtained from a model and from the structures with other guests, when Me$_3$-Tr is used as guest, following the guest induced selection path, the inclusion in the preformed host cavity is not possible due to steric reasons.

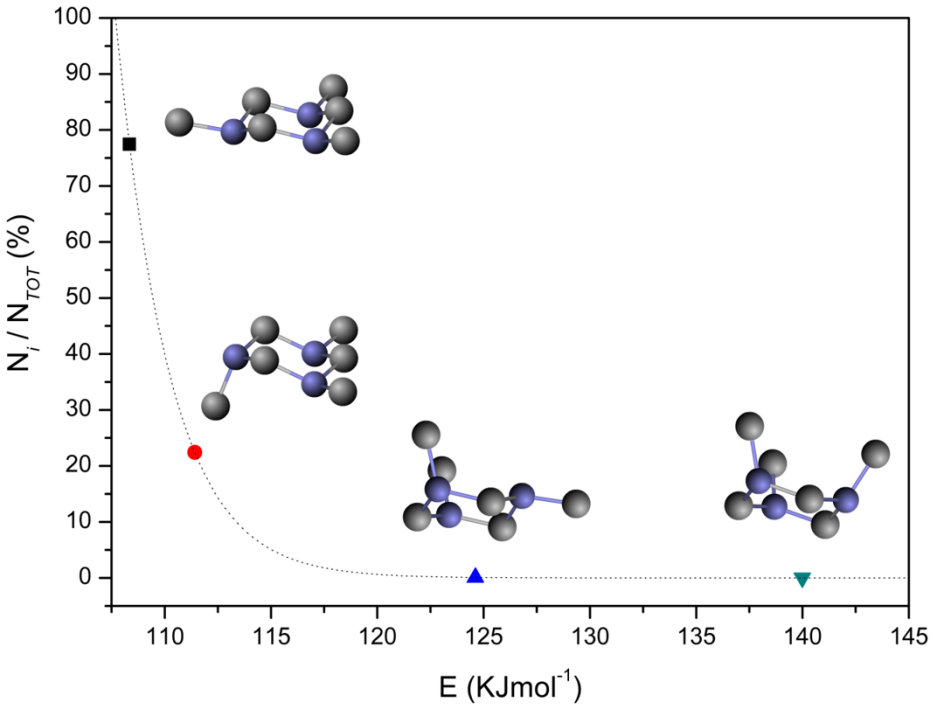

Figure 23. Boltzmann distribution of the Me$_3$-Tr conformers.

The self-assembly approach leads to more interesting results. The templating guest molecule, Me$_3$-Tr, has been added in large excess in order to force the reaction to the host-guest formation. The building blocks have been left under vigorous stirring for one day, a longer reaction time if compared with the other guest molecules that require only few minutes. UV-Vis spectrum of the compound is similar to the other {Guest@[Cu(*o*-L)]$_3$} species, especially to the {HMT@[Cu(*o*-L)]$_3$} one, and clearly different from the spectrum of the [Cu(*o*-L)]$_n$ (n = 2, 3) CDL (Figure 24). The band at 525 nm disappears

and a shoulder at 725 nm rises up. The UV-Vis spectrum is consistent with the formation of a {Guest@[Cu(*o*-L)]$_3$} host-guest species in which the nitrogen atoms of the guest coordinate the host copper ions in the apical position. After several efforts, single crystals of the new host-guest compound have been obtained. Interestingly, the obtained structural model shows the formation of a host-guest complex in which the guest molecule loses two methyl groups with a C-N bond cleavage (Figure 25). The guest trapped inside the triangular polygon is 1-methyl-1,3,5-triazinane (hereafter Me-Tr), instead of the starting Me$_3$-Tr.

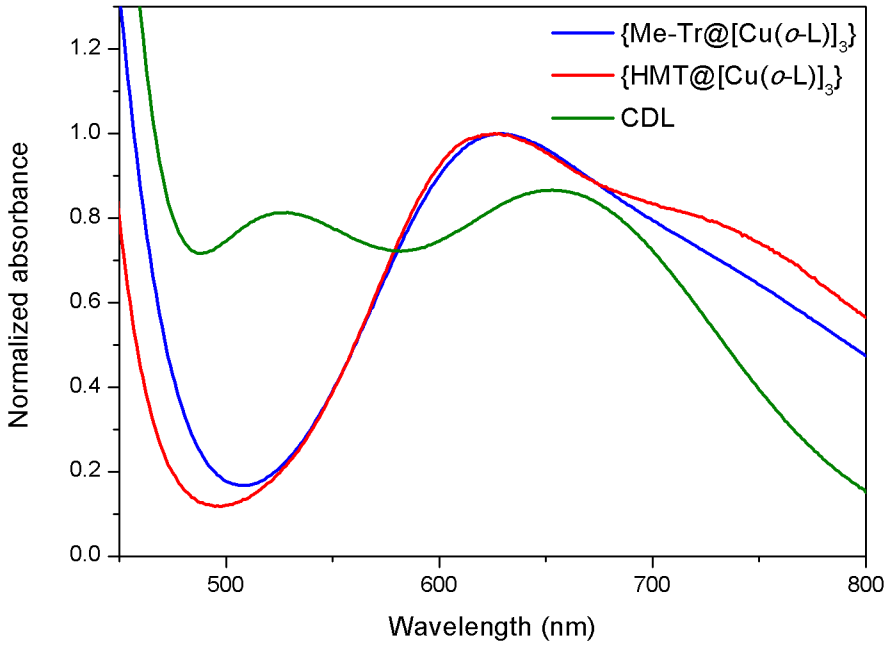

Figure 24. UV-Vis absorption spectra of {Me-Tr@[Cu(*o*-L)]$_3$} (blue line), {HMT@[Cu(*o*-L)]$_3$} (red line) and of the CDL (green line).

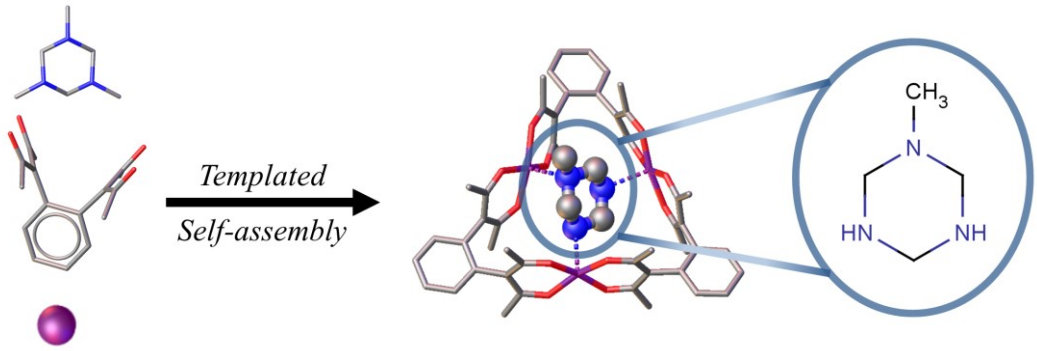

Figure 25. The templated self-assembly synthesis of Me$_3$-Tr, Cu^{2+} and *o*-LH$_2$ leads to the cleavage of two C-N bonds and the formation of {Me-Tr@[Cu(*o*-L)]$_3$}.

The reaction produces a green powder with a high yield (82 %) and crystallization of this compound from chloroform/acetonitrile or dichloromethane/acetonitrile solutions at low temperature (-18°C) is quantitative. Several single crystals from the same batch have been measured, all resulting with the same lattice parameters and confirming the exclusively formation of {Me-Tr@[Cu(*o*-L)]$_3$}. Moreover, the crystalline product is strongly affected by small variations in the crystallization conditions. The compound crystallizes with three different space groups: one is obtained from a chloroform/acetonitrile solution at -18°C, while the other two are obtained from dichloromethane/acetonitrile solutions at -18°C. The three obtained crystals differ each other's for the amount of the crystallization solvent in the structure, while the host-guest architecture is always {Me-Tr@[Cu(*o*-L)]$_3$}. Experimental details of the single crystals analyses are reported in section 6.3.2.

{Me-Tr@[Cu(*o*-L)]$_3$} crystallizes in a monoclinic C2/c space group (hereafter Me-Tr-**1**) from a chloroform/acetonitrile solution,. The unit cell has a volume of 11579.3 Å^3 and contains eight asymmetric units, each of which corresponds to one full molecule of {Me-Tr@[Cu(*o*-L)]$_3$} (Figure 26 *a* and *b*). This structure is characterized by a large fraction of void space in the unit cell, containing non-negligible residual electron density that could not be effectively modelled, likely due to disordered crystallization solvent. The contribution of that electron density has been removed using the mask routine of OLEX2 software[9]. The program calculates a total solvent accessible volume per unit cell of 2366.2 Å^3, corresponding to the 20.4% of the cell volume (Figure 26 *c*). There are a total of 16 solvent accessible voids divided in three groups composed by four voids each and related by symmetry elements. For the larger voids group, the program calculates a volume of 366.8 Å^3 each, and an electron count of 111.6, compatible with the presence of two chloroform molecules. For the second voids group, the program calculates a volume of 210.9 Å^3 each, and an electron count of 69.0, compatible with the presence of one chloroform and one water molecules. The last voids group has a smaller volume (6.9 Å^3) and no residual electron density. The total amount of residual electron density in the solvent accessible voids of Me-Tr-**1** are compatible with the presence of twelve chloroform molecules and four water molecules.

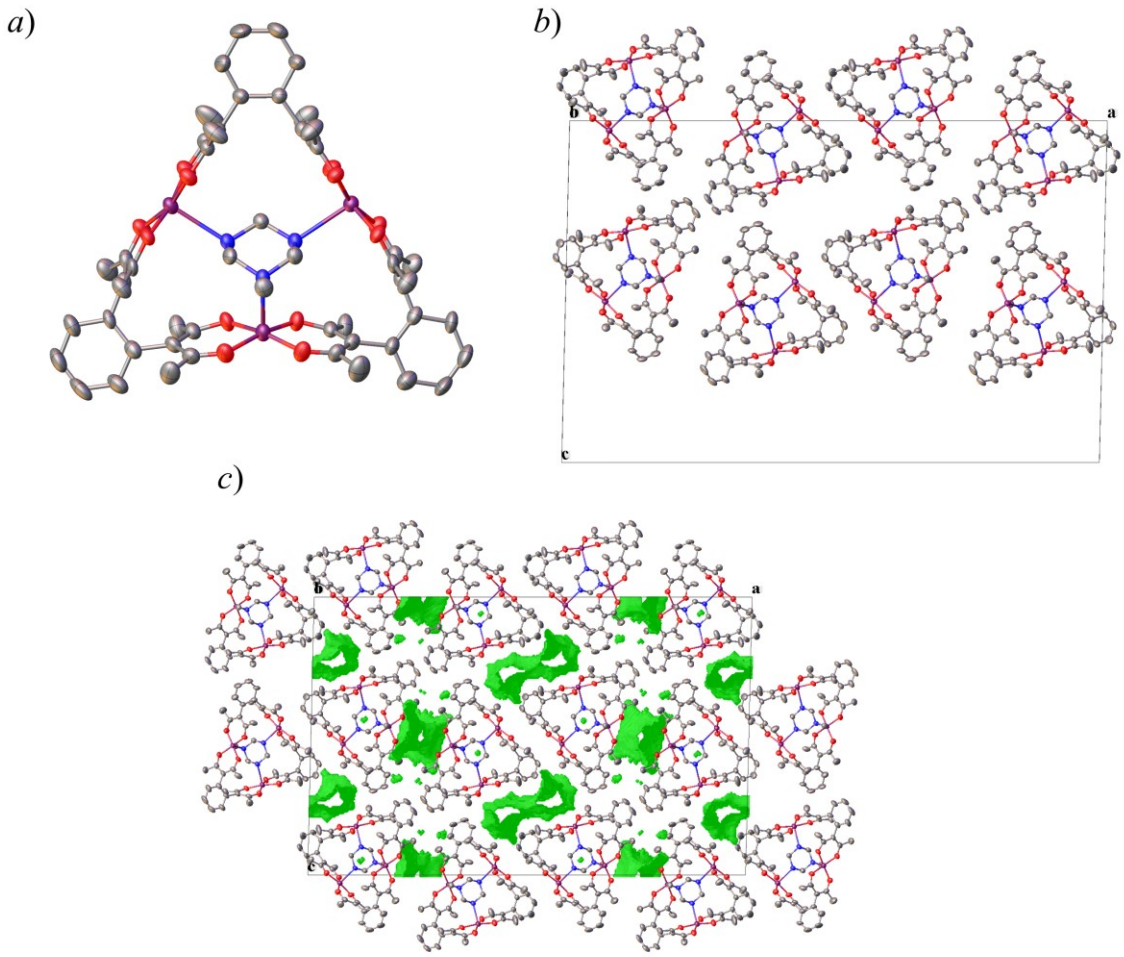

Figure 26. {Me-Tr@[Cu(*o*-L)]$_3$} structure from crystal 1: *a*) asymmetric unit, *b*) unit cell with 8 host-guest molecules, *c*) green surfaces report the map of the solvent accessible void per unit cell. Thermal ellipsoids drawn at the 50% probability level. Colour code: Cu purple, N blue, O red, C grey, H atoms are omitted for clarity.

Crystallization from a dichloromethane/acetonitrile solution leads to two different space groups, hereafter Me-Tr-**2** and Me-Tr-**3**. Me-Tr-**2** is obtained from a 1:1 solution of the two solvents and it crystallizes in a monoclinic $P2_1/n$ space group. The asymmetric unit is again the {Me-Tr@[Cu(*o*-L)]$_3$} triangle, but in this case the unit cell contains four asymmetric units and is smaller ((V=6481.5 Å^3) than the Me-Tr-**1** one (Figure 27 *a* and *b*). Also this cell is characterized by the presence of large voids, OLEX2 program calculates a total solvent accessible void of 2127.2 Å^3, corresponding to 32.8% of the unit cell volume. Again, the void space contains non-negligible residual electron density has been removed using the OLEX2 mask routine. The program calculates two identical voids, related by symmetry, each of them with a volume of 1063.6 Å^3 and an electron

count of 162.9, likely due to the presence of four dichloromethane molecules (Figure 27 *c*).

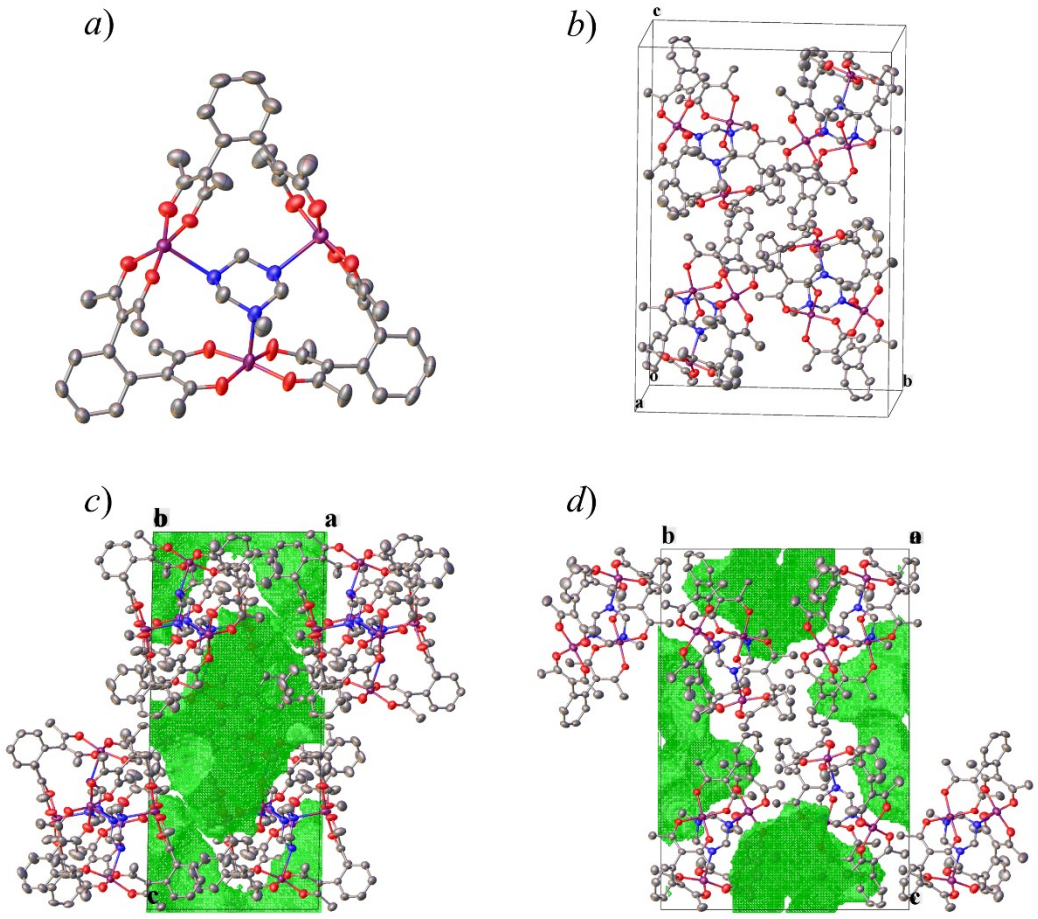

Figure 27. {Me-Tr@[Cu(*o*-L)]$_3$} structure from Me-Tr-**2**. *a*) Asymmetric unit; *b*) unit cell with 4 host-guest molecules; *c*) and *d*) green surfaces report the map of the solvent accessible void per unit cell, *c*) show the unit cell view along b axis and *d*) show the unit cell view along a axis. Thermal ellipsoids drawn at the 50% probability level. Colour code: Cu purple, N blue, O red, C grey, H atoms are omitted for clarity.

Interestingly, leaving single crystals of Me-Tr-**2** for two weeks in a solution enriched in acetonitrile, the formation of Me-Tr-**3** has been obtained through single crystal to single crystal conversion. In this case, the isolated species is {Me-Tr@[Cu(*o*-L)]$_3$}·2MeCN and it crystallizes in a triclinic P-1 space group. The asymmetric unit is the host-guest triangle with two acetonitrile molecules as crystallization solvent. The unit cell contains two asymmetric units (V=3089.6 Å^3) and is smaller than Me-Tr-**1** and Me-Tr-**2** (Figure 28 *a*, *b*). The large solvent accessible voids of Me-Tr-**2** allow a solvent exchange between dichloromethane in the crystal and the acetonitrile in the solution, leading to a single crystal to single crystal conversion. This also leads to a reduction of the voids dimensions and to a total solvent accessible volume of 574.9 Å^3, corresponding to 18.6% of the unit

cell volume. However, the void space still contains non-negligible residual electron density that has been removed using the OLEX2 mask routine. The program calculates two voids with volume of 287.5 $Å^3$ and electron count of nearly 50, compatible with the presence of one dichloromethane molecule and one water molecule deriving from the atmosphere or from acetonitrile water impurity (Figure 28 c).

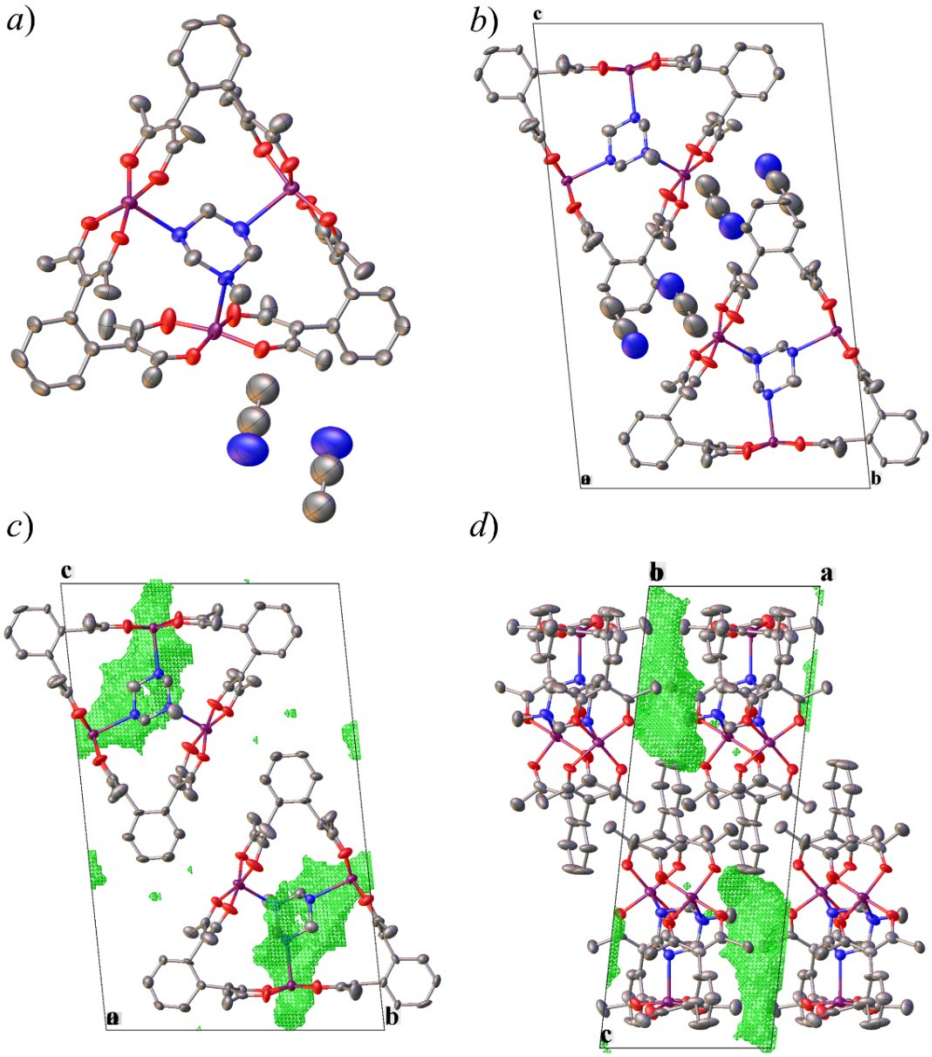

Figure 28. Me-Tr@[Cu(*o*-L)]$_3$}·2MeCN structure from Me-Tr-**3**. *a*) Asymmetric unit; *b*) unit cell with 2 host-guest molecules; *c*) and *d*) green surfaces report the map of the solvent accessible void per unit cell, *c*) show the unit cell view along a axis and *d*) show the unit cell view along b axis. Thermal ellipsoids drawn at the 50% probability level. Colour code: Cu purple, N blue, O red, C grey, H atoms are omitted for clarity.

In all the three structures, N atoms of the Me-Tr guest coordinate the Cu^{2+} ions in the apical position. Therefore, copper ions have a distorted square pyramidal coordination, with four acetylacetonate oxygen atoms at the equatorial plane in addition to the nitrogen guest atoms in the apical positions. The Cu-O_{acac} distances in all the structures span in the

interval 1.902-1.936 Å. Considering the Cu-N distances, the remaining methyl group of the guest introduce a distortion on the host triangle in order to make the coordination possible. Due to this, differently from the previously studied guests, Me-Tr does not enter in the triangular pocket with the ligand plane parallel to the plane generated by the Cu metal centres (Figure 29). Figure 29 *b* shows the {Me-Tr@[CuO_4]$_3$} moieties for the three crystal structures obtained. In Me-Tr-**1** structure, the guest enters in the triangular pocket with an angle of 50.86° between the guest plane and the plane generated by the Cu metal centres. In the structure of Me-Tr-**2**, the guest entrance angle is 49.45°, while for Me-Tr-**3**, the guest enters with an angle of 48.22°.

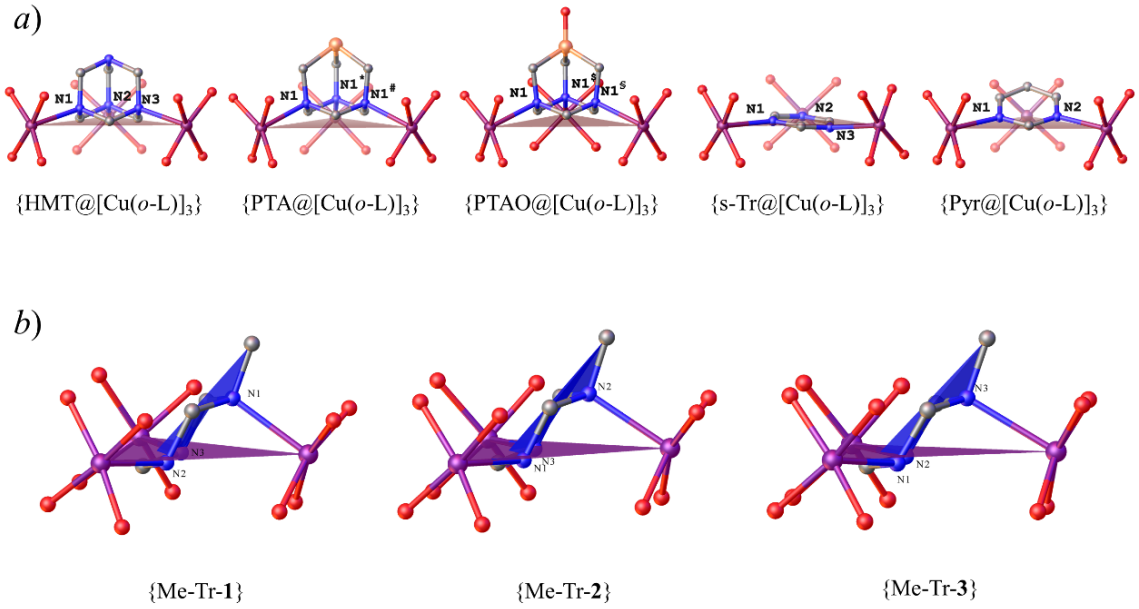

Figure 29. *a*) {G@[CuO_4]$_3$} moieties and occupation of the triangle cavity of the previously studied {G@[Cu(*o*-L)]$_3$}; *b*) {Me-Tr@[CuO_4]$_3$} moieties from Me-Tr-**1**, Me-Tr-**2** and Me-Tr-**3**. The guest plane has been defined as the plane containing the three nitrogen atoms.

Moreover, in Me-Tr-**1,** the Cu^{2+} ion coordinated to the N-CH_3 donor atom, is shifted from the triangle side, toward the triangle centre, of 1.146 Å. Due to this distortion, the host-guest triangle has two sides of length 12.36 Å and one bended side of length 12.24 Å. This effect is also seen in the Cu-N distances, the nitrogen substituted with the methyl group is closer to Cu^{2+} ions, with a distance of 2.346 Å. The other two nitrogen atoms are more than 0.1 Å far away from copper ions, with a distance of 2.471 Å and 2.478 Å. Me-Tr-**2** is less distorted, Cu^{2+} ion coordinated to the N-CH_3 donor atom is shifted from the triangle side of 0.775 Å and triangle side lengths span from 12.32 Å to 12.36 Å. In Me-

Tr-**3** the same shift is reduced to 0.524 Å and the triangle side lengths span from 12.38 Å to 12.40 Å. Me-Tr-**2** and Me-Tr-**3** are less distorted, and due to this, the Cu-N distances have less differences when comparing Cu-N-H and Cu-N-CH_3 groups, respect to what found in Me-Tr-**1**. In Me-Tr-**2** and Me-Tr-**3**, Cu-N distances span the interval of 2.394-2.446 Å.

Single crystal X-ray diffraction studies revealed a selective de-methylation of two methyl groups of the initial Me_3-Tr molecule leading, to the formation of the Me-Tr guest molecule. No evidence of other de-methylation product occurs. The metallo-supramolecular host allows to obtain an extremely selective breaking of C-N bonds leading specifically to the Me-Tr molecule. The confined space of the host pocket is fundamental in order to isolate the C-N cleavage product. When one of the [Cu(*o*-L)]$_3$ building blocks (Cu^{2+}, *o*-LH_2) is missing, the C-N cleavage does not take place. A solution of *o*-LH_2 ligand and Me_3-Tr is unreactive and stable until the addition of a Cu^{2+} source that leads to the host-guest product. To confirm that a synergic effect of the metal, the ligand and the guest is necessary, reaction with only Cu^{2+} and Me_3-Tr has been studied. Kohn and co-workers have reported the formation of a [Cu(Me_3-Tr)Cl_2]$_2$ dimeric complex, obtained reacting $CuCl_2$ and Me_3-Tr in a water/chloroform two phases synthesis[10]. Single crystals of [Cu(Me_3-Tr)Cl_2]$_2$ have been obtained in quantitative yield, reproducing the same reaction (Figure 30). No evidence of Me_3-Tr degradation has been observed. Using different copper sources, such as $CuSO_4$, $Cu(ClO_4)_2$ and $[Cu(NH_3)_4]^{2+}$, any complex formation has not been found: copper ions remain in the aqueous layer, the organic phase remains colourless and there is no evidence of any reactivity on Me_3-Tr molecule.

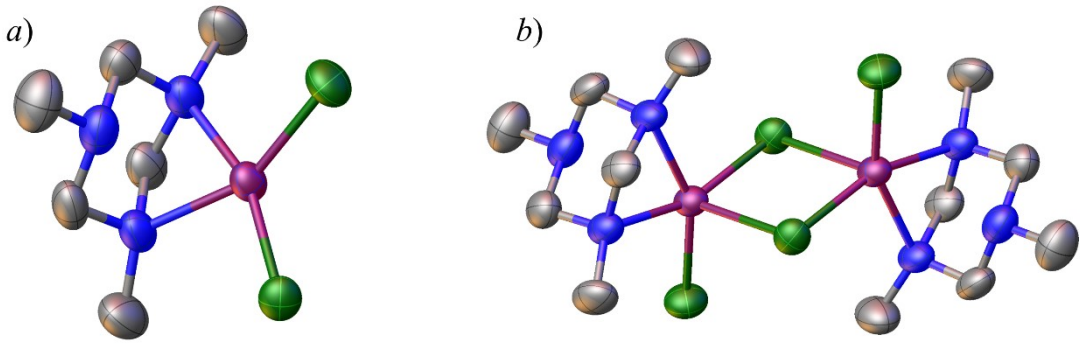

Figure 30. Structure of [Cu(Me_3-Tr)Cl_2]$_2$, *a*) asymmetric unit, *b*) dimer with μ-Cl bridge. Thermal ellipsoids drawn at the 50% probability level. Colour code: Cu purple, N blue, C grey, Cl green, H atoms are omitted for clarity.

Previous studies, performed on other guests (Figure 9), elucidated the thermodynamic behaviour of the host-guest process by determining the association constant (Table 1). The association constant can be calculated only for the guest induced selection path, since the templated self-assembly synthesis is made in a biphasic mixture. Formation of {Me-Tr@[Cu(*o*-L)]$_3$} is achieved only *via* templated self-assembly path through Me$_3$-Tr C-N cleavage. To overcome this problem, it is possible to perform a guest-exchange reaction, to calculate the exchange constant and therefore the association constant of Me-Tr (Figure 31).

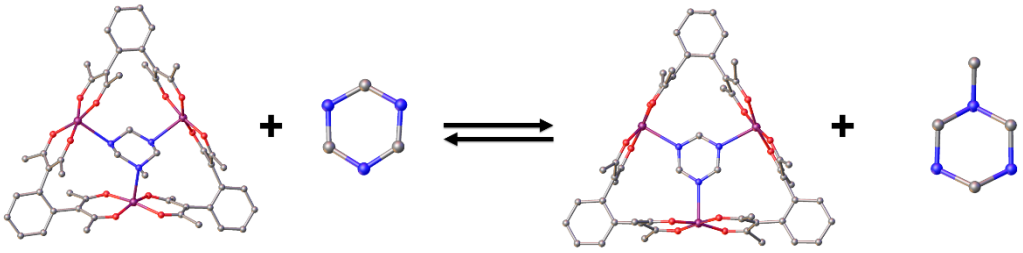

Figure 31. Guest exchange representation with ball and stick structural models derived from X-ray diffraction. Colour code: Cu purple, N blue, C grey, O red, H atoms are omitted for clarity.

For non-paramagnetic species this is usually done by NMR, but due to the presence of Cu^{2+} ions, useful NMR data cannot be obtained. UV-Vis absorption spectroscopy represents a suitable method to study the formation of the host-guest species, due to the colour variation that occurs during the process, subsequently to the guest coordination. Initially, HMT has been chosen as possible candidate for guest exchange since it has the strongest association constant, however {HMT@[Cu(*o*-L)]$_3$} UV-Vis absorption spectrum is very similar to the {Me-Tr@[Cu(*o*-L)]$_3$} one. The second strongest guest, among the guest reported in Figure 9, is s-Tr. {s-Tr@[Cu(*o*-L)]$_3$} UV-Vis spectrum is quite different from {Me-Tr@[Cu(*o*-L)]$_3$} one and for this reason s-Tr has been chosen to perform the guest-exchange reaction. In order to calculate the association constant, a titration method has been used, then data have been fitted with Hyperquad[11] software according to the model described in section 6.2.2. Previously determined equilibrium constant of the CDL ($\log K_{eq} = 4.8$) and the association constant for {s-Tr@[Cu(*o*-L)]$_3$} ($\log K_{s\text{-}Tr} = 4.64$) have been included in the speciation model. The guest has been added batchwise to a {Me-Tr@[Cu(*o*-L)]$_3$} solution at constant temperature (298 K) and absorption spectra have been collected. Titration data have been collected for different {Me-Tr@[Cu(*o*-L)]$_3$} concentrations. Upon addition of the guest, the spectra clearly change and the band in the visible range decreases in intensity. The band at 630 nm is

shifted to 610 nm and the shoulder at higher wavelengths (≈ 700nm) rises up. Figure 32 reports the spectra for the titration starting from the host-guest species at 1 mM and 2 mM concentrations. In Figure 33, the comparison between the experimental data and the calculated spectra after the addition of s-Tr are reported. From the fitting of guest-exchange titration data, the exchange constant is $\log K_{ex} = 1.50 \pm 0.02$ and the association constant of {Me-Tr@[Cu(*o*-L)]$_3$} is $\log K_{as}$(Me-Tr) = 6.14 ± 0.02. The cage effect of the supramolecular triangle, combined with the great stabilization of the final product, are probably two of the causes that drive the reaction to the selective C-N bond cleavage. Collected data evidence that the presence of the host supramolecular triangle is fundamental in order to achieve the selective C-N bond cleavage, but the mechanism of the reaction is still under investigation. Moreover, further studies will be devoted to investigate the possibility to achieve the C-N cleavage for other alkyl-triazine molecules, that fulfil the requirements to be possible guest candidates for the [Cu(*o*-L)]$_3$ host triangle.

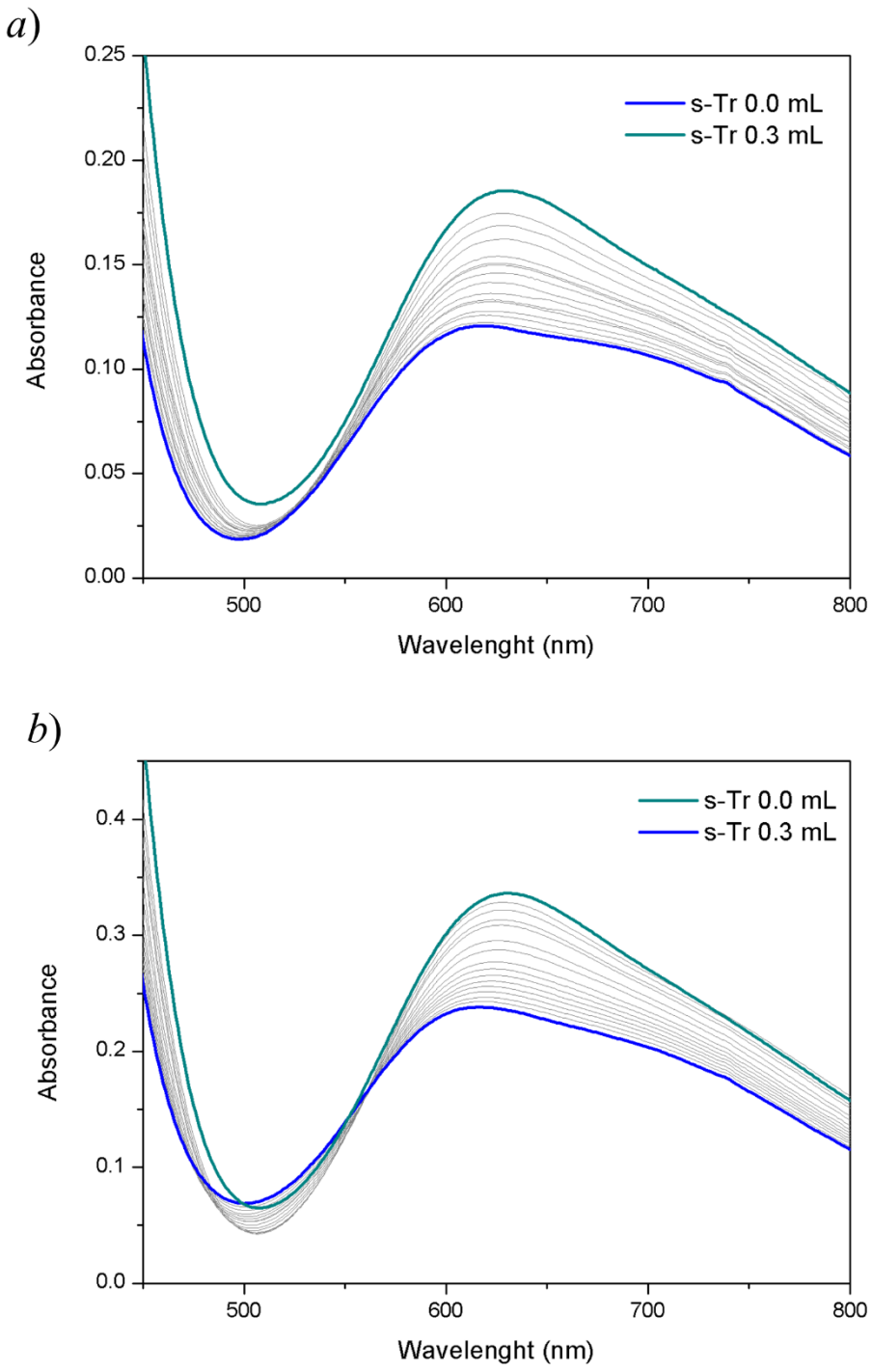

Figure 32. {Me-Tr@[Cu(*o*-L)]$_3$} guest-exchange titrations with s-Tr. Final s-Tr added volume = 0.3 mL, T = 298.15K. {Me-Tr@[Cu(*o*-L)]$_3$} concentrations: *a*) 1.05 mM, *b*) 2.19 mM.

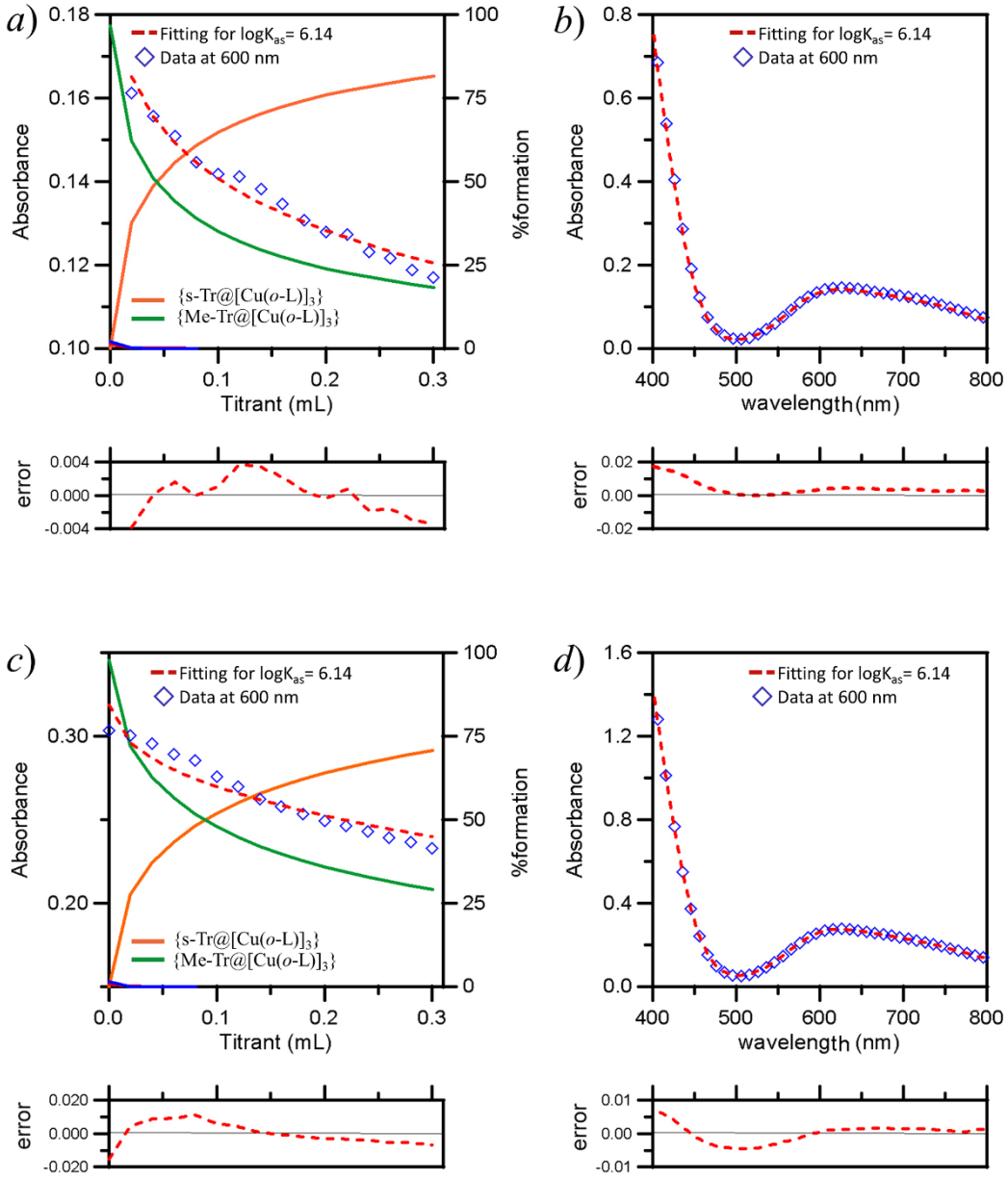

Figure 33. Titration with *s-Tr*, *a)* and *b*) report experimental and calculated results for {Me-Tr@[Cu(*o*-L)]$_3$} concentration of 1.05 mM, *c*) and *d*) for concentration of 2.19 mM. *a*) and *c*) Absorbance variation at 600 nm (blue blocks) and fitting (red dotted line). Variation of the {s-Tr@[Cu(*o*-L)]$_3$} concentration (orange line) and {Me-Tr@[Cu(*o*-L)]$_3$} concentration (green line) as a function of % of formation of the product. *b*) and *d*) Experimental (blue blocks) and calculated absorption spectra (red dotted line).

2.4 Bibliography.

1 M. Rancan, J. Tessarolo, P. L. Zanonato, R. Seraglia, S. Quici and L. Armelao, *Dalton Trans.*, **2013**, *42*, 7534.

2 M. Rancan, A. Dolmella, R. Seraglia, S. Orlandi, S. Quici and L. Armelao, *Chem. Commun.*, **2012**, *48*, 3115.

3 M. Rancan, J. Tessarolo, M. Casarin, P. L. Zanonato, S. Quici and L. Armelao, *Inorg. Chem.*, **2014**, *53*, 7276.

4 *a*) A. D. Phillips, L. Gonsalvi, A. Romerosa, F. Vizza and M. Peruzzini, *Coord. Chem. Rev.* **2004**, *248*, 955; (*b*) J. Bravo, S. Bolaño, L. Gonsalvi and M. Peruzzini, *Coord. Chem. Rev.* **2010**, *254*, 555.

5 *a*) D. J. Daigle, A. B. Pepperman Jr. and S. L. Vail, *J. Heterocycl. Chem.*, **1974**, *11*, 407; (*b*) M. Benhammou, R. Kraemer, H. Germa, J.-P. Majoral and J. Navech, *Phosphorous and Sulfur*, **1982**, *14*, 105; (*c*) M. M. Abu-Omar and J.H. Espenson, *J. Am. Chem. Soc.*, **1995**, *117*, 272.

6 *a*) D. J. Darensbourg, J. B. Robertson, D. L. Larkins and J. H. Reibenspies, *Inorg. Chem.*, **1999**, *38*, 2473; (*b*) B. J. Frost, J. L. Harkreader and C. M. Bautista, *Inor. Chem. Commun.*, **2008**, *11*, 580; (*c*) P. Smoleński and A. Kochel, *Polyhedron*, **2010**, *29*, 1561; (*d*) A. M. Kirillov, P. Smoleński, M. F. C. Guedes da Silva and A. J. L. Pombeiro, Eur. J. Inorg. Chem., **2007**, *18*, 2686.

7 B. J. Frost, C. A. Mebi and P. W. Gingrich, *Eur. J. Inorg. Chem.*, **2006**, *6*, 1182.

8 S. L. Mayo, B. D. Olafson, W. A. Goddard III, *Phys.Chem*. **1990**, *94*, 8897.

9 O. V. Dolomanov, L. J. Bourhis, R. J. Gildea, J. A. K. Howard and H. Puschmann, *J. Appl. Crystallogr.*, **2009**, *42*, 339.

10 R.D. Kohn, G. Seifert, Z. Pan, M. F. Mahon and G. Kociok-Kohn, *Angew. Chem. Int. Ed.* **2003**, *42*, 793.

11 P. Gans, A. Sabatini, A. Vacca, *Talanta* **1996**, *43*, 1739.

CHAPTER 3

Synthesis of new polytopic ligands

3.1 *β*-diketone based ligands.

Suitable ligands in order to build metallo-supramolecular architectures usually have nitrogen and oxygen atoms as coordination sites. A chelating binding site is desirable to stabilize the coordination compound. Moreover, the presence of rigid scaffolds is mandatory in order to minimize the ligand flexibility and to avoid the adoption of a wide range of conformations. For these reasons, a new class of *β*-diketones ligands, suitable for developing new MOPs, has been synthetized. The *β*-diketones, also called 1,3-diketones, are a class of molecules that bear two carbonyl groups separated by one carbon atom. Usually, in *β*-diketones the substituents lie on carbon 1 and 5, while complexes of 3-substituted *β*-diketonates (*α*-carbon) are less common. Examples of such complexes are reported in CHAPTER 2. The simplest molecule of this class is acetylacetone, a *β*-diketone where the substituents on both carbonyl groups are methyl moieties and the substituent on the *α*-carbon is hydrogen. The choice of the substituents plays an important role on the properties of the desired complexes. By modifying the substituents the solubility can be easily tuned; for instance, *tert*-butyl groups increase the solubility in organic solvents. At the same time, *tert*-butyl groups change the volatility of the deriving complexes. It is possible to increase the Lewis acidity of the ligands using fluorinated and perfluorinated groups. Addition of donor or acceptor groups for H-bond formation is useful to control the interaction with other species. This characteristic is very important when developing supramolecular host systems aimed to interact with guest molecules. Aromatic substituents enhance the light absorption and have also an influence on the

position of the energy levels of the ligand (singlet and triplet states). 1,3-diketones undergoe keto-enol tautomerism with a ketone/alcohol ratio that is strongly dependant on the substituents and the solvent. Thanks to the tautomerism, the proton on the α-carbon (alcoholic proton in the enol form) is easily removed thus forming the deprotonated β-diketonate binding group. β-diketonate ligands have good affinity with both transition metals and lanthanoid ions. Moreover, these ligands can act as an antenna to sensitize lanthanoid ions luminescence. These are important features for enhancing the functional properties of the assemblies and the host-guest interaction in the final MOPs. Various studies have been done using β-diketonate based complexes; for instance Lindoy and co-workers have developed an interesting coordination chemistry that produced metal dimers, triangles, and tetrahedra[1] based on aryl bis-β-diketone ligands and metal ions of the first transition series.

In this chapter, the design, synthesis and characterization of two new libraries of β-diketone ligands are reported: *i*) a series of bis-1,3-diketone ligands (the DPX-R library, section 3.2) and *ii*) a series of tris-1,3-diketone ligands (the TPX-R library, section 3.3). Besides the functional properties deriving from the substituents, the two libraries are designed with different scaffolds in order to tune the ligand rigidity and the ligand geometry. Different geometry of the scaffold, together with orientation of the coordinating vectors, allow the formation of supramolecular complexes with different size and shape.

3.2 DPX-R library.

The first library of ligands is a series of bis-β-diketone molecules with a biphenyl-based scaffold. Hereafter, this series of ligands has been labelled DPX-R library, where DP stays for di-phenyl, X indicates the central scaffold and R indicate the β-diketone substituent groups. A general scheme of the ligands is reported in Figure 34. These ligands have been designed in order to have a 2-fold axis through the central scaffold and coordination vectors of the two β-diketone groups that are parallel to the C_2 axis.

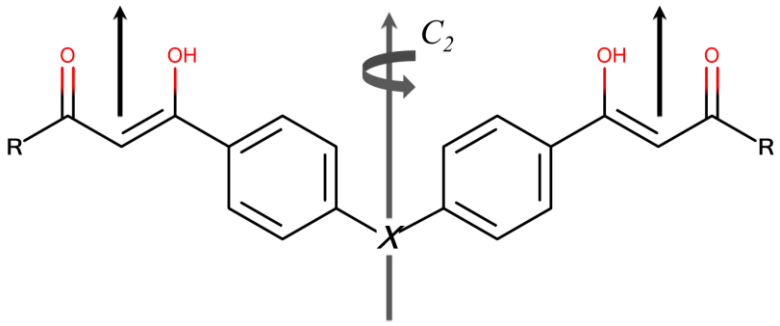

Figure 34. General scheme of DPX-R ligands.

Ligands with *β*-diketone groups bind transition metal ions or lanthanoid ions according to the models reported in Figure 35. Considering the first coordination sphere (oxygen atoms), with *i*) 4-coordinated metal ions, a square planar (D_{4h}) or a tetrahedral (T_d) coordination geometry is expected, resulting in 2-fold axis passing through the metal centre; *ii*) 6-coordinated metal ions an octahedral (O_h) coordination geometry is expected, resulting in 3-fold axis passing through the metal centre; *iii*) lanthanoid ions, that have a higher coordination number, a square antiprismatic (D_{4d}) coordination is expected, resulting in 4-fold axis passing through the metal centre.

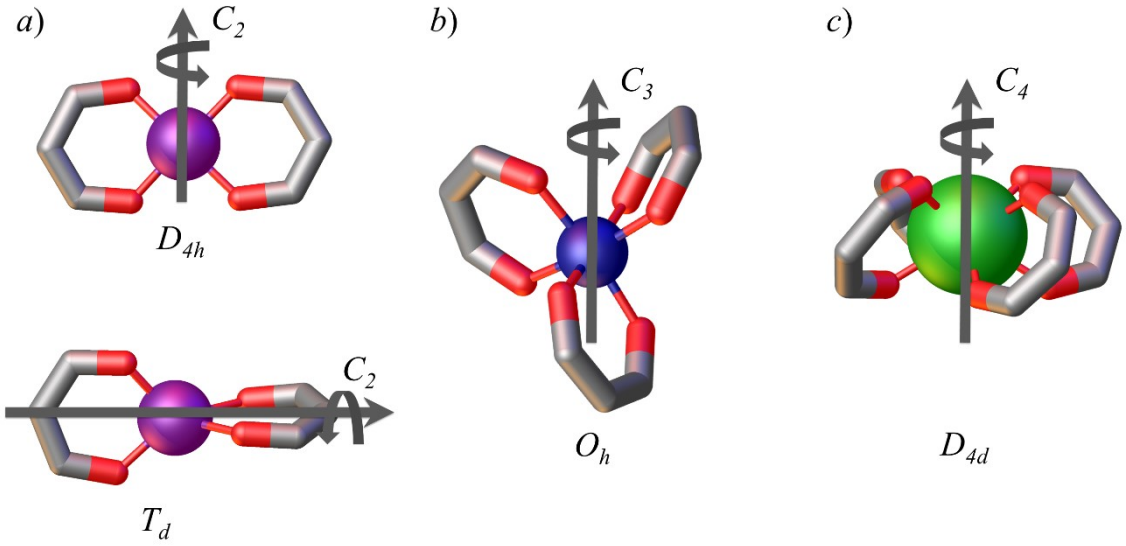

Figure 35. Coordination geometries *β*-diketonate ligands binding metal ions; considering the oxygen atoms of the first coordination sphere: *a*) 4-coordinated metals results in a D_{4h} or a T_d coordination geometry, *b*) 6-coordinated metals results in a O_h coordination geometry, *c*) 8-coordination metals results in a D_{4d} geometry.

On the basis of the directional bonding approach and symmetry considerations, by combining the metals coordination geometries (Figure 35) with the structural features of DPX-R ligands, a series of dimeric capsules can be designed, as shown in Figure 36. By combination of the DPX-R ligands with 4-coordinated metals having a D_{4h} or T_d symmetry, a dimer with two metals at the vertices (V) and two ligands on the polygon edges (E) is expected. With 6-coordinated metal ions having an O_h symmetry, the designed polyhedron will be a capsule with two metal vertices and three ligands on the edges. Finally, with lanthanoid ions, that can expand their coordination to 8-coordinated and therefore results in a D_{4d} symmetry, the expected polyhedron is a capsule with two metal vertices and four ligand edges.

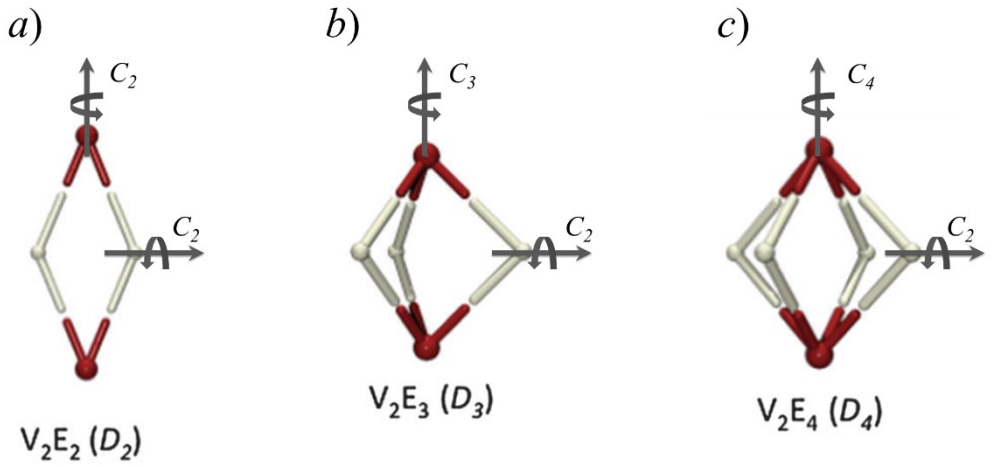

Figure 36. Coordination polygons and polyhedra from combination of DPX-R ligands with *a*) 4-coordinated metal centres, *b*) 6-coordinated metal centres, *c*) 8-coordianted metal centres.

In order to tune the structural properties of the desired MOPs, the ligand scaffold plays a major role. Changing scaffold unit allows to tune the distance between the metal centres and therefore, the dimension of the supramolecular assembly pocket. Moreover, tuning the flexibility of the ligand allows to access more complicated structures, such as helicates endowed with chiral properties. In the design of the DPX-R library, three scaffold units have been chosen, as reported in Figure 37: *i*) diphenylmethane (DPM-R), *ii*) diphenylamine derivative (DPA-R) and *iii*) *o*-diphenylbenzene (DPB-R). All the scaffolds can be seen as a diphenyl substitution of an X core molecule, where X is methane (M), a substituted amine (A) or benzene (B). DPM and DPA scaffolds have similar angles between the coordinating vectors. For DPM based ligands, an angle of *ca*. 109° is expected, while for DPA based ligands, an angle of *ca*. 107° is expected. The

ortho-diphenyl benzene has been chosen in order to vary the angle between the coordination vectors (angle = 60°) and to achieve supramolecular cages with different size and shape. The three scaffold units differ in flexibility and in the orientation angle of the *β*-diketone binding group. The differences in shape are designed in order to explore the possibility to vary the capsules dimension and the pocket size and shape.

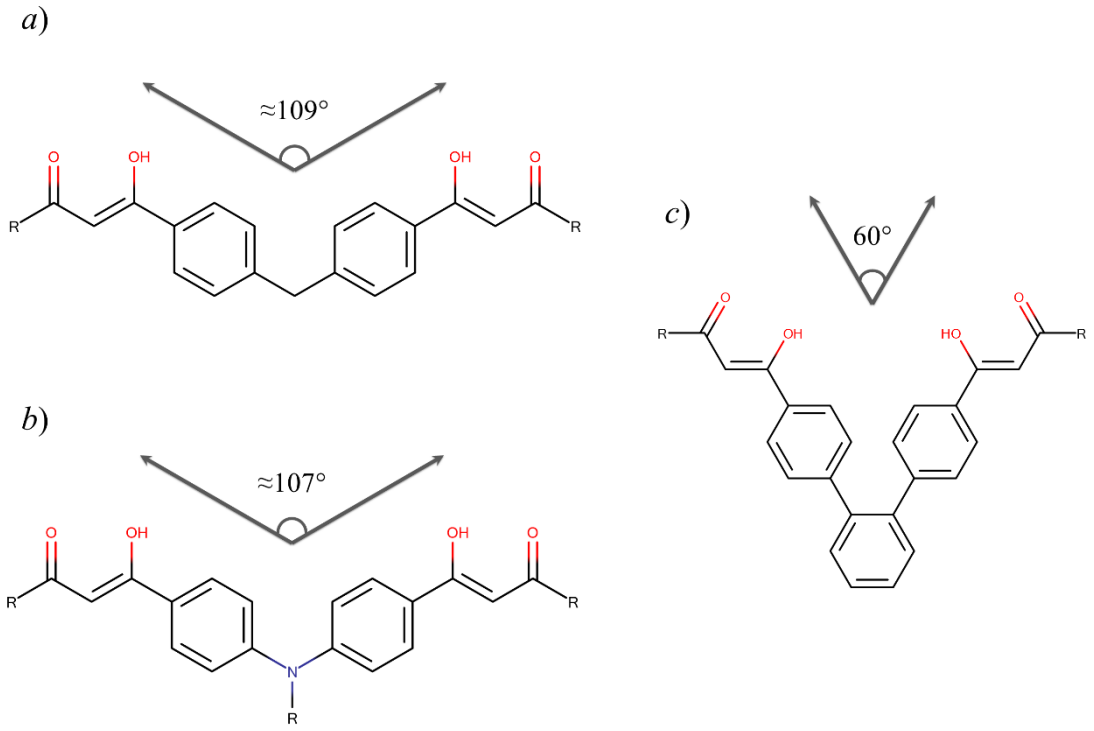

Figure 37. Scheme of the three different structures of DPX-R ligands with the orientation angles of the binding groups, generated from the scaffolds, *a*) X=M, diphenyl methane scaffold (DPM-R), *b*) X=A, diphenyl amine derivative scaffold (DPA-R), *c*) X=B, diphenyl benzene scaffold (DPB-R).

For the substituents groups (R), CF_3 and the phenyl ring have been chosen. However, the synthesis procedure allows to easily change the R group in order to tune the ligand properties. Four ligands have been synthesised, three with R = CF_3 and three different scaffolds and one with R = Ph and the diphenylmethane scaffold. The four ligands are reported in Figure 38: DPM-CF_3 (ligand **1**), DPM-Ph (ligand **2**), DPA-CF_3 (ligand **3**) and DPB-CF_3 (ligand **4**).

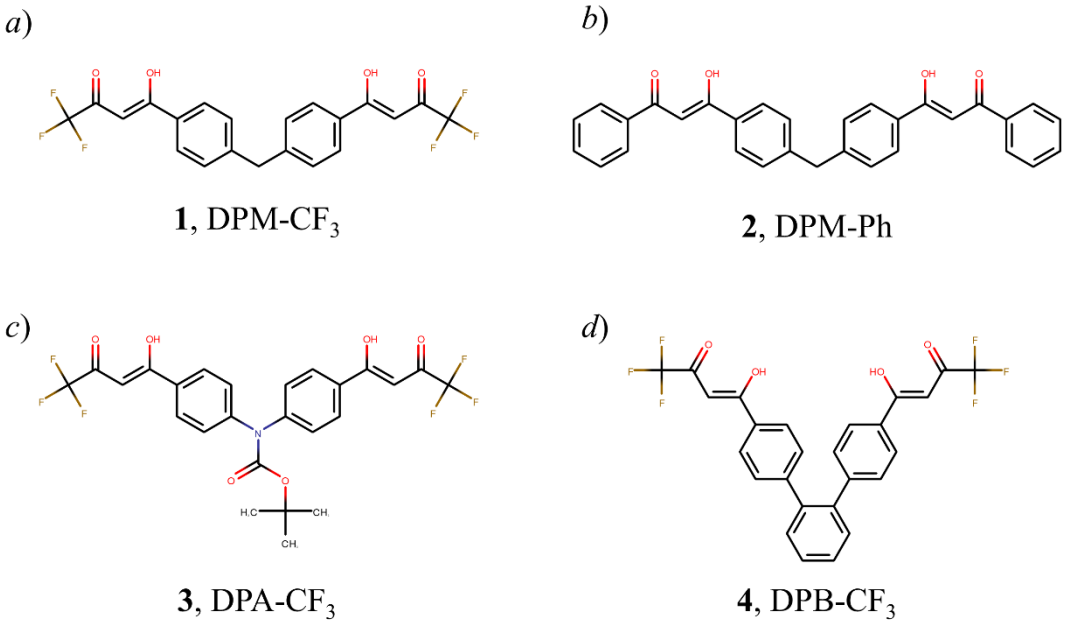

Figure 38. The DPX-R library, *a*) ligand **1**, X = M and R = CF_3; *b*) ligand **2**, X = M and R = Ph; *c*) ligand **3**, X = A and R = CF_3; *d*) ligand **4**, X = B and R = CF_3.

Ligands **1**, **2** and **4** have been synthesized following a general procedure, reported in Figure 39. Synthesis details are reported in sections 6.1.8-14. The starting reaction is the acetylation of the diphenyl scaffold, leading to the bis-acetophenone derivatives. Acetylation is performed by reacting diphenyl methane or diphenyl benzene with acetyl chloride and $AlCl_3$ in CS_2 solvent. The presence of aluminum trichloride is required in order to activate the acetylating species. The bis-acetophenone derivatives have been purified by column chromatography and characterized with ^{1}H-NMR spectroscopy. This step is followed by the Claysen condensation with R-substituted ethyl esters in the presence of strong bases, such as Na in ethanol or potassium *tert*-butoxide in tetrahydrofuran, to form the desired final *β*-diketone ligand. The obtained ligands are not easy to be purified by column chromatography since the desired product spreads across the whole silica phase. This is due to the presence of the *β*-diketone groups, which can interact with the column silica phase. Hence, the reactions have been pushed to an almost quantitative yield of the bis-*β*-diketone products, by addition of a large excess of R-substituted ethyl esters. After that, the purification is performed by recrystallization.

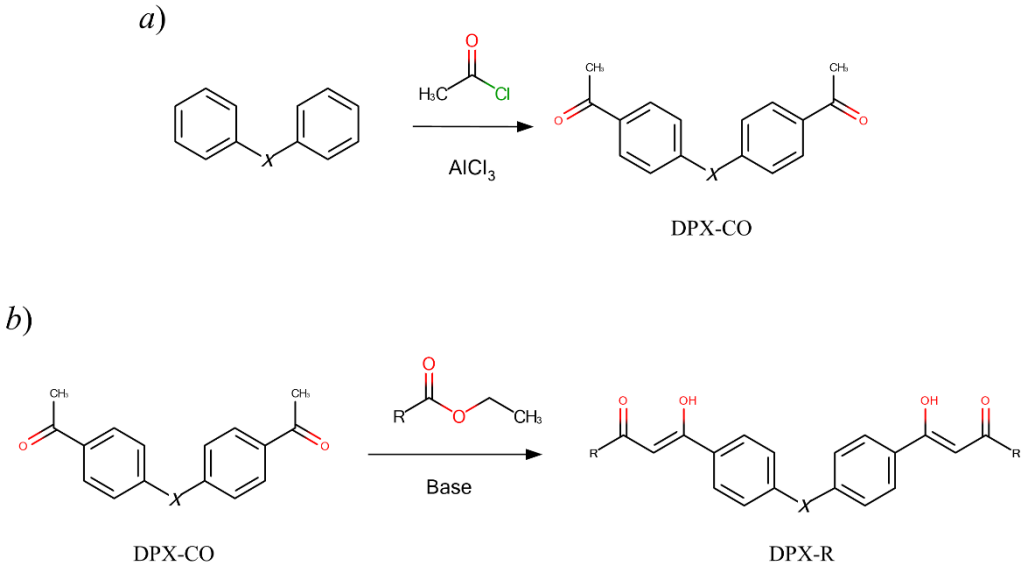

Figure 39. Synthesis of ligands **1**, **2** and **4** of the DPX-R library; *a*) acetylation of the di-phenyl scaffold, *b*) Claysen condensation with R-substitute ester to form the bis-*β*-diketone ligand.

For the synthesis of the di-phenylamine derivative (ligand **3**), it was not possible to follow the same procedure. The amine has to be protected in order to avoid reaction at the N-H group that leads to the formation of amide species. The designed ligand has been obtained through a coupling between *tert*-butyl carbamate and *p*-bromoacetophenone, using a Cu(I) catalyst (Figure 40 *a*). The bis-acetophenone derivative has been purified by column chromatography and characterized with ^{1}H-NMR. This step is followed by a Claysen condensation with ethyl trifluoroacetate (Figure 40 *b*). This leads to a bis-*β*-diketone ligand with a protected amino group that can be deprotected with trifluoroacetic acid and hence used for a further functionalization of the system. To force the reaction to a quantitative yield the ethyl trifluoroacetate has been added in excess. The obtained bis-*β*-diketone ligand has been purified by recrystallization.

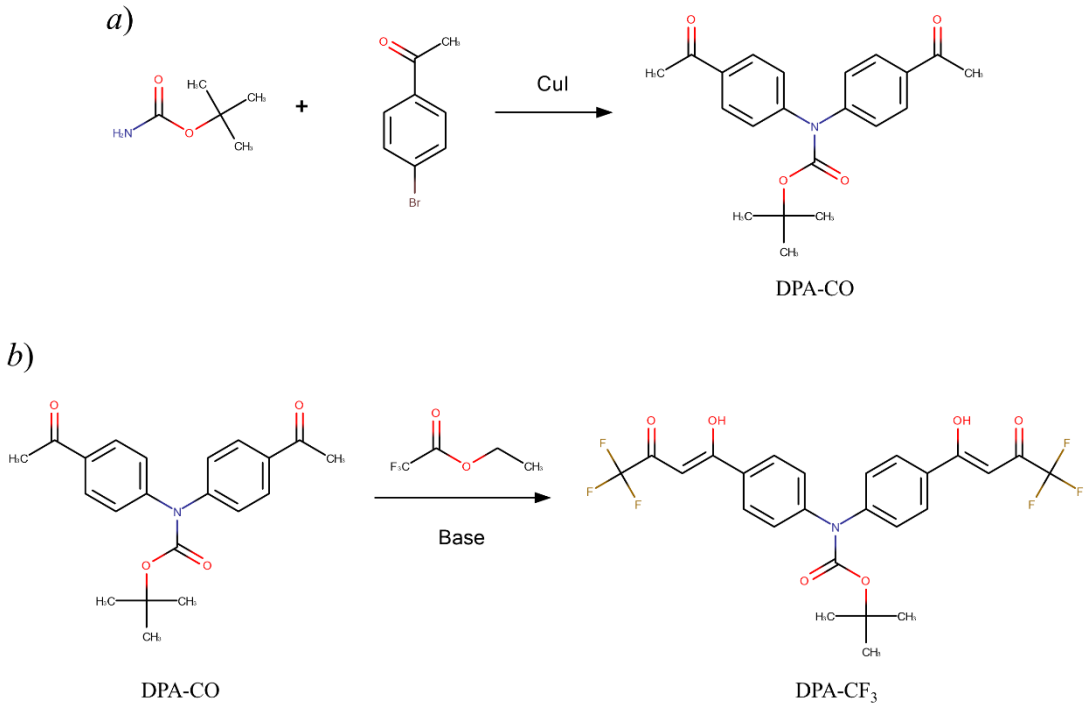

Figure 40. Synthesis of ligands **3** of the DPX-R library; *a*) Cu(I) catalysed coupling, to obtain the di-phenyl scaffold, *b*) Claysen condensation with R-substitute ester to form the bis-*β*-diketone ligand.

Ligands **1** and **2** of the DPX-R library have been characterized by ^{1}H-NMR, ^{13}C-NMR, HMQC and HMBC NMR spectroscopy (Figure 80-Figure 85 in CHAPTER 6). Ligand **3** and **4** have been characterized by ^{1}H-NMR, ^{13}C-NMR and by comparison with ligands **1** and **2** NMR spectra. Ligand **4** signals have been assigned also by comparison with ^{1}H-NMR and ^{13}C-NMR of *o*-dichlorobenzene (Figure 86-Figure 89 in CHAPTER 6).

All the spectra have some characteristics in common, deriving from the *β*-diketone group and the diphenyl units, while the differences are mainly due to the scaffold and to the substituent groups. In $CDCl_3$ the *β*-diketone is present, almost quantitatively, in the enol form. The presence of the *β*-diketone is easy detectable thanks to the diagnostic peaks deriving from the OH proton of the *β*-diketone, at 15.10 ppm *ca.* when R-group is CF_3 and at 16.85 ppm *ca.* when R-group is the phenyl ring. The *β*-diketone shows also the singlet of the proton of the α-carbon, at 6.54 ppm *ca.* with CF_3 substituent and at 6.83 ppm *ca.* with phenyl ring substituent. Moreover, all the ligands are characterized by an AA'BB' system at 7.3 ppm and 7.9 ppm deriving from the diphenyl units of the scaffold. In Figure 41 an example for the ^{1}H-NMR spectra for the ligands of the DPX-R library is reported.

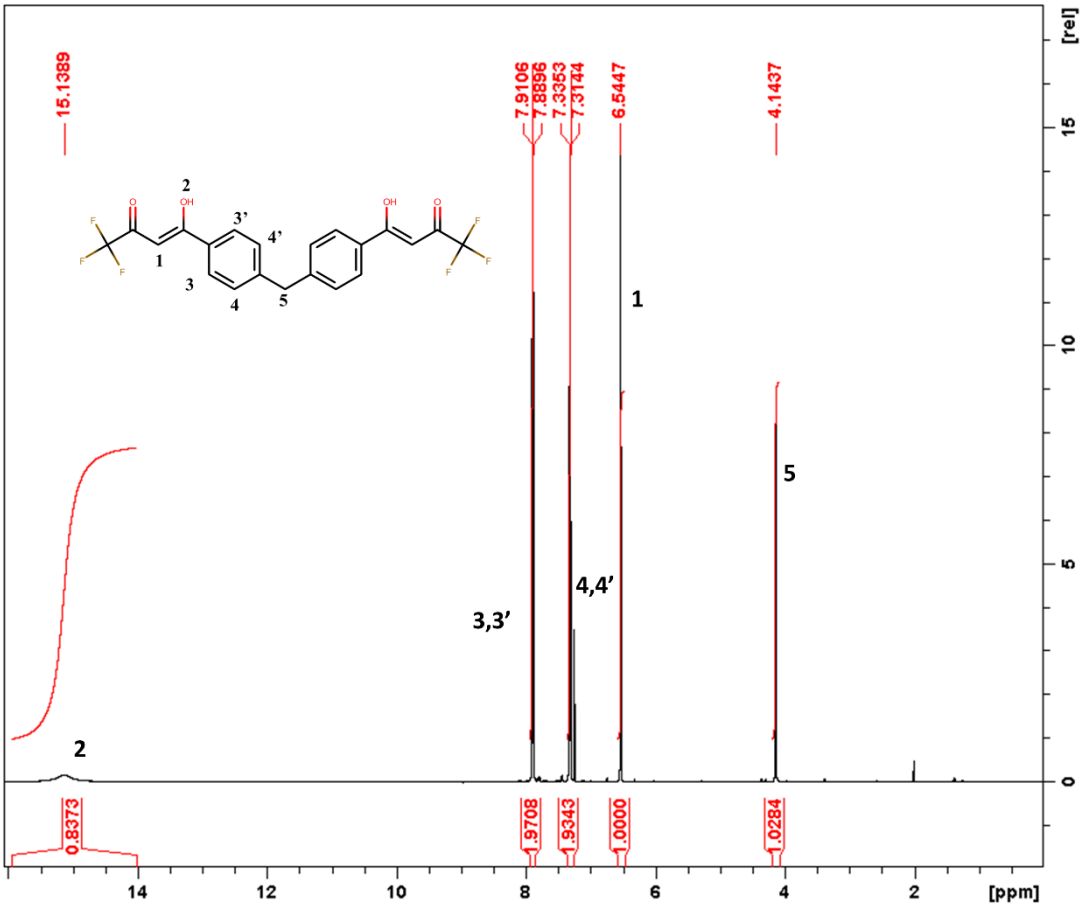

Figure 41. ^{1}H-NMR (400MHz, $CDCl_3$, 25°C) spectrum of ligand **1**.

For ligands **1** and **2**, single crystals have been obtained. In both structures, the presence of a 2-fold axis passing through the centres of the ligand is clearly confirmed. Crystallographic structures also confirm the formation of ligands with the desired angle between the coordination vectors. For ligand **1** (Figure 42) the angle between the coordination vectors is 112.0°, while for ligand **2** (Figure 43) the same angle is 115.9°. Experimental details of the single crystals analyses are reported in sections 6.3.5-6.

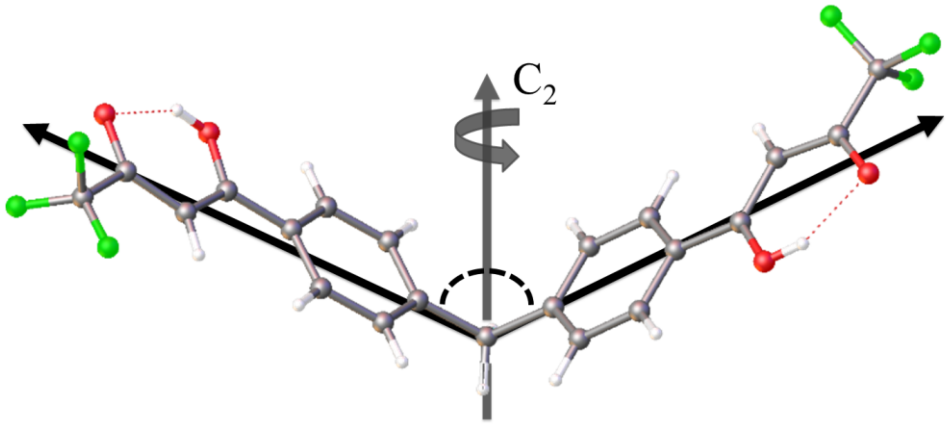

Figure 42. Ball and stick structural model of ligand **1**, obtained from X-ray diffraction data. The presence of the 2-fold axis is highlighted. The angle between the coordination vectors is 111.96°. Colour code: O red, F green, C grey, H white.

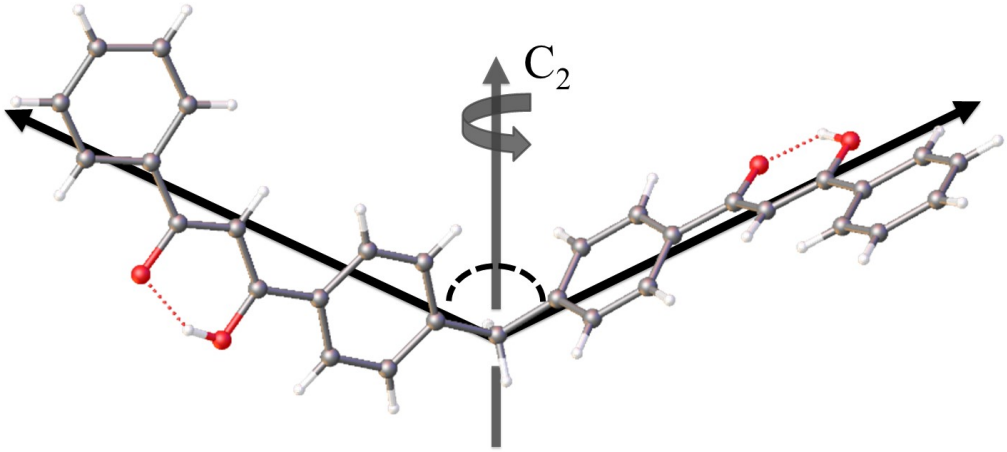

Figure 43. Ball and stick structural model of ligand **2**, obtained from X-ray diffraction data. The presence of the 2-fold axis is highlighted. The angle between the coordination vectors is 115.88°. Colour code: O red, C grey, H white.

3.3 TPX-R library.

The second library of ligands is a series of tris-*β*-diketones bearing a triphenyl-based scaffold. Similar to the the DPX-R library, this series of ligands has been labelled TPX-R library, where TP stays for tri-phenyl, X indicates the type of scaffold and R indicates the *β*-diketone substituent groups. The general scheme of the ligands is reported in Figure 44.

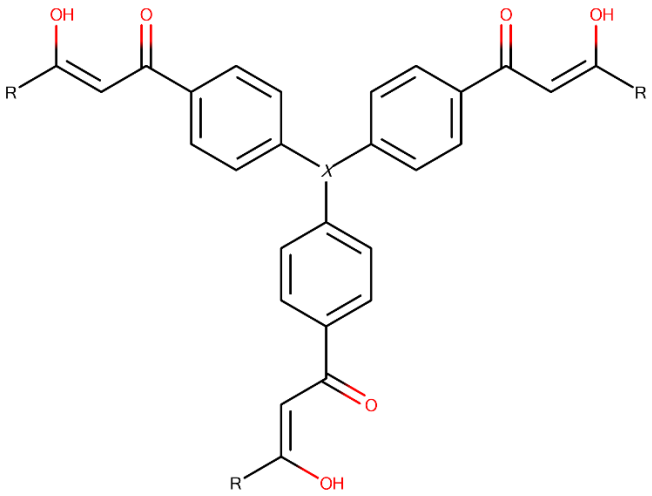

Figure 44. General scheme of TPX-R ligands.

These ligands have been designed in order to have a 3-fold axis through the central scaffold. Three scaffold units have been used in order to tune the ligands flexibility, the angle between the coordination vectors and the electronic properties. The library has been synthesised starting from the following scaffolds: *a*) triphenylmethane (TPM, X =M), *b*) triphenylamine (TPA, X = A) and *c*) triphenylbenzene (TPB, X = B) (Figure 45). All the scaffold units have a C_3 axis (passing in the middle of the structure), while they differ in flexibility, from the more flexible triphenylmethane (TPM) to the more rigid triphenylbenzene (TPB). While TPA and TPB are planar molecules, the TPM scaffold is more kinked with an angle of *ca*. 106° between the phenyl rings and the C-H core of the ligands. Again, the choice to synthesise ligands with different scaffold units plays an important role to design and develop metallo-supramolecular cages with different size and shape of the confined space. The three scaffolds have different properties, in TPB-R and in TPA-R there is an extended electronic delocalization along the ligand molecule. Moreover, triphenylamine and its derivatives, included the TPA-R ligand, have luminescent properties.

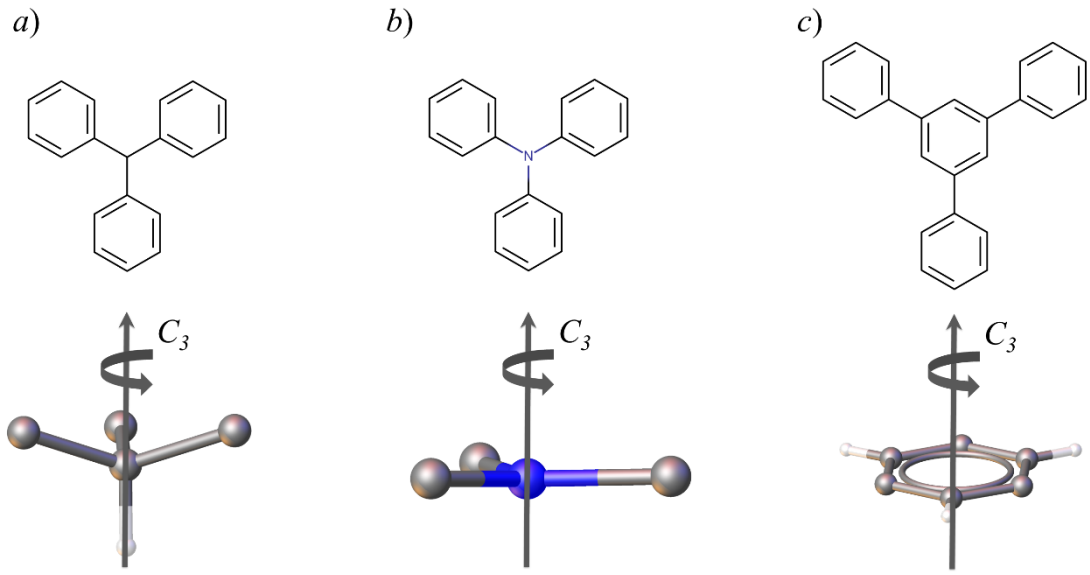

Figure 45. Three different scaffold units of TPX-R ligands with the 3-fold axis; *a*) triphenyl methane scaffold, *b*) triphenyl amine scaffold, *c*) 1,3,5 tripheynlbenzene scaffold.

On the basis of these geometrical features, the TPX-R library has been designed to develop supramolecular tetrahedra and octahedra, when combined with *d* and *f* metals, respectively (Figure 46). In particular when combined with 6-coordinated metals (O_h symmetry), the designed polyhedron will be a tetrahedron with four metal vertices (V) and four ligands lying on the faces (F). When combined with lanthanoid ions, that can adopt a square antiprismatic coordination geometry (D_{4d} symmetry), the designed polyhedron should be a octahedron with six metals on the vertices (V) and eight ligands on the faces (F). The polyhedral capsules have been designed in order to have open windows on the polyhedral edges, which will allow guest molecules to go in and out from the metallo-supramolecular pocket.

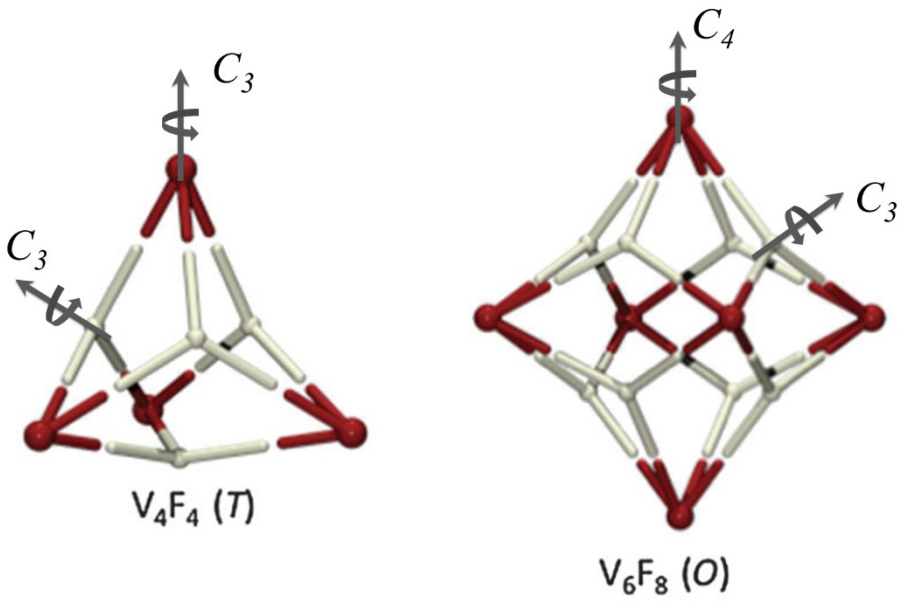

Figure 46. Coordination polyhedra from combination of TPX-R ligands with metal ions; *a*) with 6-coordinated metal centres a tetrahedron is expected, *b*) with 8-coordianted metal centres an octahedron is expected.

All the ligands of the TPX-R library have been synthesised following a general procedure reported in Figure 47. Synthesis details are reported in sections 6.1.15-23. The first step is the acetylation of the triphenyl scaffold leading to the tris-acetophenone derivatives. Acetylation is performed by reacting triphenylmethane, triphenylamine or triphenylbenzene with acetyl chloride and $AlCl_3$ in CS_2 as solvent. The tris-acetophenone derivatives have been purified by column chromatography and characterized with ^{1}H-NMR spectroscopy. This step is followed by the Claysen condensation with R-substituted ethyl esters in the presence of strong bases, such as Na in ethanol or potassium *tert*-butoxide in tetrahydrofuran, to form the desired final *β*-diketone ligand. Also in this case, the obtained ligands can not be easily purified by column. Hence, the reactions have been pushed to an almost quantitative yield of the tris-*β*-diketone product, by addition of a large excess of R-substituted ethyl esters, and the ligands have been purified by crystallization.

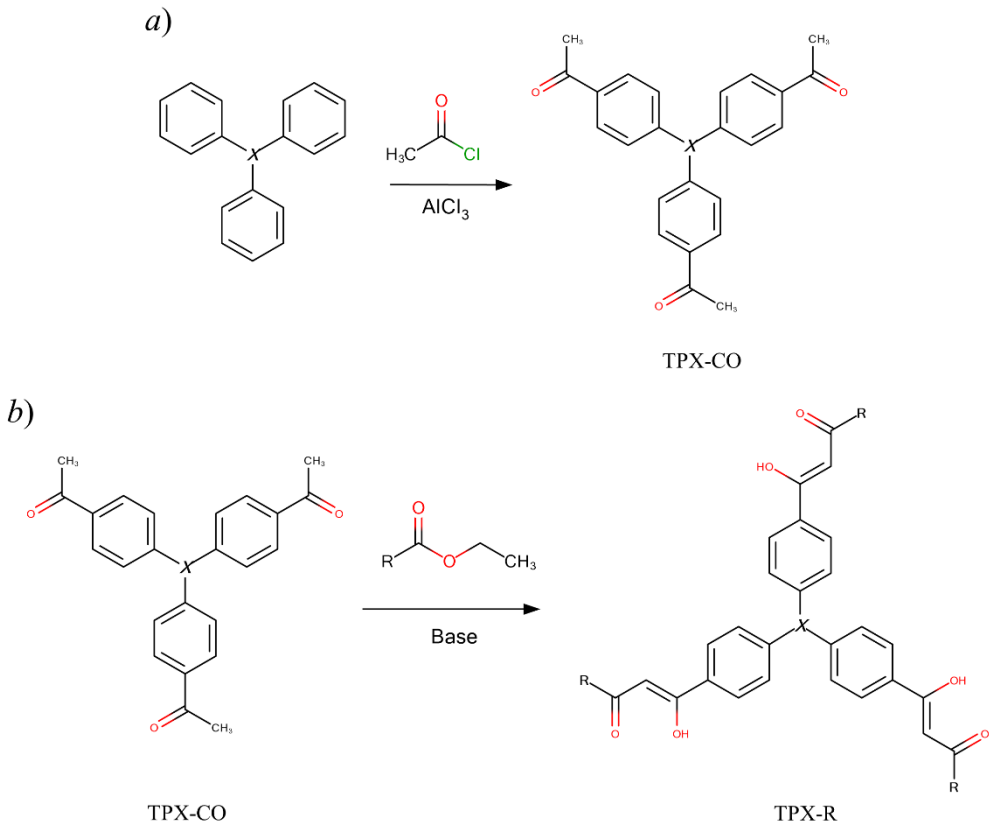

Figure 47. Synthesis of the TPX-R library; *a*) acetylation of the TPX scaffold, X = M, A, B; *b*) Claysen condensation with R-substitute esters to form the tris-*β*-diketone ligands, R = CF_3, tBu.

The TPX-R library has been designed in order to be easily functionalized by changing the R substituent. In fact, the R group can influence the ligand properties, such as solubility in organic solvents or in water, the electronic properties and the capability of the ligand and of the derived metallo-supramolecular assemblies to interact with guest molecules. Two R groups have been chosen: trifluoromethane group (R = CF3) and *tert*-butyl group (R = tBu). Moreover, the synthetic procedure allows to easily modify the substituent by changing the R group of the ethyl ester used in the Claysen condensation (Figure 47 *b*). A total of six ligands have been synthesised. The ligands of the TPX-R library are reported in Figure 48: TPM-CF_3 (ligand **5**), TPM-tBu (ligand **6**), TPA-CF_3 (ligand **7**), TPA-tBu (ligand **8**), TPB-CF_3 (ligand **9**) and TPB-tBu (ligand **10**).

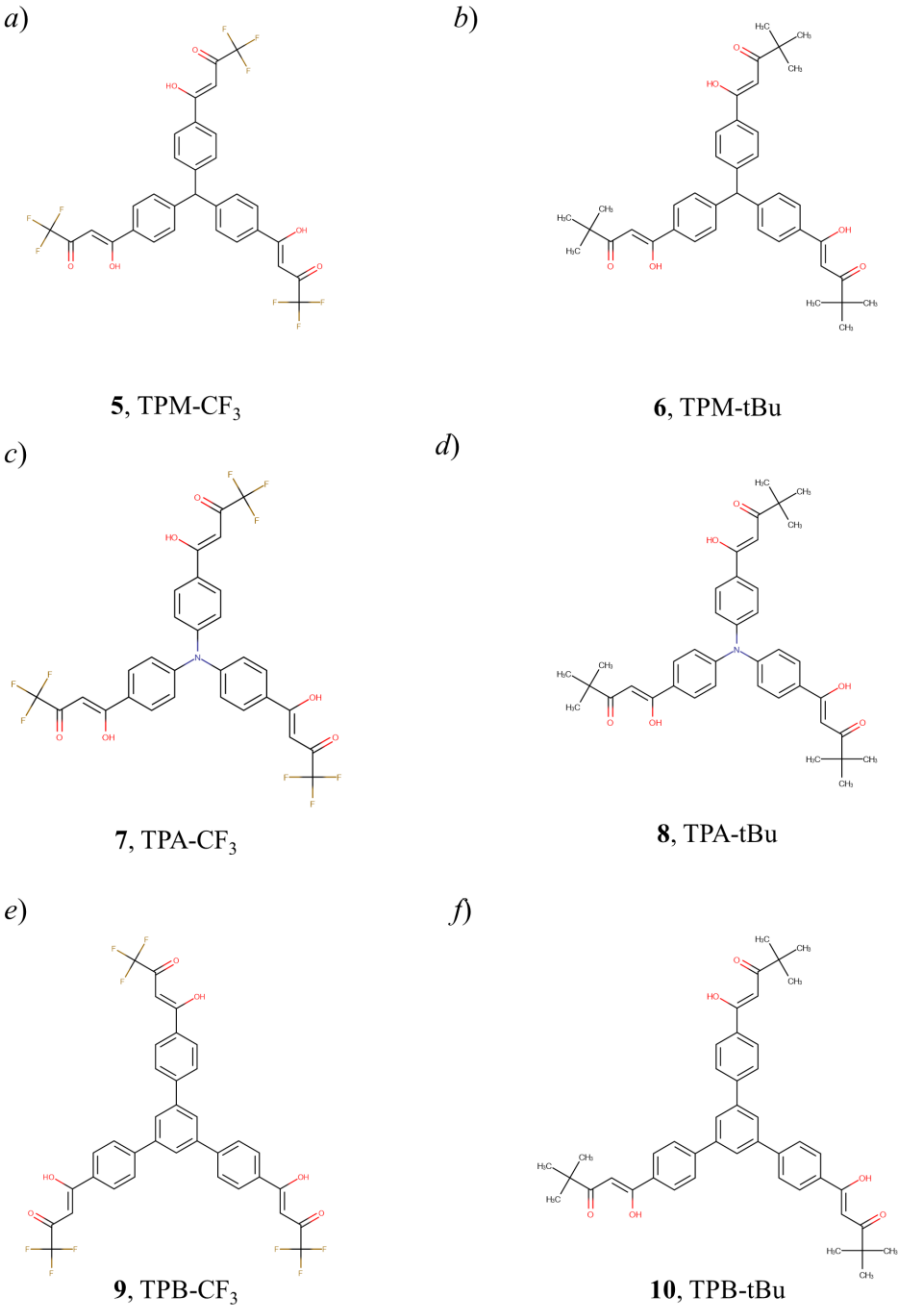

Figure 48. The TPX-R library, *a*) ligand **5**, X = M and R = CF_3; *b*) ligand **6**, X = M and R = tBu; *c*) ligand **7**, X = A and R = CF_3; *d*) ligand **8**, X = A and R = tBu; *e*) ligand **9**, X = B and R = CF_3; *f*) ligand **10**, X = B and R = tBu.

All the ligands of the TPX-R library have been characterized by ^{1}H-NMR, ^{13}C-NMR (Figure 96-Figure 106 in CHAPTER 6). All the spectra have some common characteristics, deriving from the *β*-diketone group and the triphenyl units, while the differences are mainly due to the scaffold and to the substituent groups. The presence of the *β*-diketone is easy detectable thanks to the diagnostic peaks deriving from the OH proton of the *β*-diketone, at 15.10 ppm *ca.* when R = CF_3 and at 16.46 ppm *ca.* when R =

tBu. The *β*-diketone presence shows also the singlet of the proton of the α-carbon, at 6.54 ppm with CF_3 substituent and at 6.26 ppm *ca.* with *tert*-butyl substituent. Moreover, all the ligands are characterized by an AA'BB' system at 7.3 ppm *ca.* and 7.9 ppm *ca.* deriving from the triphenyl units of the scaffold. In Figure 49 an example for the ^{1}H-NMR spectra for the ligands of the TPX-R library is reported.

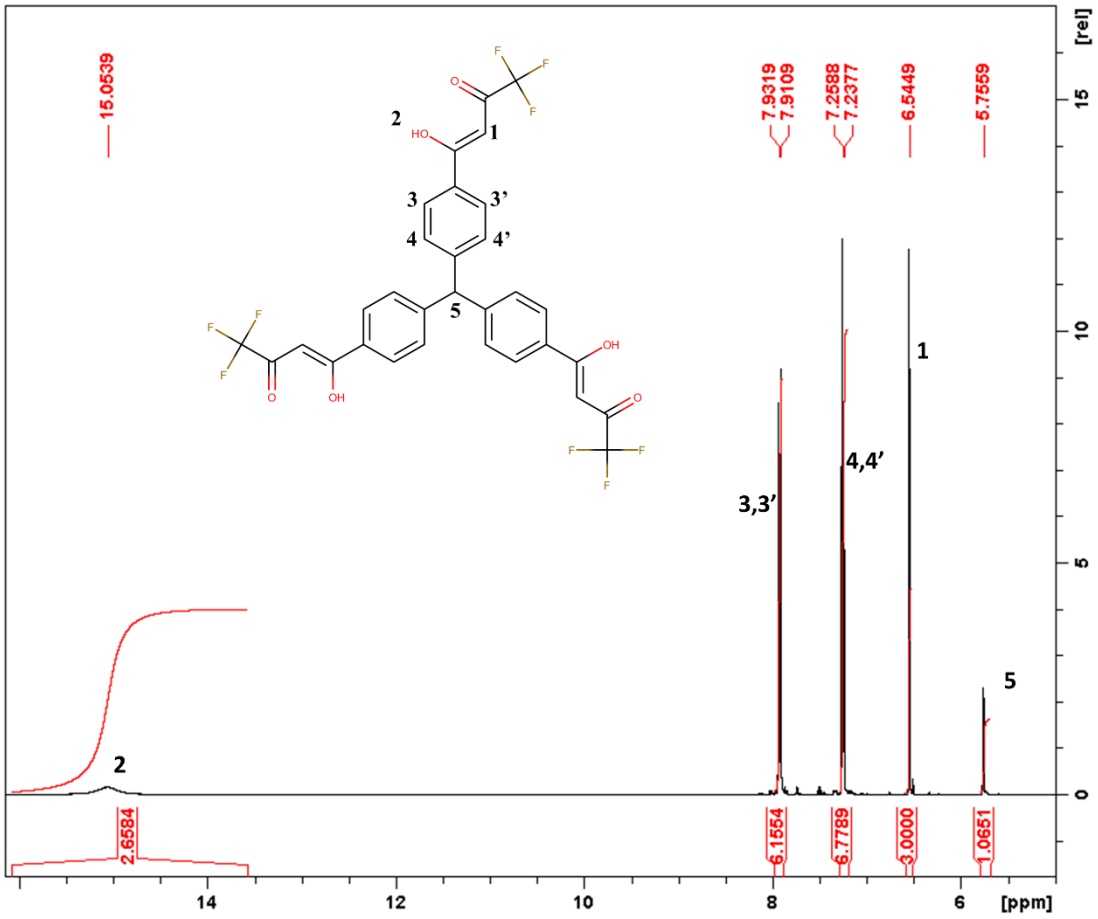

Figure 49. ^{1}H-NMR (400MHz, $CDCl_3$, 25°C) spectrum of ligand **5**.

For ligand **7**, the crystal structure has been determined. In the structure is confirmed the presence of a 3-fold axis passing through the centres of the ligand (Figure 50). Experimental details of the single crystals analysis are reported in section 6.3.7.

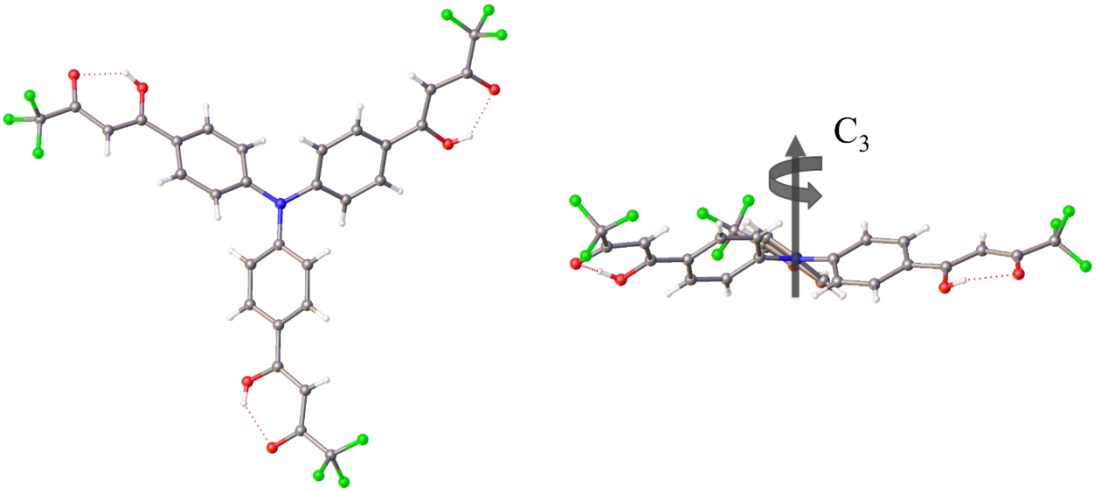

Figure 50. Ball and stick structural model of ligand **7**, obtained from X-ray diffraction data. The presence of the 3-fold axis is highlighted. Colour code: O red, N blue, F green, C grey, H white.

3.4 Bibliography.

1 For selected examples see: (a) J. K. Clegg, L. F. Lindoy, B. Moubaraki, K. S. Murray, J. C. McMurtrie, *Dalton. Trans.* **2004**, 2417. (b) J. K. Clegg, K. Gloe, M. J. Hayter, O. Kataeva, L. F. Lindoy, B. Moubaraki, J. C. McMurtrie, K. S. Murray, D. Schilter, *Dalton.Trans*. **2006**, 3977. (c) J. K. Clegg, F. Li, K. A. Jolliffe, G.V. Meehanc, L. F. Lindoy, *Chem. Commun.* **2011**, *47*, 6042.

CHAPTER 4

Synthesis of innovative coordination driven metallo-supramolecular architectures

4.1 Metallo-supramolecular tetrahedra.

In the previous chapter, the synthesis of a new tris-*β*-diketone ligands library designed specifically to build metallo-supramolecular polyhedra (MOPs) has been described. In this section, the synthesis of new metallo-supramolecular tetrahedra, built starting from the TPM-R library and Fe^{3+} ions as building blocks, is reported.

The use of transition metals as building blocks allows to partially predict and control the coordination geometries. When combined with the tris-*β*-diketone ligands, transition metals act as Lewis acidic building blocks. The choice of the metal ion, combined with a stoichiometry control and the geometry of the ligands, permits a structural design for the self-assembly of the desired metal-organic polygons or polyhedra. To develop a supramolecular tetrahedron, Fe^{3+} has been chosen as metal centre. Iron (III) ion adopts an octahedral coordination geometry thus, when combined with *β*-diketone ligands, it will be coordinated by three chelating groups (Figure 51).

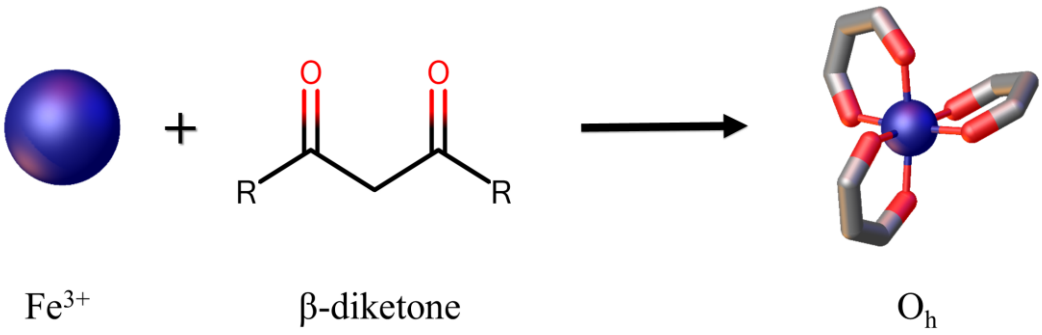

Figure 51. Fe^{3+} coordination with *β*-diketone group.

Iron (III) octahedral coordination presents 3-fold symmetry axes that, when combined with the geometrical properties of the TPX-R library, should result in the formation of a metal-organic tetrahedron (Figure 52). In fact, considering the design of the desired MOP, a combination of the C_3 axis of the ligand with the C_3 axis generated by the octahedral coordination geometry is required to generate a tetrahedral capsule (Figure 46). According to the directional bonding approach, self-assembly of Fe^{3+} ions and TPM-R ligands is expected to form a supramolecular tetrahedron where the metal centres lye on the polyhedron vertices, and the ligands on the faces, resulting in a $Fe_4(TPM\text{-}R)_4$ tetrahedral MOP. This supramolecular species has been specifically designed in order to have a cavity able to host guest molecules. Moreover, no sterical hindrance is present on the edges of the platonic solid, thus generating some open spaces suitable to act as windows for the way in and way out of the guests.

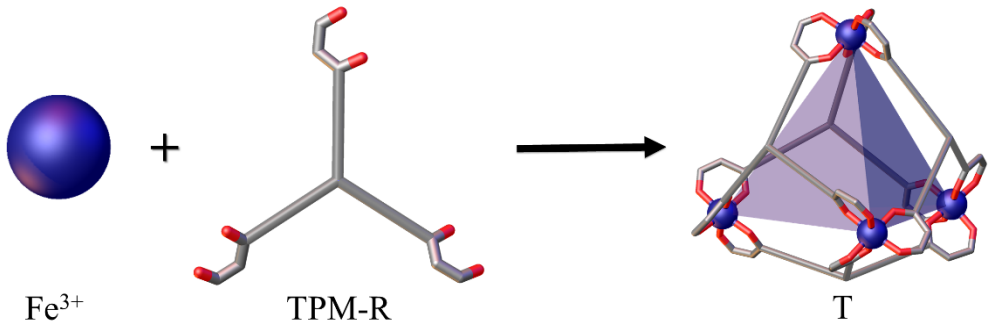

Figure 52. General design of Fe^{3+} ion and TPM-R ligands based supramolecular tetrahedra. Purple surface indicates the internal tetrahedral shape.

Fe^{3+} ions have been combined with all the ligands of the TPX-R library. However, only reactions with ligands of the TPM-R groups (ligands **5** and **6**, Figure 53) led to interesting results. These ligands have the same triphenylmethane scaffold and differ in the R-groups of the *β*-diketone unit. Reaction with TPA-R (ligands **7**, **8**) and TPB-R (ligands **9**, **10**)

sub-libraries gave some interesting preliminary results, altough, more detailed investigations are necessary.

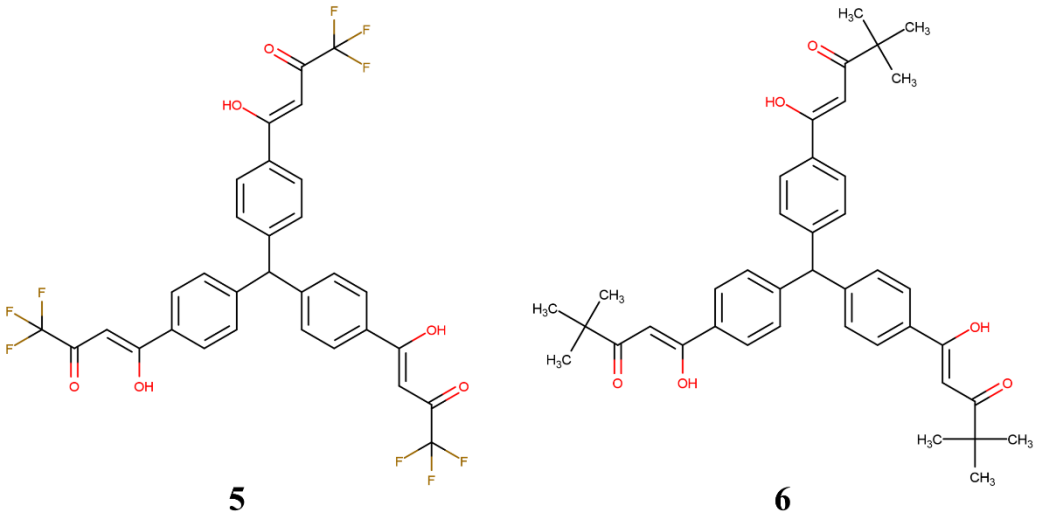

5 **6**

Figure 53. The TPM-R sub-library. Ligand **5** = TPM-CF_3, ligand **6** = TPM-tBu.

The synthesis of the metallo-supramolecular polyhedra has been conducted with two different approaches, leading to the same products. Detailed synthesis are reported in sections 6.1.24-26. In both cases $FeCl_3$ has been used as the metal source. The first approach is the self-assembly of the two building blocks in tetrahydrofuran, in the presence of a base. $FeCl_3$, TPM-R ligand and Na_2CO_3 have been combined in stoichiometric amount in a tetrahydrofuran solution. The mixture has been reacted at reflux temperature for 12 hours resulting in a dark red solution. After filtration of the by-products (NaCl) and evaporation of the solvent, a red powder has been obtained in quantitative yield.

The second approach is a two-solvent approach, in which the ligand is dissolved in chloroform and the metal salt in methanol. The Fe^{3+} methanol solution has been gently layered over the chloroform solution and the two solvents have been allowed to diffuse one into the other. In these conditions, a red layer is suddenly formed at the interface and the solution completely turns to dark red after two days. In this case, the formation of the supramolecular architecture does not require the presence of a base and the metal-organic polyhedra (MOPs) self-assemble as soon as the two solvents diffuse one into the other. Evaporation of the solvents results in a red product in quantitative yield.

In both cases, self-assembly of the TPM-R ligands with Fe^{3+} leads to the formation of Fe_4L_4 supramolecular assemblies of general formula $[Fe(TPM\text{-}R)]_4$. Two supramolecular

capsules have been obtained, $[Fe(TPM\text{-}CF_3)]_4$ (hereafter **Fe5**) and $[Fe(TPM\text{-}tBu)]_4$ (hereafter **Fe6**) (Figure 54-Figure 55). The formation of the products are supported by elemental analysis and crystallographic data.

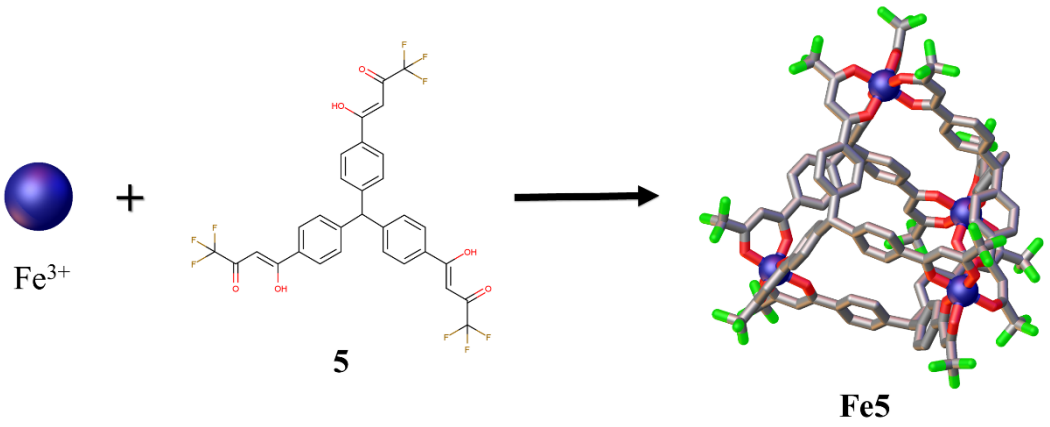

Figure 54. Self-assembly of **Fe5**. Structural model obtained from single crystal X-ray diffraction. Colour code: Fe blue, O red, F green, C grey, H atoms omitted for clarity.

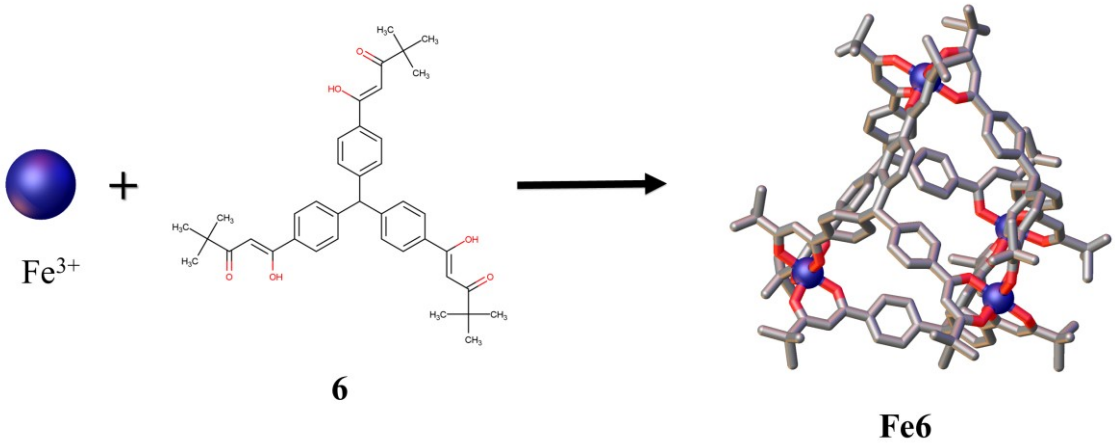

Figure 55. Self-assembly of **Fe6**. Structural model obtained from single crystal X-ray diffraction. Colour code: Fe blue, O red, C grey, H atoms omitted for clarity.

For both new supramolecular complexes, single crystals have been obtained from different crystallization conditions. In both cases, clear red crystals with plate habit have been obtained. Unfortunately, the obtained crystals were too small and showed low diffraction power for laboratory diffractometer. X-ray diffraction data have been collected using synchrotron radiation. Determination and refinement details are reported in sections 6.3.8-9. For **Fe5**, single crystals suitable for synchrotron X-ray diffraction have been obtained from a chloroform/methanol solution. In these conditions, the compound crystallizes with chloroform solvent molecules into the crystal lattice. Two

solvent molecules could be modelled, resulting in the formation of **Fe5**·2$CHCl_3$ (Figure 56 *a*). The tetrahedral species crystallize in a triclinic P-1 space group. The cell has a total volume of 7518.3 $Å^3$ and contains two asymmetric units, each of them corresponding to one full molecule of **Fe5** with two chloroform molecules (Figure 56 *b*). The structure is characterized by large solvent accessible voids; OLEX2 program calculates a total solvent accessible volume per unit cell of 1898.5 $Å^3$, corresponding to the 25.3% of the total unit cell volume (Figure 56 *c* and *d*). The void space contains non-negligible residual electron density that has been removed using the OLEX2 mask routine. The program calculates one void with an electron count of 351.3, compatible with the presence of 6 $CHCl_3$ molecules that can not be modelled.

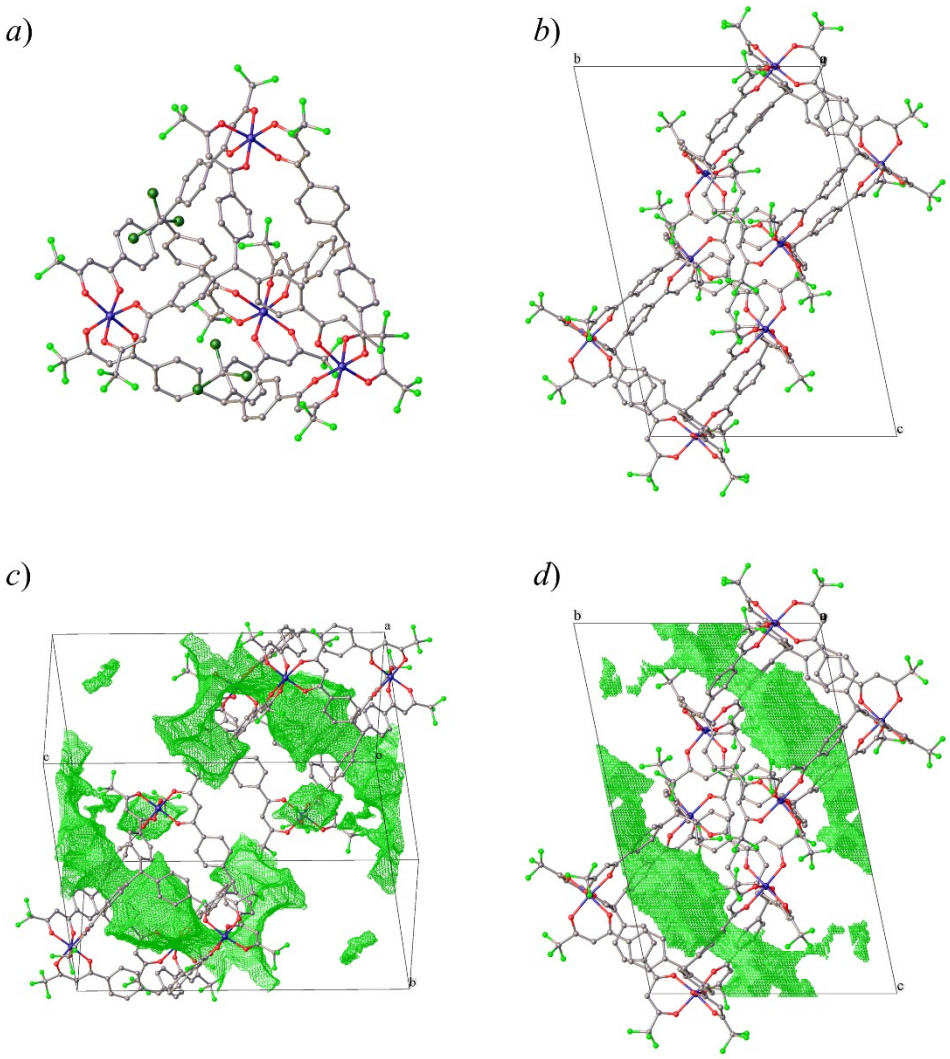

Figure 56. Ball and stick structural model, obtained from single crystal X-ray diffraction, for **Fe5**·2$CHCl_3$. *a*) Asymmetric unit; *b*) unit cell with 2 supramolecular capsules; *c*) and *d*) green surfaces report the map of the solvent accessible void per unit cell, *d*) show the unit cell view along a axis. Colour code: Fe blue, O red, F light green, Cl dark green, C grey, H atoms are omitted for clarity.

Figure 56 *c* and *d* clearly shows the presence of solvent accessible voids inside the MOP cavity. This confirms that the supramolecular structure has enough space in the pocket to host guest molecules inside. Moreover, since the ligand scaffold unit is located on the tetrahedron faces, **Fe5** has six windows on the polyhedron edges, which allow guest molecules to go in and out from the MOP cavity. This is further confirmed by the presence of two chloroform molecules located on two of the six windows. Figure 57 highlights the windows area (purple surface). The presence of $CHCl_3$ molecules clearly evidences that the windows are large enough to allow the diffusion of guest molecules inside the cavity.

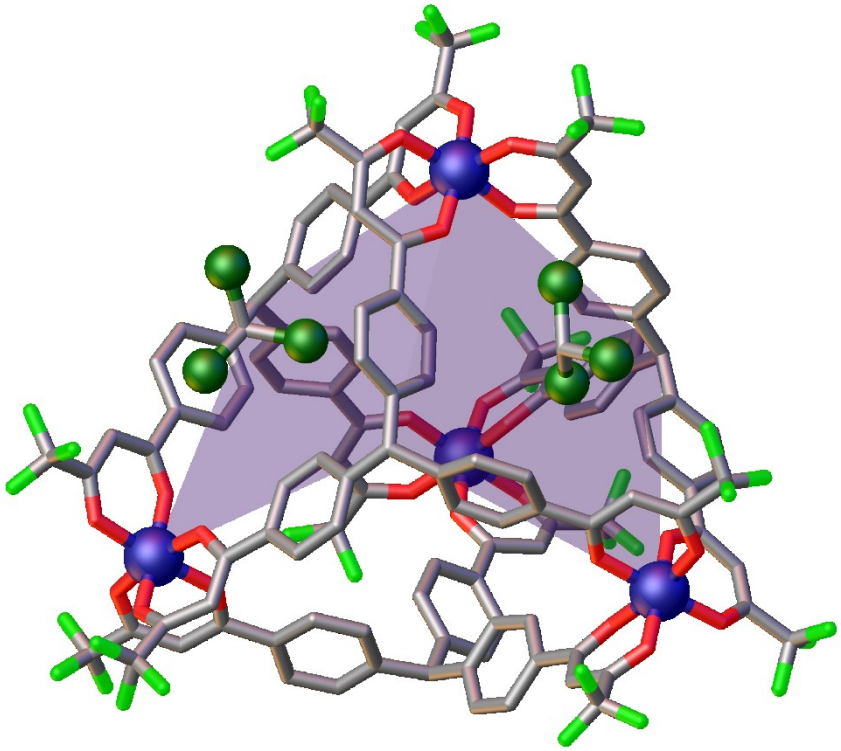

Figure 57. Structural model for **Fe5** asymmetric unit. The two $CHCl_3$ molecules are located on the supramolecular windows. Purple surfaces indicate the mean plane of the window between the MOP cavity and the external space. Colour code: Fe blue, O red, F light green, Cl dark green, C grey, H atoms are omitted for clarity.

Moreover in the crystalline packing, supramolecular pairs of **Fe5** are formed. In these pairs two **Fe5** MOPs are one in front of the other (Figure 58 *a*). This supramolecular coupling is possible thanks to a CF_3 group of a tetrahedron located inside the window of the other **Fe5** assembly. Figure 58 *b* and *c* shows the CF_3 substituent groups of the supramolecular cage along the direction of the capsule windows. Figure 58 *b* shows the same interaction for the orange capsule, in which one window is occupied by the CF_3

group of the blue capsule. Figure 58 *c* shows the same feature, but along the direction of the blue capsule.

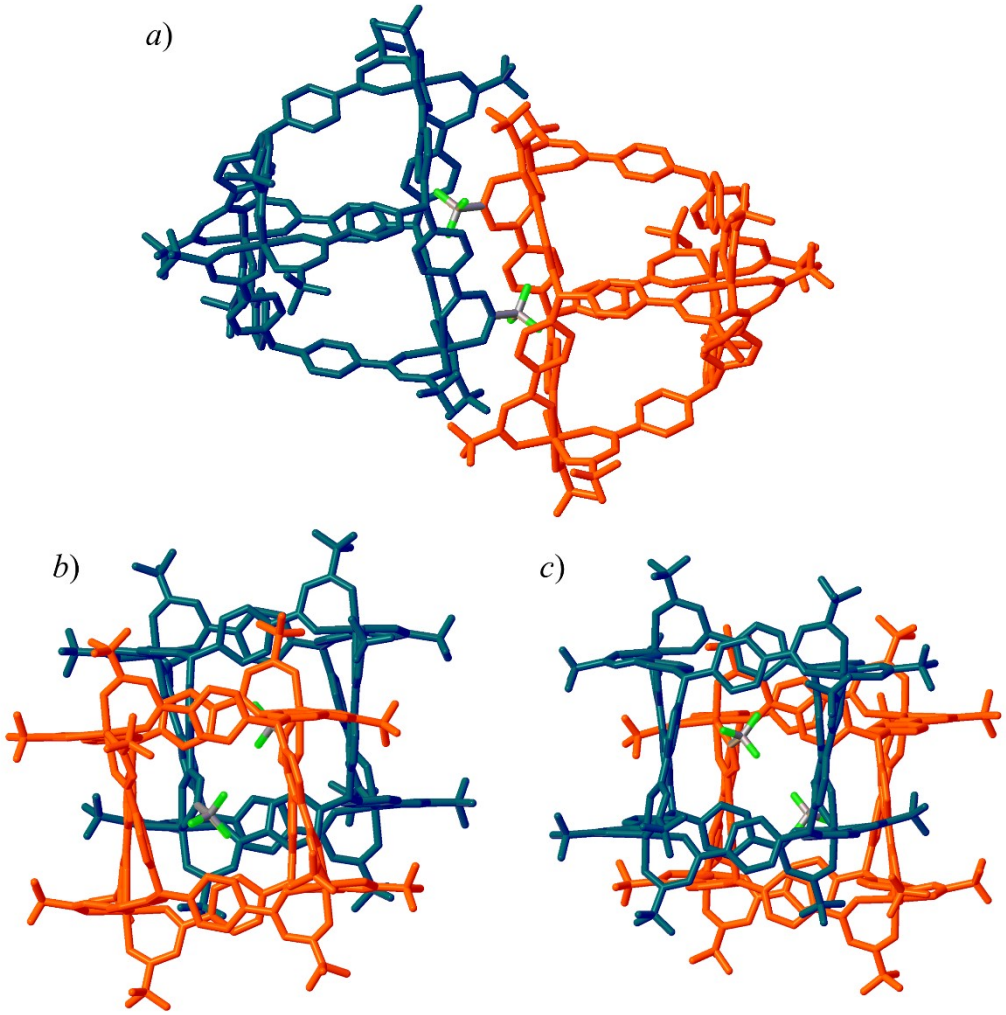

Figure 58. *a*) Structural model of two **Fe5** facing one in front of the other. *b*) The CF_3 substituent group of the blue molecule is located on the orange capsule window. *c*) The CF_3 substituent group of the orange molecule is locate on the blue capsule window. Colour code: **Fe5** capsule blue and orange, F light green, C grey, H atoms are omitted for clarity.

For **Fe6**, single crystals suitable for synchrotron X-ray diffraction have been obtained from a chloroform/isopropanol solution. In these conditions, the complex crystallizes with chloroform solvent molecules. Three of them could be modelled, resulting in the formation of **Fe6**·3$CHCl_3$ (Figure 59 *a*). The supramolecular species crystallizes in a triclinic P-3c1 space group, in which the asymmetric unit is ⅓ of the supramolecular polyhedron. The cell has a total volume of 18409.8 $Å^3$ and contains twelve asymmetric units, corresponding to four full molecules of **Fe6**·3$CHCl_3$ (Figure 59 *b*). The structure is

characterized by large solvent accessible voids. OLEX2 program calculates a total solvent accessible void of volume per unit cell = 3498.2 $Å^3$ corresponding to the 19.0% of the total unit cell volume (Figure 59 *c* and *d*). The void space contains non-negligible residual electron density that have been removed using the OLEX2 mask routine. The program calculates two major voids, related by symmetry, with volume = 1414.3 $Å^3$ each, and with an electron count of 551 each, compatible with the presence of 9.5 $CHCl_3$ molecules per void.

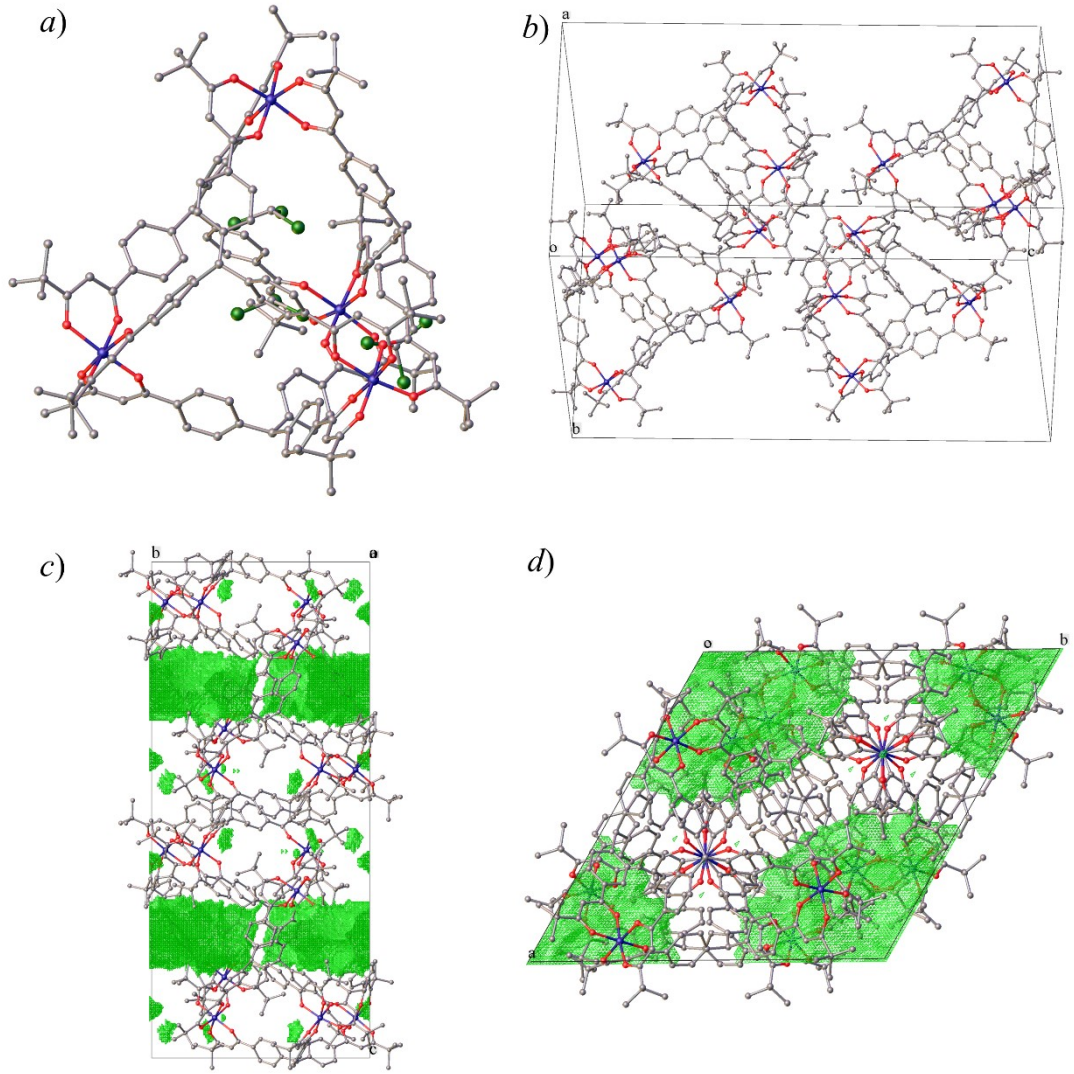

Figure 59. Ball and stick structural model, obtained from single crystal X-ray diffraction, for **Fe6**·3$CHCl_3$. *a*) Full **Fe6**·3$CHCl_3$ molecule, corresponding to ⅓ of the asymmetric unit; *b*) unit cell with 4 supramolecular capsules, corresponding to 12 asymmetric units; *c*) and *d*) green surfaces report the map of the solvent accessible void per unit cell, *c*) show the unit cell view along a axis, *d*) show the unit cell view along c axis. Colour code: Fe blue, O red, F light green, Cl dark green, C grey, H atoms are omitted for clarity.

For **Fe6**, the presence of a confined space suitable for hosting guest molecules is confirmed by two chloroform molecules inside the supramolecular cavity (Figure 60). Also in this case the ligand scaffold unit is located on the tetrahedron faces, generating six windows on the polyhedron edges. This is further confirmed by the presence of one chloroform molecule located on one of the windows of the supramolecular structure.

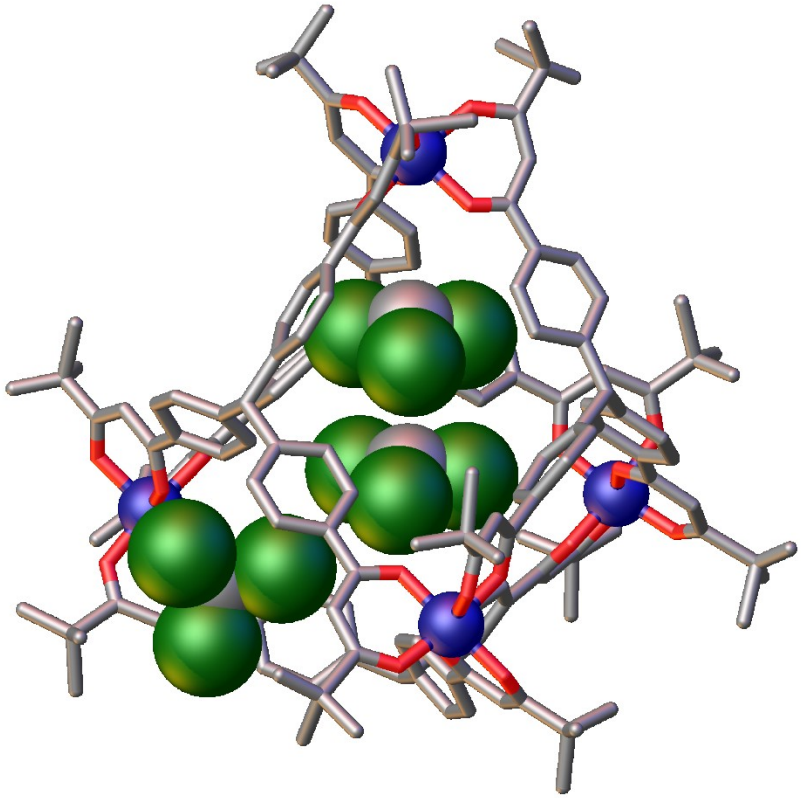

Figure 60. Structural model of **Fe6** hosting two chloroform molecules inside the supramolecular pocket. One additional chloroform molecule is located on the window opening on the tetrahedron edges. Colour code: Fe blue, O red, Cl green, C grey, H atoms omitted for clarity.

In the two presented cases, Fe_4L_4 supramolecular capsules with a confined space inside the polyhedral structure have been obtained by self-assembly of the starting building blocks (Fe^{3+}, TPM-R library). The analyses performed on the structures obtained from single crystal X-ray diffraction confirm the presence of supramolecular cavities. All the obtained MOPs self-assemble in a slightly distorted tetrahedral shape, as designed and highlighted in Figure 61 (purple surfaces). Moreover, from the Fe-Fe distances, corresponding to the tetrahedra edges, it is possible to estimate the volume of the internal cavity. Fe-Fe distances span from 12.42 Å to 13.72 Å for **Fe5** and from 12.87 Å to 13.40 Å for **Fe6**. Considering these distances the volume of the cavity is *ca*. 300 $Å^3$.

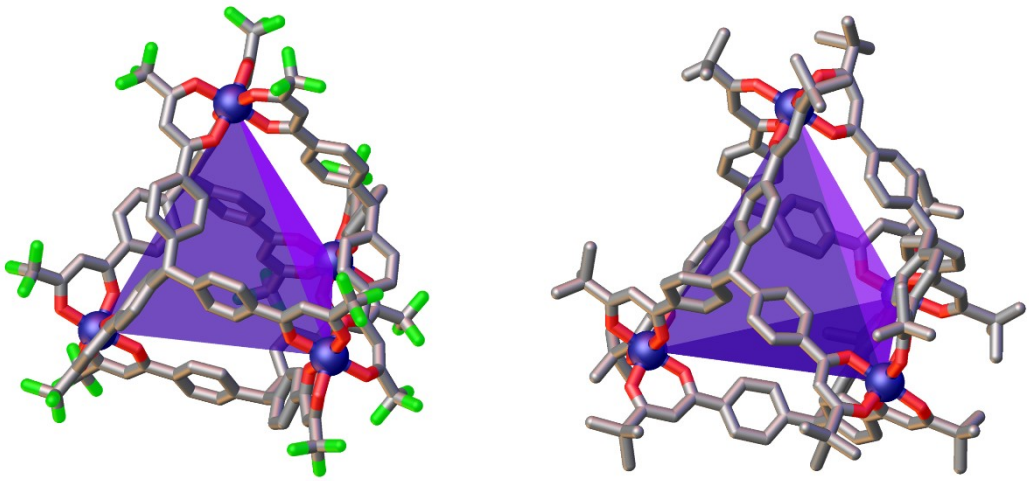

Figure 61. Tetrahedral symmetry of capsules **Fe5** and **Fe6**, purple surfaces indicate the tetrahedral faces. Colour code: Fe blue, O red, F green, C grey, H atoms omitted for clarity.

In conclusion, in this section, the rational design and subsequent self-assembly of Fe_4L_4 supramolecular tetrahedra has been described. Formation of the capsules has been confirmed by single crystal X-ray diffraction analysis. The possibility to host guest molecules inside the obtained supramolecular cavities (*ca*. 300 $Å^3$) has been demonstrated from analysis of the solvent accessible voids (**Fe5**) or from the presence of guest molecules inside the pocket (**Fe6**). The presence of windows on the tetrahedron edges allows guest molecules to go in or out from the cavity. This is further confirmed by X-ray crystallographic data, in which guest molecules ($CHCl_3$) are located on the capsule windows. These analysis confirm that self-assembly of Fe^{3+} with the TPM-R library generates promising systems for exploring host-guest supramolecular chemistry.

4.2 Supramolecular capsules with functional properties. Reaction of DPX-R with lanthanide ions.

This section describes the studies aimed at the synthesis of functional supramolecular architectures in which the structural features of MOPs are combined with the peculiar optical properties of lanthanoid ions, in order to obtain luminescent coordination-driven capsules (Lanthanoid Organic Polyhedra, LOPs). Emission spectra of lanthanide ions have line-like emission bands, mostly in the visible and near infrared range, and long-lived excited states, with luminescence lifetimes on the micro- to millisecond timescale. To this aim, Eu^{3+} lanthanide ions and the new bis-*β*-diketone ligands library (DPX-R), designed specifically to build metallo-supramolecular polyhedra, have been chosen as building blocks. As reported in section 3.2, the *β*-diketone group has been chosen as binding group due to the good affinity with both transition metals and lanthanoid ions. Moreover, it can act as an antenna to sensitize lanthanoid emission. In particular, Eu(III) has been chosen since it exhibits a characteristic red luminescence. Rare-earth *β*-diketonate complexes have been widely studied, and described in the literature[1]. Most of lanthanide *β*-diketonate complexes are eight coordinated and the coordination geometry can be described as a square antiprism (D_{4d} symmetry, considering the first coordination sphere) (Figure 62).

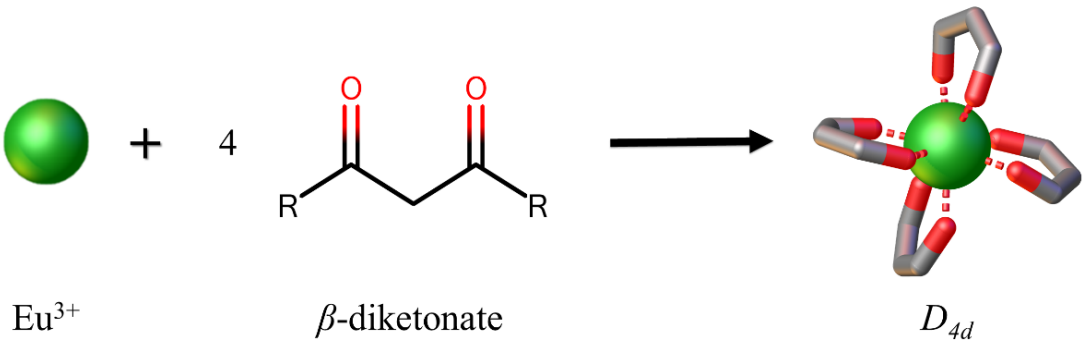

Figure 62. Eu^{3+} ion square antiprismatic coordination with *β*-diketone group: D_{4d} symmetry when considering the first coordination sphere.

By combining the 4-fold axis generated by the D_{4d} coordination with the geometrical features of the DPX-R library ligands, the formation of a dimeric capsule with a lantern shape and the presence of a cavity able to host molecular species is expected. Each Eu^{3+} atom of the capsule can be coordinated by four ligand molecules, thus generating a

negative (2-) charged supramolecular cage with two Eu(III) centres and four ligands on the edges (point group D_4) (Figure 63).

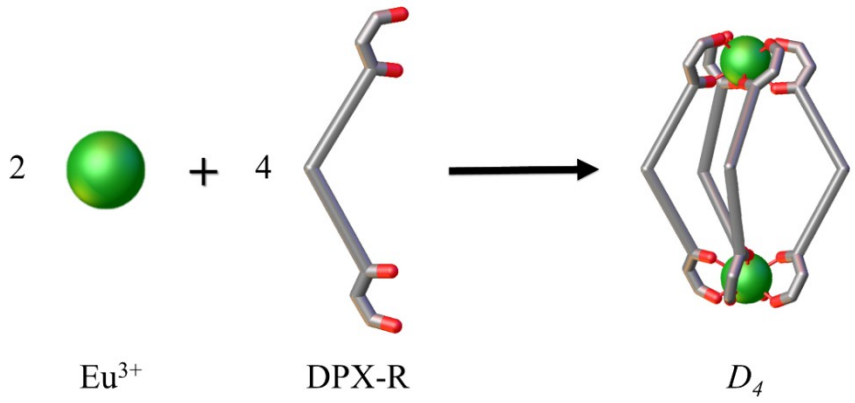

Figure 63. Design of supramolecular dimers based on Eu^{3+} ion and DPX-R.

The metal has been combined with ligands **1**, **3** and **4** from the DPX-R library, *i.e.* the ligands with CF_3 as R-group, and with the three different scaffolds diphenylmethane, diphenylamine derivative and *o*-diphenylbenzene (X = M, A, B respectively) (Figure 64).

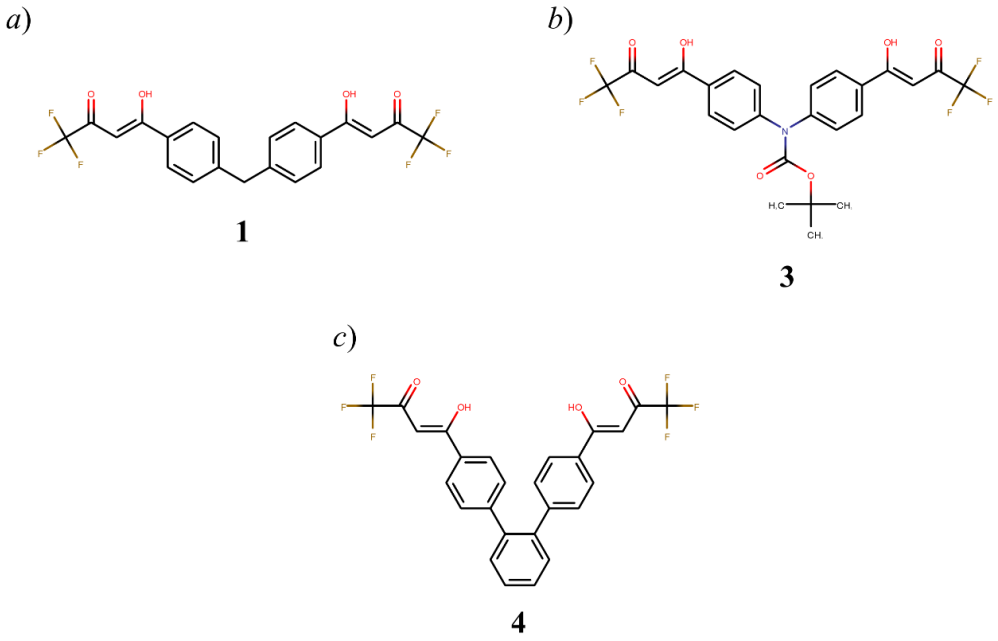

Figure 64. DPX-CF_3 group of ligands.

Self-assembly of the supramolecular cages has been pursued by reacting $EuCl_3 \cdot 6H_2O$ with the ligands, in the presence of a base. An ethanol solution of the metal has been added dropwise to an ethanol solution of the ligand and the base, in stoichiometric amount for the formation of a $[Eu_2L_4]^{2-}$ complex. As soon as the Eu^{3+} solution is added, the formation of a white precipitate occurs. Evaporation of the solvent and purification leads

to the formation of a white solid in almost quantitative yield that shows intense red luminescence upon irradiation with a UV laboratory lamp ($\lambda_{max} \approx 365$ nm). The obtained solids are complexes with general formula $\{[Eu_2(DPX\text{-}R)_4]^{2-}(HB^+)_2\}$, where HB^+ is the protonated base. The presence of the base is necessary to deprotonate the ligands; in fact, when the reaction is performed without the base, the solid precipitate and the solution do not show red luminescence at all. Three supramolecular cages have been prepared: $\{[Eu_2(DPM\text{-}CF_3)_4]^{2-}(HB^+)_2\}$ (hereafter **[Eu1$_{D4}$]**$(HB)_2$) with ligand **1**, $\{[Eu_2(DPA\text{-}CF_3)_4]^{2-}(HB^+)_2\}$ (hereafter **[Eu3$_{D4}$]**$(HB)_2$) with ligand **3**, $\{[Eu_2(DPB\text{-}CF_3)_4]^{2-}(HB^+)_2\}$ (hereafter **[Eu4$_{D4}$]**$(HB)_2$) with ligand **4**, where "HB^+" is Na^+ ion or the conjugate acid of the used base and "$_{D4}$" indicate the formation of a dimeric capsule with D_4 point group. Different bases have been used in the synthesis of the supramolecular capsules. Compounds have been obtained with B = triethylamine (TEA), 1,1,3,3-tetramethylguanidine (TMG), 1,4-diazabicyclo[2.2.2]octane (DABCO) and sodium hydroxide (NaOH). Different bases have chosen in order to tune the solubility of the complex and to change the environment when trying to obtain single crystals of the supramolecular cages. However, despite several efforts, single crystals of the compounds have not yet been isolated.

The formation of the designed metallo-supramolecular capsule is confirmed by a combination of elemental analysis, ESI-MS spectrometry and ^{1}H-NMR spectrometry. ESI-MS analysis reveals that the formation of the desired product is achieved. In Figure 65, the mass spectrum in negative mode for **[Eu1$_{D4}$]**$(HTEA)_2$ is reported. A peak at 1036.5 *m/z* and assigned to **[Eu1$_{D4}$]$^{2-}$** is clearly visible. The obtained spectrum is independent of the used base (B = TEA, TMG, DABCO and NaOH) and it is shown in Figure 65.

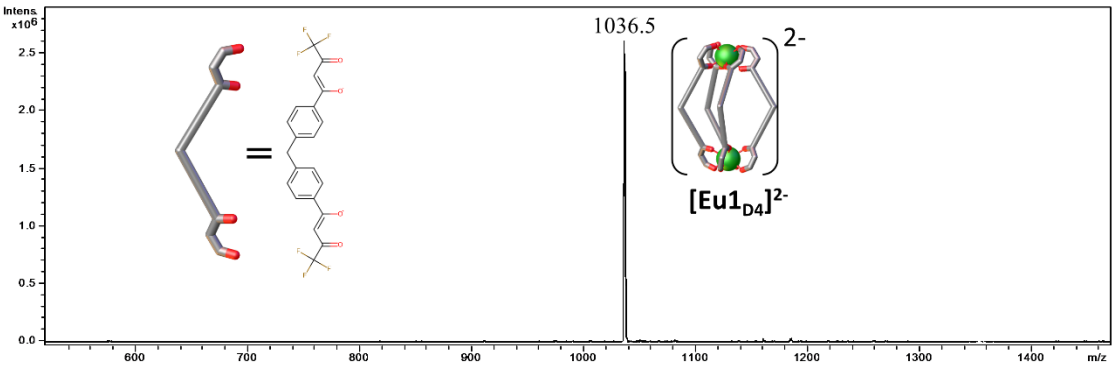

Figure 65. ESI-MS analysis for **[Eu1$_{D4}$]$^{2-}$**.

Same results have obtained for **[Eu3$_{D4}$]$^{2-}$** and **[Eu4$_{D4}$]$^{2-}$** cages, ESI-MS analysis reveals a clear peak at 1238.5 *m/z* and 1160.6 *m/z*, respectively. Also in this case, the obtained spectra are independent of the used base. ESI-MS details and spectra are reported in section 6.6. Values obtained by mass spectrometry (Table 4) are in agreement with the formation of dimeric capsules with two europium ions and four bis-1,3-diketonate ligands. Moreover, the self-assembly of the complexes appears to be both kinetically and thermodynamically favorable. ESI-MS analyses performed immediately after the reaction, after one month and after three months show the immediate formation of the complexes and that no equilibration to other species occurred.

Table 4. Molecular peaks for europium based capsules.

Compounds	**Molecular peaks *(m/z)***
[Eu1$_{D4}$]$^{2-}$	1036.5
Eu1$_{D3}$	1630.2
[Eu3$_{D4}$]$^{2-}$	1238.6
[Eu4$_{D4}$]$^{2-}$	1160.6

In the previous synthesis, the ligand has been added in the stoichiometric condition necessary to form a $[Eu_2L_4]^{2-}$ dimeric capsule (point group D_4). However, by controlling the stoichiometry of the reaction, in principle it should be possible to direct the self-assembly through the formation of the neutral Eu_2L_3 dimeric capsules (point group D_3) (Figure 66). In fact, rare-earth β-diketonate complexes can adopt various coordination geometries[1], where the coordination sphere can be filled by other species, such as solvent molecules (for instance alcohol, water, *etc.*).

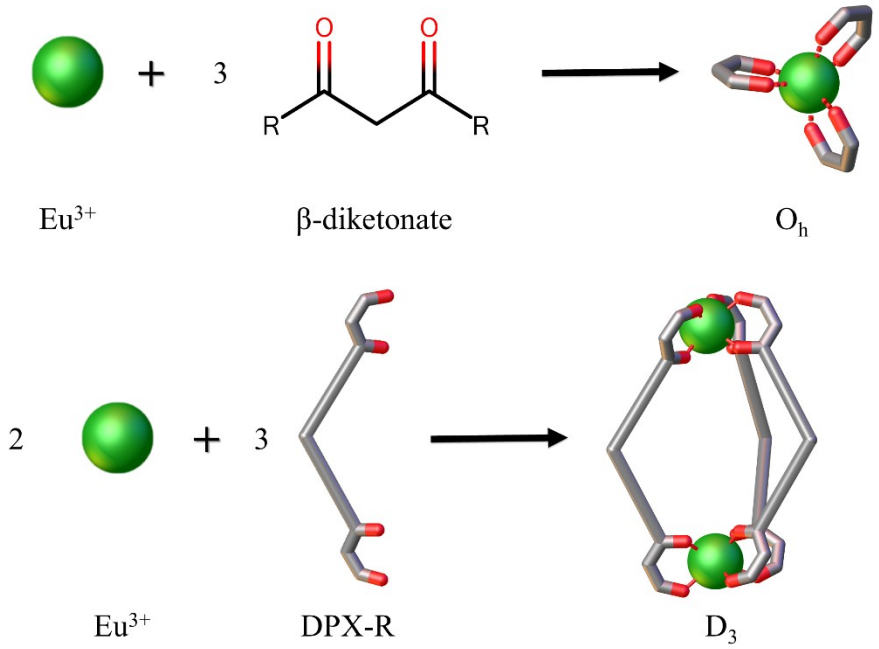

Figure 66. Synthesis of the neutral Eu_2L_3 capsules under stoichiometric control.

For these reasons, Eu^{3+}, ligand **1** and NaOH have been reacted with stoichiometry 2:3:6, respectively. The synthesis has been carried out with the same conditions reported for the preparation of $[\mathbf{Eu1_{D4}}]^{2-}$. Also in this case, after the addition of an Eu^{3+} ethanol solution, to an ethanol solution of ligand **1** and NaOH, the formation of a white precipitate occurs. The solid has been obtained in quantitative yield and exhibits intense red luminescence upon irradiation with UV light (laboratory UV lamp). In these conditions the self-assembly leads to the formation of $[Eu_2(DPM\text{-}CF_3)_3]$ (hereafter $\mathbf{Eu1_{D3}}$) dimeric capsule. The formation of the desired product is confirmed by ESI-MS analysis. Figure 67 shows the mass spectrum in positive mode for $\mathbf{Eu1_{D3}}$. A peak at 1630.2 *m/z* and assigned to $[\mathbf{Eu1_{D3}}]H^+$ is clearly visible. The same synthesis has been reproduced to obtain $\mathbf{Eu3_{D3}}$ and $\mathbf{Eu4_{D3}}$; in this case, although mass balance and elemental analysis suggest the formation of the desired capsules, ESI-MS analysis is still in progress. To obtain reliable mass spectra for this species results more challenging than for the $[\mathbf{EuL_{D4}}]^{2-}$ capsule. In fact, $\mathbf{EuL_{D3}}$ is a neutral species and protonation of the system, necessary to reveal the molecular peaks by ESI-MS analysis, can lead to a disassembly of the capsule. For this reason, it is challenging to find the optimal analysis parameters.

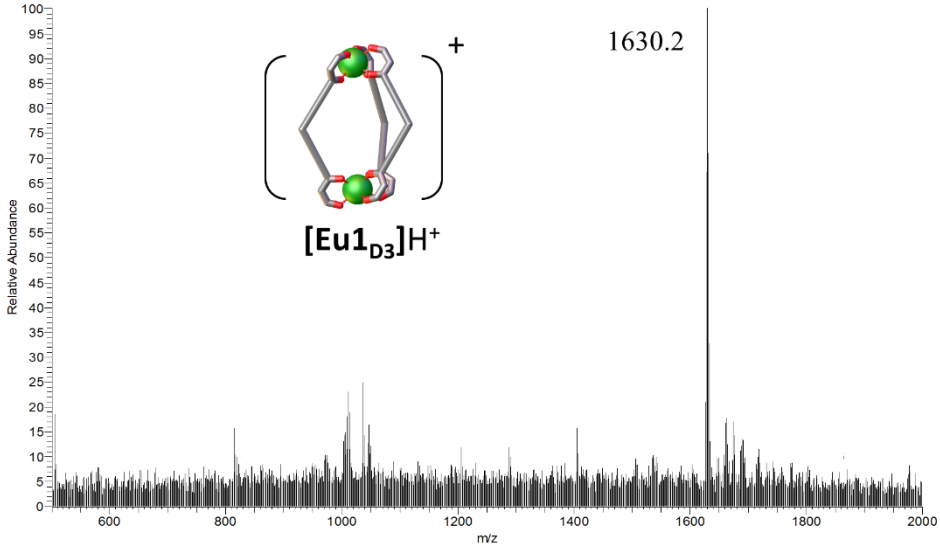

Figure 67. ESI-MS analysis for **Eu1$_{D3}$**.

It has been demonstrated that the three different ligands of the DPX-CF_3 library can be used for the self-assembly of Eu-based supramolecular capsules. Then, the complexity of the system has been increased by performing self-sorting studies in which the Eu^{3+} ion and the three ligands (ligand **1**, **3** and **4**) have been reacted concomitantly. The reaction has been followed by ESI-MS spectrometry and experimental details are reported in section 6.6. Interestingly, ESI-MS spectra show that ligands **1** and **3** undergo social self-sorting, while ligand **4** undergoes narcissistic self-sorting[2]. This means that ligand **4** leads exclusively to the formation of capsule made by Eu^{3+} ion and ligand **4** (narcissistic self-sorting), while ligands **1** and **3** lead to the formation of a mixture of capsules with all the possible combinations of the two ligands (social self-sorting) (Figure 68). In fact, ESI-MS reveals the formation of the $[Eu_2L_4]^{2-}$ capsule with all the combinations of ligands **1** and **3** and some of their adducts with the solvent, plus the formation of capsule **Eu4$_{D3}$** and some of its adducts with the solvent (Figure 69). The self-sorting behaviour can be explained considering that the main difference between the three ligands depends on the scaffold units. Ligand **4**, with an *o*-diphenylbenzene scaffold, has an angle of 60° between the *β*-diketone binding groups, while ligands **1** and **3** have very similar structures with angles of 110° *ca.* between the binding groups. Moreover, ligand **1** and **3** are more flexible, compared to ligand **4**, and this probably allows some structural distortion that leads to a complex mixture of all the possible combinations of the two ligands.

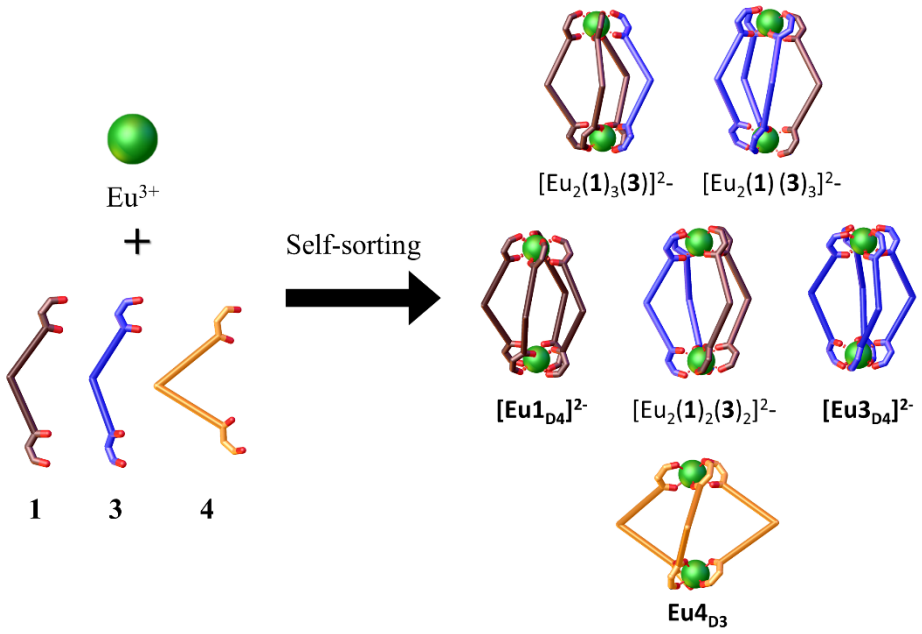

Figure 68. Self-sorting of Eu^{3+} ion, with ligands **1**, **3** and **4**. Ligands **1** and **3** undergo to social self-sorting, ligand **4** undergoes to narcissistic self-sorting.

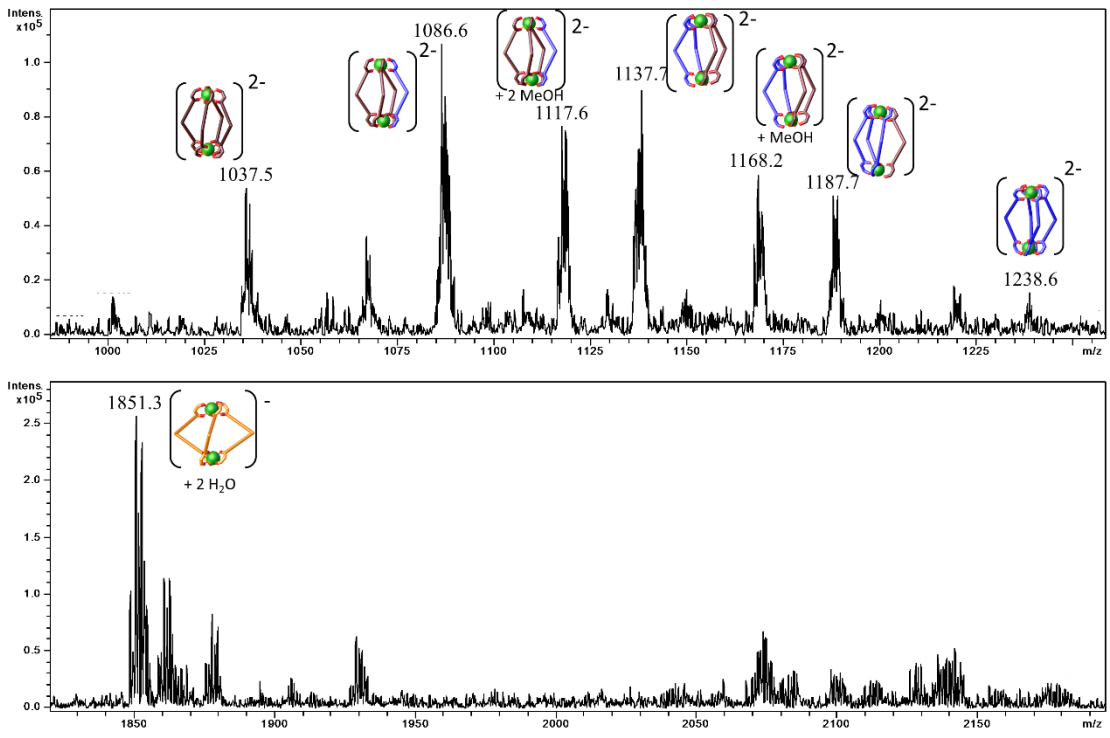

Figure 69. ESI-MS of for the self-sorting experiment of Eu^{3+} ion with ligands **1**, **3** and **4**.

Table 5. Molecular peaks for the self-sorting experiment.

Self-sorted cage	Molecular peaks *m/z*
[Eu1$_{D4}$]$^{2-}$	1037.5
[Eu$_2$(**1**)$_3$(**3**)]$^{2-}$	1086.6
[Eu$_2$(**1**)$_3$(**3**)]$^{2-}$ + 2 MeOH	1117.6
[Eu$_2$(**1**)$_2$(**3**)$_2$]$^{2-}$	1137.7
[Eu$_2$(**1**)$_2$(**3**)$_2$]$^{2-}$ + 2 MeOH	1168.2
[Eu$_2$(**1**)$_1$(**3**)$_3$]$^{2-}$	1187.7
[Eu3$_{D4}$]$^{2-}$	1238.6
[Eu4$_{D3}$]$^{-}$ + 2 H$_2$O	1851.3

Along with ESI-MS analysis, the formation of the dimeric $[Eu_2L_4]^{2-}$ capsules is also supported by NMR analysis. Preliminary results have been obtained from ^{1}H-NMR of **[Eu3$_{D4}$]**Na$_2$ capsule (Figure 70). Europium(III) ion, with electronic configuration [Xe]4f^6, is a paramagnetic species. The coordination of ligand **3** to the paramagnetic Eu^{3+} ion results in a shift and in a broadening of the ^{1}H signals as shown in Figure 70. The ligand spectrum in acetone-d$_6$ is composed by a AA'BB' spin system integrating eight protons with two signals at 8.20 ppm (H$_{2,2'}$) and 7.50 ppm (H$_{3,3'}$), a singlet of the proton of the acetylacetonate α-carbon at 6.95 ppm (H$_1$) and a singlet at 1.48 ppm (H$_5$), due to the *tert*-butyl group. All the signals are subjected to paramagnetic shift that is more effective for the protons closest to the paramagnetic centre. The signal of proton H$_1$ is shifted from 6.95 to -1.58 ppm, protons H$_{2,2'}$ of the AA'BB' spin system are shifted from 8.20 to 11.58 ppm, and protons H$_{3,3'}$ are shifted from 7.50 to 9.86 ppm. Finally, the signal of protons H$_4$ undergoes the less strong shift (from 1.48 to 0.98 ppm) since these are the farthest protons from the paramagnetic ion.

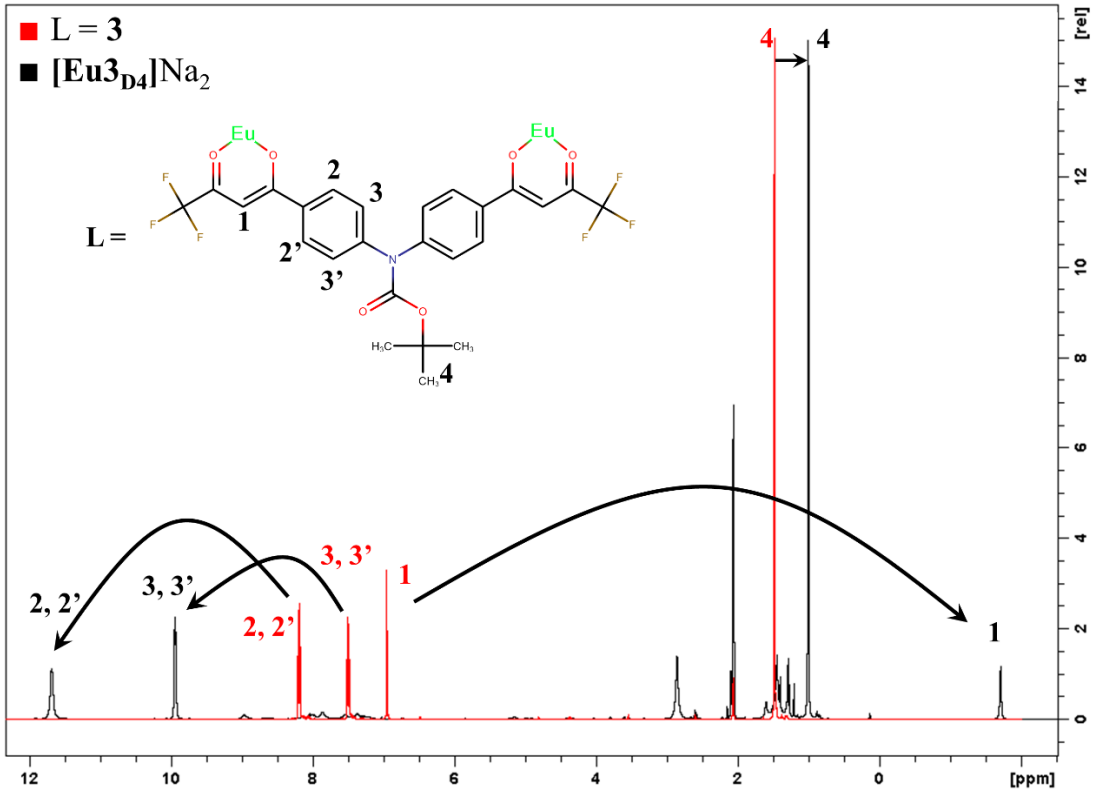

Figure 70. Comparison between ^{1}H-NMR (600 MHz, Acetone-d_6, 25°C) of ligand **3** and of dimeric capsule **[Eu3$_{D4}$]**Na_2. Once the ligand coordinate Eu^{3+} paramagnetic ion, signal undergoes to strong paramagnetic shift.

Since 1,3-diketone ligands are well known sensitizer for lanthanide ions luminescence, the lanthanoid based capsules have been characterized by UV-Vis absorption spectroscopy and emission spectroscopy. Experimental details are reported in section 6.2.3. The absorption, excitation and emission spectra of **[Eu3$_{D4}$]**$(HTEA)_2$ in acetonitrile are reported in Figure 71 *a* and *b*, respectively. Excitation spectra demonstrate sensitization of the Eu(III) excited state by antenna effect of the ligands. Upon excitation in the ligand levels centered at λ_{ex} = 330 nm, **[Eu3$_{D4}$]**$(HTEA)_2$ exhibits red luminescence, with emission composed by several bands associated with $^{5}D_0 \rightarrow {}^{7}F_J$ transitions (J = 0, 1, 2, 3 and 4), the higher the J value, the lower the transition energy. The highest intensity peak occurs at λ_{em} = 613 nm, corresponding to the $^{5}D_0 \rightarrow {}^{7}F_2$ transition, and the emission spectrum is independent from the used base. The same optical characterization has been performed on the **[Eu1$_{D4}$]**$(HB)_2$ and **[Eu4$_{D4}$]**$(HB)_2$ complexes, resulting in very similar outcomes.

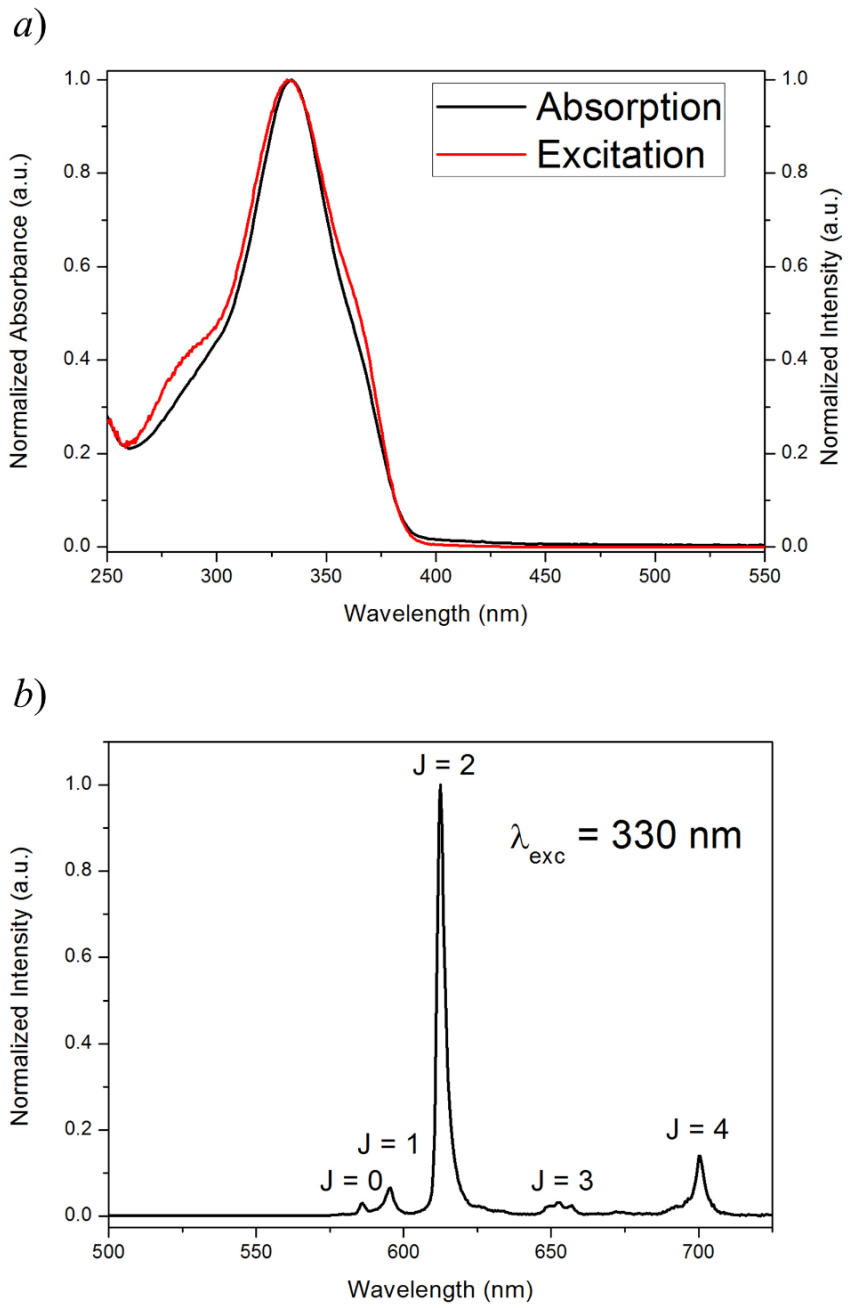

Figure 71. Photoluminescence studies for **[Eu3D4]Na2** in acetonitrile. *a*) Absorption and excitation spectra, *b*) emission spectrum for the $^5D_0 \rightarrow {}^7F_J$ europium ion transitions.

Moreover, the photoluminescence quantum yields for the $[Eu_2L_4](HTEA)_2$ complexes have been measured in acetonitrile, resulting in good values for lanthanide complexes. The obtained results are reported in Table 6.

Table 6. Photoluminescent quantum yields for $[Eu_2L_4](HTEA)_2$ complexes in Acetonitrile

Sample	PLQY in MeCN (%)
[Eu1$_{D4}$]$(HTEA)_2$	47
[Eu3$_{D4}$]$(HTEA)_2$	44
[Eu4$_{D4}$]$(HTEA)_2$	44

Photoluminescence analysis for the coordination-driven cage **[Eu1$_{D4}$]**Na_2 has been carried out also in H_2O and D_2O. In order to solubilize the compound in the aqueous solvent, **[Eu1$_{D4}$]**Na_2 has been dissolved in a small amount of acetone in order to obtain a 10^{-3} M solution, and then it has been diluted with water to 10^{-5} M and 10^{-6} M solutions. Excitation and emission spectra for **[Eu1$_{D4}$]**Na_2 have been recorded in acetonitrile, H_2O and D_2O, and are reported in Figure 72 and Figure 73. The excitation spectra have been recorded at λ_{em} = 613 nm, corresponding to the maximum of the highest intensity peak of the emission spectra, assigned to the $^5D_0$ → $^7F_2$ Eu(III) transition. Compared to acetonitrile, when the compound is dissolved in water, the maximum of the excitation spectrum is red shifted from 319 nm (CH_3CN) to 322 nm (H_2O). Moreover, the spectrum recorded in water shows a shoulder at 355 nm. When the coordination-driven cage is dissolved is D_2O, the excitation spectrum undergoes a small blue shift compared to acetonitrile, from 319 nm (CH_3CN) to 314 nm (D_2O).

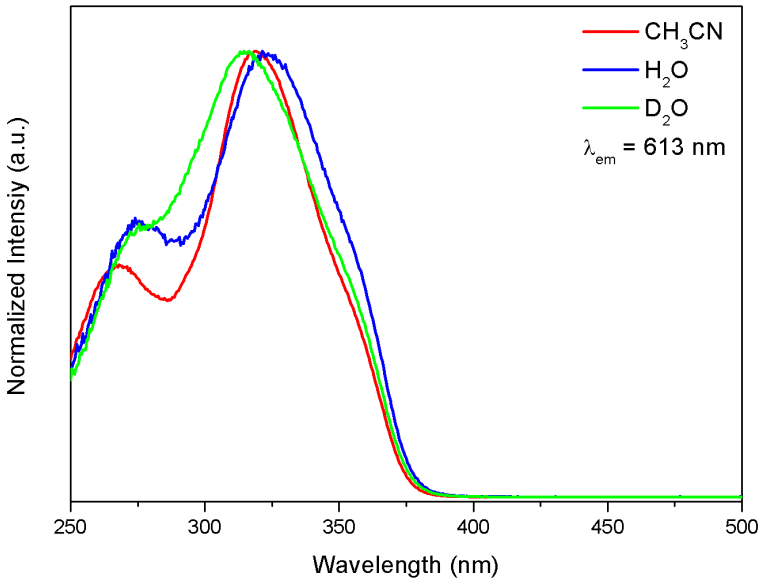

Figure 72. Comparison of the excitation spectra for **[Eu1$_{D4}$]**Na_2 in CH_3CN, H_2O and D_2O, λ_{em} = 613 nm.

The emission behaviour in H_2O and in D_2O is similar whereas more marked differences are observed for the spectra recorded in the aqueous or in the organic solvent (Figure 73). Moving from acetonitrile to H_2O (or D_2O) the $^5D_0 \rightarrow {}^7F_0$ transition is shifted from 586 nm to 579 nm, and the $^5D_0 \rightarrow {}^7F_1$ transition becomes broader (Figure 73 *b*). Regarding the $^5D_0 \rightarrow {}^7F_2$ transition, two shoulders at 617 and 623 nm, rise up in the aqueous solvents (Figure 73 *c*). Finally, looking at the $^5D_0 \rightarrow {}^7F_4$ transition, its maximum is shifted from 700 nm in acetonitrile, to 702 nm in H_2O (or D_2O) (Figure 73 *d*). The differences in shape of the emission spectra in the organic and in the aqueous solvents suggest a modification of the Eu^{3+} ion coordination sphere due to the presence of water molecules.

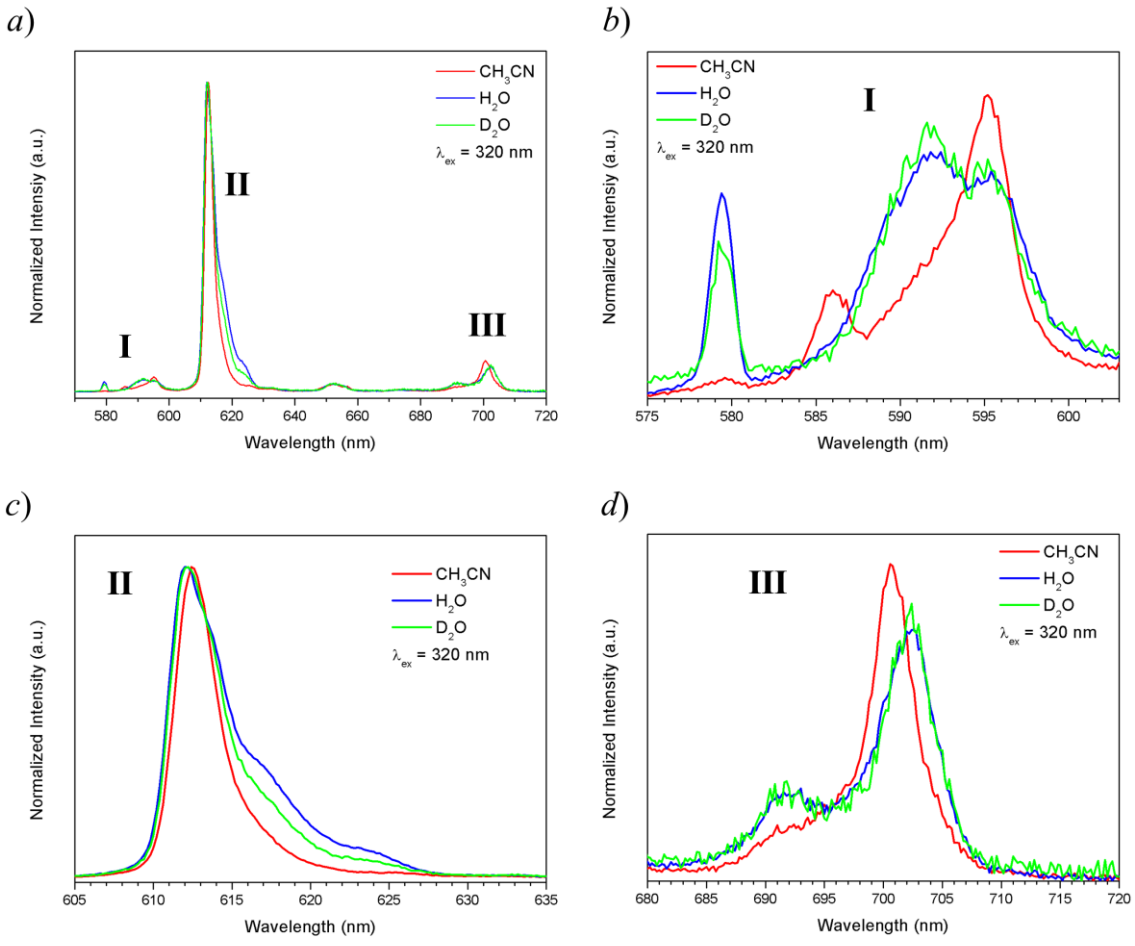

Figure 73. Comparison of the emission spectra of **[Eu1$_{D4}$]**Na_2 in CH_3CN, H_2O and D_2O, λ_{ex} = 320 nm; *a*) full spectra, *b*) zoom of the $^5D_0 \rightarrow {}^7F_{J\,(J=0,1)}$ transitions (Zone I), *c*) zoom of the $^5D_0 \rightarrow {}^7F_3$ transition (Zone II), zoom of the $^5D_0 \rightarrow {}^7F_4$ transition (Zone III).

This hypothesis is supported by emission quantum yield determination in the three different solvents. Table 7 reports the obtained values for the **[Eu1$_{D4}$]**Na_2 cage. The values obtained in acetonitrile are in agreement with those previously obtained (Table 6).

Water is a well-known quencher for the emission of europium ions and this leads to a low value for the quantum yield (4%). However, when D_2O is used as solvent, no quenching effect should be observed. When **[Eu1$_{D4}$]**Na_2 is dissolved in D_2O, the values of quantum yield (15%) is significantly decreased compared to acetonitrile. Again, this effect suggests a change in the Eu^{3+} ion coordination sphere. More detailed studies on the role of water molecules in the Eu^{3+} ions coordination environment of the $[Eu_2L_4](HB)_2$ dimeric cages are currently underway.

Table 7. Photoluminescent quantum yields for **[Eu1$_{D4}$]**Na_2 in different solvents

Solvent	PLQY (%)
CH_3CN	45
H_2O	4
D_2O	15

In conclusion, the self-assembly of coordination driven metallo-supramolecular architectures endowed with functional properties has been successfully achieved. The formation of a series of dimeric capsules based on the europium ion and bis-*β*-diketone ligands has been carried out. Capsule formation has been demonstrated by means of ESI-MS spectrometry supported by ^{1}H-NMR spectroscopy. The possibility to modulate the system by controlling the stoichiometry allows the self-assembly of both charged $[Eu_2L_4]^{2-}$ and neutral $[Eu_2L_3]$ cages. Moreover, the self-sorting of the system with Eu^{3+} ion and ligands **1**, **3** and **4** has been studied. This generates a complex system in which ligand **4** undergoes narcissistic self-sorting and leads to the formation of **Eu4$_{D3}$** metal-organic capsule. Ligands **1** and **3** undergo social self-sorting, leading to the formation of a series of $[Eu_2L_4]^{2-}$ capsules in which all the ligands combinations are achieved. Finally, the luminescence properties of the systems are under investigation. Preliminary results show that the bis-*β*-diketone ligand acts as an antenna and sensitize Eu(III) emission, achieving a red luminescent supramolecular cage with quantum yield of ≈ 45% in acetonitrile. The luminescence properties of the obtained compounds are dependent on the solvent. The use of H_2O or D_2O as solvents affects the emission spectra and leads to a decrease of the quantum yields, suggesting a modification in the Eu^{3+} ions coordination sphere.

This system is very promising for studies on coordination driven architectures in which the capsule structural properties, such as host guest behaviour, are combined with the functional properties deriving from the synergy of the ligand and the metal centre, such as luminescence promoted by antenna effect. These systems are promising for application in fields like sensing, due to the possibility to have an influence of the guest molecules on the luminescence behaviour, or for imagining of targeted species that can interact with the functional MOPs.

4.3 Bibliography.

1 K. Binnemans, chapter 225 Handbook on the Physics and Chemistry of Rare Earths 35, **2005**.

2 L. Yan, C. Tan, G. Zhang, L. Zhou, J.-C. Bünzli and Q. Sun, *J. Am. Chem. Soc.*, **2015**, *137***,** 8550.

CHAPTER 5

Conclusions and outlooks

Aim of this work has been the synthesis and characterization of coordination driven metallo-supramolecular architectures as paradigm towards new functional systems. The possibility to use coordination driven architectures, endowed with space confined cavities, in order to modulate the reactivity of guest molecules has been explored. In particular, a system obtained by the self-assembly of Cu^{2+} ions with *o*-LH_2 ligands has been studied[1]. The system self-assembles in a CDL composed by a $[Cu(o\text{-}L)]_2$ dimer and a $[Cu(o\text{-}L)]_3$ trimer. The trimeric species can be selected from the CDL by the introduction of well-designed guest molecules[2,3]. Among the guest molecules, PTA has been chosen as good candidate to explore a post-assembly functionalization on the guest phosphorous atom. It has been demonstrated that the $[Cu(o\text{-}L)]_3$ metallo-supramolecular cage can be used as a suitable environment for PTA oxidation under mild conditions. The triangular capsule activates the reactivity of the guest molecule and the addition of a co-solvent acts as a trigger to promote the oxidation. The oxidation of the product has been demonstrated by FT-IR spectroscopy studies and single crystal X-ray analysis. The effect of the solvent has been studied, showing that polar co-solvents as acetone, methanol, ethanol, acetonitrile, ethyl acetate or tetrahydrofuran allow the air oxidation of $\{PTA@[Cu(o\text{-}L)]_3\}$ to $\{PTAO@[Cu(o\text{-}L)]_3\}$, while using alkane co-solvents, as *n*-hexane, *n*-heptane or cyclohexane, the oxidation does not occurs. Moreover, the solvent effect on the crystallization of the studied host-guest compound has been explored. The use of an alkane co-solvent leads to single crystals of $\{PTA@[Cu(o\text{-}L)]_3\}$ allowing to access the crystal structure of the starting assembly. Acetonitrile co-solvent acts as trigger for the guest oxidation and allows to isolate the crystal structure of the triangular host with the oxidised guest, the $\{PTAO@[Cu(o\text{-}L)]_3\}$ triangle. Using ethanol as co-solvent the

oxidation of the guest molecules is obtained together with an host structural rearrangement into a 1D coordination polymer. Finally, the possibility to recover the oxidised guest with a guest-exchange reaction has been explored, and the oxidised guest has been recovered in almost quantitative yield[4].

Again, it has been demonstrated that the same metallo-supramolecular box is able to activate a selective C-N bond cleavage in the guest molecule. In this case, Cu^{2+} ion, *o*-LH_2 ligand and Me_3-Tr molecule, have been chosen as building blocks. The reaction has been performed following the templated self-assembly path. The formation of a {Me-Tr@[Cu(*o*-L)]$_3$} host-guest supramolecular triangle, in which the guest has lost two methyl groups as consequence of a selective C-N bond cleavage, has been demonstrated. The product formation has been proved by single crystal X-ray diffraction analysis. In order to investigate the guest reactivity, promoted by the formation of the supramolecular cage, the host-guest association constant for {Me-Tr@[Cu(*o*-L)]$_3$} has been determined, resulting in $\log K_{as}$(Me-Tr) = 6.14. The cage effect of the supramolecular triangle, combined with the great stabilization of the final product, are probably two of the causes that drive the reaction to the selective C-N bond cleavage. Collected data evidence that the presence of the host supramolecular triangle is fundamental in order to achieve the de-methylated product, but the mechanism of the reaction is still under investigation. This represents an interesting system due to its high degree of selectivity and the achievement of an unusual C-N bond cleavage. For this reason, further studies will be devoted to investigate the possibility to activate the C-N cleavage for other alkyl-triazine guest molecules.

Besides the study of the metallo-supramolecular architectures to tune the guest reactivity, the possibility to rationalize the design of new metal-organic polygons and polyhedra has been explored. To this aim, two new libraries of *β*-diketone ligands have been synthesized: *i*) a series of bis-1,3-diketone ligands (DPX-R), and *ii*) a series of tris-1,3-diketone ligands (TPX-R). The ligands of both libraries have been designed in order to be easily functionalizable by changing the substituent group. This will affect the properties of the deriving MOPs. The two libraries have been designed with different scaffold units in order to tune the ligand rigidity and geometry. The two libraries have been combined with both transition metal and lanthanoid ions, in order to self-assemble metal-organic polyhedra. By reaction of the TPM-R ligand groups with Fe^{3+} metal ions, the rational design and the self-assembly of a series of Fe_4L_4 supramolecular tetrahedra

has been reported (**Fe5** and **Fe6**). Formation of the capsules has been confirmed by single crystal X-ray diffraction measures. Single crystals X-ray diffraction data clearly show the formation of a space confined cavity inside the MOPs. The cavity dimension can be roughly estimated, calculating the volume of the internal tetrahedron obtained connecting the Fe vertices of the capsule, resulting in a volume of *ca*. 300 $Å^3$. The possibility to host guest molecules inside the obtained supramolecular cavities has been demonstrated by the presence of solvent molecules inside the pocket (**Fe6**). The presence of molecular windows on the tetrahedron edges allows guest molecules to go and or out the cavity. This analysis confirms that self-assembly of Fe^{3+} ions with the TPM-R library generates a promising system for exploring host-guest supramolecular chemistry.

Finally, the ligands from the DPX-R library have been reacted with Eu^{3+} ions, in order to self-assemble coordination driven metallo-supramolecular architectures endowed with functional properties. Reaction of these building blocks leads to the formation of a series of dimeric capsules, suitable for hosting guest molecules. Capsule formation has been demonstrated by means of ESI-MS spectrometry supported by ^{1}H-NMR spectroscopy. It has been demonstrated that it is possible to modulate the system by controlling the stoichiometry of the building blocks and this has allowed to obtain a series of charged $[Eu_2L_4]^{2-}$ and neutral $[Eu_2L_3]$ dimeric cages. A more complex system can be generated, by reacting the three different ligands (ligand **1**, **3** and **4**) and Eu^{3+} concomitantly. This reaction leads to a complex system in which both social and narcissistic self-sorting are operating, according to the geometrical features of the ligands. The luminescence properties of these systems have been explored. The Eu^{3+} capsules show an intense emission in the red region, with the main emission peak at λ_{em} = 613 nm. The emission spectrum is affected by the solvent and the use of water leads to modification of the shape and positions of the emission bands. More detailed investigations, such as the life times and solvatochromism properties, in order to obtained a better characterization of the functional properties of these assemblies, are currently under study.

These systems are very promising. The possibility to modulate the luminescence properties of the capsule by the introduction of guest molecules is one of the major goals. This is an important feature to develop luminescence-based sensors with high selectivity on analyte species by virtue of LOPs confined spaces and host-guest properties. At the same time, the possibility to change the starting metal building blocks will allow tuning of the emission properties in the green (Tb^{3+}) or in the near visible IR (Yb^{3+}, Nd^{3+} and

Er^{3+}). Moreover, all aspects explored with the DPX-R library can be used to design and self-assemble metal-organic polyhedra based on lanthanide ions and the TPX-R library. On the basis of ligand coordination vectors and metal coordination geometry, the self-assembly of such building blocks is expected to result in octahedral LOPs endowed with luminescence or magnetic properties, and characterized by bigger cavities when compared to the capsules obtained with DPX-R ligands.

5.1 Bibliography.

1. M. Rancan, J. Tessarolo, P. L. Zanonato, R. Seraglia, S. Quici and L. Armelao, *Dalton Trans.*, **2013**, *42*, 7534
2. M. Rancan, A. Dolmella, R. Seraglia, S. Orlandi, S. Quici and L. Armelao, *Chem. Commun.*, **2012**, *48*, 3115.
3. M. Rancan, J. Tessarolo, M. Casarin, P. L. Zanonato, S. Quici and L. Armelao, *Inorg. Chem.*, **2014**, *53*, 7276.
4. M. Rancan, J. Tessarolo, S. Quici and L. Armelao, C*hem. Comm.*, **2014**, *50*, 13761.

CHAPTER 6

Experimental

6.1 Synthesis.

Reagents were purchased from Aldrich and used as received. The ligand 1,2-bis-(3-acetylacetone)benzene (*o*-LH_2),[1] PTA[2] and PTAO[2] have been prepared as reported in the literature. Single crystals of {PTA@[Cu(*o*–L)]$_3$} have been obtained from a chloroform/*n*-hexane solution by slow evaporation.[3] The {G@[Cu(*o*–L)]$_3$} host-guest species have been prepared according to our previous procedures.[3]

6.1.1 PTA@[Cu(*o*–L)]$_3$} oxidation to {PTAO@[Cu(*o*–L)]$_3$}.

A 10^{-3} M chloroform-acetonitrile (1:1) green solution of {PTA@[Cu(*o*–L)]$_3$} has been left in a closed vial. After one week, dark green cubic shaped crystals have been obtained. After three weeks, a quantitative crop of single crystals has been obtained. X-ray single crystal analysis on several crystals revealed that the unit cell corresponds to {PTAO@[Cu(*o*–L)]$_3$}[3] (CCDC 971598). Elemental analysis: C 58.73 %, N 2.48%, H 5.33% (exp.); C 58.80%, N 2.54 %, H 5.48% (calc.). The same experiment repeated in a Schlenk tube under an argon atmosphere did not evidence PTA oxidation.

6.1.2 {PTA@[Cu(*o*–L)]$_3$} oxidation to {[(PTAO)$_2$@[Cu$_8$][Cu$_2$]}$_\infty$.

A 10^{-3} M chloroform-ethanol (1:1) green solution of {PTA@[Cu(*o*–L)]$_3$} has been left in a closed vial. After two weeks the solution turned gradually from green to blue. After three weeks, a crystalline blue precipitate has been obtained. X-ray single crystal analysis revealed that this material is a coordination polymer with formula {[(PTAO)$_2$(H$_2$O)[Cu(*o*–L)]$_8$][Cu(*o*–L)]$_2$}$_\infty$. Elemental analysis: C 54.15 %, N 2.36%, H 5.20% (exp.); C 55.23%, N 2.25 %, H 5.07% (calc.). The same experiment repeated in a Schlenk tube under an argon atmosphere did not evidence PTA oxidation. Moreover, the solution colour remained green and did not change toward blue.

6.1.3 {PTA@[Cu(*o*–L)]$_3$} oxidation by air bubbling.

{PTA@[Cu(*o*–L)]$_3$} (30 mg, 0.026 mmol) has been dissolved in a 1:1 chloroform/co-solvent solution (total volume 6 ml). Co-solvents: methanol, ethanol, acetonitrile, ethyl acetate, tetrahydrofuran, 1,4-dioxane, acetone, *n*-hexane, cyclo-hexane and *n*-heptane. The solution has been air bubbled under continuous stirring and FT-IR spectra have been periodically collected. All the collected FT-IR spectra are reported in section 6.2.1.

6.1.4 {PTA@[Cu(*o*–L)]$_3$} oxidation by air bubbling and guest exchange.

a) {PTA@[Cu(*o*–L)]$_3$} (30 mg, 0.026 mmol) has been dissolved in 3 ml of chloroform and the UV-Vis spectrum of the solution has been collected. Acetonitrile (3 ml) has been added and the solution has been air bubbled overnight under continuous stirring. FT-IR confirmed the PTA oxidation, the solvent has been evaporated and the green powder has been dissolved in 3 ml of chloroform. HMT (3.6 mg, 0.026 mmol) has been added and the solution colour changed from green to turquoise indicating the formation of {HMT@[Cu(*o*–L)]$_3$}. The solvent has been removed and the solid dissolved in toluene (5 ml) at 50° C. A turquoise solution with a white solid has been obtained. After centrifugation, the solution has been removed and the white solid has been washed with three toluene aliquots (3 ml each) and vacuum dried. The white solid has been identified as PTAO through FT-IR and elemental analysis (C 45.78 %, N 26.80 %, H 7.65 % (exp.); C 45.86%, N 26.73 %, H 7.70% (calc.)). PTAO yield 4.5 mg (96 %).

b) Similar results have been obtained by bubbling air for 6 hours in a {PTA@[Cu(*o*–L)]$_3$} $CHCl_3$-THF solution. PTAO yield 98 %.

6.1.5 Synthesis of [Cu(*o*-L)]$_n$ (n = 2, 3) + Me_3-Tr: guest-induced selection.

A chloroform solution (1 mL) of Me_3-Tr (0.05 mL, 0.36 mmol) has been added to a [Cu(*o*-L)]$_n$ (*n* = 2, 3) CDL solution, prepared dissolving 122 mg of [Cu(*o*-L)]$_n$ (*n* = 2, 3) (0.36 mmol of Cu^{2+} ions) in 5 mL of chloroform. The resulting solution has been left under stirring for two days. UV-Vis absorption spectra showed the formation of the dimer-trimer CDL and the absence of other species. It is possible to assert that Me_3-Tr does not react with the pre-formed [Cu(*o*-L)]$_n$ (*n* = 2, 3) CDL system.

6.1.6 Synthesis of {Me-Tr@[Cu(*o*–L)]$_3$}: templated self-assembly.

$CuSO_4 \cdot 5H_2O$ (60 mg, 0.24 mmol) has been dissolved in 3 mL of water and converted to $[Cu(NH_3)_4]^{2+}$ by addition of a NH_3 solution (28 %) in excess (1-2 ml). This solution has been added to a dichloromethane (10 mL) and methanol (1 mL) solution of *o*-LH_2 (50 mg, 0.18 mmol) and Me_3-Tr (85 µL, 1.80 mmol). The biphasic system has been stirred for one day. The two phases have been separated and the organic one has been evaporated under reduced pressure. The obtained green powder has been washed with methanol (40 mL, four aliquots), with acetone (5 mL) and air dried. Yield 82 %. Single crystals have been obtained from chloroform/acetonitrile at -18°C and from dichloromethane/acetonitrile at -18°C.

6.1.7 Synthesis of [Cu(Me_3-Tr)Cl_2]$_2$.

$CuCl_2 \cdot 2H_2O$ (84 mg, 0.5 mmol) has been dissolved in 5 mL of water. This solution has been added to 5 mL of a chloroform solution of Me_3-Tr (70 µL, 0.5 mmol). The biphasic system has been stirred for 12 hours, resulting in a clear green solution in the organic phase. The two phases have been separated and by slow evaporation of chloroform, single crystals of [Cu(Me_3-Tr)Cl_2]$_2$ have been obtained in quantitative yield. The same reaction starting from 0.5 mmol of $CuSO_4 \cdot 5H_2O$, $Cu(ClO_4)_2 \cdot 6H_2O$ or $[Cu(NH_3)_4]^{2+}$, did not react with Me_3-Tr, as evidenced by the absence of colour in the organic phase.

6.1.8 Synthesis of DPM-CO.

Diphenylmethane (1.68 g, 10 mmol) has been dissolved in 30 mL of dry CS_2, in a 100 mL 3 necks round bottom flask, under nitrogen atmosphere. $AlCl_3$ (3.47 g, 26 mmol) has been added to the solution, under vigorous stirring. The reaction mixture has been cooled to 0 °C, then a solution of acetyl chloride (1.85 mL, 26 mmol) in 5 mL of CS_2 has been added. The mixture has been stirred at room temperature for 30 minutes, then it has been reacted at reflux temperature for 3 hours. After that, the solvent has been removed under reduced pressure and 100 g of ice, together with 25 mL of HCl 12 M, have been added to the remaining solid. The mixture has been extracted with CH_2Cl_2 (150 mL) and the organic phase has been collected. The organic phase has been washed with a 5% $NaHCO_3$ aqueous solution (100 mL) and then with a saturated NaCl aqueous solution (80 mL). The organic phase has been dried over $MgSO_4$ and the solvent has been removed under reduced pressure resulting in 3.3 g of pale yellow solid. The product has been purified by SiO_2 column chromatography (*n*-hexane/ethyl acetate 6:4) to give 1.7 g (yield 67.5%) of white solid.

^{1}H-NMR (400MHz, $CDCl_3$, T = 25°C): δ [ppm] = 7.89 (4H, AA' part of an AA'BB' m, $H_{2,2'}$), 7.27 (4H, BB' part of an AA'BB' m, $H_{3,3'}$), 4.09 (2H, s, H_4), 2.58 (6H, s, H_1).

Elemental analysis for DPM-CO ($C_{17}H_{16}O_2$), experimental (calculated): C 80.45% (80.93%), H 6.54% (6.39%).

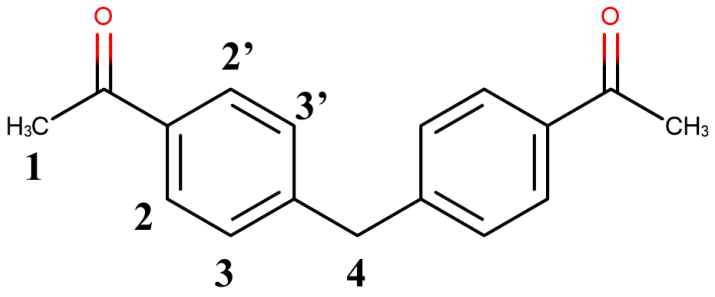

Figure 74. Scheme of DPM-CO.

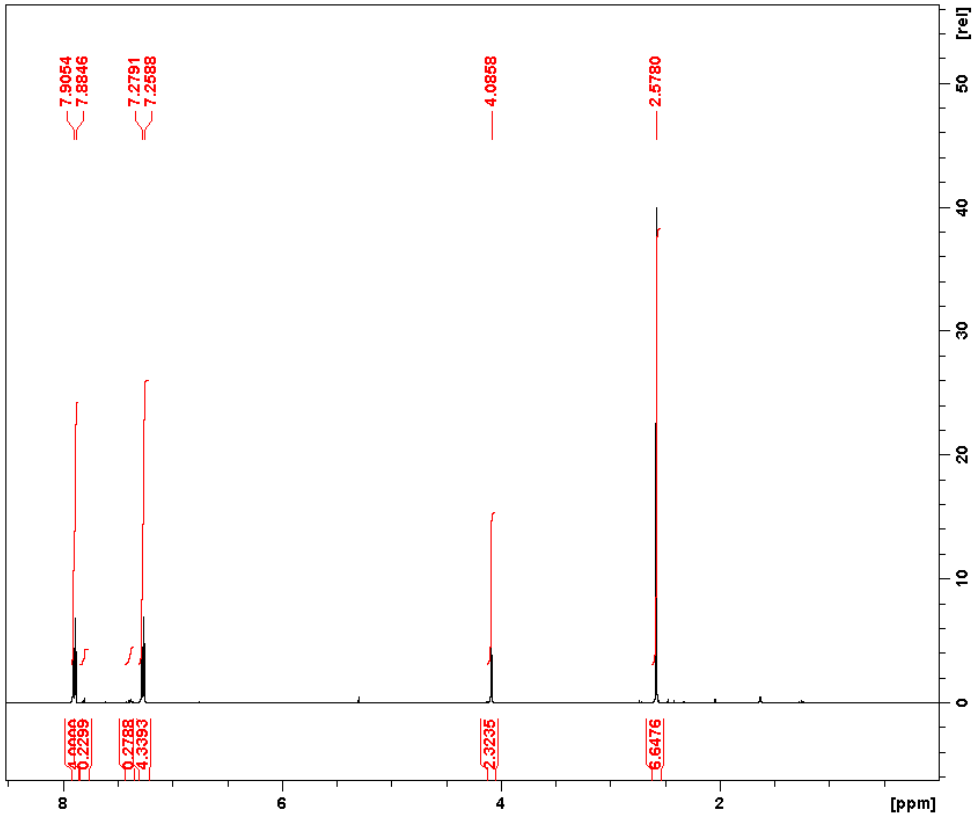

Figure 75. ^{1}H-NMR (400MHz, $CDCl_3$, 25°C) spectrum of DPM-CO.

6.1.9 Synthesis of DPA-CO.

p-bromoacetophenone (5.97 g, 30 mmol), *tert*-butylcarbammate (1.17 g, 10 mmol), K_3PO_4 (12.8 g, 60 mmol) and CuI (0.57 g, 3 mmol), have been added in a Schlenk tube under nitrogen atmosphere. Then, toluene has been added as solvent (50 mL), together with N,N-dimethylethylenediamine (1 mL, 9 mmol). The mixture has been reacted at 110 °C for 45 hours, under vigorous stirring. The reaction has been quenched by the addition of water (150 mL) and ethyl acetate (300 mL). The aqueous phase has been removed with a separating funnel. The organic phase has been washed with water (2 x 150 mL), dried over $MgSO_4$ and the solvent removed under reduced pressure resulting in 6.0 g of a yellow dense oil. The product has been purified by SiO_2 column chromatography (*n*-hexane/ethyl acetate 6:4) to give 2.77 g (yield 78.5%) of desired product (DPA-CO) and 2.41 g of starting reagent *p*-bromoacetophenone.

^{1}H-NMR (400MHz, $CDCl_3$, T = 25°C): δ [ppm] = 7.92 (4H, AA' part of an AA'BB' m, $H_{2,2'}$), 7.26 (4H, BB' part of an AA'BB' m, $H_{33'}$), 2.58 (6H, s, H_1), 1.46 (6H, s, H_4).

Elemental analysis for DPA-CO ($C_{21}H_{23}NO_4$), experimental (calculated): C 71.24% (71.37%), H 6.68% (6.56%), N 4.06% (3.96%).

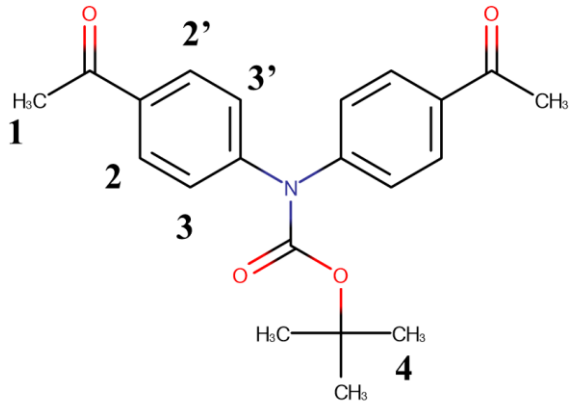

Figure 76. Scheme of DPA-CO.

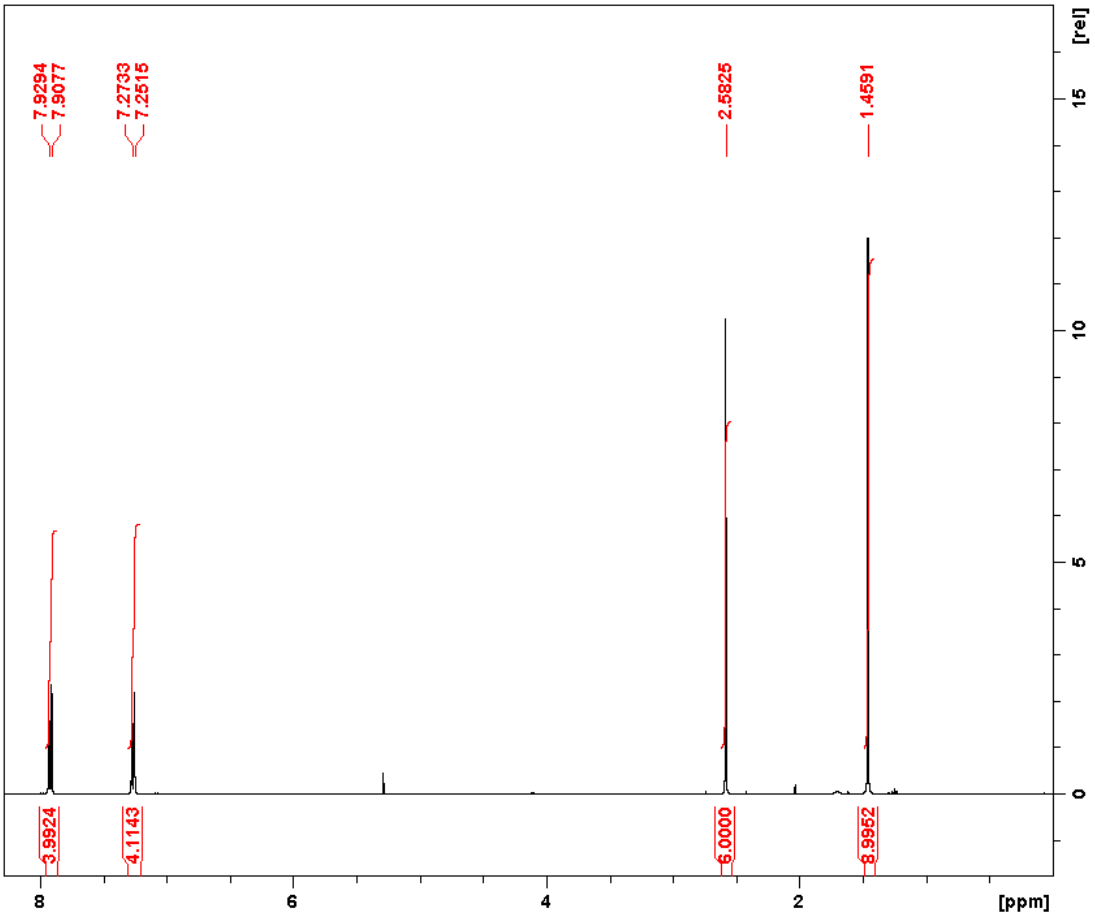

Figure 77. ^{1}H-NMR (400MHz, $CDCl_3$, 25°C) spectrum of DPA-CO

6.1.10 Synthesis of DPB-CO.

o-triphenylbenzene (2.30 g, 10 mmol) has been dissolved in 30 mL of dry CS_2, in a 100 mL 3 necks round bottom flask, under nitrogen atmosphere. $AlCl_3$ (3.47 g, 26 mmol) has been added to the solution, under vigorous stirring. The reaction mixture has been cooled to 0 °C, then a solution of acetyl chloride (1.85 mL, 26 mmol) in 5 mL of CS_2 has been added. The mixture has been stirred at room temperature for 30 minutes, then it has been reacted at reflux temperature for 3 hours. After that, the solvent has been removed under reduced pressure and 100 g of ice, together with 25 mL of HCl 12 M, have been added to the remaining solid. The mixture has been extracted with CH_2Cl_2 (150 mL) and the organic phase has been collected. The organic phase has been washed with a 5% $NaHCO_3$ aqueous solution (100 mL) and then with a saturated NaCl aqueous solution (80 mL). The organic phase has been dried over $MgSO_4$ and the solvent has been removed under reduced pressure resulting in 3.33 g of pale yellow solid. The product has been purified by SiO_2 column chromatography (CH_2Cl_2) to give 2.40 g (yield 76.4%) of white solid.

^{1}H-NMR (400MHz, $CDCl_3$, T = 25°C): δ [ppm] = 7.81 (4H, AA' part of an AA'BB' m, $H_{2,2'}$), 7.46 (4H, AA'BB' m, $H_{4,4'}$ and $H_{5,5'}$), 7.22 (4H, BB' part of an AA'BB' m, $H_{3,3'}$), 2.57 (6H, s, H_1).

Elemental analysis for DPB-CO ($C_{22}H_{18}O_2$), experimental (calculated): C 84.26% (84.05%), H 5.51 % (5.77%).

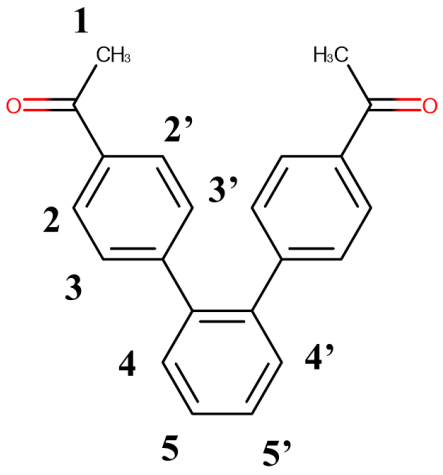

Figure 78. Scheme of DPB-CO.

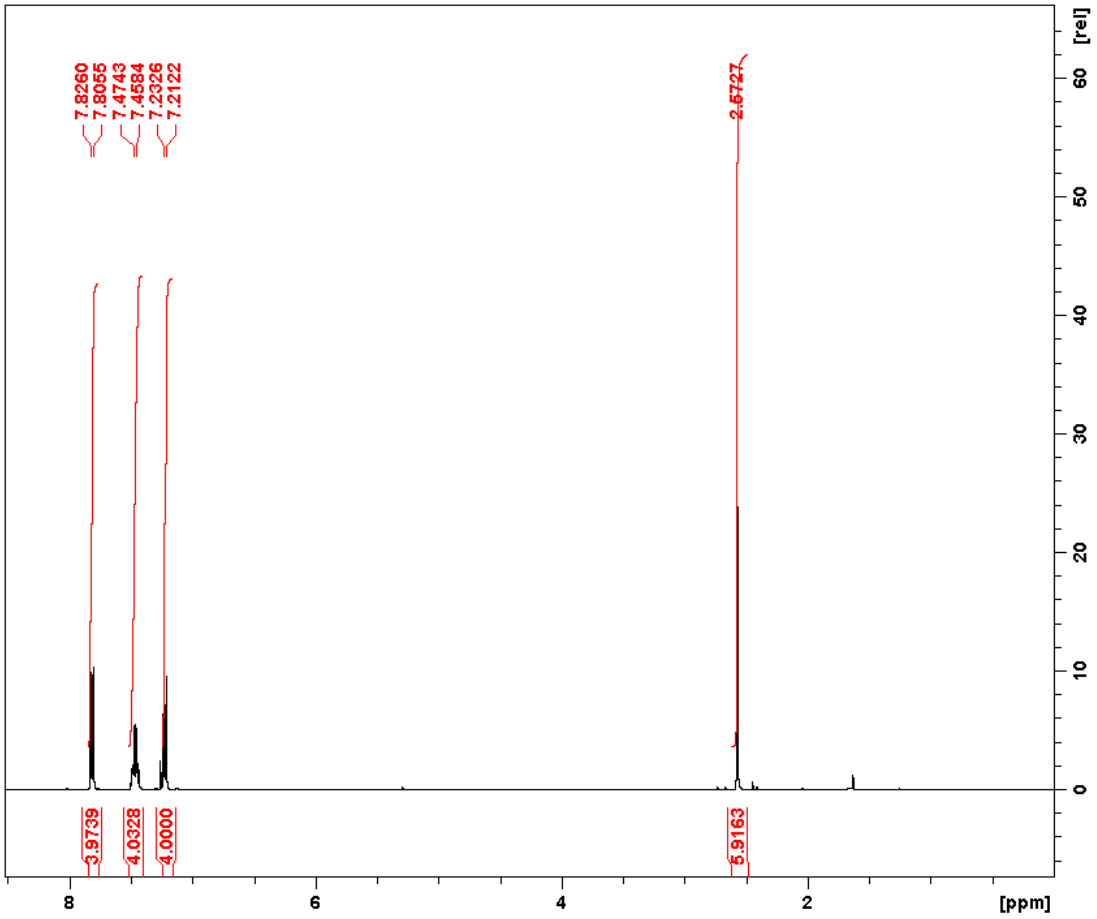

Figure 79. ^{1}H-NMR (400MHz, $CDCl_3$, 25°C) spectrum of DPB-CO.

6.1.11 Synthesis of ligand 1, DPM-CF_3.

Metallic Na (0.64 g, 28 mmol) has been dissolved in 50 mL of absolute ethanol, in a 100 mL 3 necks round bottom flask, under nitrogen atmosphere. After the solution reached RT, ethyl trifluoroacetate (5.0 mL, 42 mmol) and DPM-CO (1.51 g, 6 mmol) have been added, under vigorous stirring. The solution has been heated to 65 °C in order to solubilize DPM-CO. The mixture has been stirred at room temperature for 16 hours (overnight). The solvent has been removed under reduced pressure. After addition of water (100 mL) and an HCl 10% aqueous solution, the formation of a beige precipitate occurred. The solution has been extracted with CH_2Cl_2 and the organic phase has been collected. The organic phase has been dried over $MgSO_4$ and the solvent has been removed under reduced pressure resulting in 2.60 g of a white solid. The product has been purified by recrystallization from CH_3CN to give 2.0 g of pure product with quantitative yield.

^{1}H-NMR (400MHz, $CDCl_3$, T = 25°C): δ [ppm] = 15.14 (2H, s, H_2), 7.90 (4H, AA' part of an AA'BB' m, $H_{3,3'}$), 7.32 (4H, BB' part of an AA'BB' m, $H_{4,4'}$), 6.55 (2H, s, H_1), 4.14 (2H, s, H_5).

13C-NMR ((400MHz, $CDCl_3$, T = 25°C): δ [ppm] = 185.69 (s, C_4), 177.23 (q, C_2, $^{2}J_{C-F}$ = 37.5 Hz), 146.49 (s, C_8), 131.24 (s, C_5), 129.60 (s, C_6), 128.10 (s, C_7), 117.06 (q, C_1, $^{1}J_{C-F}$ = 280.5 Hz), 92.13 (q, C_3, $^{3}J_{C-F}$ = 2.0 Hz), 41.88 (s, C_9).

Elemental analysis for **1** ($C_{21}H_{14}F_6O_4$), experimental (calculated): C 56.58% (56.77%), H 3.15% (3.18%).

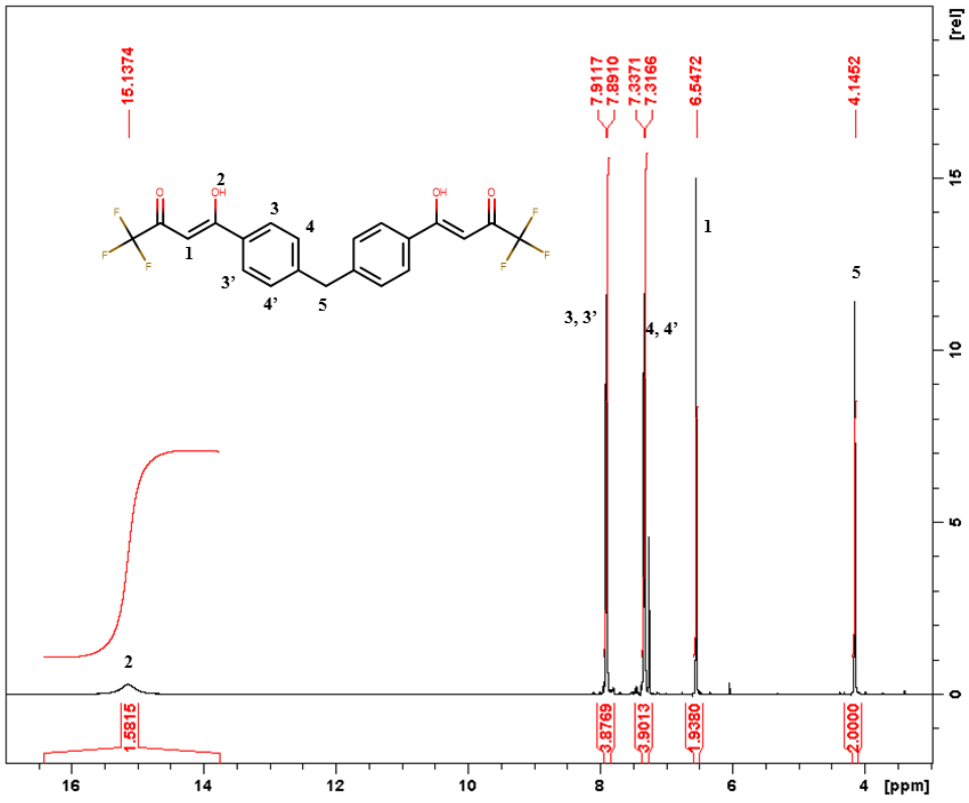

Figure 80. ^{1}H-NMR (400MHz, $CDCl_3$, 25°C) spectrum of ligand **1**.

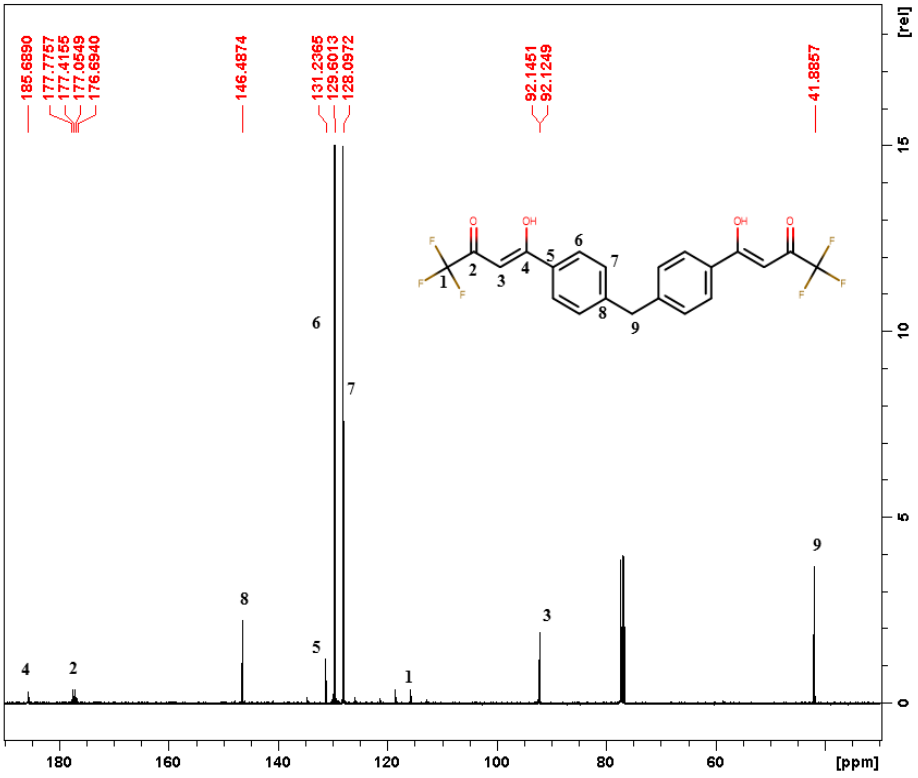

Figure 81. ^{13}C-NMR (400MHz, $CDCl_3$, 25°C) spectrum of ligand **1**.

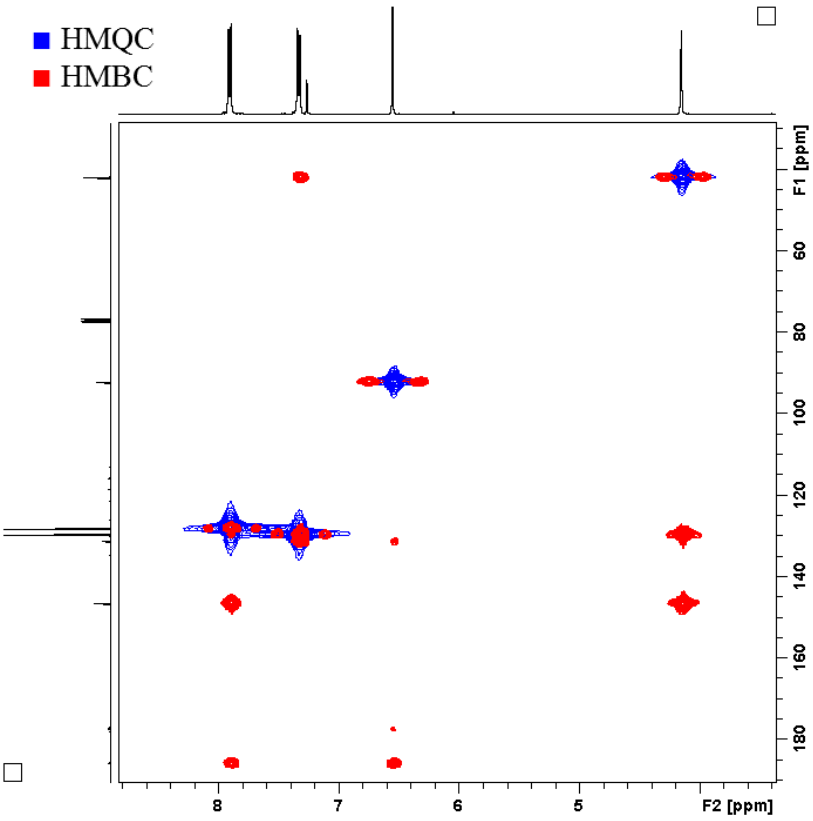

Figure 82. HMQC (400MHz, $CDCl_3$, 25°C, blue) spectrum and HMBC (400MHz, $CDCl_3$, 25°C, red) spectrum of ligand **1**.

6.1.12 Synthesis of ligand 2, DPM-Ph.

DPM-CO (1.51 g, 6 mmol) has been dissolved in 30 mL of dry DMF, in a 100 mL 3 necks round bottom flask, under nitrogen atmosphere. To this solution, ethyl benzoate (3.5 mL, 24 mmol) and potassium *tert*-butoxide (2.02 g, 18 mmol) have been added, maintaining the solution at room temperature and under vigorous stirring. The mixture have been stirred at room temperature for 16 hours (overnight). After this time, water (100 mL) and an HCl 10% aqueous solution, have been added to the solution. The mixture has been extracted with ethyl acetate (200 mL) and the organic phase has been collected. The organic phase has been washed with water (2 x 100 mL), dried over $MgSO_4$ and the solvent has been removed under reduced pressure resulting in 2.40 g of a white solid. The product has been purified by recrystallization from 25 mL of CH_3CN to give 1.7 g of pure product with quantitative yield. Compound purity has been confirmed by NMR and elemental analysis.

^{1}H-NMR (400MHz, $CDCl_3$, T = 25°C): δ [ppm] = 16.88 (2H, s, H_5), 7.98 (4H, BB' part of an AA'BB' m, $H_{3,3'}$), 7.94 (4H, AA' part of an AA'BB' m, $H_{6,6'}$), 7.55 (2H, m, H_1), 7.49 (4H, AA' part of an AA'BB' m, $H_{2,2'}$), 7.32 (4H, BB' part of an AA'BB' m, $H_{7,7'}$), 6.84 (2H, s, H_4), 4.13 (2H, s, H_8).
^{13}C-NMR (400MHz, $CDCl_3$, T = 25°C): δ [ppm] =185.58, 185.53 (s, C_5, C_7), 145.13 (s, C_{11}), 135.52 (s, C_4), 133.85 (s, C_8), 132.47 (s, C_1), 129.35 (s, C_{10}), 128.71 (s, C_2), 127.61 (s, C_9), 127.16 (s, C_3), 93.02 (s, C_6), 41.86 (s, C_{12}).

Elemental analysis for **2** ($C_{31}H_{24}O_4$), experimental (calculated): C 80.74% (80.85%), H 5.32% (5.25%).

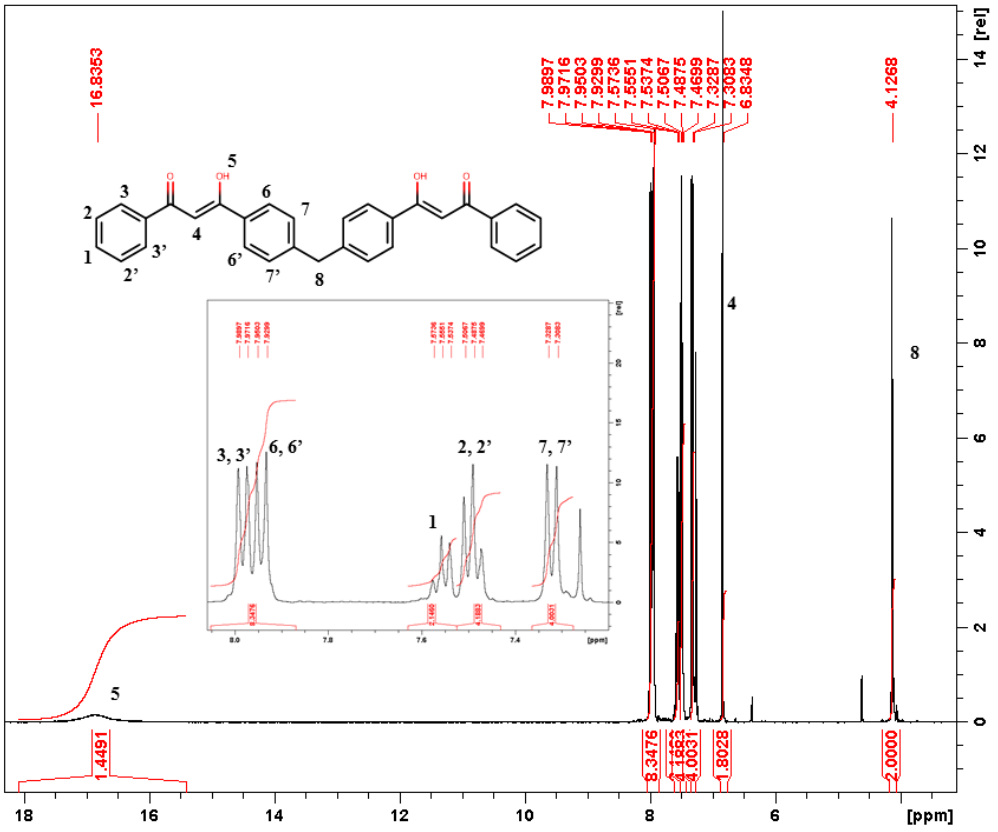

Figure 83. ^{1}H-NMR (400MHz, $CDCl_3$, 25°C) spectrum of ligand **2**.

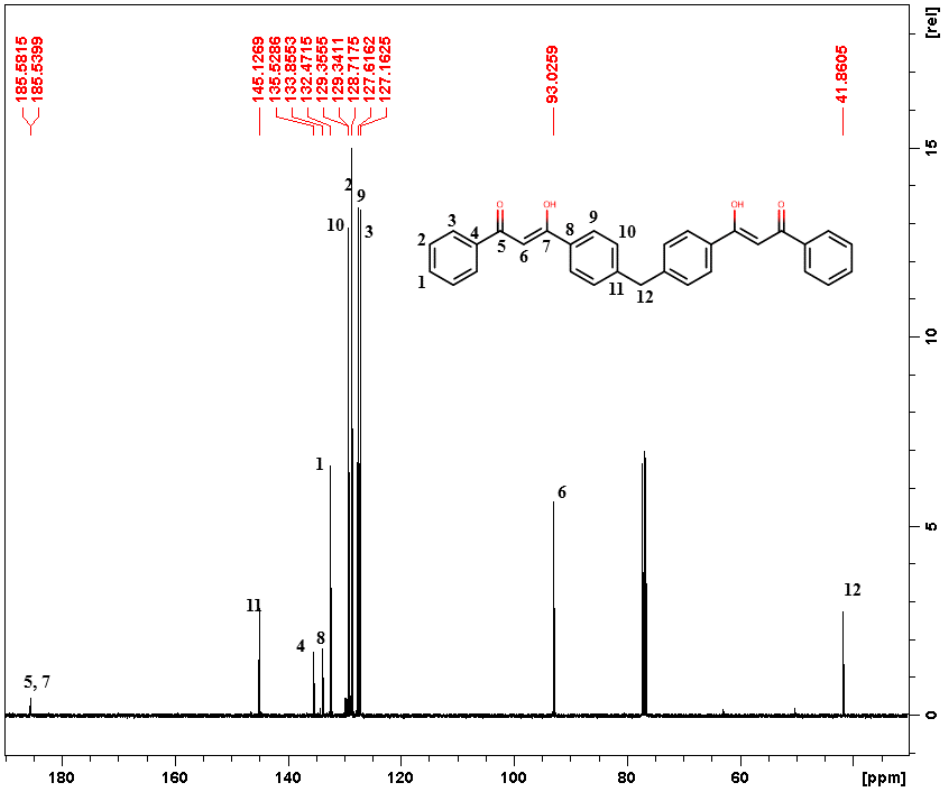

Figure 84. ^{13}C-NMR (400MHz, $CDCl_3$, 25°C) spectrum of ligand **2**.

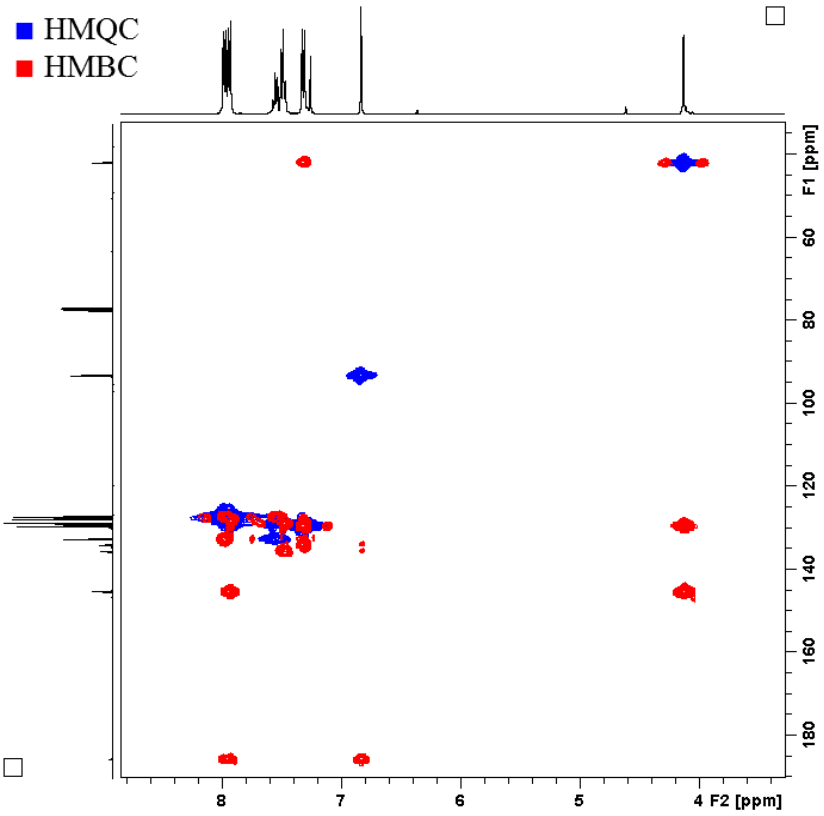

Figure 85. HMQC (400MHz, $CDCl_3$, 25°C, blue) spectrum and HMBC (400MHz, $CDCl_3$, 25°C, red) spectrum of ligand **2**.

6.1.13 Synthesis of ligand 3, DPA-CF_3.

Metallic Na (0.42 g, 18 mmol) has been dissolved in 50 mL of absolute ethanol, in a 100 mL 3 necks round bottom flask, under nitrogen atmosphere. After the solution reached RT, ethyl trifluoroacetate (3.5 mL, 28 mmol) and DPA-CO (1.41 g, 4 mmol) have been added, under vigorous stirring. The solution has been heated to 65 °C in order to solubilize DPA-CO. The mixture has been stirred at room temperature for 16 hours (overnight). The solvent has been removed under reduced pressure. After addition of water (100 mL) and an HCl 10% aqueous solution, the formation of a yellow precipitate occurred. The solution has been extracted with CH_2Cl_2 (150 mL) and the organic phase has been collected. The organic phase has been dried over $MgSO_4$ and the solvent has been removed under reduced pressure resulting in 2.19 g of a yellow solid (quantitative yield). Compound purity has been confirmed by NMR and elemental analysis.

^{1}H-NMR (400MHz, $CDCl_3$, T = 25°C): δ [ppm] = 15.13 (2H, s, H_2), 7.93 (4H, AA' part of an AA'BB' m, $H_{3,3'}$), 7.32 (4H, BB' part of an AA'BB' m, $H_{4,4'}$), 6.54 (2H, s, H_1), 1.48 (9H, s, H_5).

^{13}C-NMR (400MHz, $CDCl_3$, T = 25°C): δ [ppm] = 184.86 (s, C_4), 177.27 (q, C_2, $^{2}J_{C\text{-}F}$ = 36.7 Hz), 152.44 (s, C_9), 147.31 (s, C_8), 130.13 (s, C_5), 128.49 (s, C_6), 126.91 (s, C_7), 116.88 (q, C_1, $^{1}J_{C\text{-}F}$ = 281.5 Hz), 92.22 (q, C_3, $^{3}J_{C\text{-}F}$ = 2.0 Hz), 83.16 (s, C_{10}), 28.07 (s, C_{11}).

Elemental analysis for **3** ($C_{25}H_{21}F_6NO_6$), experimental (calculated): C 54.95% (55.05%), H 3.76% (3.88%), N 2.68% (2.57%).

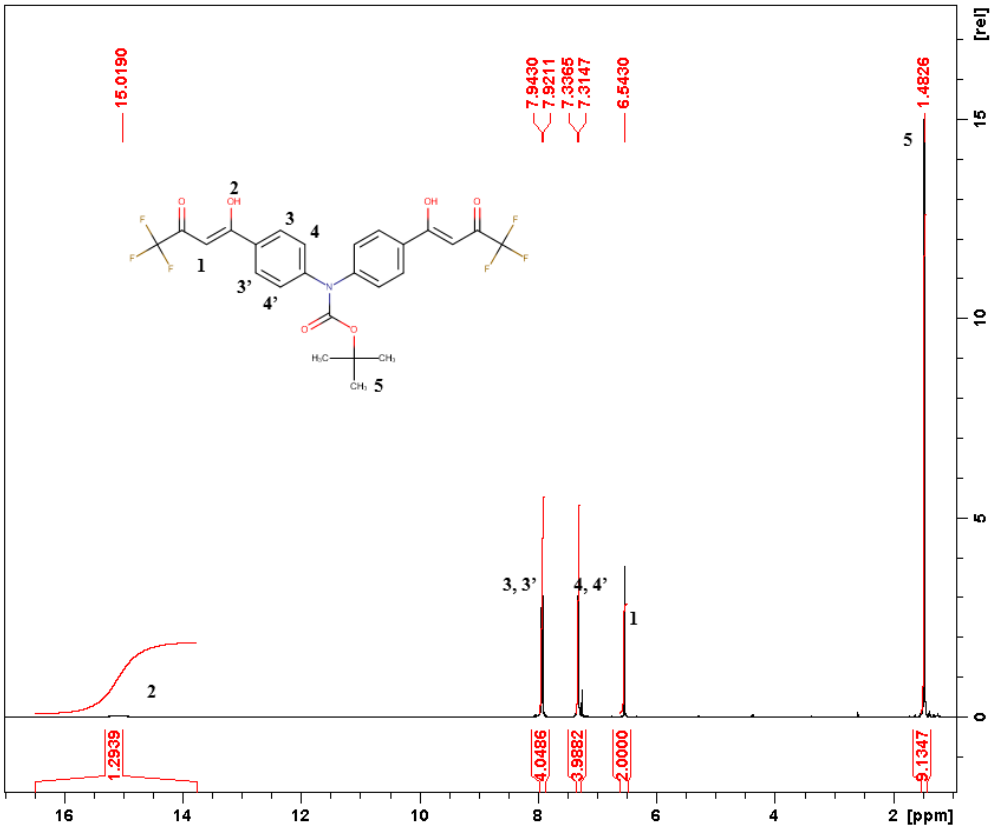

Figure 86. ^{1}H-NMR (400MHz, $CDCl_3$, 25°C) spectrum of ligand **3**.

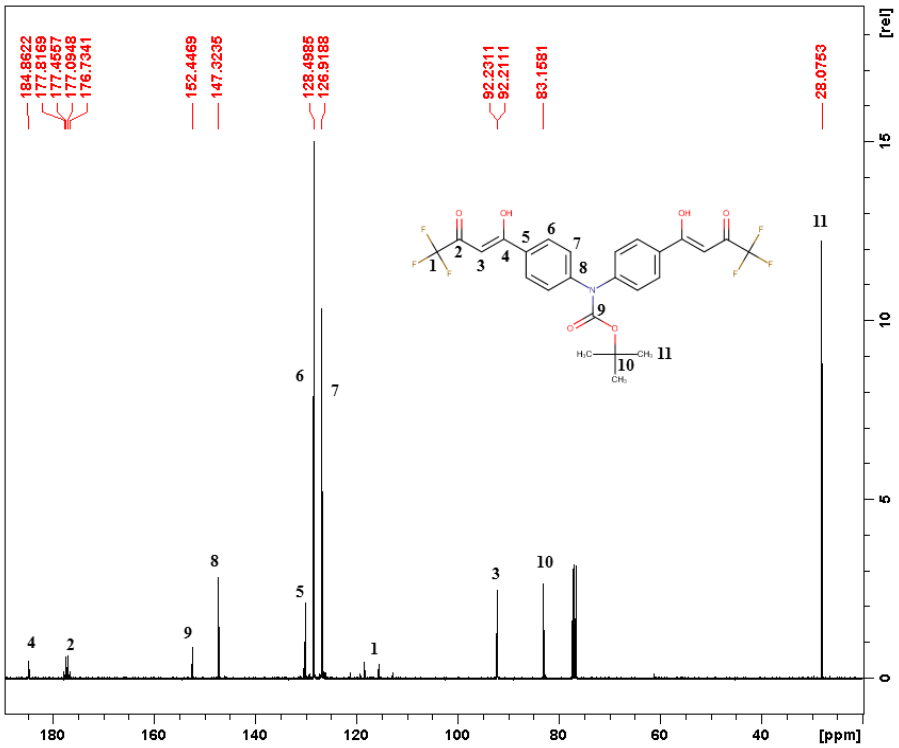

Figure 87. ^{13}C-NMR (400MHz, $CDCl_3$, 25°C) spectrum of ligand **3**.

6.1.14 Synthesis of ligand 4, DPB-CF_3.

Metallic Na (0.64 g, 28 mmol) has been dissolved in 50 mL of absolute ethanol, in a 100 mL 3 necks round bottom flask, under nitrogen atmosphere. After the solution reached RT, ethyl trifluoroacetate (5.0 mL, 42 mmol) and DPB-CO (1.89 g, 6 mmol) have been added, under vigorous stirring. The solution has been heated to 65 °C in order to solubilize DPA-CO. The mixture has been stirred at room temperature for 16 hours (overnight). The solvent has been removed under reduced pressure. After addition of water (100 mL) and an HCl 10% aqueous solution, the formation of a white precipitate occurs. The solution has been extracted with CH_2Cl_2 (150 mL) and the organic phase has been collected. The organic phase has been dried over $MgSO_4$ and the solvent has been removed under reduced pressure resulting in 3.0 g of a white solid, (quantitative yield). Compound purity has been confirmed by NMR and elemental analysis.

^{1}H-NMR (400MHz, $CDCl_3$, T = 25°C): δ [ppm] = 15.13 (2H, s, H_2), 7.83 (4H, AA' part of an AA'BB' m, $H_{3,3'}$), 7.50 (4H, AA'BB' m, $H_{5,5'}$ and $H_{6,6'}$), 7.27 (4H, BB' part of an AA'BB' m, $H_{4,4'}$), 6.54 (2H, s, H_1).

^{13}C-NMR (400MHz, $CDCl_3$, T = 25°C): δ [ppm] = 185.45 (s, C_4), 177.44 (q, C_2, $^2J_{C-F}$ = 37.8 Hz), 147.05 (s, C_8), 139.09 (s, C_9), 131.21 (s, C_5), 130.66 (s, C_{10}), 130.48 (s, C_6), 128.75 (s, C_{11}), 127.57 (s, C_7), 118.53 (s, C_1), 92.28 (q, C_3, $^3J_{C-F}$ = 1.8 Hz).

Elemental analysis for **4** ($C_{26}H_{16}F_6O_4$), experimental (calculated): C 61.72% (61.67%), H 3.07% (3.18%).

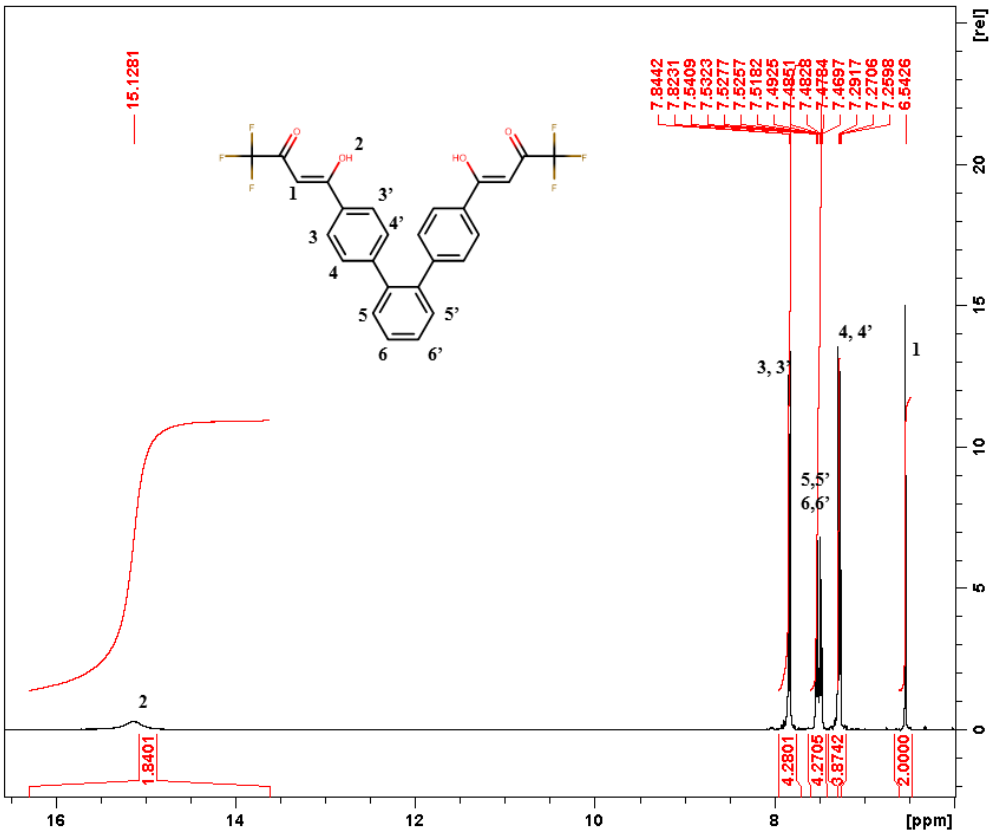

Figure 88. ^{1}H-NMR (400MHz, $CDCl_3$, 25°C) spectrum of ligand **4.**

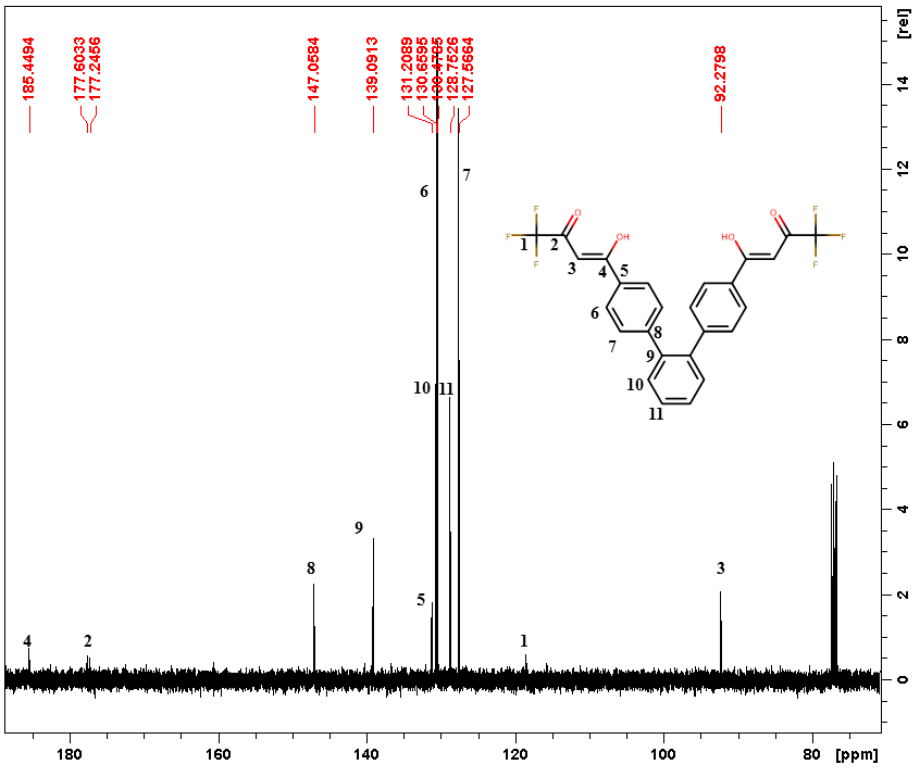

Figure 89. ^{13}C-NMR (400MHz, $CDCl_3$, 25°C) spectrum of ligand **4**.

6.1.15 Synthesis of TPM-CO.

Triphenylmethane (2.44 g, 10 mmol) has been dissolved in 60 mL of dry CS_2, in a 250 mL 3 necks round bottom flask, under nitrogen atmosphere. $AlCl_3$ (5.33 g, 40 mmol) has been added to the solution, under vigorous stirring. The reaction mixture has been cooled to 0 °C, then a solution of acetyl chloride (2.84 mL, 40 mmol) in 20 mL of CS_2 has been added. The mixture has been stirred at room temperature for 30 minutes, then it has been reacted at reflux temperature for 4 hours. After that, the solvent has been removed under reduced pressure and 100 g of ice, together with 50 mL of a 10% HCl aqueous solution, have been added to the remaining solid. The mixture has been extracted with CH_2Cl_2 (100 mL) and the organic phase has been collected. The organic phase has been washed with a 10% HCl aqueous solution (100 mL), with water (100 mL) and finally with a saturated NaCl aqueous solution (80 mL). The organic phase has been dried over $MgSO_4$ and the solvent has been removed under reduced pressure resulting in 3.7 g of pale yellow solid. The product has been purified by SiO_2 column chromatography (*n*-hexane/ethyl acetate 6:4) followed by recrystallization from methanol, to give 2.9 g (yield 80.0%) of white solid.

^{1}H-NMR (400MHz, $CDCl_3$, T = 25°C): δ [ppm] = 7.90 (6H, AA' part of an AA'BB' m, $H_{2,2'}$), 7.19 (6H, BB' part of an AA'BB' m, $H_{3,3'}$), 5.69 (1H, s, H_4), 2.58 (9H, s, H_1).

Elemental analysis for TPM-CO ($C_{25}H_{22}O_3$), experimental (calculated): C 80.03% (81.06%), H 6.18% (5.99%).

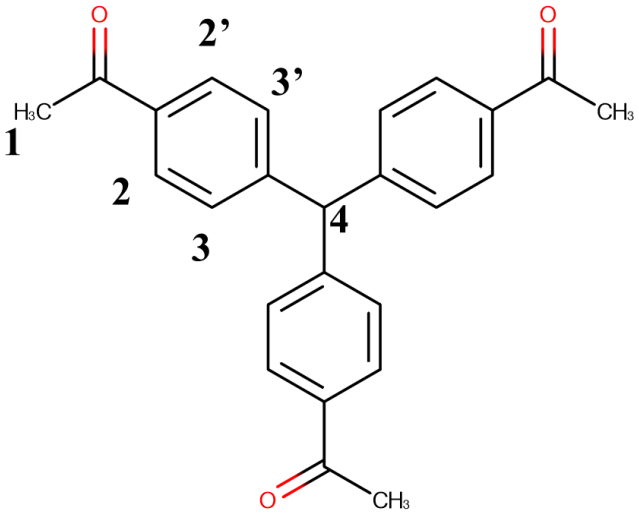

Figure 90. Scheme of TPM-CO.

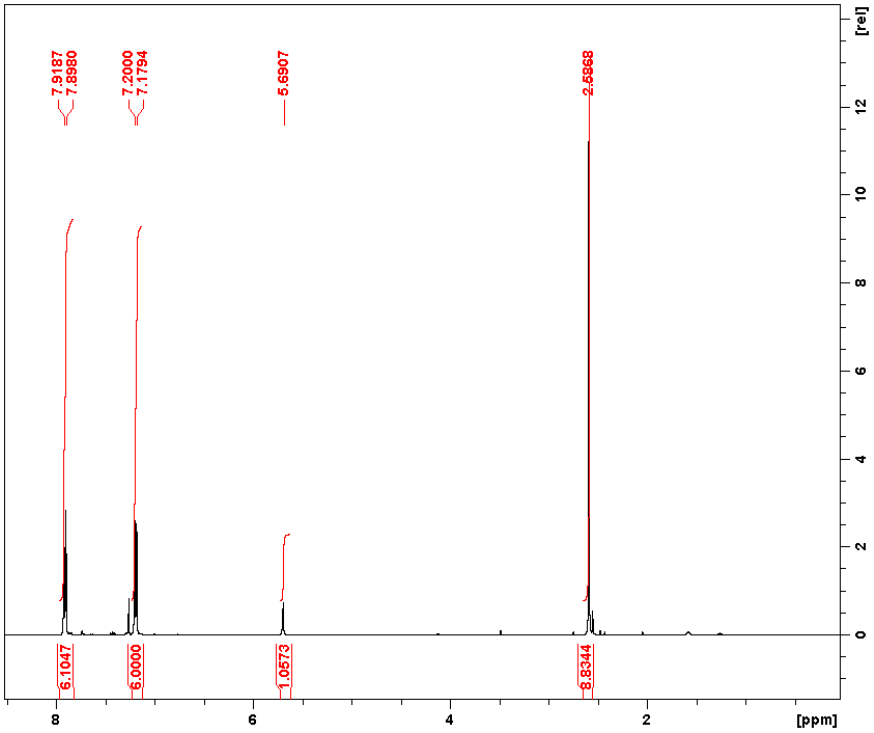

Figure 91. ^{1}H-NMR (400MHz, $CDCl_3$, 25°C) spectrum of TPM-CO.

6.1.16 Synthesis of TPA-CO.

Triphenylamine (2.45 g, 10 mmol) has been dissolved in 60 mL of dry CS_2, in a 250 mL 3 necks round bottom flask, under nitrogen atmosphere. $AlCl_3$ (5.33 g, 40 mmol) has been added to the solution, under vigorous stirring. The reaction mixture has been cooled to 0 °C, then a solution of acetyl chloride (2.84 mL, 40 mmol) in 20 mL of CS_2 has been added. The mixture has been stirred at room temperature for 30 minutes, then it has been reacted at reflux temperature for 4 hours. After that, the solvent has been removed under reduced pressure and 100 g of ice, together with 50 mL of a 10% HCl aqueous solution, have been added to the remaining solid. The mixture has been extracted with CH_2Cl_2 (100 mL) and the organic phase has been collected. The organic phase has been washed with a 10% HCl aqueous solution (100 mL), with water (100 mL) and with a saturated NaCl aqueous solution (80 mL) subsequently. Finally, the organic phase have been washed with 10% NaOH aqueous solution. The organic phase has been dried over $MgSO_4$ and the solvent has been removed under reduced pressure resulting in 3.7 g of yellow solid. The product has been purified by SiO_2 column chromatography (*n*-hexane/ethyl acetate 6:4) followed by recrystallization from methanol, to give 2.41 g (yield 65.3%) of yellow solid.

^{1}H-NMR (400MHz, $CDCl_3$, T = 25°C): δ [ppm] = 7.90 (6H, AA' part of an AA'BB' m, $H_{2,2'}$), 7.15 (6H, BB' part of an AA'BB' m, $H_{3,3'}$), 2.58 (9H, s, H_1).

Elemental analysis for TPA-CO ($C_{24}H_{21}NO_3$), experimental (calculated): C 76.84% (77.61%), H 5.86% (5.7%), N 3.92% (3.77%).

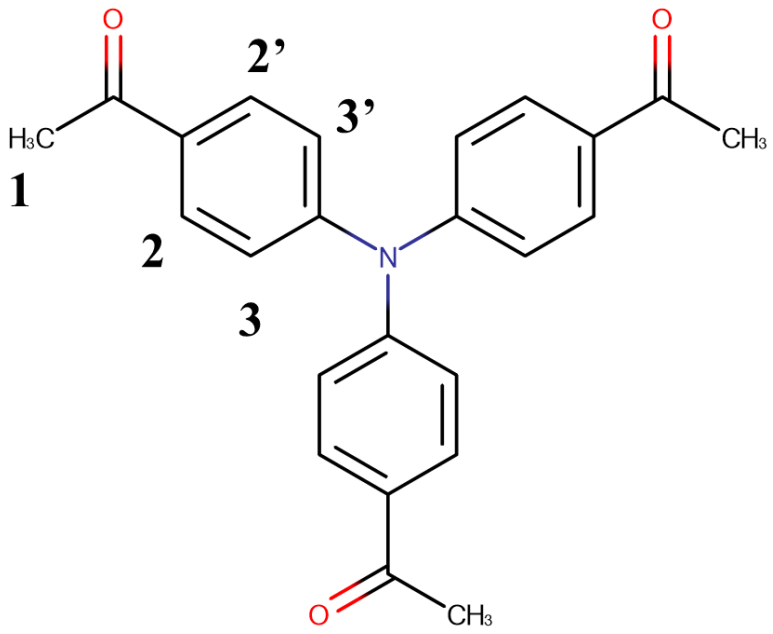

Figure 92. Scheme of TPA-CO.

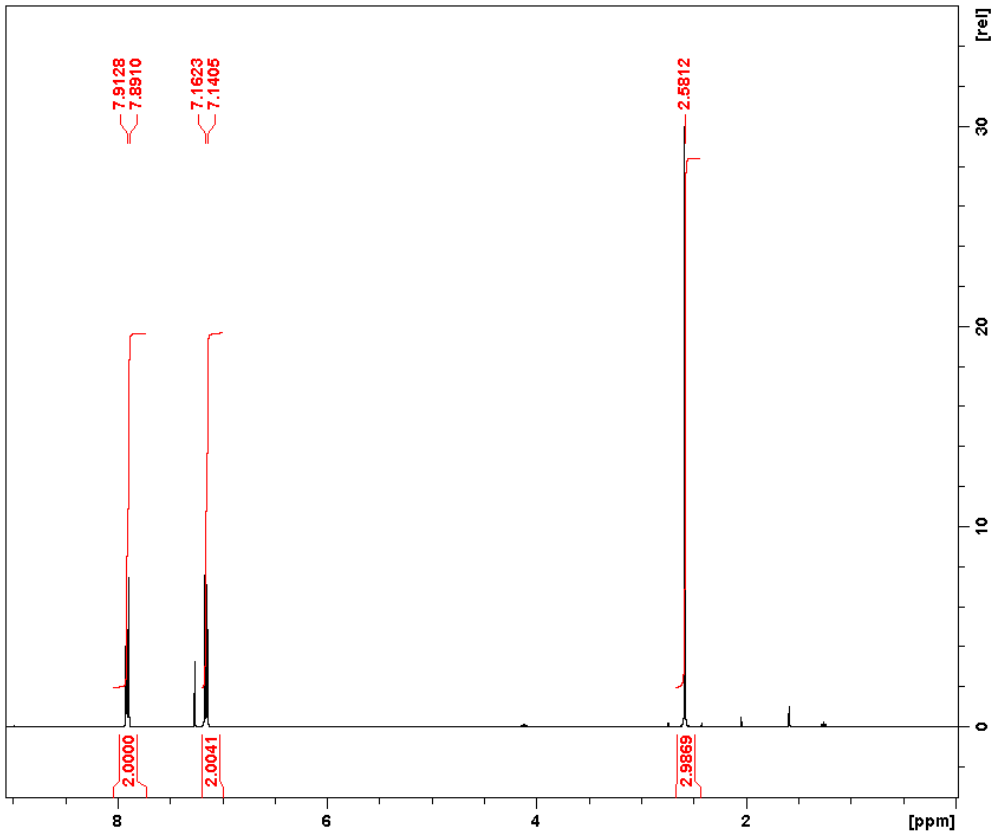

Figure 93. ^{1}H-NMR (400MHz, $CDCl_3$, 25°C) spectrum of TPA-CO.

6.1.17 Synthesis of TPB-CO.

1,3,5-triphenylbenzene (3.06 g, 10 mmol) has been dissolved in 60 mL of dry CS_2, in a 250 mL 3 necks round bottom flask, under nitrogen atmosphere. $AlCl_3$ (5.33 g, 40 mmol) has been added to the solution, under vigorous stirring. The reaction mixture has been cooled to 0 °C, then a solution of acetyl chloride (2.84 mL, 40 mmol) in 20 mL of CS_2 has been added. The mixture has been stirred at room temperature for 30 minutes, then it has been reacted at reflux temperature for 4 hours. After that, the solvent has been removed under reduced pressure and 100 g of ice, together with 50 mL of a 10% HCl aqueous solution, have been added to the remaining solid. The mixture has been extracted with CH_2Cl_2 (100 mL) and the organic phase has been collected. The organic phase has been washed with a 10% HCl aqueous solution (100 mL), with water (100 mL) and with a saturated NaCl aqueous solution (80 mL) subsequently. The organic phase has been dried over $MgSO_4$ and the solvent has been removed under reduced pressure resulting in 4.3 g of yellow solid. The product has been purified by recrystallization from hot ethanol, to give 3.64 g (yield 84.3%) of yellow solid.

^{1}H-NMR (400MHz, $CDCl_3$, T = 25°C): δ [ppm] = 8.09 (6H, AA' part of an AA'BB' m, $H_{2,2'}$), 7.87 (3H, s, H_4), 7.79 (6H, BB' part of an AA'BB' m, $H_{3,3'}$), 2.67 (9H, s, H_1).

Elemental analysis for TPB-CO ($C_{30}H_{24}O_3$), experimental (calculated): C 84.40% (83.31%), H 5.72% (5.59%).

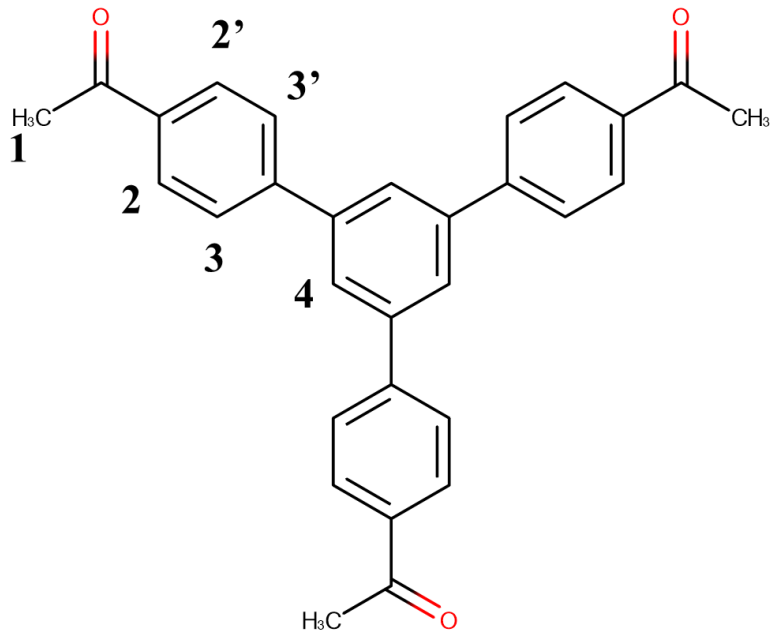

Figure 94. Scheme of TPB-CO.

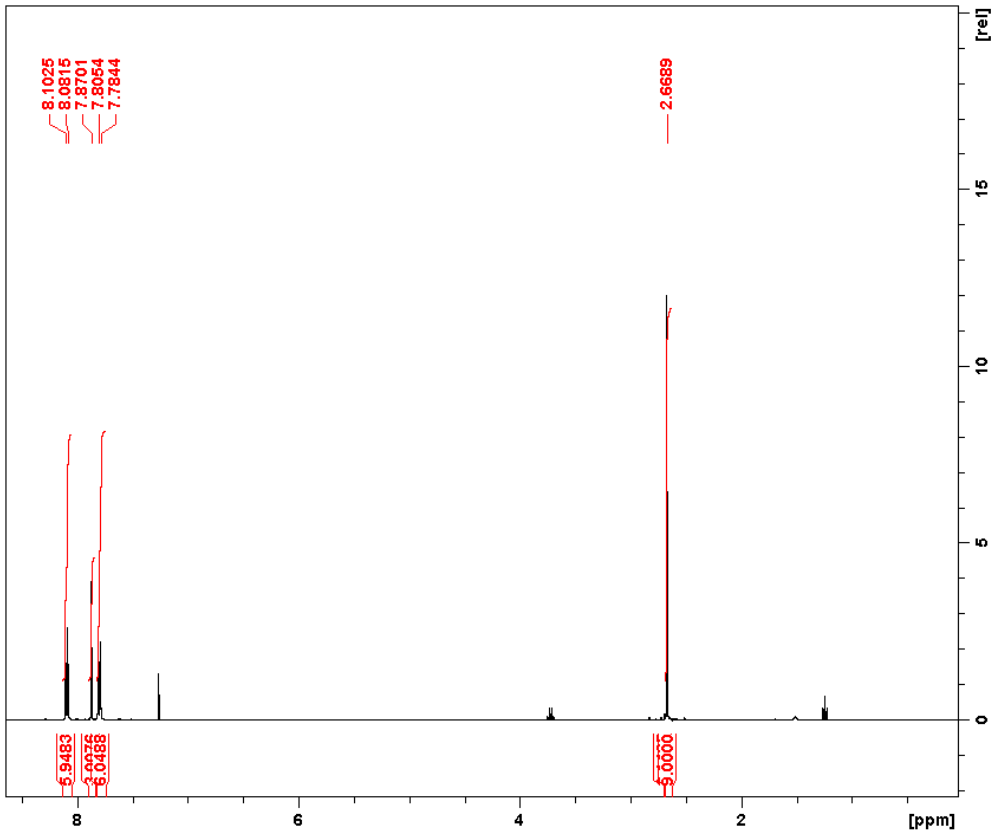

Figure 95. ^{1}H-NMR (400MHz, $CDCl_3$, 25°C) spectrum of TPB-CO

6.1.18 Synthesis of ligand 5, TPM-CF_3.

Metallic Na (0.46 g, 20 mmol) has been dissolved in 50 mL of absolute ethanol, in a 100 mL 3 necks round bottom flask, under nitrogen atmosphere. After the solution reached RT, ethyl trifluoroacetate (3.4 mL, 28.5 mmol) and TPM-CO (1.11 g, 3 mmol) have been added, under vigorous stirring. The solution has been heated to 65 °C in order to solubilize TPM-CO. The mixture has been stirred at room temperature for 24 hours. The solvent has been removed under reduced pressure. After addition of water (100 mL) and an HCl 10% aqueous solution, the formation of a white precipitate occurred. The obtained solid has been washed first with water (50 mL), then with *n*-pentane (50 mL) and ethyl ether (50 mL) subsequently obtaining 1.97 g of pure product (quantitative yield). Compound purity has been confirmed by NMR and elemental analysis.

^{1}H-NMR (400MHz, $CDCl_3$, T = 25°C): δ [ppm] = 15.05 (3H, s, H_2), 7.92 (6H, AA' part of an AA'BB' m, $H_{3,3'}$), 7.24 (6H, BB' part of an AA'BB' m, $H_{4,4'}$), 6.55 (3H, s, H_1), 5.75 (1H, s, H_5).
13C-NMR ((400MHz, $CDCl_3$, T = 25°C): δ [ppm] = 185.33 (s, C_4), 177.69 (q, C_2, $^2J_{C-F}$ = 36.4 Hz), 148.23 (s, C_8), 131.99 (s, C_5), 130.09 (s, C_6), 128.27 (s, C_7), 117.20 (q, C_1, $^1J_{C-F}$ = 281.7 Hz), 92.46 (q, C_3, $^3J_{C-F}$ = 2.1 Hz), 56.78 (s, C_9).

Elemental analysis for **5** ($C_{31}H_{19}F_9O_6$), experimental (calculated): C 56.12% (56.55%), H 3.01% (2.91%).

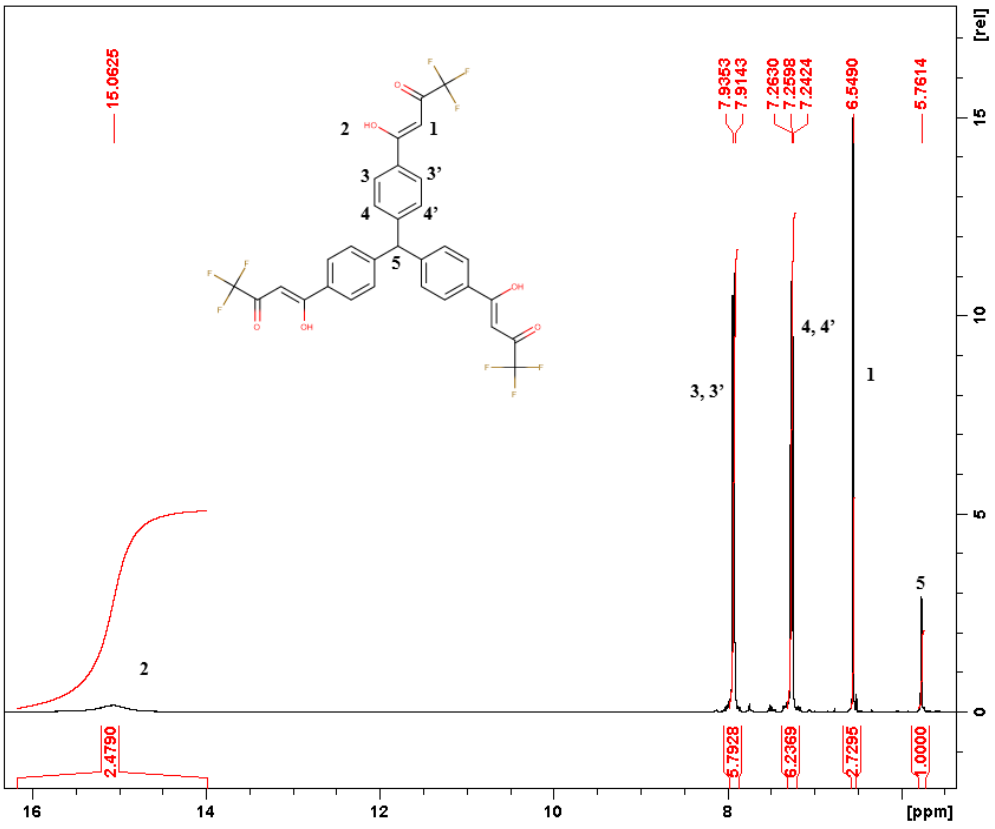

Figure 96. ^{1}H-NMR (400MHz, $CDCl_3$, 25°C) spectrum of ligand **5**.

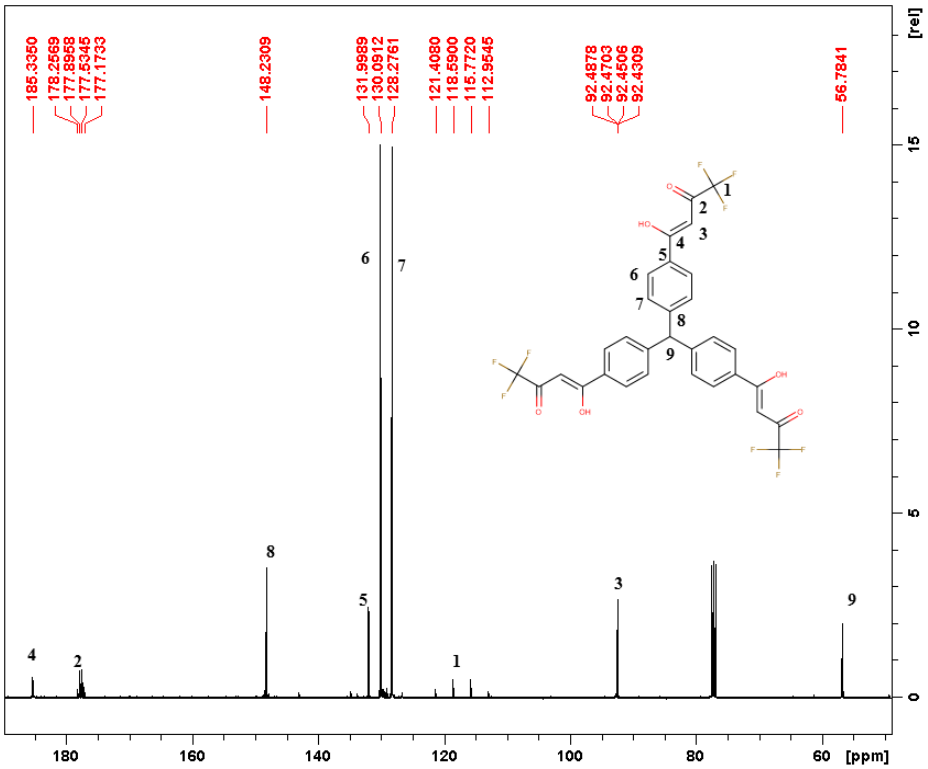

Figure 97. ^{13}C-NMR (400MHz, $CDCl_3$, 25°C) spectrum of ligand **5**.

6.1.19 Synthesis of ligand 6, TPM-tBu.

Potassium *tert*-butoxide (2.42 g, 20 mmol) has been dissolved in 30 mL of dry DMF, in a 100 mL 3 necks round bottom flask, under nitrogen atmosphere. To this solution, ethyl trimethylacetate (4.5 mL, 29.5 mmol) and TPM-CO (1.11 g, 3 mmol) have been added in this order. The mixture has been stirred at 50 °C for 24 hours. To this solution, water and an HCl 10% aqueous solution have been added. The mixture has been extracted with ethyl acetate and the organic phase has been collected. Solvent has been removed under reduced pressure. The product has been purified by recrystallization from hot ethyl ether to give 1.86 g of a white solid (quantitative yield). Compound purity has been confirmed by NMR and elemental analysis.

^{1}H-NMR (400MHz, $CDCl_3$, T = 25°C): δ [ppm] = 16.43 (3H, s, H_3), 7.83 (6H, AA' part of an AA'BB' m, $H_{4,4'}$), 7.18 (6H, BB' part of an AA'BB' m, $H_{5,5'}$), 6.26 (3H, s, H_2), 5.68 (1H, s, H_6), 1.24 (27H, s, H_1).
13C-NMR ((400MHz, $CDCl_3$, T = 25°C): δ [ppm] = 203.05 (s, C_3), 184.17 (s, C_5), 144.94 (s, C_9), 134.36 (s, C_6), 129.71 (s, C_7), 127.45 (s, C_8), 92.24 (s, C_4), 56.61 (s, C_{10}), 39.99 (s, C_2), 27.51 (s, C_1).

Elemental analysis for **6** ($C_{40}H_{46}O_6$), experimental (calculated): C 76.86% (77.14%), H 7.41% (7.45%).

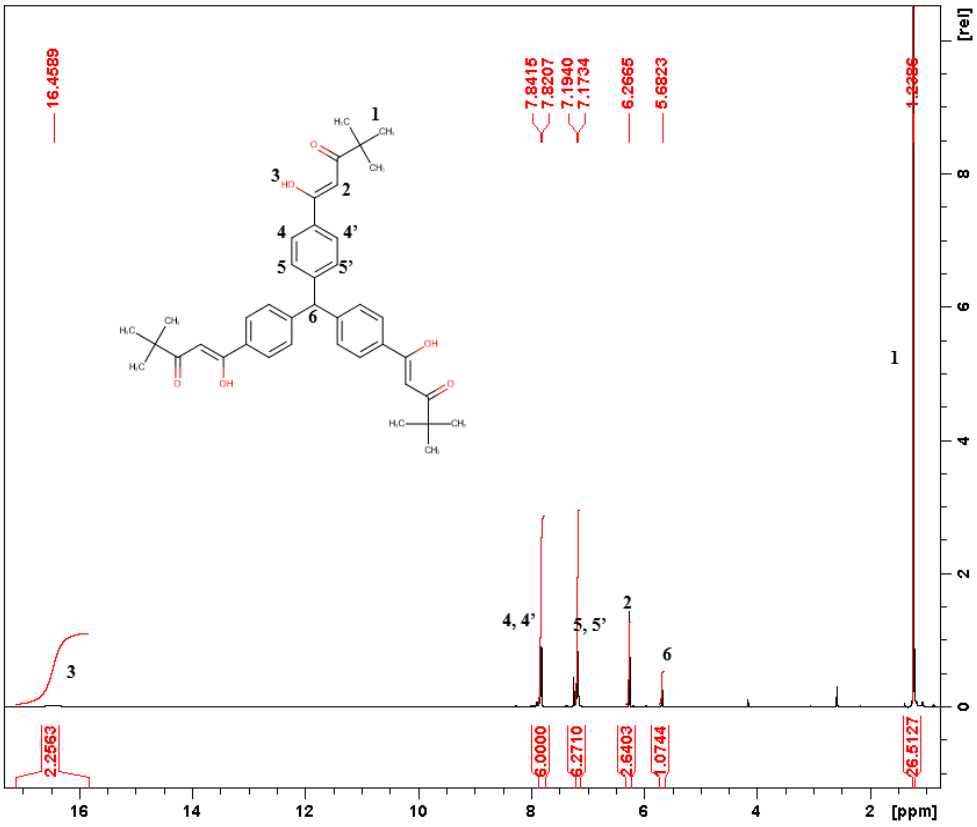

Figure 98. ^{1}H-NMR (300MHz, $CDCl_3$, 25°C) spectrum of ligand **6**.

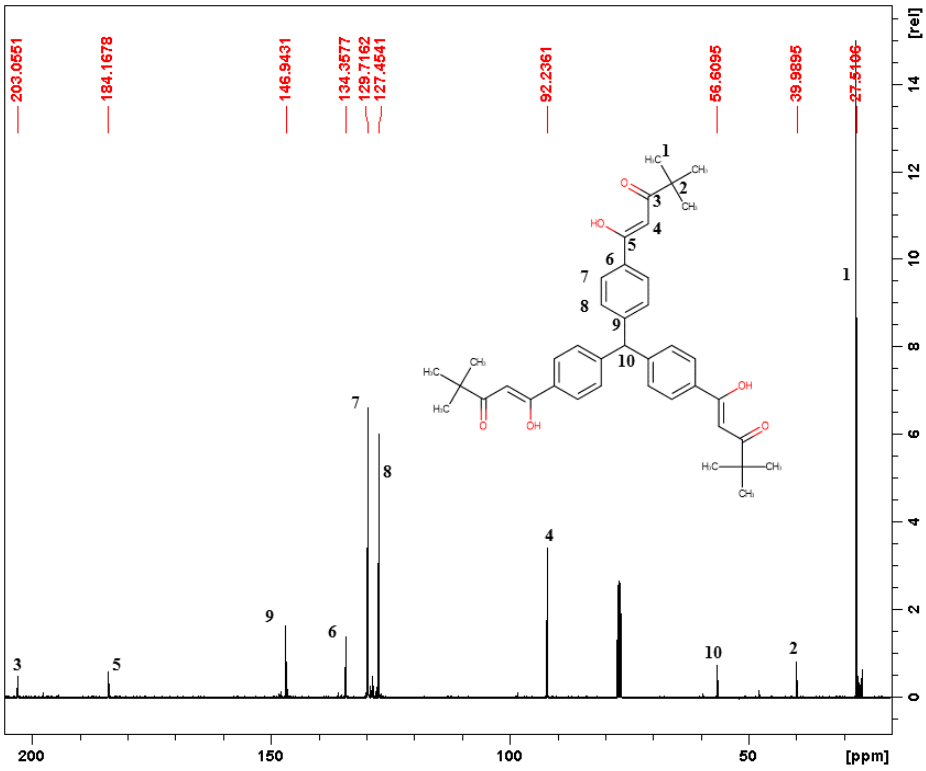

Figure 99. ^{13}C-NMR (300MHz, $CDCl_3$, 25°C) spectrum of ligand **6**.

6.1.20 Synthesis of ligand 7, TPA-CF_3.

Metallic Na (0.46 g, 20 mmol) has been dissolved in 50 mL of absolute ethanol, in a 100 mL 3 necks round bottom flask, under nitrogen atmosphere. After the solution reached RT, ethyl trifluoroacetate (3.4 mL, 28.5 mmol) and TPA-CO (1.1 g, 3 mmol) have been added, under vigorous stirring. The solution has been heated to 65 °C in order to solubilize TPA-CO. The mixture has been stirred at room temperature for 24 hours. The solvent has been removed under reduced pressure. After addition of water (100 mL) and an HCl 10% aqueous solution, the formation of a green-yellow precipitate occurred. The obtained solid has been washed first with water (50 mL), then with *n*-pentane (50 mL) and ethyl ether (50 mL) subsequently, obtaining 1.98 g of pure product (quantitative yield). Compound purity has been confirmed by NMR and elemental analysis.

^{1}H-NMR (400MHz, $CDCl_3$, T = 25°C): δ [ppm] = 15.20 (3H, s, H_2), 7.92 (6H, AA' part of an AA'BB' m, $H_{3,3'}$), 7.22 (6H, BB' part of an AA'BB' m, $H_{4,4'}$), 6.52 (3H, s, H_1).
13C-NMR ((400MHz, $CDCl_3$, T = 25°C): δ [ppm] = 184.67 (s, C_4), 177.20 (q, C_2, $^2J_{C-F}$ = 36.7 Hz), 150.74 (s, C_8), 129.72 (s, C_6), 128.91 (s, C_5), 124.55 (s, C_7), 117.30 (q, C_1, $^1J_{C-F}$ = 282.8 Hz), 92.11 (q, C_3, $^3J_{C-F}$ = 2.0 Hz).

Elemental analysis for **7** ($C_{30}H_{18}F_9NO_6$), experimental (calculated): C 54.36% (54.64%), H 2.82% (2.75%), N 2.38% (2.12%).

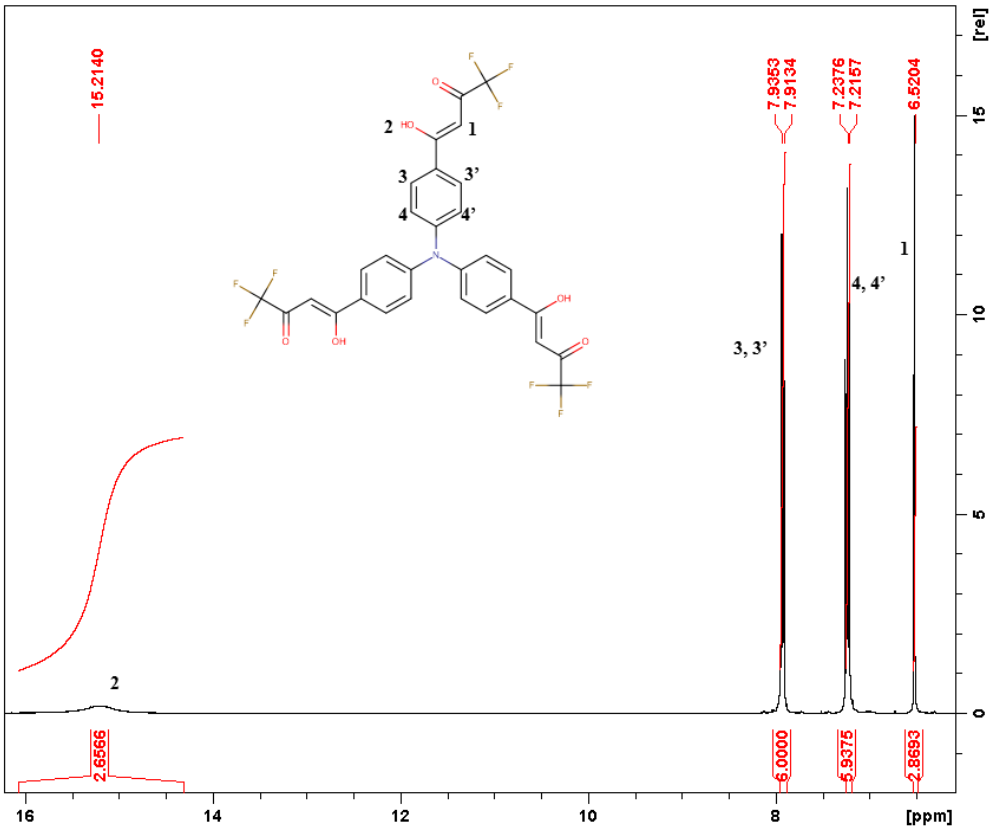

Figure 100. ^{1}H-NMR (400MHz, $CDCl_3$, 25°C) spectrum of ligand **7**.

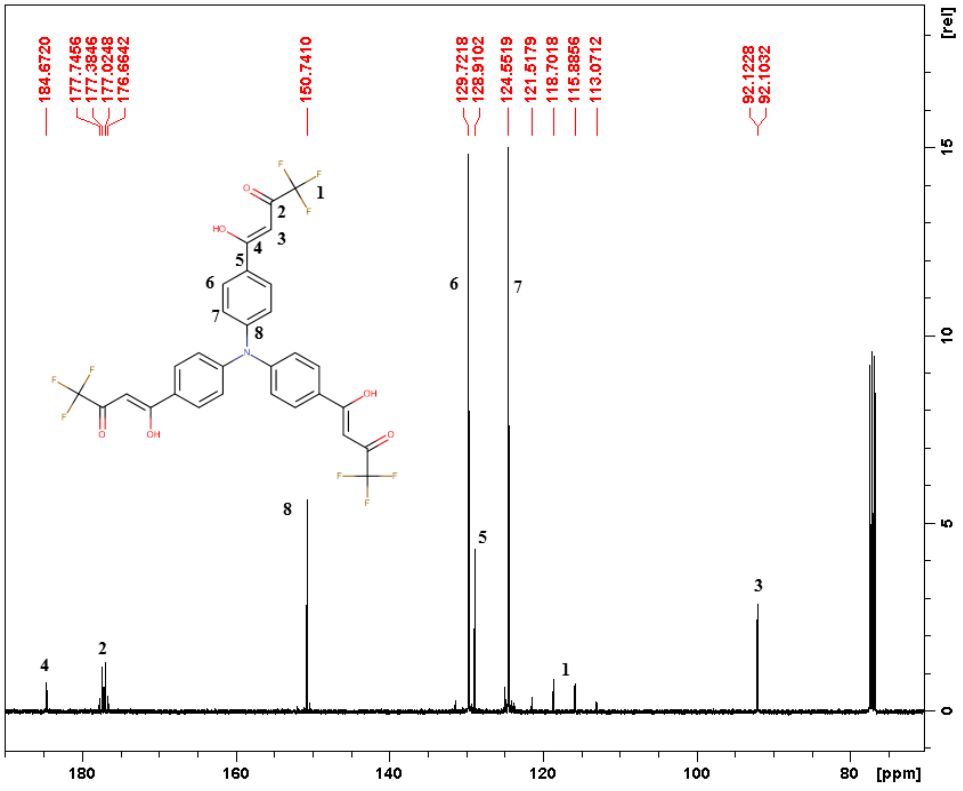

Figure 101. ^{13}C-NMR (400MHz, $CDCl_3$, 25°C) spectrum of ligand **7**.

6.1.21 Synthesis of ligand 8, TPA-tBu.

Potassium *tert*-butoxide (2.42 g, 20 mmol) has been dissolved in 30 mL of dry DMF, in a 100 mL 3 necks round bottom flask, under nitrogen atmosphere. To this solution, ethyl trimethylacetate (4.5 mL, 29.5 mmol) and TPA-CO (1.11 g, 3 mmol) have been added in this order. The mixture have been stirred at 50 °C for 24 hours. To this solution, water and an HCl 10% aqueous solution have been added. The mixture has been extracted with ethyl acetate and the organic phase has been collected. Solvent has been removed under reduced pressure leading to the formation of a dark red oil. Purification of the product is ongoing.

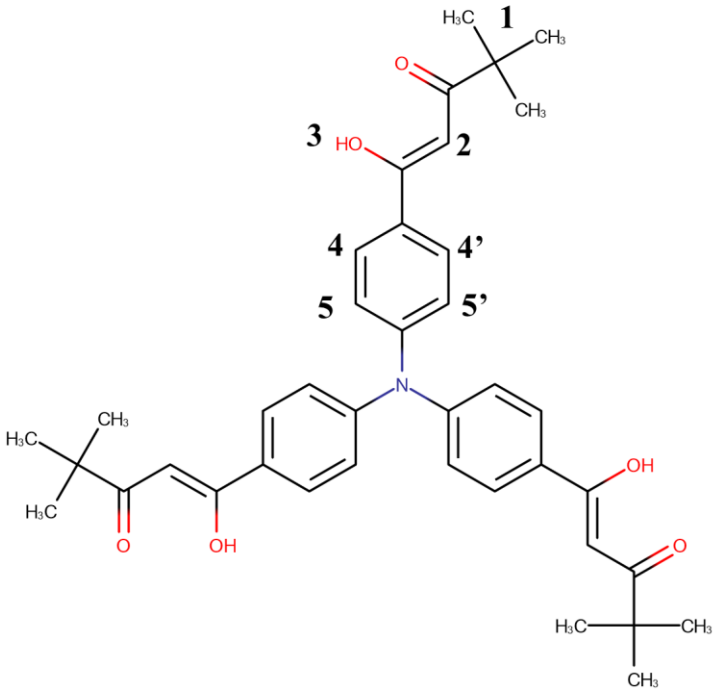

Figure 102. Scheme of ligand **8**.

6.1.22 Synthesis of ligand 9, TPB-CF_3.

Metallic Na (0.46 g, 20 mmol) has been dissolved in 25 mL of absolute ethanol, in a 100 mL 3 necks round bottom flask, under nitrogen atmosphere. After Na dissolved, 25 mL of dry THF have been added. Then, ethyl trifluoroacetate (3.4 mL, 28.5 mmol) and TPB-CO (1.1 g, 3 mmol) have been added, under vigorous stirring. The solution has been heated to 65 °C in order to solubilize TPB-CO. The mixture has been stirred at room temperature for 24 hours. The solvent has been removed under reduced pressure. After addition of water (100 mL) and an HCl 10% aqueous solution, the formation of a green-yellow precipitate occurred. The obtained solid has been washed first with water (50 mL) then with *n*-pentane (50 mL) and ethyl ether (50 mL) subsequently, obtaining 2.16 g of pure product (quantitative yield). Compound purity has been confirmed by NMR and elemental analysis.

^{1}H-NMR (400MHz, $CDCl_3$, T = 25°C): δ [ppm] = 15.16 (3H, s, H_2), 8.10 (6H, AA' part of an AA'BB' m, $H_{3,3'}$), 7.90(3H, s, H_5), 7.84 (6H, BB' part of an AA'BB' m, $H_{4,4'}$), 6.64 (3H, s, H_1).
^{1}C-NMR (400MHz, $CDCl_3$, T = 25°C): δ [ppm] = 185.3 (s, C_4), 177.9 (m, C_2), 145.7 (s, C_8), 141.7 (s, C_9), 132.4 (s, C_5), 128.5 (s, C_6), 128.0 (s, C_7), 126.5 (s, C_{10}), 92.5 (s, C_3).

Elemental analysis for **9** ($C_{36}H_{21}F_9O_6$), experimental (calculated): C 60.35% (60.01%), H 2.82% (2.94%).

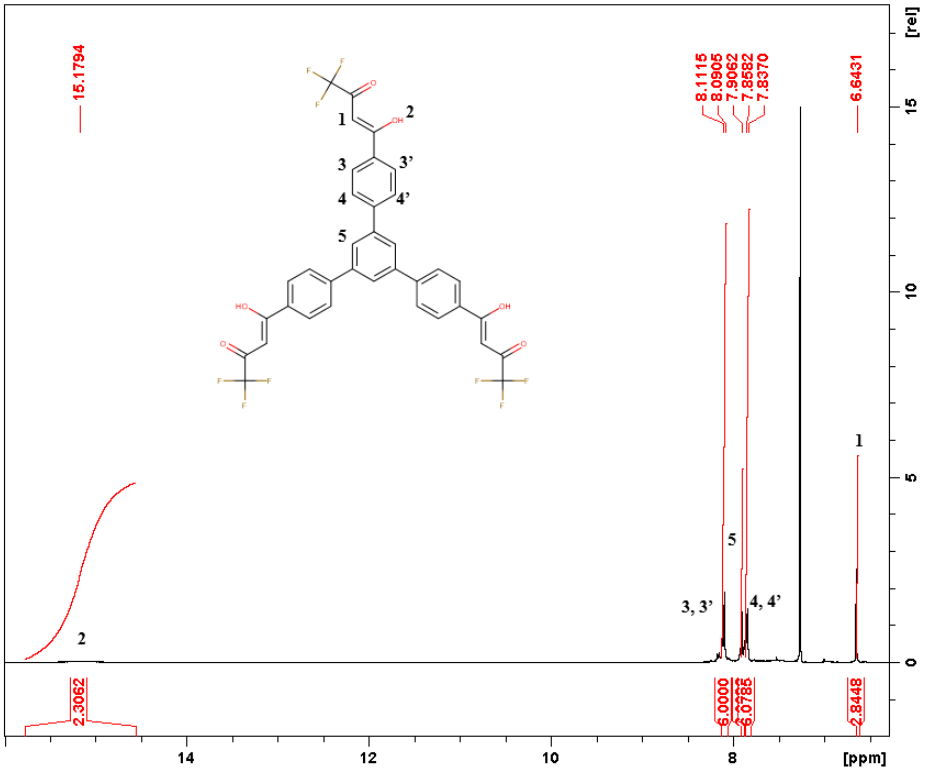

Figure 103. ^{1}H-NMR (400MHz, $CDCl_3$, 25°C) spectrum of ligand **9**.

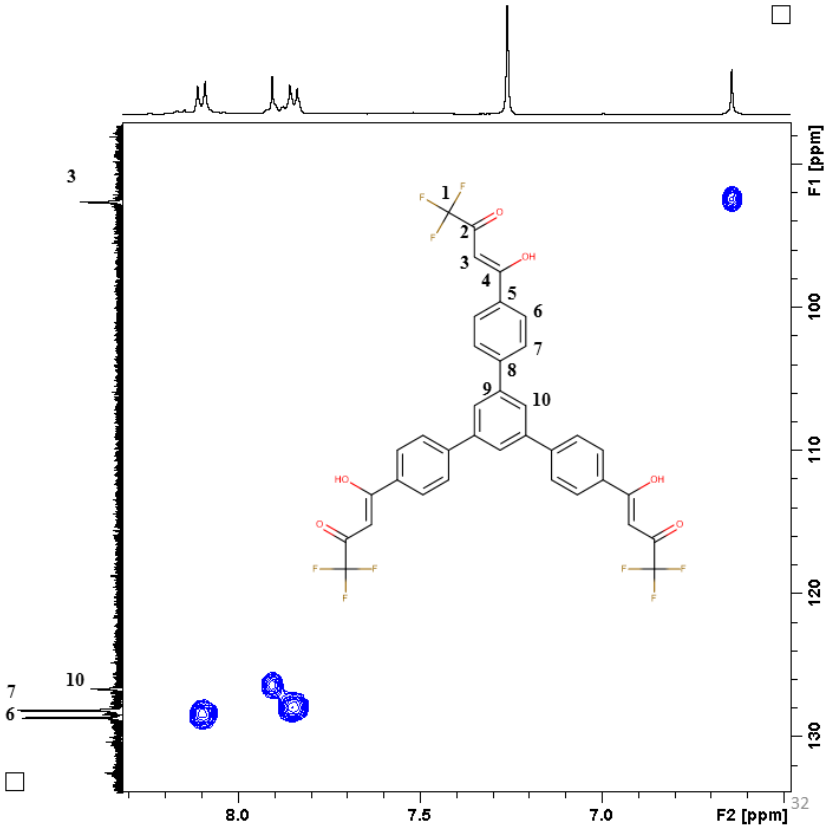

Figure 104. HMQC (400MHz, $CDCl_3$, 25°C) spectrum of ligand **9**.

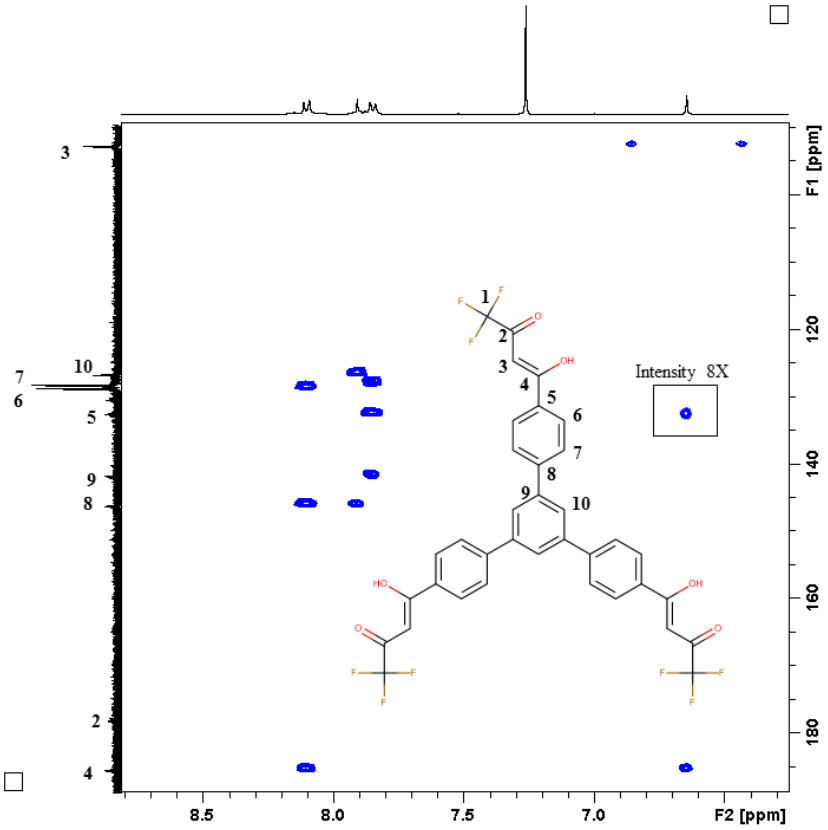

Figure 105. HMBC (400MHz, $CDCl_3$, 25°C) spectrum of ligand **9.**

6.1.23 Synthesis of ligand 10, TPB-tBu.

Potassium *tert*-butoxide (2.42 g, 20 mmol) has been dissolved in 30 mL of dry DMF, in a 100 mL 3 necks round bottom flask, under nitrogen atmosphere. To this solution, ethyl trimethylacetate (4.5 mL, 29.5 mmol) and TPB-CO (1.11 g, 3 mmol) have been added in this order. The mixture have been stirred at 50 °C for 24 hours. After addition of water and HCl 10% aqueous solution, a brown precipitate occurred. The solid has been dissolved in CH_2Cl_2 and the solution has been filtered in order to remove some insoluble by-products. Solvent has been removed under reduced pressure leading to the formation of a brown powder. Purification of the product is ongoing.

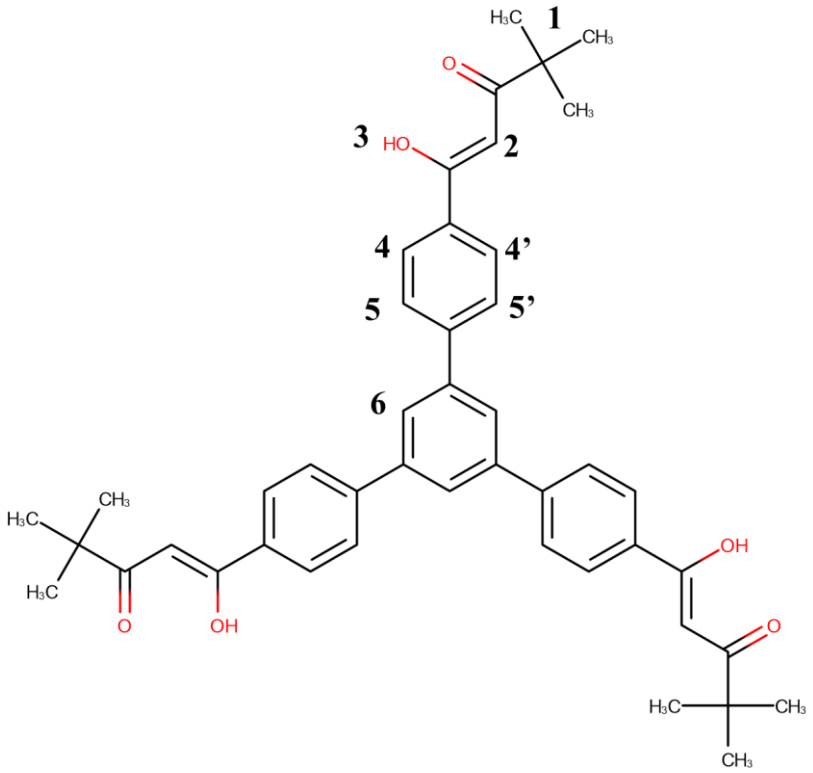

Figure 106. Scheme of ligand **10**.

6.1.24 Synthesis of Fe5: path 1.

A mother solution of Fe^{3+} has been prepared dissolving $FeCl_3$ (43.1 mg, 0.266 mmol) in 13 mL of methanol. Separately, ligand **5** (13.7 mg, 0.02 mmol) has been dissolved in 1 mL of chloroform. 1 mL of the Fe^{3+} methanol mother solution has been gently layered over the ligand chloroform solution (molar ratio Fe^{3+}:L 1:1). The two layers have been left diffuse one into the other for three days resulting in a dark red solution. Single crystals of **Fe5**·$2CHCl_3$ have been obtained by slow evaporation of the solvents after one week.

Elemental analysis for dried **Fe5** ($C_{124}H_{64}F_{36}Fe_4O_{24}$), experimental (calculated): C 54.12% (52.35%), H 2.31% (2.27%).

6.1.25 Synthesis of Fe5: path 2.

$FeCl_3$ (9.7 mg, 0.06 mmol), ligand **5** (41.1 mg, 0.06 mmol) and sodium carbonate (31.8 mg, 0.3 mmol) have been dissolved in 15 mL of THF. The mixture has been reacted at reflux temperature for 16 hours (overnight). The solution has been filtered to remove the NaCl by-product. The solvent has been removed under reduced pressure and the resulting solid has been washed with methanol, to give 44.1 mg of red powder (quantitative yield).

Elemental analysis for **Fe5** ($C_{124}H_{64}F_{36}Fe_4O_{24}$), experimental (calculated): C 54.65% (52.35%), H 2.12% (2.27%).

6.1.26 Synthesis of Fe6.

A mother solution of Fe^{3+} has been prepared dissolving $FeCl_3$ (43.1 mg, 0.266 mmol) in 13 mL of methanol. Separately, ligand **7** (12.5 mg, 0.02 mmol) has been dissolved in 1 mL of chloroform. 1 mL of the Fe^{3+} methanol mother solution has been gently layered over the ligand chloroform solution (molar ratio Fe^{3+}:L 1:1). The two layers have been left diffuse one into the other for three days resulting in a dark red solution. After complete diffusion of the two solvents, the mixture has been evaporated to give 13.5 mg (quantitative yield) of a red solid product. Single crystals of **Fe6**·$3CHCl_3$ have been obtained by slow evaporation of a chloroform/*iso*-propanol solution, after two weeks.

Elemental analysis for **Fe6** ($C_{160}H_{172}Fe_4O_{24}$), experimental (calculated): C 70.98% (71.11%), H 6.57% (6.42%).

6.1.27 Synthesis of $[Eu_2L_4](HB)_2$ capsules.

All the $[Eu_2L_4](HB)_2$ capsules have been obtained following a general procedure. The ligand (0.05 mmol) and the base (0.1 mmol) have been dissolved in 10 mL of ethanol. To this solution, a solution of $EuCl_3·6H_2O$ (0.025 mmol) in 5 mL of ethanol, has been added dropwise. Suddenly the formation of a white precipitate occurred. The mixture has been left under vigorous stirring for 3 hours, then the solvent has been removed. The obtained powder has been washed with cold ethanol to give a white solid with quantitative yield.

6.1.28 Synthesis of Eu_2L_3 capsules.

All the Eu_2L_3 capsules have been obtained following a general procedure. The ligand (0.03 mmol) and the base (0.06 mmol) have been dissolved in 10 mL of ethanol. To this solution, a solution of $EuCl_3 \cdot 6H_2O$ (0.02 mmol) in 5 mL of ethanol, has been added. Suddenly the formation of a white precipitate occurred. The mixture has been left under vigorous stirring for 3 hours, then the solvent has been removed. The obtained powder has been washed with cold ethanol to give a white solid with quantitative yield.

6.1.29 Self-sorting of Eu^{3+} with ligands 1, 3 and 4.

A 30 mL methanol solution containing ligand **1** (0.05 mmol) ligand **3** (0.05 mmol), ligand **4** (0.05 mmol) and NaOH (0.3 mmol) have been prepared. To this solution, an ethanol solution of $EuCl_3 \cdot 6H_2O$ (0.075 mmol) in 15 mL of methanol has been added. The mixture has been left under vigorous stirring for 6 hours. A sample of the solution has been diluted to 10^{-5} M *ca.* in order to perform ESI-MS analysis.

6.2 Spectroscopic analysis.

6.2.1 FT-IR Spectroscopy.

FT-IR analysis was performed with a Nexus 870 FTIR (Nicolet), operating in the transmission range 500–4000 cm^{-1}, collecting 32 scans with a spectral resolution of 4 cm^{-1}. The samples were prepared by drop casting the solution on a NaCl round cell window.

6.2.1.1 {PTA@[Cu(*o*–L)]$_3$} oxidation by air bubbling.

{PTA@[Cu(*o*–L)]$_3$} (30 mg, 0.026 mmol) has been dissolved in a 1:1 chloroform-co-solvent (total volume 6 ml) solution. Co-solvents: methanol, ethanol, acetonitrile, ethyl acetate, tetrahydrofuran, 1,4-dioxane, acetone, *n*-hexane, cyclo-hexane and *n*-heptane. The solution has been air bubbled under continuous stirring and FT-IR spectra have been periodically collected.

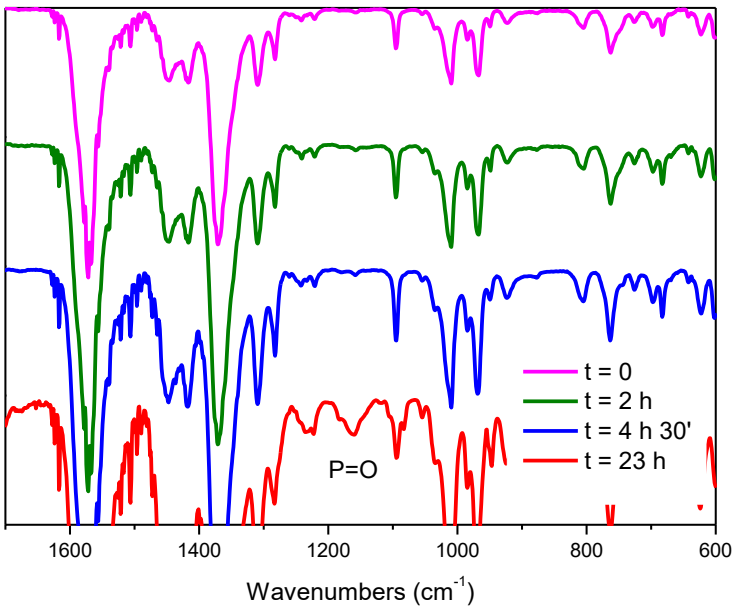

Figure 107. Normalized FT-IR spectra of {PTA@[Cu(o–L)]$_3$} in an air bubbled chloroform-acetonitrile solution. The increase in the P=O band intensity with time.

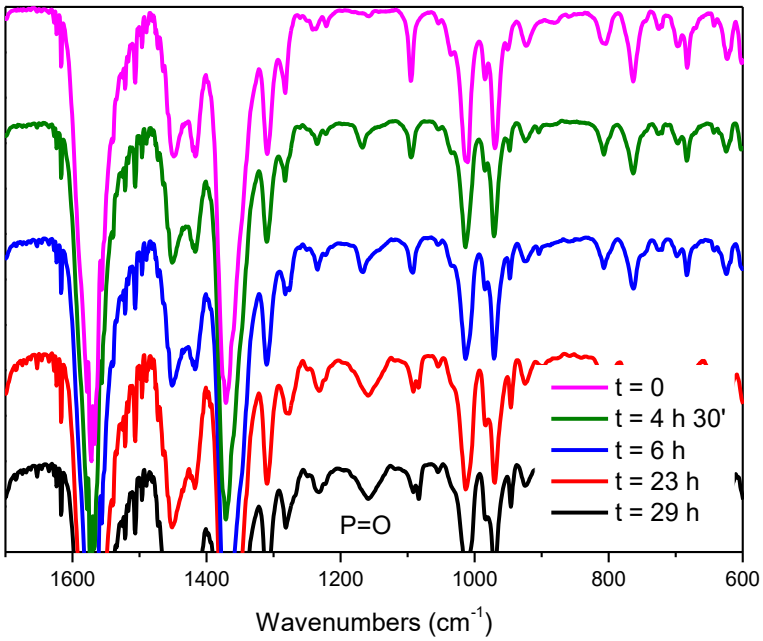

Figure 108. Normalized FT-IR spectra of {PTA@[Cu(o–L)]$_3$} in an air bubbled chloroform-ethanol solution. The increase in the P=O band intensity with time.

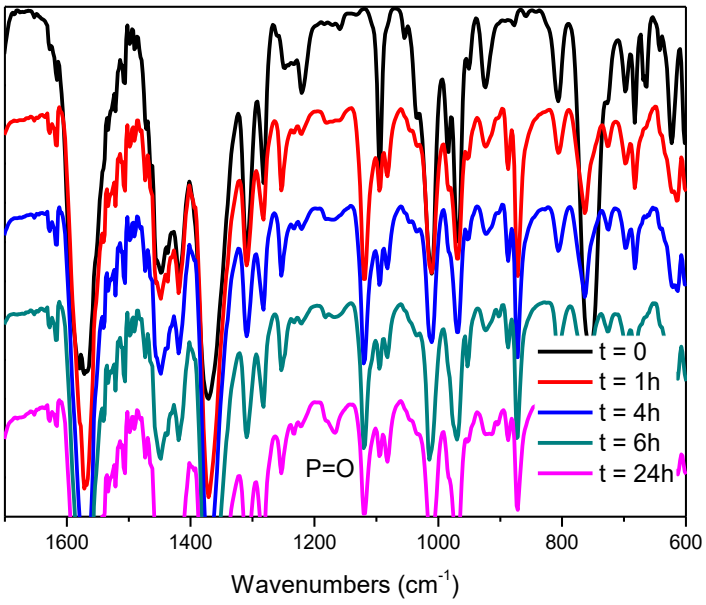

Figure 109. Normalized FT-IR spectra of {PTA@[Cu(o–L)]$_3$} in an air bubbled chloroform-1,4-dioxane solution. The increase in the P=O band intensity with time.

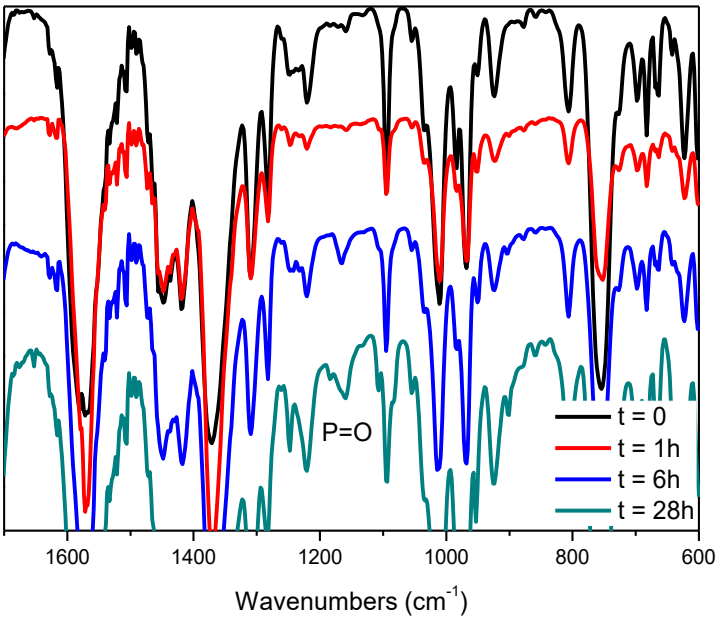

Figure 110. Normalized FT-IR spectra of {PTA@[Cu(o–L)]$_3$} in an air bubbled chloroform-acetone solution. The increase in the P=O band intensity with time.

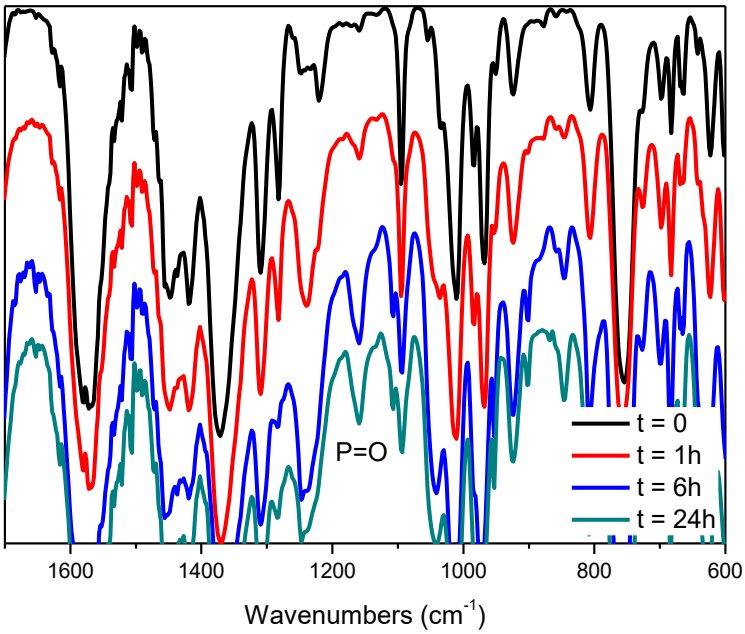

Figure 111. Normalized FT-IR spectra of {PTA@[Cu(o–L)]$_3$} in an air bubbled chloroform-ethyl acetate solution. The increase in the P=O band intensity with time.

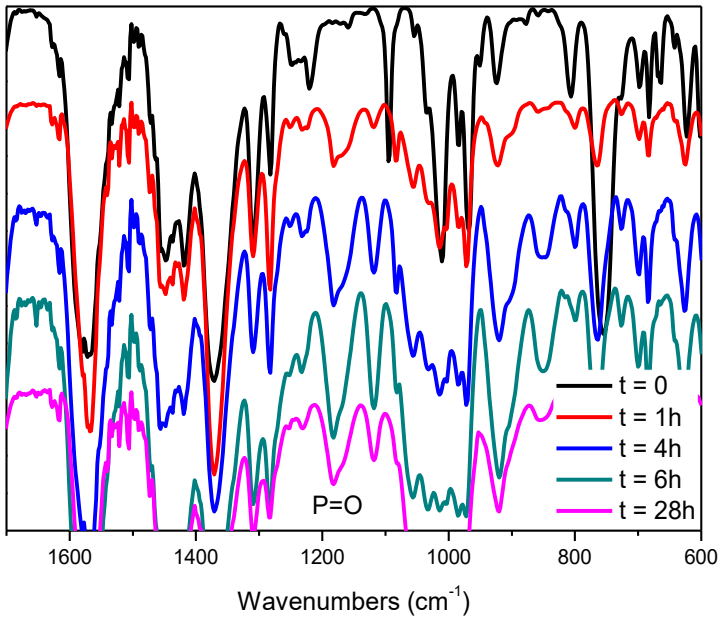

Figure 112. Normalized FT-IR spectra of {PTA@[Cu(o–L)]$_3$} in an air bubbled chloroform-tetrahydrofuran solution. The increase in the P=O band intensity with time.

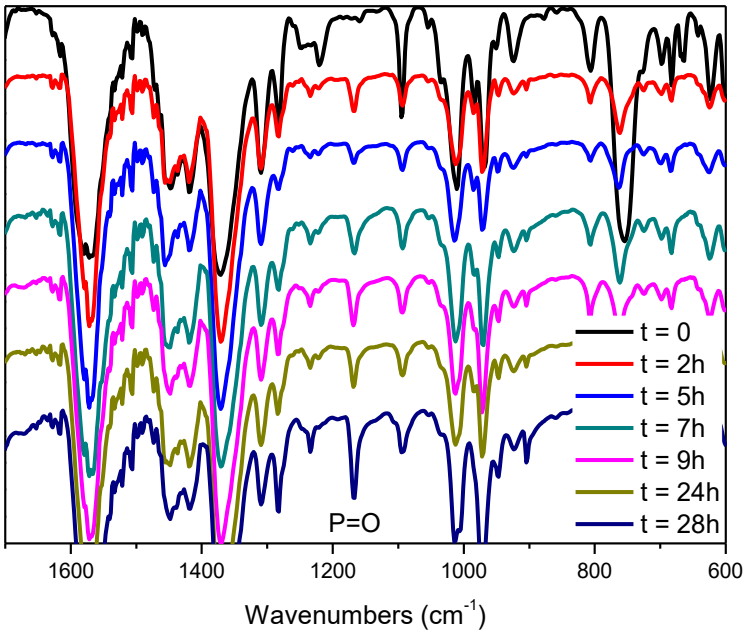

Figure 113. Normalized FT-IR spectra of {PTA@[Cu(o–L)]$_3$} in an air bubbled chloroform-methanol solution. The increase in the P=O band intensity with time.

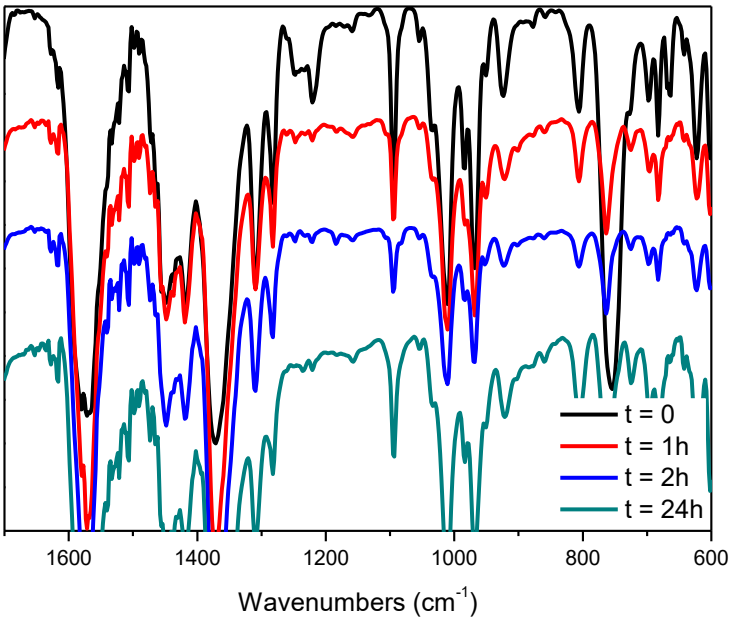

Figure 114. Normalized FT-IR spectra of {PTA@[Cu(o–L)]$_3$} in an air bubbled chloroform-cyclo-hexane solution.

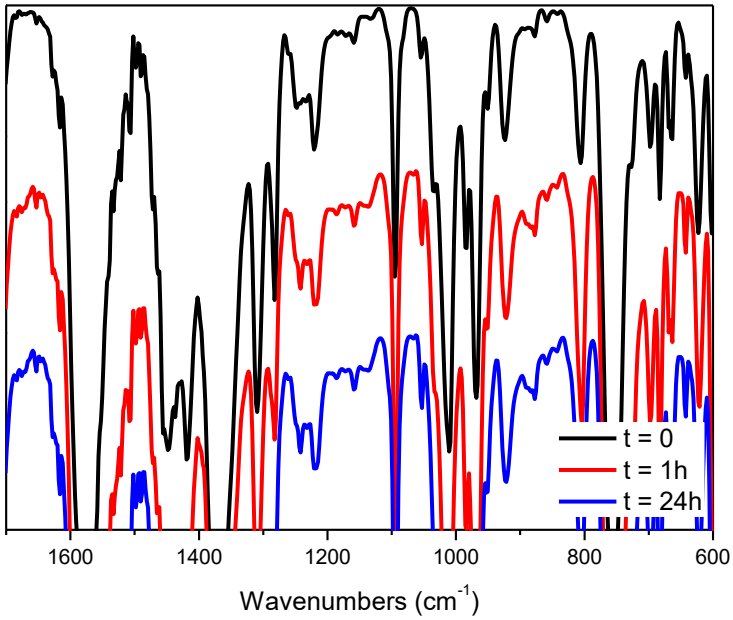

Figure 115. Normalized FT-IR spectra of {PTA@[Cu(o–L)]$_3$} in an air bubbled chloroform-n-hexane solution.

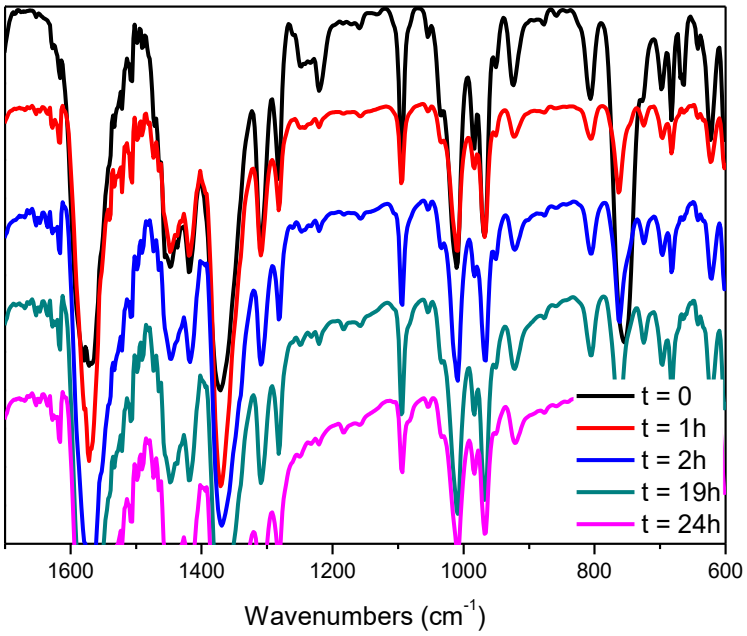

Figure 116. Normalized FT-IR spectra of {PTA@[Cu(o–L)]$_3$} in an air bubbled chloroform-n-heptane solution.

6.2.2 UV-Vis Absorption Spectroscopy.

Absorption spectra were recorded on a CARY5E double-beam spectrophotometer with a spectral bandwidth of 2 nm and on a CARY 4000 double beam spectrophotometer equipped with a Peltier thermostat, with a spectral bandwidth of 1 nm. The contribution due to the solvent was subtracted.

6.2.2.1 Guest-exchange titration.

In a quartz-suprasil cuvette, to 3.0 ml of a 1.05 mM and of a 2.19 mM chloroform solutions of {Me-Tr@[Cu(o–L)]$_3$} a 1.18 M sTr methanol solution has been added in different aliquots (starting volume 3.00 ml, final volume 3.3 ml). After each addition, the solution has been stirred for 3 minutes and the spectrum recorded. The cuvette has been kept at 25 °C using a Peltier thermostat. Spectra are shown in Figure 117 and Figure 118.

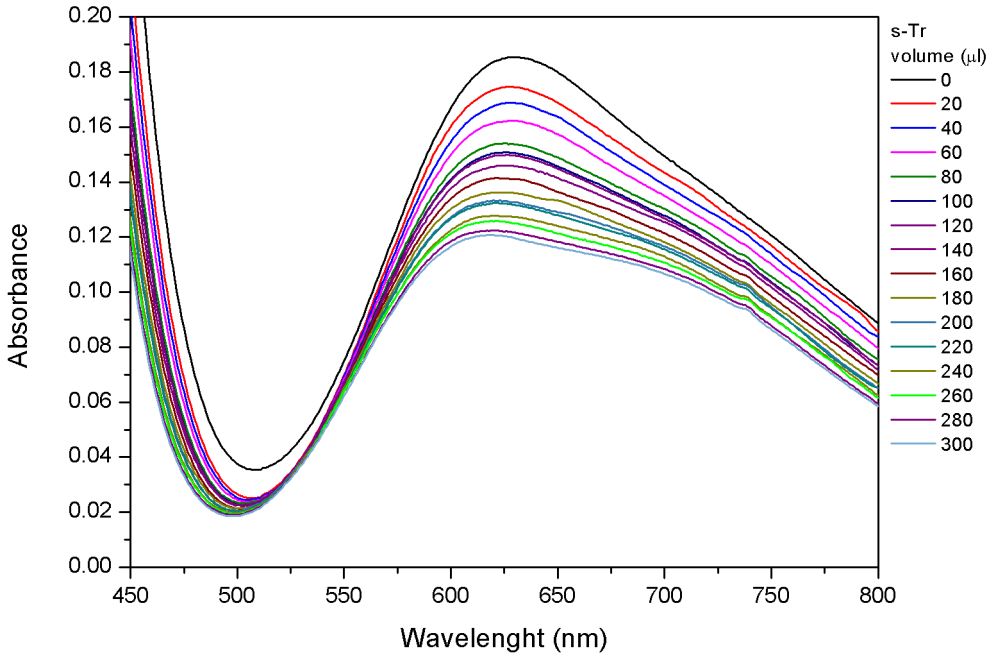

Figure 117. Guest-exchange titrations with s-Tr, {Me-Tr@[Cu(*o*-L)]$_3$} concentration = 1.05 mM, T = 298.15 K.

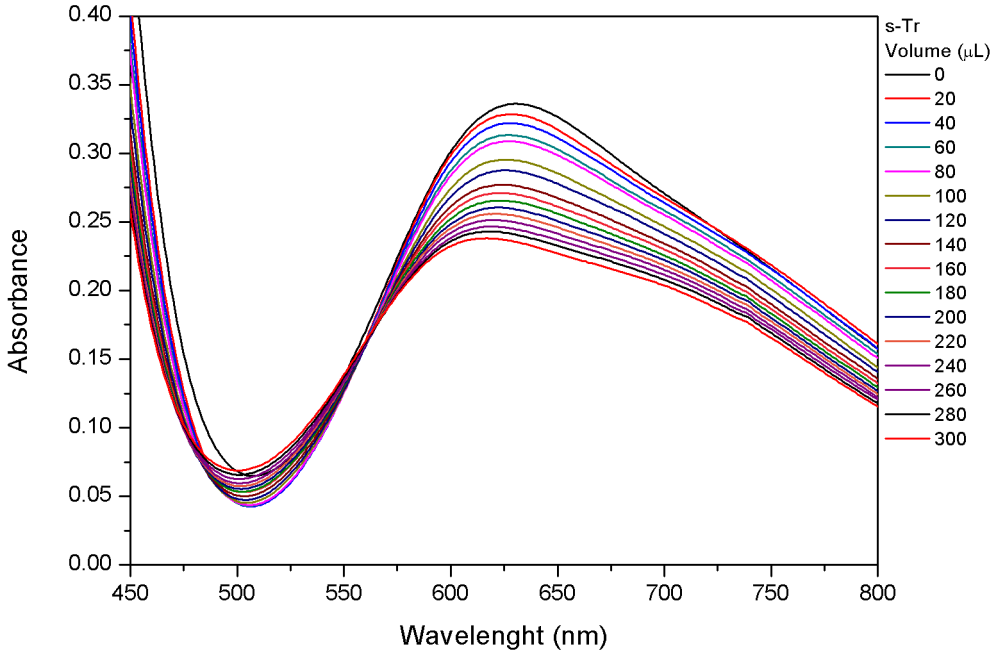

Figure 118. Guest-exchange titrations with s-Tr, {Me-Tr@[Cu(*o*-L)]$_3$} concentration = 2.19 mM, T = 298.15 K.

6.2.2.2. Data analysis.

Titration data have been computed using Hyperquad software[1] according to the model here described. For sake of clarity, compounds $[Cu(o\text{-}L)]_2$, $[Cu(o\text{-}L)]_3$, {s-Tr@$[Cu(o\text{-}L)]_3$} and {Me-Tr@$[Cu(o\text{-}L)]_3$} are denoted as D, T, TG_1, and TG_2 respectively. While free guest species s-Tr and Me-Tr are denoted as G_1 and G_2 respectively. The minimization program required, for a correct mass balance, the introduction of a virtual monomer "[Cu(o-L)]" denoted as M. The guest exchange constant (K_{ex}) is related to M by the following equilibria, where β_{TG1} and β_{TG2} are the the host-guest systems formation constants, respectively.

$$TG_1 \rightleftharpoons 3M + G_1 \quad (1/\beta_{TG1}) \tag{1}$$

$$3M + G_2 \rightleftharpoons TG_2 \quad (\beta_{TG2}) \tag{2}$$

$$TG_1 + G_2 \rightleftharpoons TG_2 + G_1 \tag{3}$$

Since the trimer concentration is governed by the CDL equilibrium, it has to be taken into account in the adopted model. Dimer and trimer species are related to M by the following equilibria, where β_D and β_T are the dimer and trimer formation constants, respectively. Their determination has been previosly reported[2].

$$2M \rightleftharpoons D \quad (\beta_D) \tag{4}$$

$$3M \rightleftharpoons T \quad (\beta_T) \tag{5}$$

The system absorbance (A^i_λ) at a given wavelength λ for the i-th concentration is:

$$A^i_\lambda = \varepsilon_{D,\lambda}[D] + \varepsilon_{T,\lambda}[T] + \varepsilon_{TG1,\lambda}[TG_1] + \varepsilon_{TG2,\lambda}[TG_2] \tag{6}$$

where $\varepsilon_{D,\lambda}$, $\varepsilon_{T,\lambda}$, $\varepsilon_{TG1,\lambda}$ and $\varepsilon_{TG2,\lambda}$ are the molar extinction coefficients of the dimer, trimer and of the host-guest species at the same wavelength. The total concentration balance (calculated on the basis of a virtual monomer M) can be written as:

$$C_{Tot,M} = 2\beta_D[M]^2 + 3\beta_T[M]^3 + 3\beta_{TG1}[M]^3[G_1] + 3\beta_{TG2}[M]^3[G_2] \tag{7}$$

$$C_{Tot,G1} = 3\beta_{TG1}[M]^3[G_1] + [G_1] \tag{8}$$

$$C_{Tot,G2} = 3\beta_{TG2}[M]^3[G_2] + [G_2] \tag{9}$$

The Hyperquad program[1], by minimizing the difference between experimental and calculated absorbance values (equation 10), can determine β_{TG2}, [D], [T], [TG_2], [G_1], $\varepsilon_{D,\lambda}$, $\varepsilon_{T,\lambda}$, $\varepsilon_{TG1,\lambda}$ and $\varepsilon_{TG2,\lambda}$. In order to improve the fit, the parameters $\varepsilon_{D,\lambda}$, $\varepsilon_{T,\lambda}$, $\varepsilon_{TG1,\lambda}$, β_D, β_T and β_{TG1}, obtained from previous works[2,3], have been input to Hyperquad as fixed values.

$$\Sigma(A^i_\lambda - A_{calc})^2 \qquad (10)$$

Finally, the guest exchange constant and the TG_2 host-guest association constant are calculated as follows:

$$Kex = \beta_{TG2}/\beta_{TG1} \quad \text{or} \quad \log K_{ex} = \log\beta_{TG2} - \log\beta_{TG1} \qquad (11)$$

$$Kas = \beta_{TG2}/\beta_T \quad \text{or} \quad \log K_{as} = \log\beta_{TG2} - \log\beta_T \qquad (12)$$

6.2.3 Emission spectrometry.

The luminescence spectra were recorded on acetonitrile, water and deuterated water solutions at room temperature using a Fluorolog-3 (Horiba Jobin–Yvon) spectrofluorimeter equipped with a double-grating monochromator in both the excitation and emission sides coupled to a R928P Hamamatsu photomultiplier and a 450 W Xe arc lamp as the excitation source. The emission spectra were corrected for detection and optical spectral response of the spectrofluorimeter through a calibration curve supplied by the manufacturer. The excitation spectra were corrected for the spectral distribution of the lamp intensity using a photodiode reference detector. Absolute photoluminescence quantum yields were calculated by corrected emission spectra obtained from an apparatus that consisted of a Spectralon-coated integrating sphere accessory (4“, F-3018,Horiba Jobin–Yvon) fitted in the fluorimeter sample chamber. Three independent measurements were carried out on each complex with an estimated error of ± 20 %. Quantum yield values are independent of the excitation wavelength in the investigated range.

6.3 Single crystals X-ray diffraction.

Single crystals of Cu^{2+} compounds and ligands have been fastened on the top of a Lindemann glass capillary or mounted using Paratone-N oil and centered on the head of a four circle kappa goniometer Oxford Diffraction Gemini E diffractometer, equipped with a 2K × 2K EOS CCD area detector and sealed-tube Enhance (Mo) and (Cu) X-ray sources. Data have been collected by means of the ω-scans technique using graphite-monochromated radiation, in a 1024 × 1024 pixel mode, using 2 × 2 pixel binning. Detector distance has been set at 45 mm. The diffraction intensities have been corrected for Lorentz/polarization effects as well as with respect to absorption. Empirical multi-scan absorption corrections using equivalent reflections have been performed with the scaling algorithm SCALE3 ABSPACK. Data collections for **Fe5** and **Fe6** have been performed at the X-ray diffraction beamline (XRD1) of the Elettra Synchrotron, Trieste (Italy). Complete datasets have been collected at 100 K (nitrogen stream supplied through an Oxford Cryostream 700) with a monochromatic wavelength of 0.700 Å through the rotating crystal method. Images were acquired using a Pilatus 2M image plate detector. Single crystals were dipped in N-paratone and mounted on the goniometer head with a nylon loop. Data reduction, finalization and cell refinement were carried out through the CrysAlisPro software. Accurate unit cell parameters were obtained by leastsquares refinement of the angular settings of strongest reflections, chosen from the whole experiment.

In all the cases, structures were solved by means of direct methods using SHELXS[4], intrinsic phasing method using SHELXT[5] or charge flipping method using OLEX2[6] and refined by full-matrix leastsquares methods based on F_o^2 with SHELXL-97[4] in the framework of OLEX2[6] software. In the last cycles of refinement, ordered nonhydrogen atoms were refined anisotropically whereas disordered partial occupancy non-hydrogen atoms were refined isotropically. Hydrogen atoms connected to carbon atoms were included in idealized positions, and a riding model was used for their refinement. A summary of the crystallographic data and of the refinement parameters for each compound is provided in the following sections.

6.3.1 $\{[(PTAO)_2@[Cu_8][Cu_2]\}_\infty$ determination and refinement details.

Despite several efforts to improve the crystals quality, the only useful specimens were not significantly diffracting at d < 0.85 Å. The data collection has been set to obtain a 100 % completeness at d = 0.90 Å. Structures were solved by means of charge flipping method with OLEX2[6] and refined by full–matrix least–squares methods based on F_o^2 with SHELXL[4] in the framework of OLEX2[6] software. During the refinement, a phenyl ring and a methyl group have been splitted in two parts the occupancies of which were constrained to sum to 1.0 (SADI and FLAT restrains have been applied). Ordered non-hydrogen atoms were refined anisotropically whereas disordered non-hydrogen atoms with partial occupancy were refined isotropically. Hydrogen atoms connected to carbon atoms were included in idealised positions and a riding model was used for their refinement. DFIX and DANG instructions have been applied to better model the water molecule H atoms. The final difference Fourier map revealed the presence of non-negligible residual peaks. They could likely be assigned to four ethanol molecule but they could not be effectively modelled. The contribution of these peaks was removed using the mask routine of OLEX2. The program calculated a total solvent accessible volume/cell of 2207.6 $Å^3$ (39 %), and a total electron-count/cell of 107 electrons. Such values closely fit four ethanol molecules.

Table 8. Crystal data and structure refinement for $\{[(PTAO)_2@[Cu_8][Cu_2]\}_\infty$

Crystallization solvent	Chloroform/ethanol
Empirical formula	$C_{86}H_{94}Cu_5N_3O_{22}P$
Formula weight	1870.31
Temperature/K	295.9(7)
Crystal system	Triclinic
Space group	P-1
a/Å	17.0466(7)
b/Å	18.6805(7)
c/Å	21.1943(5)
α/°	72.532(3)
β/°	66.428(3)
γ/°	68.592(4)
Volume/$Å^3$	5664.3(3)
Z	2
$\rho_{calc}g/cm^3$	1.272
μ/mm^{-1}	1.747
Radiation	MoKα (λ = 0.71073)

Reflections collected	37372
Independent reflections	18165
Goodness-of-fit on F^2	0.994
Final R indexes [I>=2σ (I)]	R_1 = 0.0528, wR_2 = 0.1510
Final R indexes [all data]	R_1 = 0.0703, wR_2 = 0.1619
Largest diff. peak/hole / e Å^{-3}	0.34/-0.36
CCDC number	1013528

$R_1 = (\Sigma \, ||F_o| - |F_c||/\Sigma \, |F_o|)$; $wR_2 = \{\Sigma[w(F_o^2 - F_c^2)^2]/ \Sigma[w(F_o^2)^2]\}^{1/2}$; GOF = $\Sigma[w(F_o^2 - F_c^2)^2]/(n - p)\}^{1/2}$ where n is the number of data and p is the number of parameters refined.

Table 9. Lengths comparison for the two compounds hosting PTAO.

	{PTAO@[Cu(*o*–L)]$_3$}	**{[(PTAO)$_2$@[Cu$_8$][Cu$_2$]}$_\infty$**
Cu-O min. and max. lengths (Å)	1.908(3) – 1.934(3) [3]	1.901(3) – 1.924(3)
Cu-N min. and max. lengths (Å)	2.474(3) [3]	2.386(3) – 2.499(3)
P=O length (Å)	1.486(5) [3]	1.486(3)

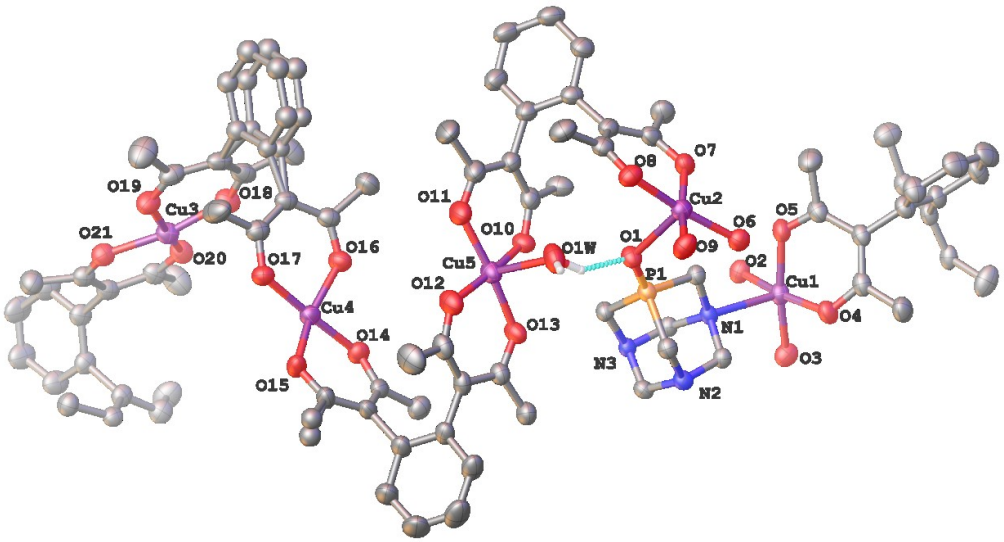

Figure 119. Asymmetric unit in the {[(PTAO)$_2$@[Cu$_8$][Cu$_2$]}$_\infty$ single crystal. Thermal ellipsoids drawn at the 30% probability level. Disordered parts are drawn as isotropic ball and stick. H atoms are omitted for clarity. H bond: O1···H 2.06 Å, O1···O1W 2.816(4) Å, O1···H···O1w 142°.

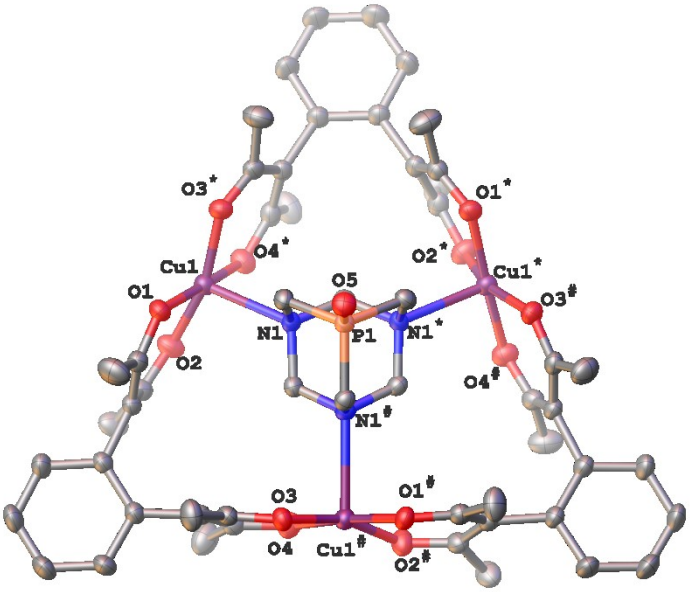

Figure 120. Structure of {PTAO@[Cu(*o*-L)]$_3$} (CCDC 971598)[3] with thermal ellipsoids drawn at the 30% probability level. Symmetry operations: * (*1+y –x, 1–x, +z*), # (*1–y, +x –y, +z*). H atoms are omitted for clarity.

Table 10. Lengths comparison in the {Cu_2} subunit and the [Cu(*o*–L)]$_2$ dimer.

	{Cu_2} subunit	**[Cu(*o*–L)]$_2$**
Cu-O min. and max. lengths (Å)	1.906(3) – 1.922(3)	1.861(10) – 1.883(9)
Cu···Cu	4.968	4.551

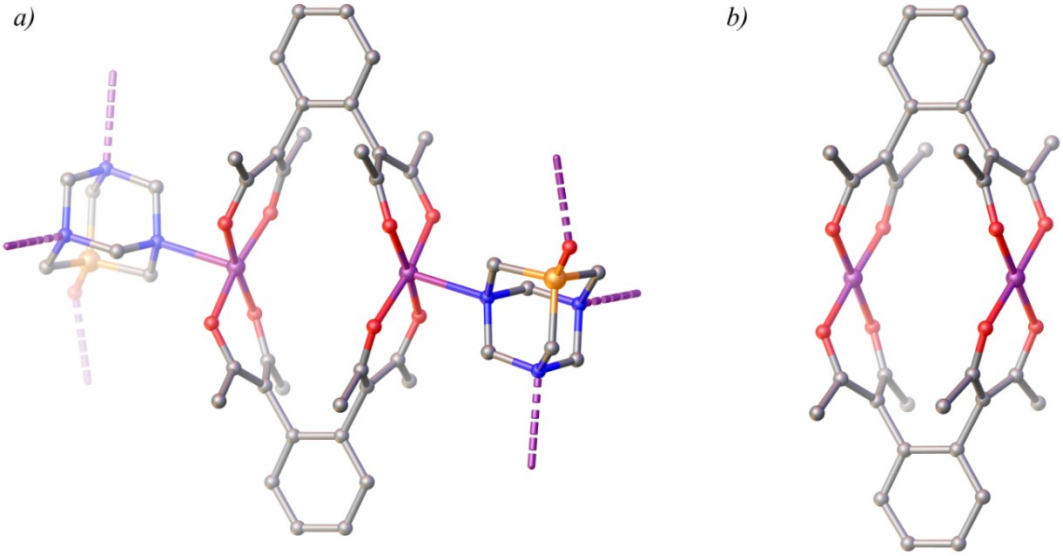

Figure 121. *a*) {Cu_2} subunit in {[(PTAO)$_2$@[Cu_8][Cu_2]}$_\infty$ and *b*) [Cu(*o*–L)]$_2$ dimer crystallized from a chloroform/acetone mixture. H atoms are omitted for clarity.

6.3.2 Me-Tr-1 determination and refinement details.

Despite several efforts to improve the crystals quality, the only useful specimens were not significantly diffracting at d < 0.95 Å. Cu radiation has been used and the data collection has been set to obtain a full completeness at d = 0.99 Å. Structure was solved by means of direct methods with ShelXS[4] program and refined by full–matrix least–squares methods based on F_o^2 with SHELXL[4] in the framework of OLEX2[6] software. The final difference Fourier map revealed the presence of non-negligible residual peaks. The contribution of these peaks was removed using the mask routine of OLEX2[6]. The program calculated a total solvent accessible volume/cell of 2366.2 Å^3 (20.4 %), and a total electron-count/cell of 722.7 electrons, likely due to the presence of twelve chloroform molecules and four water molecules.

Table 11. Crystal data and structure refinement for {Me-Tr@[Cu(*o*-L)]$_3$}, crystal Me-Tr-**1**.

Crystallization solvent	Chloroform/acetonitrile
Empirical formula	$C_{52}H_{59}Cu_3N_3O_{12}$
Formula weight	1108.64
Temperature/K	298.4(7)
Crystal system	Monoclinic
Space group	C2/c
a/Å	48.6203(9)
b/Å	7.66368(16)
c/Å	31.0847(6)
α/°	90
β/°	91.3324(18)
γ/°	90
Volume/Å^3	11579.3(4)
Z	8
ρ_{calc}g/cm^3	1.272
μ/mm^{-1}	1.747
Radiation	CuKα (λ = 1.54184)
2Θ range for data collection/°	5.688 to 102.802
Reflections collected	6271
Independent reflections	6271 [R_{sigma} = 0.0318]
Data/restraints/parameters	6271/0/644
Goodness-of-fit on F^2	1.084
Final R indexes [I>=2σ (I)]	R_1 = 0.0459, wR_2 = 0.1267
Final R indexes [all data]	R_1 = 0.0525, wR_2 = 0.1316
Largest diff. peak/hole / e Å^{-3}	0.34/-0.36

$R_1 = (\Sigma\ ||F_o| - |F_c||/\Sigma\ |F_o|)$; $wR_2 = \{\Sigma[w(F_o^2 - F_c^2)^2]/\ \Sigma[w(F_o^2)^2]\}^{1/2}$; GOF = $\Sigma[w(F_o^2 - F_c^2)^2]/(n - p)\}^{1/2}$ where n is the number of data and p is the number of parameters refined.

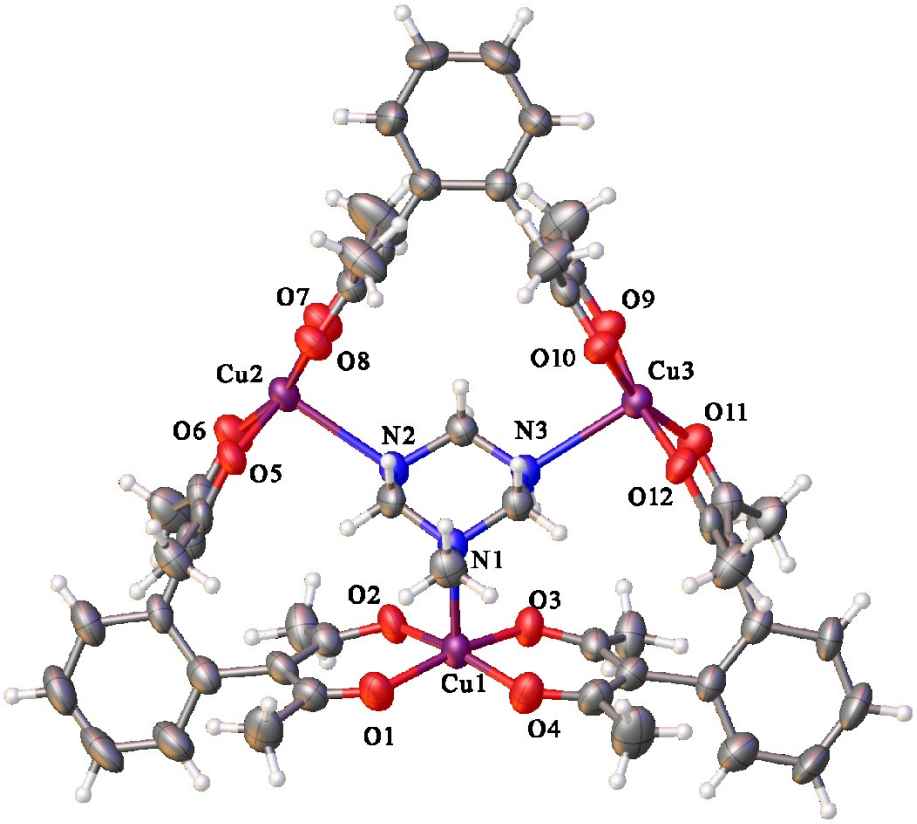

Figure 122. Asymmetric unit for {Me-Tr@[Cu(*o*-L)]$_3$}, crystal 1, with thermal ellipsoid drawn at the 50% level. Colour code: Cu purple, N blue, O red, C grey, H white.

Table 12. Selected bond distances in Me-Tr-1.

Atom	Atom	Length/Å	Atom	Atom	Length/Å
Cu1	O1	1.935(3)	Cu2	O8	1.914(3)
Cu1	O2	1.913(3)	Cu2	N2	2.478(3)
Cu1	O3	1.915(3)	Cu3	O9	1.909(3)
Cu1	O4	1.925(3)	Cu3	O10	1.925(3)
Cu1	N1	2.345(4)	Cu3	O11	1.921(3)
Cu2	O5	1.928(3)	Cu3	O12	1.925(3)
Cu2	O6	1.931(3)	Cu3	N3	2.471(3)
Cu2	O7	1.903(3)			

Table 13. Selected angles in Me-Tr-**1**.

Atom	Atom	Atom	Angle/°	Atom	Atom	Atom	Angle/°
O10	Cu3	N3	93.62(13)	O6	Cu2	N2	101.47(14)
O12	Cu3	O10	88.22(13)	O7	Cu2	O8	90.94(14)
O12	Cu3	N3	95.68(12)	O7	Cu2	N2	95.31(13)
O11	Cu3	O10	165.22(14)	O7	Cu2	O5	170.30(14)
O11	Cu3	O12	88.90(13)	O7	Cu2	O6	89.57(14)

O11	Cu3	N3	101.09(14)	O4	Cu1	O1	94.00(14)
O9	Cu3	O10	90.42(14)	O4	Cu1	N1	92.13(14)
O9	Cu3	O12	170.23(14)	O1	Cu1	N1	92.49(14)
O9	Cu3	N3	94.06(13)	O3	Cu1	O4	90.10(13)
O9	Cu3	O11	89.96(14)	O3	Cu1	O1	165.77(15)
O8	Cu2	N2	92.55(13)	O3	Cu1	N1	100.98(13)
O8	Cu2	O5	87.85(13)	O2	Cu1	O4	167.32(15)
O8	Cu2	O6	165.86(14)	O2	Cu1	O1	89.30(13)
O5	Cu2	N2	94.36(12)	O2	Cu1	N1	99.97(13)
O5	Cu2	O6	89.27(13)	O2	Cu1	O3	83.92(13)

6.3.3 Me-Tr-2 determination and refinement details.

Mo Kα radiation has been used and the data collection has been set to obtain a full completeness at d = 0.85 Å. Structure was solved by means of intrinsic phasing with ShelXT[5] program and refined by full–matrix least–squares methods based on F_o^2 with SHELXL[4] in the framework of OLEX2[6] software. The final difference Fourier map revealed the presence of non-negligible residual peaks. The contribution of these peaks was removed using the mask routine of OLEX2[6]. The program calculated a total solvent accessible volume/cell of 2127.2 $Å^3$ (32.8 %), and a total electron-count/cell of 218.9 electrons, likely due to the presence of four dichloromethane molecules.

Table 14. Crystal data and structure refinement for Me-Tr-**2.**

Crystallization solvent	Dichloromethane/acetonitrile
Empirical formula	$C_{52}H_{59}Cu_3N_3O_{12}$
Formula weight	1108.64
Temperature/K	302.1(6)
Crystal system	monoclinic
Space group	$P2_1/n$
a/Å	12.4687(7)
b/Å	18.9175(9)
c/Å	27.4821(13)
α/°	90
β/°	90.951(4)
γ/°	90
Volume/$Å^3$	6481.5(6)
Z	4
$\rho_{calc}g/cm^3$	1.136
μ/mm^{-1}	1.026
Radiation	MoKα (λ = 0.71073)
2Θ range for data collection/°	4.876 to 49.32

Reflections collected	35585
Independent reflections	10978 [R_{int} = 0.0307, R_{sigma} = 0.0305]
Data/restraints/parameters	10978/0/644
Goodness-of-fit on F^2	1.047
Final R indexes [I>=2σ (I)]	R_1 = 0.0399, wR_2 = 0.1065
Final R indexes [all data]	R_1 = 0.0481, wR_2 = 0.1106
Largest diff. peak/hole / e $Å^{-3}$	0.58/-0.46

$R_1 = (\Sigma \, ||F_o| - |F_c||/\Sigma \, |F_o|)$; $wR_2 = \{\Sigma[w(F_o^2 - F_c^2)^2]/ \Sigma[w(F_o^2)^2]\}^{1/2}$; GOF = $\Sigma[w(F_o^2 - F_c^2)^2]/(n - p)\}^{1/2}$
where n is the number of data and p is the number of parameters refined.

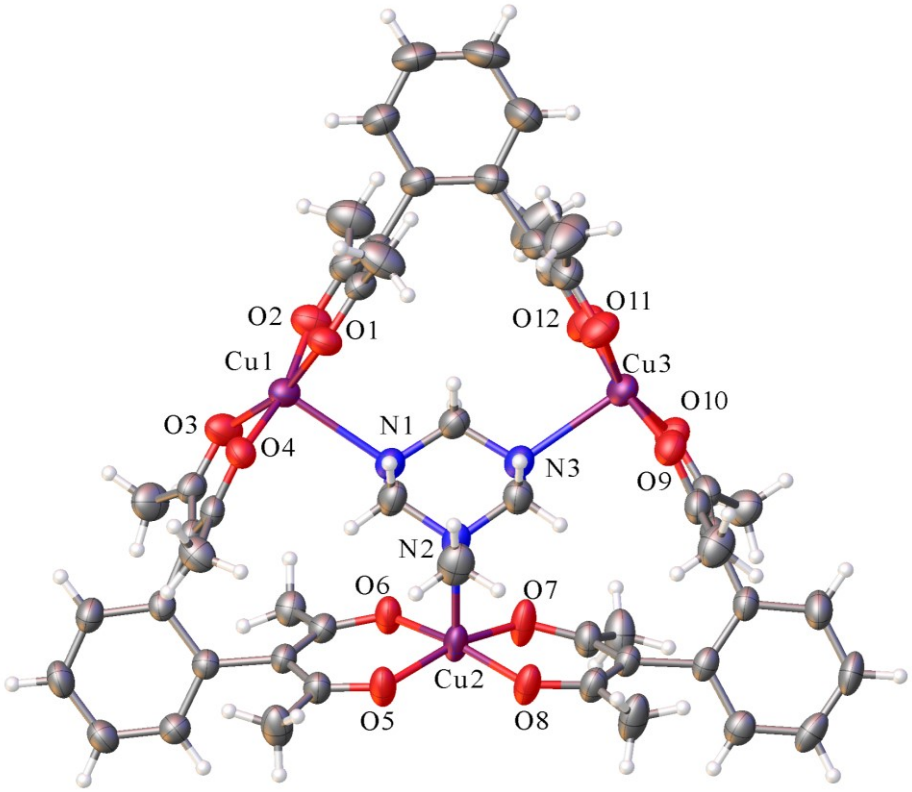

Figure 123. Asymmetric unit for {Me-Tr@[Cu(*o*-L)]$_3$}, crystal 2, with thermal ellipsoid drawn at the 50% level. Colour code: Cu purple, N blue, O red, C grey, H white.

Table 15. Selected bond distances in Me-Tr-**2**.

Atom	Atom	Length/Å	Atom	Atom	Length/Å
Cu1	O4	1.9189(18)	Cu2	O7	1.9095(19)
Cu1	O1	1.9141(18)	Cu2	N2	2.394(2)
Cu1	O3	1.9285(19)	Cu3	O9	1.913(2)
Cu1	O2	1.907(2)	Cu3	O10	1.9363(19)
Cu1	N1	2.446(2)	Cu3	O11	1.924(2)
Cu2	O6	1.9155(19)	Cu3	O12	1.907(2)
Cu2	O5	1.9270(18)	Cu3	N3	2.409(2)
Cu2	O8	1.9202(19)			

Table 16. Selected angles in Me-Tr-**2**.

Atom	Atom	Atom	Angle/°	Atom	Atom	Atom	Angle/°
O4	Cu1	O3	89.27(8)	O8	Cu2	N2	91.65(9)
O4	Cu1	N1	93.09(8)	O7	Cu2	O6	84.81(8)
O1	Cu1	O4	88.97(8)	O7	Cu2	O5	162.86(10)
O1	Cu1	O3	165.61(9)	O7	Cu2	O8	90.41(8)
O1	Cu1	N1	90.17(8)	O7	Cu2	N2	103.28(9)
O3	Cu1	N1	104.18(9)	O9	Cu3	O10	89.91(8)
O2	Cu1	O4	168.49(9)	O9	Cu3	O11	87.44(9)
O2	Cu1	O1	90.25(8)	O9	Cu3	N3	93.73(8)
O2	Cu1	O3	88.64(9)	O10	Cu3	N3	97.66(8)
O2	Cu1	N1	98.39(9)	O11	Cu3	O10	162.12(9)
O6	Cu2	O5	90.18(8)	O11	Cu3	N3	100.15(9)
O6	Cu2	O8	169.13(10)	O12	Cu3	O9	171.59(9)
O6	Cu2	N2	98.94(8)	O12	Cu3	O10	89.65(9)
O5	Cu2	N2	93.68(8)	O12	Cu3	O11	90.40(9)
O8	Cu2	O5	91.59(8)	O12	Cu3	N3	94.65(9)

6.3.4 Me-Tr-3 determination and refinement details.

Despite several efforts to improve the crystals quality, the only useful specimens were not significantly diffracting at d < 0.85 Å. The data collection has been set to obtain a full completeness at d = 0.90 Å. Mo Kα radiation has been used. Structure was solved by means of intrinsic phasing with ShelXT[5] program and refined by full–matrix least–squares methods based on F_o^2 with SHELXL[4] in the framework of OLEX2[6] software. RIGU restraint has been used to better model two MeCN solvent molecules. The final difference Fourier map revealed the presence of non-negligible residual peaks. The contribution of these peaks was removed using the mask routine of OLEX2[6]. The program calculated a total solvent accessible volume/cell of 574.9 $Å^3$ (18.6 %), and a total electron-count/cell of 100.5 electrons, likely due to the presence of two dichloromethane molecules and two water molecules.

Table 17. Crystal data and structure refinement for Me-Tr-**3**.

Crystallization solvent	Dichloromethane/acetonitrile
Empirical formula	$C_{56}H_{65}Cu_3N_5O_{12}$
Formula weight	1190.75
Temperature/K	302.3(6)
Crystal system	triclinic

Space group	P-1
a/Å	9.0233(6)
b/Å	15.1880(9)
c/Å	23.6457(16)
α/°	94.324(5)
β/°	94.637(6)
γ/°	105.943(6)
Volume/Å^3	3089.6(4)
Z	2
ρ_{calc}g/cm^3	1.28
μ/mm^{-1}	1.082
Radiation	MoKα (λ = 0.71073)
2Θ range for data collection/°	4.682 to 46.512
Index ranges	-10 ≤ h ≤ 10, -16 ≤ k ≤ 16, -26 ≤ l ≤ 25
Reflections collected	26721
Independent reflections	8843 [R_{int} = 0.1426, R_{sigma} = 0.1287]
Data/restraints/parameters	8843/18/676
Goodness-of-fit on F^2	1.019
Final R indexes [I>=2σ (I)]	R_1 = 0.0746, wR_2 = 0.1947
Final R indexes [all data]	R_1 = 0.1081, wR_2 = 0.2109
Largest diff. peak/hole / e Å^{-3}	0.92/-0.65

$R_1 = (\Sigma\ ||F_o| - |F_c||/\Sigma\ |F_o|)$; $wR_2 = \{\Sigma[w(F_o^2 - F_c^2)^2]/\ \Sigma[w(F_o^2)^2]\}^{1/2}$; GOF = $\Sigma[w(F_o^2 - F_c^2)^2]/(n - p)\}^{1/2}$
where *n* is the number of data and *p* is the number of parameters refined.

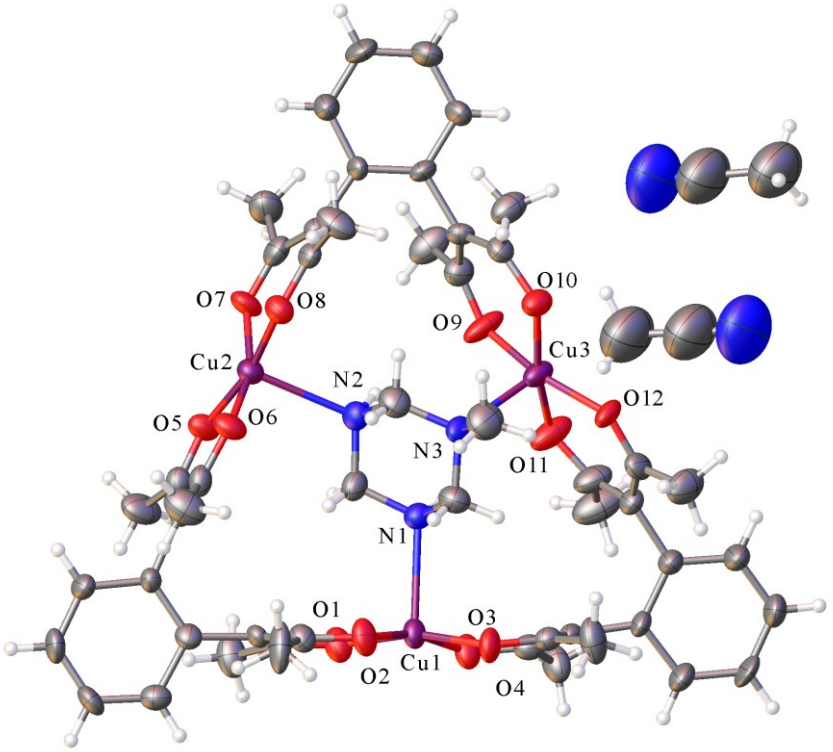

Figure 124. Asymmetric unit for Me-Tr-**3**, with thermal ellipsoid drawn at the 50% level. Colour code: Cu purple, N blue, O red, C grey, H white.

Table 18. Selected bond distances in Me-Tr-**3**.

Atom	Atom	Length/Å	Atom	Atom	Length/Å
Cu1	O1	1.911(5)	Cu2	O5	1.919(4)
Cu1	O4	1.941(5)	Cu2	N2	2.410(6)
Cu1	O3	1.924(5)	Cu3	O10	1.909(4)
Cu1	O2	1.899(5)	Cu3	O12	1.935(5)
Cu1	N1	2.431(5)	Cu3	O9	1.923(5)
Cu2	O8	1.928(4)	Cu3	N3	2.433(6)
Cu2	O6	1.910(5)	Cu3	O11	1.892(5)
Cu2	O7	1.927(5)			

Table 19. Selected angles in Me-Tr-**3**.

Atom	Atom	Atom	Angle/°	Atom	Atom	Atom	Angle/°
O1	Cu1	O4	165.67(19)	O7	Cu2	N2	101.0(2)
O1	Cu1	O3	90.6(2)	O5	Cu2	O8	167.9(2)
O1	Cu1	N1	97.4(2)	O5	Cu2	O6	90.29(19)
O4	Cu1	N1	96.84(19)	O5	Cu2	O7	89.5(2)
O3	Cu1	O4	88.7(2)	O5	Cu2	N2	96.2(2)
O3	Cu1	N1	98.7(2)	O10	Cu3	O12	90.7(2)
O2	Cu1	O1	90.4(2)	O10	Cu3	O9	90.4(2)
O2	Cu1	O4	87.0(2)	O10	Cu3	N3	89.72(19)
O2	Cu1	O3	166.2(2)	O12	Cu3	O9	167.5(2)
O2	Cu1	N1	94.8(2)	O12	Cu3	N3	90.7(2)
O8	Cu2	N2	95.7(2)	O9	Cu3	N3	101.8(2)
O6	Cu2	O8	86.56(19)	O11	Cu3	O10	168.0(2)
O6	Cu2	N2	96.9(2)	O11	Cu3	O12	89.8(2)
O7	Cu2	O8	89.9(2)	O11	Cu3	O9	86.5(2)
O7	Cu2	O6	162.0(2)	O11	Cu3	N3	102.3(2)

6.3.5 Ligand 1, DPM-CF_3 determination and refinement details.

Cu Kα radiation has been used and the data collection has been set to obtain a full completeness at d = 0.9Å. Structure was solved by means of intrinsic phasing with ShelXT[5] program and refined by full–matrix least–squares methods based on F_o^2 with SHELXL[4] in the framework of OLEX2[6] software. SADI, RIGU and EADP restraints have been applied in order to better model a disorder CF_3 moiety.

Table 20. Crystal data and structure refinement for Ligand **1**.

Crystallization solvent	Dichloromethane/Toluene + TPPO
Empirical formula	$C_{21}H_{14}F_6O_4$
Formula weight	444.32
Temperature/K	298.8(6)
Crystal system	monoclinic
Space group	$P2_1/c$
a/Å	18.7105(9)
b/Å	12.3543(5)
c/Å	8.5986(3)
α/°	90
β/°	90.627(4)
γ/°	90
Volume/Å^3	1987.49(14)
Z	4
ρ_{calc}g/cm^3	1.485
μ/mm^{-1}	1.228
Radiation	Cu Kα (λ = 1.54184)
2Θ range for data collection/°	4.724 to 122.946
Index ranges	$-20 \leq h \leq 21$, $-13 \leq k \leq 12$, $-7 \leq l \leq 9$
Reflections collected	5988
Independent reflections	3026 [R_{int} = 0.0143, R_{sigma} = 0.0147]
Data/restraints/parameters	3026/294/304
Goodness-of-fit on F^2	1.073
Final R indexes [I>=2σ (I)]	R_1 = 0.0880, wR_2 = 0.2954
Final R indexes [all data]	R_1 = 0.1044, wR_2 = 0.3205
Largest diff. peak/hole / e Å^{-3}	0.42/-0.20

$R_1 = (\Sigma\ ||F_o| - |F_c||/\Sigma\ |F_o|)$; $wR_2 = \{\Sigma[w(F_o^2 - F_c^2)^2]/\ \Sigma[w(F_o^2)^2]\}^{1/2}$; $GOF = \Sigma[w(F_o^2 - F_c^2)^2]/(n - p)\}^{1/2}$
where n is the number of data and p is the number of parameters refined.

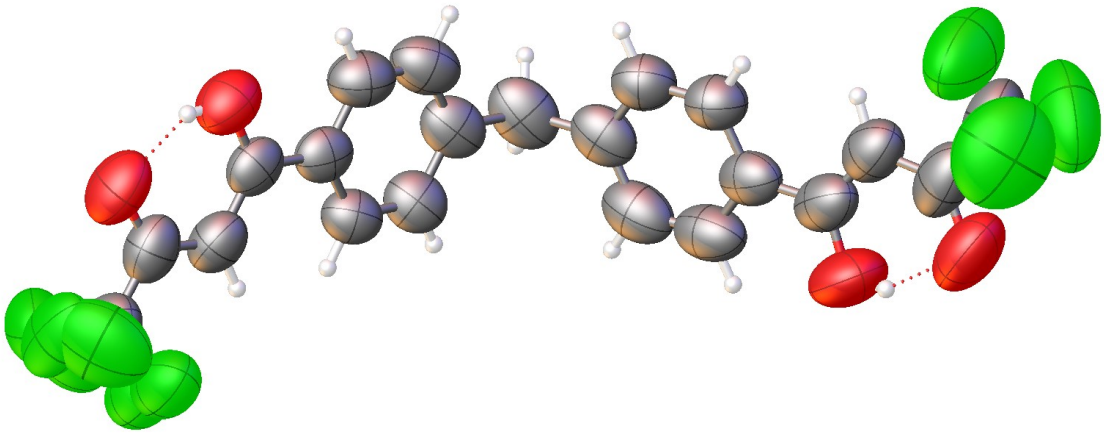

Figure 125. Asymmetric unit for ligand **1**, with thermal ellipsoid drawn at the 50% level. Colour code: F green, O red, C grey, H white.

6.3.6 Ligand 2, DPM-Ph determination and refinement details.

Cu Kα radiation has been used and the data collection has been set to obtain a full completeness at d = 0.9 Å. Structure was solved by means of intrinsic phasing with ShelXT[5] program and refined by full–matrix least–squares methods based on F_o^2 with SHELXL[4] in the framework of OLEX2[6] software. RIGU, DELU and SIMU restraints have been applied to the whole moleucule in order to obtain a better structural model.

Table 21. Crystal data and structure refinement for Ligand **2**.

Crystallization solvent	Dichloromethane/Toluene + TPPO
Empirical formula	$C_{62}H_{48}O_8$
Formula weight	921
Temperature/K	298.6(7)
Crystal system	triclinic
Space group	P1
a/Å	5.2576(11)
b/Å	11.7412(6)
c/Å	19.2637(8)
α/°	81.813(5)
β/°	89.783(17)
γ/°	90.017(11)
Volume/Å^3	1177.0(3)
Z	1
ρ_{calc}g/cm^3	1.299
μ/mm^{-1}	0.683
Radiation	Cu Kα (λ = 1.54184)
2Θ range for data collection/°	4.634 to 120.378
Index ranges	-5 ≤ h ≤ 5, -13 ≤ k ≤ 13, -21 ≤ l ≤ 21
Reflections collected	8582
Independent reflections	4850 [R_{int} = 0.0741, R_{sigma} = 0.0395]
Data/restraints/parameters	4850/1171/635
Goodness-of-fit on F^2	1.514
Final R indexes [I>=2σ (I)]	R_1 = 0.0755, wR_2 = 0.2622
Final R indexes [all data]	R_1 = 0.0976, wR_2 = 0.3278
Largest diff. peak/hole / e Å^{-3}	0.30/-0.34
Flack parameter	0.6(5)

$R_1 = (\Sigma \, ||F_o| - |F_c||/\Sigma \, |F_o|)$; $wR_2 = \{\Sigma[w(F_o^2 - F_c^2)^2]/ \Sigma[w(F_o^2)^2]\}^{1/2}$; GOF = $\Sigma[w(F_o^2 - F_c^2)^2]/(n - p)\}^{1/2}$
where *n* is the number of data and *p* is the number of parameters refined.

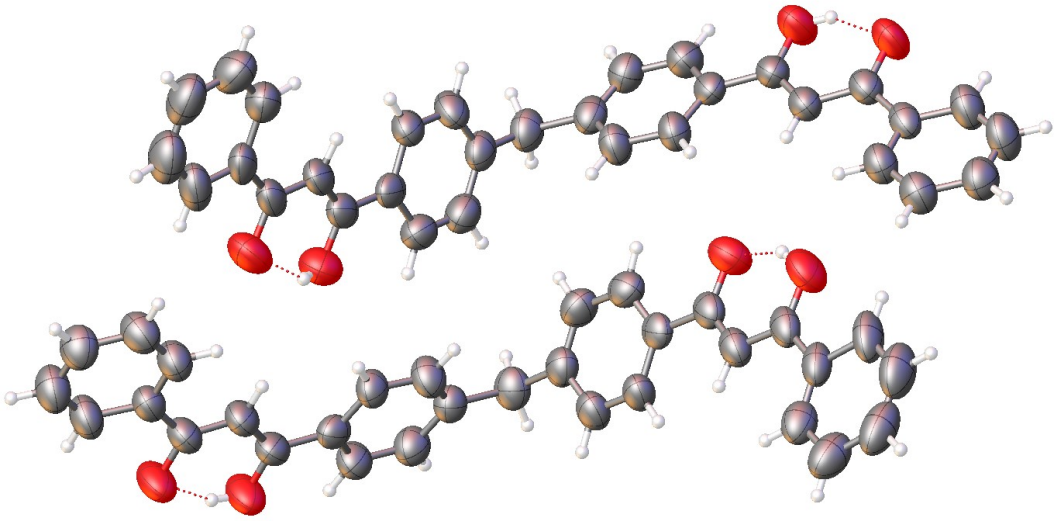

Figure 126. Asymmetric unit for ligand **2**, with thermal ellipsoid drawn at the 50% level. Colour code: O red, C grey, H white.

6.3.7 Ligand 7, TPA-CF_3 determination and refinement details.

Mo Kα radiation has been used and the data collection has been set to obtain a full completeness at d = 1.00Å. Structure was solved by means of intrinsic phasing with ShelXT[5] program and refined by full–matrix least–squares methods based on F_o^2 with SHELXL[4] in the framework of OLEX2[6] software. In the last cycles of refinement, ordered non-hydrogen atoms were refined anisotropically whereas disordered partial occupancy non-hydrogen atoms were refined isotropically. SADI, DELU and SIMU restraints have been applied in order to better model a disorder CF_3 moiety.

Table 22. Crystal data and structure refinement for Ligand **7**.

Crystallization solvent	Dichloromethane/Toluene
Empirical formula	$C_{30}H_{18}F_9NO_6$
Formula weight	659.45
Temperature/K	305(3)
Crystal system	triclinic
Space group	P-1
a/Å	9.8110(5)
b/Å	12.0324(8)
c/Å	13.0566(7)
α/°	86.567(5)
β/°	78.739(5)
γ/°	75.593(5)
Volume/Å^3	1464.03(15)
Z	2

ρ_{calc}g/cm^3	1.496
μ/mm^{-1}	0.141
Radiation	Mo Kα (λ = 0.71073)
2Θ range for data collection/°	4.364 to 41.54
Index ranges	-9 ≤ h ≤ 9, -11 ≤ k ≤ 11, -13 ≤ l ≤ 11
Reflections collected	7555
Independent reflections	3015 [R_{int} = 0.0157, R_{sigma} = 0.0187]
Data/restraints/parameters	3015/23/415
Goodness-of-fit on F^2	1.052
Final R indexes [I>=2σ (I)]	R_1 = 0.0970, wR_2 = 0.2753
Final R indexes [all data]	R_1 = 0.1054, wR_2 = 0.2852
Largest diff. peak/hole / e Å^{-3}	1.03/-0.62

$R_1 = (\Sigma\ ||F_o| - |F_c||/\Sigma\ |F_o|)$; $wR_2 = \{\Sigma[w(F_o^2 - F_c^2)^2]/\ \Sigma[w(F_o^2)^2]\}^{1/2}$; GOF = $\Sigma[w(F_o^2 - F_c^2)^2]/(n - p)\}^{1/2}$
where n is the number of data and p is the number of parameters refined.

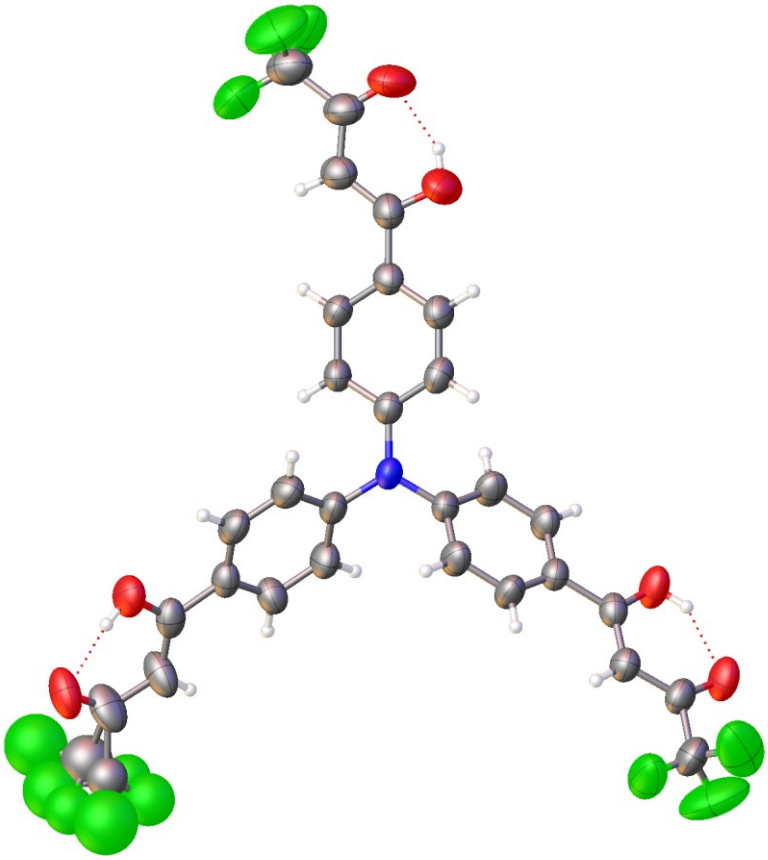

Figure 127. Asymmetric unit for ligand **7**, with thermal ellipsoid drawn at the 50% level. Colour code: N blue, O red, C grey, H white.

6.3.8 Fe5: [Fe(TPM-CF_3)]$_4$·2$CHCl_3$ determination and refinement details.

For **Fe5**, synchrotron radiation at wavelength 0.7 Å has been used as X-ray source. Due to crystal quality, the sample was not significantly diffracting at d < 0.8 Å. Data obtained al lower d values have been discarded, resulting in a completeness of 92.2% for d = 0.8

Å. Structure was solved by means of intrinsic phasing with ShelXT[5] program and refined by full–matrix least–squares methods based on F_o^2 with SHELXL[4] in the framework of OLEX2[6] software. Rigid body (RIGU) restrains have been applied to the entire molecules in order to obtain a better model. The final difference Fourier map revealed the presence of non-negligible residual peaks. The contribution of these peaks was removed using the mask routine of OLEX2[6]. The program calculated a total solvent accessible volume/cell of 1898.5 $Å^3$ (25.3 %), and a total electron-count/cell of 262.6 electrons, likely due to the presence of 4.5 chloroform molecules per unit cell.

Table 23. Crystal data and structure refinement for **Fe5**·2$CHCl_3$.

Crystallization solvent	$CHCl_3$/MeOH
Empirical formula	$C_{126}H_{66}Cl_6F_{36}Fe_4O_{24}$
Formula weight	3083.88
Temperature/K	293(2)
Crystal system	triclinic
Space group	P-1
a/Å	16.9062(3)
b/Å	18.8021(3)
c/Å	26.5239(4)
α/°	98.6180(10)
β/°	95.0720(10)
γ/°	113.876(2)
Volume/$Å^3$	7518.3(2)
Z	2
$\rho_{calc}g/cm^3$	1.362
μ/mm^{-1}	0.571
F(000)	3088.0
Crystal size/mm^3	0.01 × 0.01 × 0.005
Radiation	Synchrotron (λ = 0.700)
2Θ range for data collection/°	3.102 to 51.886
Reflections collected	55068
Independent reflections	28337 [R_{int} = 0.0394, R_{sigma} = 0.0576]
Data/restraints/parameters	28337/3696/1765
Goodness-of-fit on F^2	1.221
Final R indexes [I>=2σ (I)]	R_1 = 0.1051, wR_2 = 0.3193
Final R indexes [all data]	R_1 = 0.1389, wR_2 = 0.3501
Largest diff. peak/hole / e $Å^{-3}$	1.33/-0.97

$R_1 = (\Sigma\ ||F_o| - |F_c||/\Sigma\ |F_o|)$; $wR_2 = \{\Sigma[w(F_o^2 - F_c^2)^2]/\ \Sigma[w(F_o^2)^2]\}^{1/2}$; $GOF = \Sigma[w(F_o^2 - F_c^2)^2]/(n - p)\}^{1/2}$
where *n* is the number of data and *p* is the number of parameters refined.

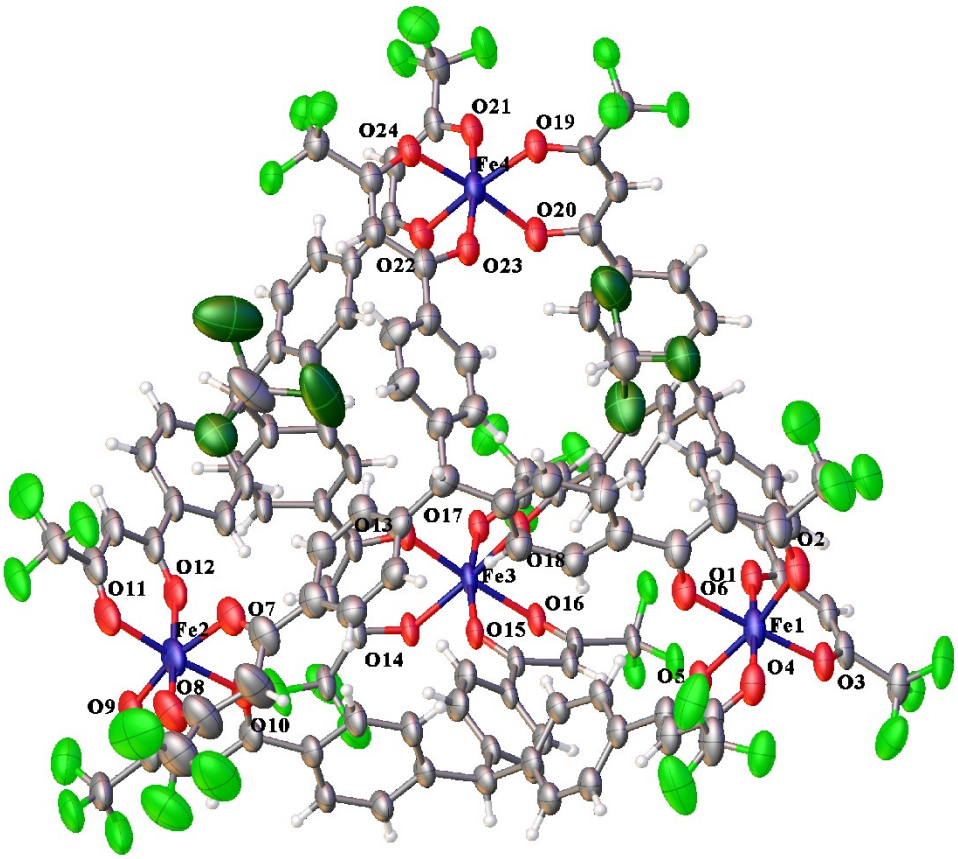

Figure 128. Asymmetric unit of **Fe5**·2CHCl$_3$ with thermal ellipsoids drawn at the 30% probability level. Colour code: Fe blue, O red, F light green, Cl dark green, C grey, H white.

Table 24. Selected bond distances in **Fe5**·2CHCl$_3$.

Atom	Atom	Length/Å	Atom	Atom	Length/Å
Fe1	O1	1.989(5)	Fe3	O18	2.010(3)
Fe1	O2	2.007(5)	Fe3	O16	1.988(3)
Fe1	O3	1.968(4)	Fe3	O15	2.024(4)
Fe1	O4	1.977(5)	Fe3	O14	1.979(3)
Fe1	O5	1.998(4)	Fe3	O17	1.977(4)
Fe1	O6	2.003(4)	Fe3	O13	1.983(3)
Fe2	O10	2.019(4)	Fe4	O22	2.011(4)
Fe2	O12	1.995(6)	Fe4	O23	1.983(4)
Fe2	O9	1.955(5)	Fe4	O24	2.000(4)
Fe2	O11	2.002(5)	Fe4	O21	1.935(4)
Fe2	O7	1.994(6)	Fe4	O19	1.967(4)
Fe2	O8	1.925(7)	Fe4	O20	1.992(4)

Table 25. Selected angles in **Fe5**·2$CHCl_3$.

Atom	Atom	Atom	Angle/°	Atom	Atom	Atom	Angle/°
O5	Fe1	O6	84.62(17)	O18	Fe3	O15	86.58(14)
O5	Fe1	O2	170.2(2)	O16	Fe3	O18	90.03(14)
O1	Fe1	O5	87.04(17)	O16	Fe3	O15	85.69(14)
O1	Fe1	O6	90.41(18)	O14	Fe3	O18	169.57(13)
O1	Fe1	O2	91.3(2)	O14	Fe3	O16	98.07(14)
O3	Fe1	O5	95.79(17)	O14	Fe3	O15	87.49(15)
O3	Fe1	O1	87.03(17)	O14	Fe3	O13	86.39(14)
O3	Fe1	O6	177.4(2)	O17	Fe3	O18	87.24(15)
O3	Fe1	O4	92.59(19)	O17	Fe3	O16	86.22(15)
O3	Fe1	O2	93.77(19)	O17	Fe3	O15	169.81(13)
O6	Fe1	O2	85.7(2)	O17	Fe3	O14	99.79(15)
O4	Fe1	O5	87.11(19)	O17	Fe3	O13	94.12(16)
O4	Fe1	O1	174.06(19)	O13	Fe3	O18	85.41(14)
O4	Fe1	O6	90.02(19)	O13	Fe3	O16	175.40(13)
O4	Fe1	O2	94.7(2)	O13	Fe3	O15	93.44(15)
O12	Fe2	O10	90.78(18)	O23	Fe4	O22	87.59(17)
O12	Fe2	O11	84.8(2)	O23	Fe4	O24	86.14(17)
O9	Fe2	O10	86.26(19)	O23	Fe4	O20	87.97(18)
O9	Fe2	O12	96.0(2)	O24	Fe4	O22	91.00(17)
O9	Fe2	O11	97.6(2)	O21	Fe4	O22	86.83(17)
O9	Fe2	O7	167.7(2)	O21	Fe4	O23	172.88(16)
O11	Fe2	O10	174.4(2)	O21	Fe4	O24	89.54(18)
O7	Fe2	O10	82.5(2)	O21	Fe4	O19	90.35(17)
O7	Fe2	O12	89.4(2)	O21	Fe4	O20	95.97(19)
O7	Fe2	O11	93.9(2)	O19	Fe4	O22	171.26(17)
O8	Fe2	O10	94.6(3)	O19	Fe4	O23	95.81(17)
O8	Fe2	O12	172.1(3)	O19	Fe4	O24	97.25(16)
O8	Fe2	O9	90.1(3)	O19	Fe4	O20	86.76(16)
O8	Fe2	O11	89.4(3)	O20	Fe4	O22	85.32(17)
O8	Fe2	O7	85.7(3)	O20	Fe4	O24	173.18(19)

6.3.9 Fe7: [Fe(TPM-tBu)]$_4$·3$CHCl_3$ determination and refinement details.

For **Fe7**, synchrotron radiation at wavelength 0.7 Å has been used as X-ray source. Due to crystal quality, the sample was not significantly diffracting at d < 0.8 Å. Data obtained al lower d values have been discarded, resulting in a completeness of 100% for d = 0.8 Å. Structure was solved by means of intrinsic phasing with ShelXT[5] program and refined

by full–matrix least–squares methods based on F_o^2 with SHELXL[4] in the framework of OLEX2[6] software. During the refinement, a chloroform molecule has been splitted in two parts the occupancies of which were constrained to sum to 1.0 (SADI and EADP restrains have been applied). SADI restrains has been applied to three of the *tert*-butyl groups to obtain a better model. Rigid body (RIGU) restrains have been applied to the entire molecules in order to obtain a better model. The final difference Fourier map revealed the presence of non-negligible residual peaks. The contribution of these peaks was removed using the mask routine of OLEX2[6]. The program calculated a total solvent accessible volume/cell of 3498.2 Å^3 (19.0 %), and a total electron-count/cell of 955.1 electrons, likely due to the presence of 18 chloroform molecules per unit cell.

Table 26. Crystal data and structure refinement for **Fe7**·3$CHCl_3$.

Crystallization solvent	$CHCl_3$/iPrOH
Empirical formula	$C_{55}H_{57}O_8Cl_5Fe_{1.3}$
Formula weight	1095.86
Temperature/K	100
Crystal system	trigonal
Space group	P-3c1
a/Å	22.0926(5)
b/Å	22.0926(5)
c/Å	43.5538(13)
α/°	90
β/°	90
γ/°	120
Volume/Å^3	18409.8(10)
Z	12
ρ_{calc}g/cm^3	1.186
μ/mm^{-1}	0.556
F(000)	6838.0
Crystal size/mm^3	0.01 × 0.01 × 0.01
Radiation	Synchrotron (λ = 0.700)
2Θ range for data collection/°	3.632 to 51.882
Reflections collected	73616
Independent reflections	12528 [R_{int} = 0.0888, R_{sigma} = 0.0425]
Data/restraints/parameters	12528/619/650
Goodness-of-fit on F^2	1.726
Final R indexes [I>=2σ (I)]	R_1 = 0.1516, wR_2 = 0.4605
Final R indexes [all data]	R_1 = 0.1820, wR_2 = 0.4868
Largest diff. peak/hole / e Å^{-3}	0.97/-0.65

$R_1 = (\Sigma\ ||F_o| - |F_c||/\Sigma\ |F_o|)$; $wR_2 = \{\Sigma[w(F_o^2 - F_c^2)^2]/\ \Sigma[w(F_o^2)^2]\}^{1/2}$; GOF = $\Sigma[w(F_o^2 - F_c^2)^2]/(n - p)\}^{1/2}$
where *n* is the number of data and *p* is the number of parameters refined.

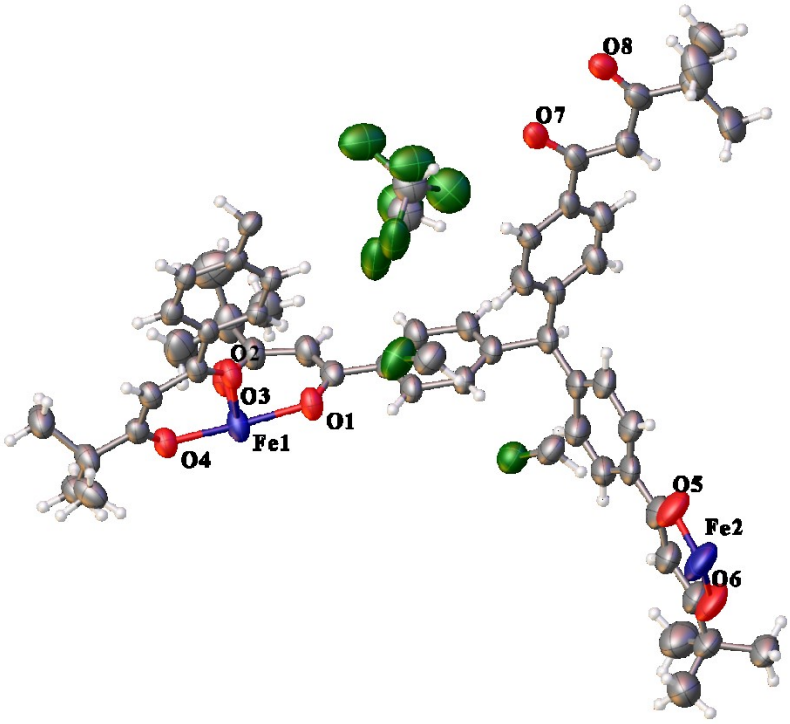

Figure 129. Asymmetric unit of **Fe7**·3$CHCl_3$ with thermal ellipsoids drawn at the 30% probability level. Colour code: Fe blue, O red, F light green, Cl dark green, C grey, H white.

Table 27. Selected bond distances in **Fe5**·2$CHCl_3$.

Atom	Atom	Length/Å	Atom	Atom	Length/Å
Fe1	O4	1.991(5)	Fe2	$O5^2$	1.978(11)
Fe1	$O7^1$	1.998(6)	Fe2	$O5^1$	1.978(11)
Fe1	O2	1.949(5)	Fe2	O5	1.979(11)
Fe1	O1	2.012(5)	Fe2	$O6^1$	2.010(11)
Fe1	$O8^1$	2.021(6)	Fe2	$O6^2$	2.010(12)
Fe1	O3	1.955(6)	Fe2	O6	2.010(12)

^{1}+Y-X,1-X,+Z; ^{2}1-Y,1+X-Y,+Z

Table 28. Selected angles in **Fe7**·3$CHCl_3$.

Atom	Atom	Atom	Angle/°	Atom	Atom	Atom	Angle/°
O4	Fe1	O1	173.2(2)	C50	O8	$Fe1^2$	127.2(5)
O4	Fe1	$O8^1$	93.6(2)	C5	O3	Fe1	132.5(5)
$O7^1$	Fe1	O1	85.1(2)	$O5^1$	Fe2	$O5^2$	84.4(4)
$O7^1$	Fe1	$O8^1$	85.4(2)	$O5^1$	Fe2	O5	84.4(4)
O2	Fe1	O4	86.4(2)	$O5^2$	Fe2	O5	84.4(4)
O2	Fe1	$O7^1$	90.2(2)	$O5^1$	Fe2	$O6^1$	85.8(4)
O2	Fe1	O1	87.1(2)	$O5^2$	Fe2	$O6^1$	97.2(4)
O2	Fe1	$O8^1$	175.7(3)	O5	Fe2	$O6^1$	169.9(5)

O2	Fe1	O3	94.6(3)	$O5^{1}$	Fe2	$O6^{2}$	169.9(5)
O1	Fe1	$O8^{1}$	92.7(2)	$O5^{2}$	Fe2	$O6^{2}$	85.8(4)
O3	Fe1	O4	95.4(2)	O5	Fe2	$O6^{2}$	97.2(4)
O3	Fe1	$O7^{1}$	170.8(2)	$O5^{2}$	Fe2	O6	169.9(5)
O3	Fe1	O1	87.2(2)	$O5^{1}$	Fe2	O6	97.2(4)
O3	Fe1	$O8^{1}$	89.7(3)	O5	Fe2	O6	85.8(4)
C32	O4	Fe1	129.5(4)	$O6^{1}$	Fe2	O6	92.8(4)
C48	O7	$Fe1^{2}$	126.3(5)	$O6^{1}$	Fe2	$O6^{2}$	92.8(4)
C34	O2	Fe1	130.9(4)	$O6^{2}$	Fe2	O6	92.8(4)
C7	O1	Fe1	128.7(5)				

^{1}+Y-X,1-X,+Z; ^{2}1-Y,1+X-Y,+Z

6.4 Powder X-ray diffraction.

PXRD measurements were carried out by means of a Bruker D8 Advance diffractometer equipped with a Göbel mirror and a Cu-Kα source (40 kV, 40 mA).

Sample has been obtained by evaporation of a chloroform/ethanol solution containing $\{[(PTAO)_2@[Cu_8][Cu_2]\}_\infty$. Simulated spectra has been obtained from single crystal X-ray diffraction data, with Mercury 3.6 software.

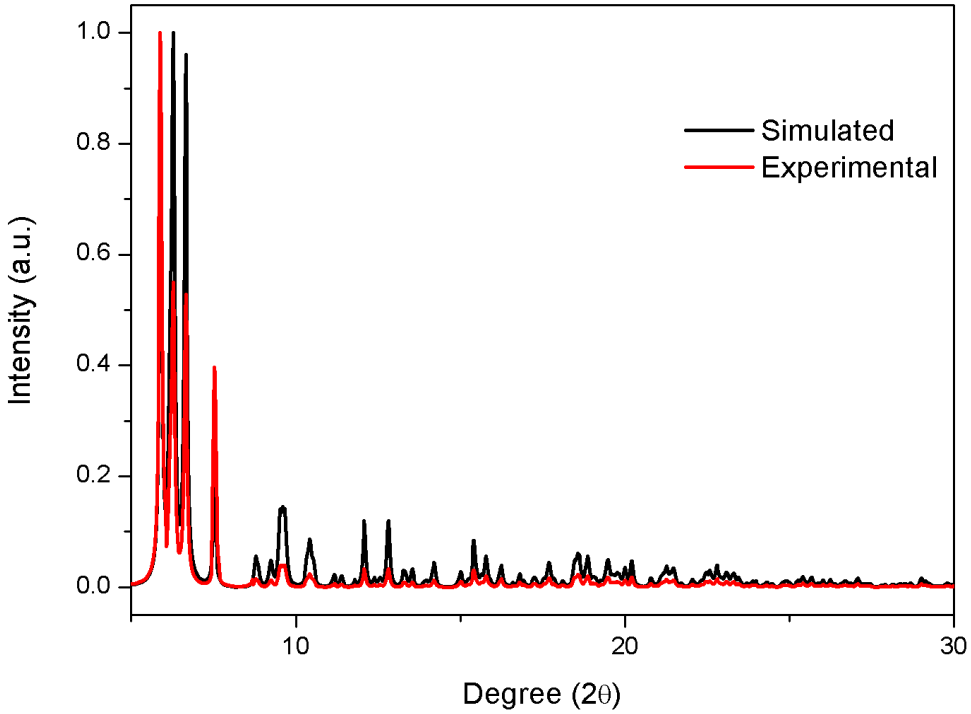

Figure 130. Experimental and simulated $\{[(PTAO)_2@[Cu_8][Cu_2]\}_\infty$ PXRD patterns (normalized intensity).

6.5 ESI-MS analysis.

ESI-MS analyses and mass spectra were performed with an Agilent Technologies 1100 Series system, equipped with binary pump (G1312A) and MSD SL Trap mass spectrometer (G2445D SL) with ESI source or using a LCQ DECA ion trap instrument (ThermoFisher Scientific, San Josè, CA, USA), operating in positive ion mode. The entrance capillary temperature was 280 °C and the capillary voltage was 4 kV. The compounds under study have been dissolved in acetonitrile or in methanol to obtain a 10^{-6} M concentration. The solution was introduced into ESI ion source by direct infusion at a flow rate of 10 µL/min. The He pressure inside the trap was kept constant. The pressure directly read by ion gauge, in the absence of the N_2 stream, was $2.8 \cdot 10^{-5}$ torr. MS/MS experiments were performed by resonant excitation of the ion of interest through a supplementary radio frequency voltage in the range 30-35% of its maximum value (5 V peak-to peak). The isolation width was set at 1 mass unit.

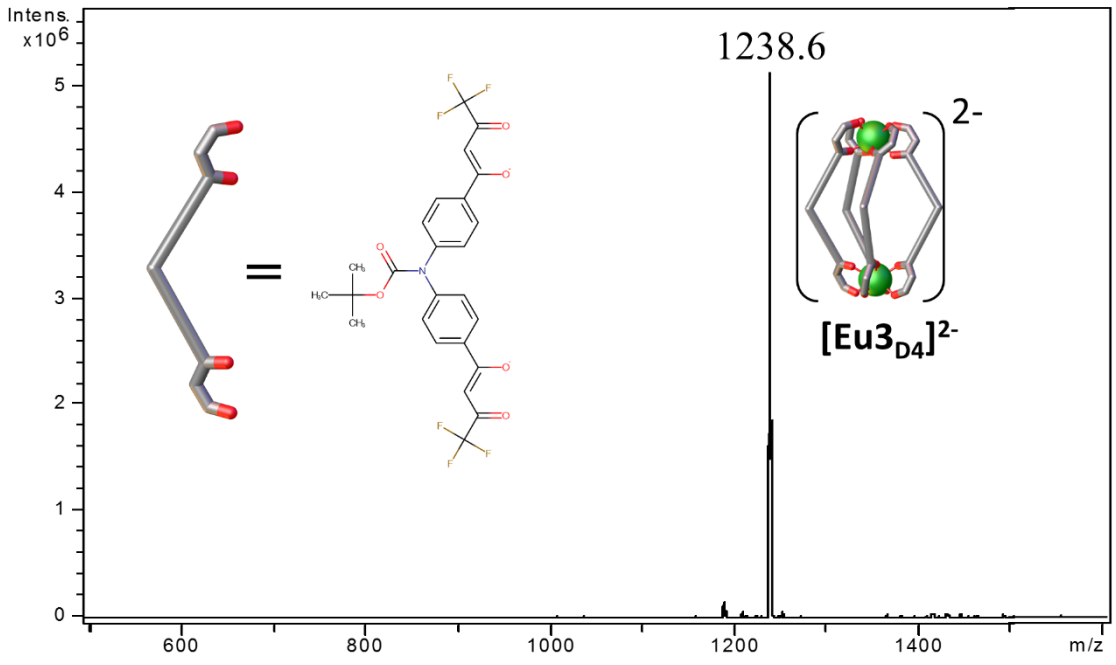

Figure 131. ESI-MS analysis for **$[Eu3_{D4}]^{2-}$**.

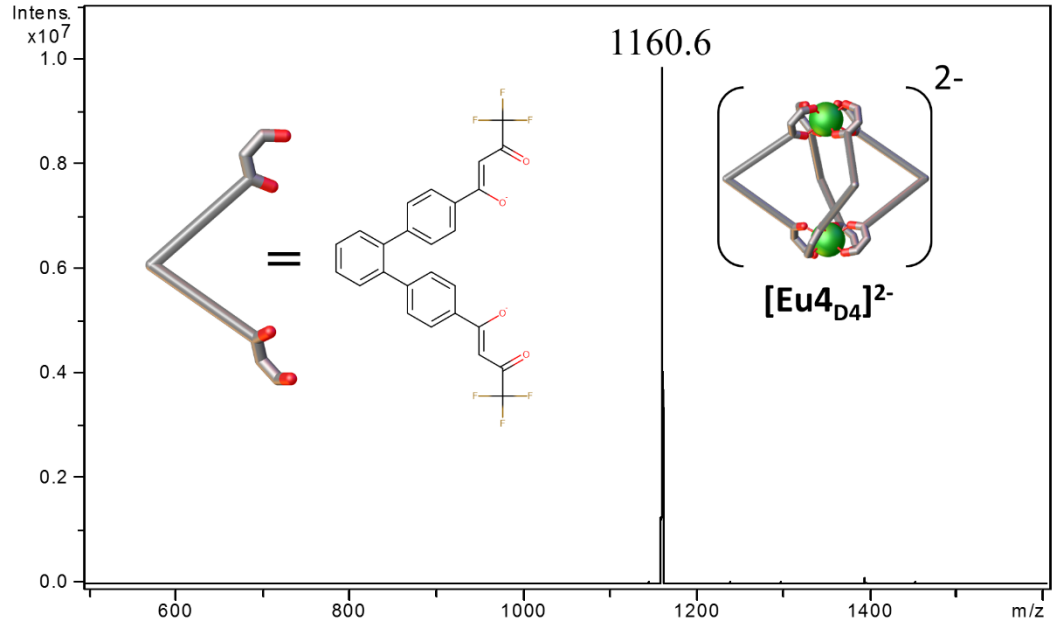

Figure 132. ESI-MS analysis for $[Eu4_{D4}]^{2-}$.

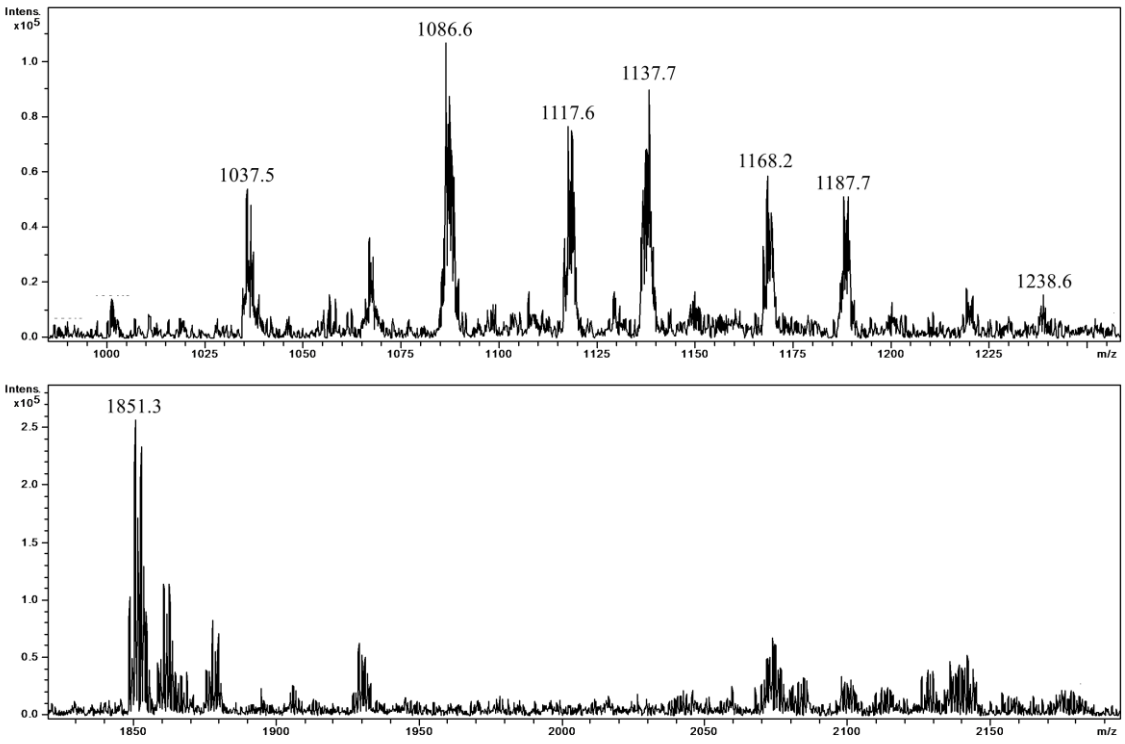

Figure 133. ESI-MS analysis for the self-sorting experiment of Eu^{3+} ion with ligands **1**, **3** and **4**.

Table 29. Molecular peaks for the self-sorting experiment.

Self-sorted cage	Molecular peaks
[Eu1$_{D4}$]$^{2-}$	1037.5
[Eu$_2$(**1**)$_3$(**3**)]$^{2-}$	1086.6
[Eu$_2$(**1**)$_3$(**3**)]$^{2-}$ + 2 MeOH	1117.6
[Eu$_2$(**1**)$_2$(**3**)$_2$]$^{2-}$	1137.7
[Eu$_2$(**1**)$_2$(**3**)$_2$]$^{2-}$ + 2 MeOH	1168.2
[Eu$_2$(**1**)$_1$(**3**)$_3$]$^{2-}$	1187.7
[Eu3$_{D4}$]$^{2-}$	1238.6
[Eu4$_{D3}$]$^{-}$ + 2 H$_2$O	1851.3

6.6 Bibliography.

1 P. Gans, A. Sabatini, A. Vacca, *Talanta* **1996**, *43*, 1739.

2 M. Rancan, J. Tessarolo, P. L. Zanonato, R. Seraglia, S. Quici and L. Armelao, *Dalton Trans.*, **2013**, *42*, 7534.

3 M. Rancan, J. Tessarolo, M. Casarin, P. L. Zanonato, S. Quici and L. Armelao, *Inorg. Chem.*, **2014**, *53*, 7276.

4 G. M. Sheldrick, *Acta Crystallogr*., **2008**, *A64*, 112.

5 G. M. Sheldrick, *Acta Crystallogr*., **2015**, *A71*, 3.

6 O. V. Dolomanov, L. J. Bourhis, R. J. Gildea, J. A. K. Howard and H. Puschmann, *J. Appl. Crystallogr.*, **2009**, *42,* 339.

Acknowledgments

At first I would like to thank the Ca.Ri.Pa.Ro foundations for granting me a Ph.D. scholarship. Then I would like to thank Prof. Lidia Armelao and Dr. Marzio Rancan from the ICMATE-CNR institute in Padova, for supervising my Ph.D. project. My deepest thanks goes to Dr. Silvio Quici and his research group at the ISTM-CNR institute in Milano, for the great help on the synthesis of all the ligands used in this work and for all the precious advices. I would like to thank all the people that helped me, giving an important contribution to this research work: Prof. Pier Luigi Zanonato from the University of Padova, for the help in the determination of the thermodynamic parameters of the copper-based systems; Dr. Alfonso Venzo from the ICMATE-CNR institute in Padova, Dr. Ileana Menegazzo from the University of Padova and Dr. Marco Cavazzini from the ISTM-CNR institute in Milano, for the help with the NMR measurements and interpretations; Dr. Roberta Seraglia from the ICMATE-CNR institute in Padova, Dr. Andrea Mattarei and Dr. Matteo Romio from the University of Padova, for the help with ESI-MS measures, Dr. Doriano Lamba from the IC-CNR institute in Trieste for the precious help with the X-ray diffraction beamline of the Elettra Synchrotron, Dr. Cristian Pezzato from the Northwestern University in Evanston and Dr. Luca Gabrielli from the University of Padova for the helpful discussions. Finally, I would like to thank Prof. Gateano Granozzi from the University of Padova, for the great work done as coordinator of the Ph.D. course in science and engineering of materials and nanostructures.